

Hydroelastic response of Very Flexible free Floating Structures in Faraday waves

Bram Christiaens

Thesis for the degree of MSc in Marine Technology in the specialization
of Ship Hydromechanics

Hydroelastic response of Very Flexible free Floating Structures in Faraday waves

By

Bram Christiaens

This thesis MT.25/26.003.M is classified as confidential in accordance
with the general conditions for projects performed by the TU Delft.

Tuesday, October 7, 2025

Thesis Examination Committee

Chair / Responsible Professor:	Dr.-Ing.	S. Schreier
Thesis Supervisor:	Prof.dr.ir.	W. van de Water
Committee Member:	Prof.dr.ir.	J. Westerweel
Co-supervisor / Project Mentor:	Ir., PhD candidate	H. Pot

Author details

Study number: 5319420

Abstract

This study investigates the hydroelastic response of very flexible, free floating structures in Faraday waves, with a focus on the influence of sheet thickness. The motivation for this work arises from the need to understand wave-structure interactions involving very flexible floating structures (VFFS), which are relevant for applications such as (offshore) floating photovoltaic panels ((O)FPV).

Laboratory-scale experiments were conducted using vertically oscillated membranes of varying thicknesses ($20\text{ }\mu\text{m}$ to $200\text{ }\mu\text{m}$) floating on a water surface. To ensure a reliable comparison and establish baseline measurements, free-surface reference experiments were first performed using silicone oil, which provided controlled conditions with minimal contamination effects. Additional experiments on deionized water allowed for direct comparison between hydroelastic and purely fluid cases. The experimental setup combined imaging, digital image correlation (DIC), and synthetic Schlieren methods to capture the coupled wave-membrane dynamics. These techniques provided quantitative measurements of both membrane deformation and underlying wave fields, including amplitudes and wavelengths, across a range of excitation frequencies and acceleration amplitudes. This enabled precise determination of the onset of Faraday-wave instabilities and a detailed characterization of the spatial deformation patterns of the floating membranes.

The results demonstrate a strong dependence of hydroelastic behavior on sheet thickness. Increasing thickness enhances the bending stiffness and inertia of the membrane, resulting in longer dominant wavelengths, higher critical accelerations, and modified wave amplitudes compared to very thin membranes. For the thinnest membranes, classified as VFFS, localized wrinkles were observed at low excitation frequencies. Their presence indicates dynamic stress variations and local in-plane tensions induced by wave-membrane interactions, phenomena not captured by standard continuum models. Furthermore, the onset of instabilities and wave amplitude behavior for thicker membranes revealed the combined effects of increased mass and bending stiffness, highlighting the transition from highly compliant to more rigid floating regimes.

Taken together, these findings provide experimental evidence for the critical role of sheet thickness in governing hydroelastic response. The results clarify how very flexible floating structures interact with surface waves and how this interaction evolves as thickness increases. Beyond fundamental fluid-structure physics, this work offers practical insights for the design and modeling of VFFS in engineering applications, such as optimizing the stability of floating photovoltaic modules, controlling wave-induced motion of thin maritime membranes.

Preface

The topic of this thesis emerged naturally from my strong interest in fluid-structure interactions. Within the Marine Technology master's program, I especially enjoyed the course *Fluid-Structure Interaction in Maritime Structures* (MT44090), which offered a first look on the coupling between hydrodynamic forces and structural responses. Although I originally planned to graduate within the fluid mechanics track, I also developed a growing interest in structural engineering through several related courses. The fluid-structure interaction provided the ideal middle ground, allowing me to combine both fields that appealed to me the most.

This graduation project also connected to my earlier academic interests in sustainability. During my bachelor's degree, I completed the minor *Climate Change Adaptation and Mitigation* and participated in the honors program, where I took interdisciplinary courses such as *Can We Cool Down the Earth?* and *Sustainability*, offered in collaboration with the University of Rotterdam and Leiden University. Bringing together technical expertise and the environmental challenge of developing offshore floating solar solutions made this project particularly meaningful to me.

Working on this research has helped me grow into a more critical and reflective student. In the beginning, I found it challenging to assess papers or calculations with a critical eye. I often got caught up in doing things simply because they seemed useful, without always stepping back to consider whether they were essential to the research question. It took time to define a clear research direction, and that lack of clarity made it harder to evaluate my own progress at times. However, over time, I learned to better distinguish between what was important and what was merely interesting, which ultimately helped me refine both the scope and focus of my work.

The setup and conduct of the experiment came with its own set of challenges. Although I am usually fairly realistic in planning, I experienced significant delays. Building the setup was more time-consuming than expected; getting everything in the right place and ensuring it functioned properly involved many trial-and-error moments. Since the setup had not been used before at the Department of Maritime & Transport Technology (M&TT), I encountered issues that required creative and sometimes unconventional solutions. These setbacks turned out to be highly instructive: they taught me to pay close attention to measurement accuracy and to focus on capturing the data I actually needed. I eventually decided to run small tests and analyze the results immediately, rather than collecting everything first and reviewing it only afterward. This iterative approach worked well for me. Over the course of several weeks, I performed various preliminary tests and adjusted the setup based on what I learned. Looking back, I am glad I approached it this way, as it allowed the experimental phase to evolve naturally with the insights gained.

I express my sincere gratitude to my supervisors, Professor Willem van de Water and PhD candidate Hanna Pot, for their invaluable guidance, encouragement, and support throughout this research. I am also thankful to Professor Sebastian Schreier for his supervision and advice at the Department of Maritime & Transport Technology, Faculty of Mechanical Engineering (ME), TU Delft. Special thanks go to the staff and colleagues at the Ship Hydromechanics Lab, whose assistance was essential in setting up and conducting the experiments. Finally, I would like to acknowledge the helpful role of AI tools such as ChatGPT, which supported code development and language refinement, thereby facilitating the writing process of this thesis.

*Bram Christiaens
Delft, October 2025*

Contents

List of Figures	xi
List of Tables	xiii
Nomenclature	xv
1 Introduction	1
2 Literature review and theoretical background	5
2.1 Motivation from floating photovoltaic systems	5
2.2 Fluid-Structure Interactions with Very Flexible Floating Structures	5
2.3 Experimental investigations of Fluid-Structure Interactions	6
2.3.1 Large-scale hydroelastic models	6
2.3.2 Simplified elastic sheets	7
2.3.3 Thin and compliant membranes	7
2.3.4 Modern optical measurement techniques	7
2.3.5 Summary and link to present work.	7
2.4 Fundamentals of Faraday waves	7
2.4.1 Classical description	7
2.4.2 Viscous effects and dispersion relation	7
2.4.3 Elastic sheet extensions	8
2.4.4 Summary and relevance	9
2.5 Challenges of scaling in laboratory studies	9
2.6 Summary and knowledge gaps	10
3 Methodology	11
3.1 Measurement Objectives and Target Ranges	11
3.2 Experimental setup	13
3.2.1 Motion control and data acquisition	13
3.2.2 Imaging system	14
3.2.3 Floating structure preparation, deployment and characterization	14
3.2.4 Working fluids and tank configuration	15
3.3 Optical method: Synthetic Schlieren	16
3.3.1 Principle	16
3.3.2 Implementation	16
3.4 Analysis methods	20
3.4.1 Analytical fluid-fluid Faraday instability model	20
3.4.2 Wavelength derivation	21
3.4.3 Critical acceleration derivation	26
3.4.4 Surface reconstruction and amplitude estimation	28
3.5 Experimental procedure and data treatment	29
3.6 Accuracy assessment	31
3.6.1 Liquid depth uncertainty	31
3.6.2 Multifunction synthesizer uncertainty	31
3.6.3 Laser distance meter uncertainty	32
3.6.4 Accelerometer and acceleration measurement uncertainty	32
3.6.5 Uncertainty propagation from images to wavelength	32

4	Results	39
4.1	DIC observations	39
4.2	Wavelength measurements	42
4.2.1	Silicone oil	42
4.2.2	Deionized water	42
4.3	Critical acceleration measurements	44
4.3.1	Silicone oil	44
4.3.2	Deionized water	44
4.4	Wave amplitude estimates	45
5	Discussion and Analysis of the Results	49
5.1	Validation with silicone oil	50
5.2	Deviation from theory for free surface deionized water	51
5.3	Dispersion relation deionized water with floating films	52
5.4	Wrinkle formation in thin membranes	55
6	Conclusion	57
7	Recommendations	59
7.1	Fluid selection and material compatibility	59
7.2	Imaging methodology and optical setup	59
7.3	Trigger synchronization and measurement procedure	60
7.4	Experimental scope and coverage	60
7.5	Future outlook	61
	Bibliography	63
A	Derivation of the linear gravity wave dispersion relation	67
A.1	Finite depth	67
A.1.1	Wave velocity potential	67
B	Derivation of the linear capillary wave dispersion relation	73
B.1	Finite depth	73
C	Derivation of the linear gravity-capillary wave dispersion relation	77
C.1	Finite depth	77
D	Derivation of the fluid–structure dispersion relation based on Euler-Bernoulli beam theory and linear gravity wave theory	81
D.1	Finite depth	81
D.1.1	Governing equation	81
D.1.2	Dispersion relation	83
E	Derivation of the fluid–structure dispersion relation based on Kirchhoff-Love beam theory and linear gravity wave theory	85
E.1	Finite depth	85
E.1.1	Governing equation	85
E.1.2	Dispersion relation	87
F	Derivation of the fluid–structure dispersion relation based on Föppl–von Kármán plate theory and linear gravity wave theory	89
F.1	Finite depth	89
F.1.1	Governing equation	89
F.1.2	Dispersion relation	91
F.2	Full Cauchy stress tensor	93
F.2.1	Governing equation	93
F.2.2	Dispersion relation	94
F.3	Oblique waves incidence	97
F.3.1	Governing equation	97
F.3.2	Dispersion relation	98
F.3.3	Special cases	100

G	Device and Material Specifications	103
G.1	Function generator NF Electronics Instruments 1930A.	104
G.2	DC power supply Tenma 72-10480 (0–30 V, 3 A).	106
G.3	Vibration exciter Brüel & Kjær Type 4808	108
G.4	Power amplifier Brüel & Kjær Type 2719	111
G.5	Micro-Epsilon optoNCDT ILD 1420-200 laser distance sensor	114
G.6	PCB Piezotronics Model 482B11 ICP signal conditioner	117
G.7	Silicone oil 5 cSt	119
G.8	ELASTOSIL® Film 2030	122
H	Camera calibration	125
H.1	Silicon oil setup	125
H.2	Deionized water setup	126
I	Validation of phase-locked imaging	127
J	Convergence study: wavelength stabilization	133
J.1	Test setup	133
J.2	Results	133
J.3	Discussion and conclusion	134
J.4	Figures	135
J.4.1	Deionized water at 60 Hz.	135
J.4.2	Deionized water with 20 μm floating film at 60 Hz.	136
J.4.3	Deionized water with 50 μm floating film at 60 Hz.	136
J.4.4	Deionized water with 100 μm floating film at 60 Hz	137
K	Convergence study: radial bin size	139
K.1	Test setup	139
K.2	Results	139
K.3	Discussion and Conclusion	140
K.4	Figures	141
K.4.1	Deionized water at 60 Hz.	141
K.4.2	Deionized water with 20 μm floating film at 60 Hz.	141
K.4.3	Deionized water with 50 μm floating film at 60 Hz.	142
K.4.4	Deionized water with 100 μm floating film at 60 Hz	142
L	Accelerometer calibration	143
L.1	Test setup	143
L.2	Calibration accuracy	143
L.3	Results	144
L.3.1	Check repeatability	146
L.4	Accelerometer calibration data.	147
L.4.1	Overview measured data repetition 1	147
M	DIC noise	149
M.1	Uncertainty in DIC Measurements	149
N	Signal extraction from laser distance measurements	153
N.1	Test setup	153
N.2	Results	153
N.3	Discussion and conclusion.	154
O	Signal Extraction from Accelerometer Measurements	155
O.1	Test setup	155
O.2	Results	155
O.3	Discussion and Conclusion	156

P	Measured displacement at different sample intervals	157
Q	Measured voltage at different sample intervals	161
R	Wavelength uncertainty data	165

List of Figures

1.1	Comparison of hydroelastic response diagrams of floating structures	4
2.1	Example: Faraday wave stability boundaries (glycerine–water mixture)	8
2.2	Example: Faraday wave stability: theory vs. experiment	9
3.1	Predicted Faraday wave stability for silicone oil–air system	12
3.2	Experimental setup: perspective and right views	13
3.3	Measured and theoretical wrinkle wavelengths vs film thickness	15
3.4	Synthetic Schlieren experimental setup: overview and zoom	16
3.5	Example: phase-locked acquisition of subharmonic surface motion (even frequency divider value)	18
3.6	Example: phase-locked acquisition of subharmonic surface motion (odd frequency divider value)	19
3.7	Faraday wave stability diagram of water–air system at 30 Hz	20
3.8	Predicted Faraday wave stability for water–air system	21
3.9	Example: DIC images for silicone oil at 80 Hz	22
3.10	Example: synthetic surface height field	23
3.11	Example: synthetic displacement fields derived from surface height	23
3.12	2D and radially averaged spectra of experimental and synthetic displacement fields	25
3.13	Example: simulated surface displacement fitted with logistic growth	27
3.14	Effect of frame selection on logistic fit for onset time	27
3.15	Accuracy of dominant wavelength measurements	37
4.1	Displacement fields for free surface water and silicone oil at 60 Hz	40
4.2	Displacement fields showing localized wrinkles for deionized water with 20 μm and 50 μm membranes at 30 Hz	40
4.3	Displacement fields for deionized water with elastic membranes at 60 Hz	41
4.4	Faraday wave wavelengths in silicone oil (free surface)	43
4.5	Faraday wave wavelengths in deionized water (free surface and covered with elastic membranes)	43
4.6	Measured accelerations for Faraday waves in silicone oil (free surface)	44
4.7	Critical accelerations for Faraday waves in deionized water (free surface and covered with elastic membranes)	45
4.8	Reconstructed surfaces for deionized water and silicone oil at 60 Hz	46
4.9	Reconstructed surfaces showing localized wrinkles for deionized water with 20 μm and 50 μm membranes at 30 Hz	46
4.10	Reconstructed surfaces for deionized water with elastic membranes at 60 Hz	47
5.1	Comparison of hydroelastic response diagrams including tested films	49
5.2	Mean Faraday wave wavelengths of (free surface) silicone oil and deionized water compared with theoretical dispersion relations	50
5.3	Critical acceleration for Faraday waves in (free surface) deionized water compared with theoretical values	51
5.4	Comparison of measured Faraday wave wavelengths with theoretical predictions of Faraday wave FSI dispersion relation, including damping	53
5.5	Comparison of measured Faraday wave wavelengths with theoretical predictions of FvK–linear wave dispersion relation, including additional tension term	54
5.6	Comparison of measured Faraday wave wavelengths with theoretical predictions of Faraday wave FSI dispersion relation, including additional tension term	54

5.7	Analysis of localized wrinkles in a 20 μm elastic membrane at 30 Hz	55
-----	--	----

List of Tables

3.1	Physical properties of working fluids	15
3.2	Acquisition settings for different excitation frequencies	30
5.1	Overview of material and wave properties, tensions, and fitted coefficients	53

Nomenclature

$\delta\lambda_{\text{DIC}}$	Contribution to wavelength uncertainty from DIC noise (px)
$\delta\lambda_{\text{FFT}}$	Contribution to wavelength uncertainty from FFT grid spacing (px)
$\delta\lambda_{\text{mm}}$	Wavelength uncertainty in millimetres (mm)
$\delta\lambda_{\text{px}}$	Wavelength uncertainty in pixels (px)
$\delta\lambda_{\text{rad}}$	Contribution to wavelength uncertainty from radial-bin quantisation (px)
δa_a	Uncertainty in acceleration amplitude [g]
δC	Uncertainty in calibration factor of the accelerometer [mV/g]
Δd	Change in displacement [m,px]
δf_{DIC}	Frequency uncertainty from DIC noise (px^{-1})
δf_{FFT}	Frequency uncertainty due to FFT grid spacing (px^{-1})
δf_{px}	Total frequency uncertainty combining all contributions (px^{-1})
δf_{rad}	Frequency uncertainty from radial-bin quantisation (px^{-1})
δh	Uncertainty in liquid height [m]
δp	Uncertainty in pixel size calibration (mm/px)
δV	Uncertainty in volume [m^3]
δ	Damping factor [-]
ϵ	Wave steepness [-]
η	Dynamic viscosity []
γ	m_A/ρ [m]
λ	Wavelength [m]
λ_{mm}	Wavelength in millimetres (mm)
λ_{px}	Wavelength in pixels (px)
λ_c	Characteristic length [m]
λ_{crit}	Critical wavelength [m]
\mathcal{F}	Fourier transform
d_x	DIC displacement in x -direction [m]
d_y	DIC displacement in y -direction [m]
ν	Poisson's ratio [-]
ω	Angular frequency of the fluid surface [1/s]
ω_s	Angular frequency of the shaker [1/s]

ϕ	Velocity potential [m ² /s]
ρ	Fluid density [kg/m ³]
ρ_e	Material density [kg/m ³]
σ_{DIC}	DIC noise standard deviation [px]
$\tilde{\nu}$	Kinematic viscosity [m ² /s]
$\tilde{\zeta}(x, y)$	Complex displacement field
ζ	Surface elevation [m]
$\zeta(x, y)$	Surface elevation in function of x and y [m]
ζ_a	Surface elevation amplitude [m]
A	Cross-sectional area of the container [m ²]
a	Vertical acceleration [m/s ²]
a_a	Vertical acceleration amplitude [m/s ²]
a_{crit}	Critical acceleration [m/s ²]
B	Plate bending stiffness [N m]
C	Calibration factor of the accelerometer [mV/g]
c_w	Wave velocity [m/s]
D	Diameter of the container [m]
d	Plate thickness [m]
d_0	Initial displacement [m,px]
DFT	Discrete Fourier Transform
DIC	Digital Image Correlation
E	Young's modulus [Pa]
f_{peak}	Dominant spatial frequency corresponding to the peak (px ⁻¹)
f_r	Radial spatial frequency [px]
f_s	Frequency of the shaker, excitation frequency [Hz]
f_x	Spatial frequency in x -direction [px]
f_y	Spatial frequency in y -direction [px]
FFT	Fast Fourier Transform
FPV	Floating Photovoltaic
FSI	Fluid-Structure Interaction
FvK	Föppl–von Kármán
H	Harmonic
h	Height of liquid layer [m]
K	Growth rate [1/s]

k	Angular wavenumber, wavenumber [1/m]
k_H	Harmonic wavenumber [1/m]
k_{crit}	Critical wavenumber [1/m]
k_{SH}	Subharmonic wavenumber [1/m]
m_A	Mass per unit area [kg/m ²]
N	Number of DIC points
N_{bin}	Number of radial bins used in spectral averaging
P	Pressure [Pa]
p	Pixel size (mm/px)
P_0	Atmospheric pressure [Pa]
P_{ext}	External pressure [Pa]
<i>PDMS</i>	Polydimethylsiloxaan
<i>PV</i>	Photovoltaic
r	In-plane (horizontal) position vector (x, y) [m]
R_1, R_2	Principle radii of curvature [m]
<i>RSS</i>	Root-Sum-Square
s	Subset setp in pixels [px]
s	Subset step spacing in DIC analysis (px)
<i>SH</i>	Subharmonic
T	Nondimensionalized time [–]
t	Time [s]
t_0	Onset time [s]
u	Velocity in x -direction [m/s]
V	Liquid volume [m ³]
v	Velocity in y -direction [m/s]
V_a	Voltage amplitude [V]
<i>VFFS</i>	Very Flexible Floating Structures
<i>VLFS</i>	Very Large Floating Structures
w	Velocity in z -direction [m/s]
x	Horizontal coordinate in the x -direction [m]
y	Horizontal coordinate in the y -direction [m]
z	Vertical coordinate [m]
z_a	Vertical displacement amplitude [m]
<i>BEM</i>	Boundary Element Method
<i>FEM</i>	Finite Element Method
<i>SEM</i>	Standard Error of the Mean

Introduction

The world urgently needs to scale up renewable energy solutions to address the growing impacts of climate change. The decade leading up to 2023 has been the warmest in recorded history, with the ten-year average global temperature (2014-2023) surpassing all previous records (World Meteorological Organization, 2023). 2024 set a new record as the warmest year on record, with global mean temperatures estimated at approximately 1.55 °C above pre-industrial levels (World Meteorological Organization, 2025b). Looking ahead, the World Meteorological Organization projects an 80 % likelihood that at least one year between 2025 and 2029 will exceed this 2024 record, underscoring the clear upward trajectory of global temperatures (World Meteorological Organization, 2025a). These rising temperatures emphasize the critical need for sustainable energy solutions to reduce greenhouse gas emissions, which are primarily driven by fossil fuel combustion. Fossil fuels account for over 75 % of global greenhouse gas emissions, and their continued use contributes significantly to the devastating impacts of climate change (Marouani, 2024).

Renewable energy offers a promising pathway to mitigate these impacts. Studies show a clear correlation between the adoption of renewable energy and decreased temperature anomalies, indicating that scaling up renewable energy could help limit global warming (Abidi & Nsaibi, 2024). Renewable energy is defined as energy derived from natural sources that are replenished at a rate faster than they are consumed, such as wind, solar, and hydropower (United Nations, 2024). Wind and sunlight, in particular, are abundant, inexhaustible resources that offer vast potential for clean energy production. However, a major challenge in harnessing these resources is intermittency, as fluctuations in energy generation can make it difficult to maintain a stable and reliable electricity supply (Oliveira-Pinto & Stokkermans, 2020; Trapani & Santafé, 2014; Wu & West, 2024).

One of the most widely adopted renewable technologies is solar photovoltaic (PV) energy. PV cells harness the photovoltaic effect, first observed by Edmond Becquerel in 1839, and have since undergone significant improvements in efficiency and affordability (Chu & Tarazano, 2017). Traditionally, PV panels are installed on rooftops or ground-mounted on large pieces of land for grid-scale electricity production (Sahu et al., 2016). However, as land availability becomes increasingly constrained, attention has shifted toward alternative deployment strategies.

Floating solar technology has emerged as a compelling solution. By placing PV panels on water bodies, this approach maximizes surface area without competing for land and offers performance benefits due to the natural cooling effect of water (Sahu et al., 2016). The first widely implemented floating solar systems were pontoon-based arrays deployed in Japan in 2007 at the National Institute of Advanced Industrial Science and Technology (Claus & López, 2022; Oliveira-Pinto & Stokkermans, 2020; Trapani & Santafé, 2014). These platforms are typically limited to calm inland waters, where the risk of wave-induced damage is low. In addition to preserving land, pontoon-based floating solar systems can reduce water evaporation from reservoirs and enhance energy efficiency (Sahu et al., 2016). Despite these advantages, they are typically restricted to calm inland waters and can compete with existing human uses or impact local ecosystems. Consequently, pontoon-based systems are not well-suited to the open ocean, leaving vast marine areas untapped for solar deployment.

Addressing this limitation requires new structural concepts capable of withstanding dynamic water

environments. One promising approach is the development of ultra-thin, flexible floating solar panels made from amorphous silicon photovoltaic materials (Claus & López, 2022; Oliveira-Pinto & Stokkermans, 2020; Trapani et al., 2013). Unlike rigid, pontoon-supported systems, these panels are designed to move passively with surface waves. Their natural buoyancy and compliant structure eliminate the need for pontoons and allow scalable deployment on open ocean surfaces.

However, this flexibility introduces a new set of challenges. These structures behave fundamentally differently from conventional very large floating structures (VLFS), whose hydroelastic responses are relatively well characterized. Thin, compliant solar panels enter an underexplored regime of fluid-structure interaction (FSI), where traditional models may no longer apply. Unlike wave energy converters, which are engineered to extract energy from wave motion, these floating panels aim to minimize wave-induced stress and deformation (Trapani et al., 2013).

Understanding how very flexible floating structures (VFFS) interact with surface waves is essential, both from a mechanical standpoint and from a fundamental FSI perspective. Ultra-thin, compliant structures experience large deformations under wave forcing, and their energy absorption, damping behavior, and internal stress distribution remain largely unexplored. The design of such structures therefore, challenges existing FSI models and calls for new approaches to wave-structure coupling.

Historically, the behavior of floating structures under surface waves has been studied extensively for rigid or semi-rigid platforms, such as pontoons and VLFS. For instance, the Megafloat project in Japan examined hydroelastic responses of large, stiff platforms under wave forcing (Suzuki, 2005), while floating ice sheets have served as natural analogues for large-scale hydroelastic analysis (Zeng et al., 2021). Squire (2008) highlighted the similarities between floating ice dynamics and VLFS hydroelasticity, typically modeled using classical linear theories.

Conventional floating structures, such as pontoons and VLFS, have relatively high thickness-to-length ratios and exhibit limited deformation. In contrast, the thin, flexible photovoltaic sheets proposed for offshore deployment represent a distinct regime: extreme flexibility and low bending stiffness mean that even moderate wave forcing can induce significant deformation. At offshore scales, the dominant restoring forces are gravitational, and capillary effects are negligible. The relevant physics at this scale are hydroelastic in nature, governed primarily by membrane tension, bending stiffness, and gravity-driven fluid motion.

Studying these interactions directly at full scale is experimentally challenging due to infrastructure requirements, environmental variability, and limited control over wave forcing. To gain mechanistic insight, this study employs small-scale laboratory experiments using Faraday waves. These standing waves, generated by vertical oscillation of a fluid layer above a critical threshold (Miles & Henderson, 1990), provide a controlled platform to probe fundamental mechanisms such as deformation, energy dissipation, and wave-structure coupling in flexible membranes. Crucially, these Faraday wave experiments are used as a tool to understand hydroelastic response, rather than as an end in themselves, analogous to conventional wave flumes or large-scale wave tanks in hydrodynamics research.

The relevance of small-scale Faraday experiments to offshore structures lies in dimensionless scaling and the relative balance of forces. While offshore-scale waves are dominated by gravity, small-scale Faraday waves often operate in a capillary-gravity regime, where surface tension influences the wave response. Despite this difference, the underlying hydroelastic mechanisms, bending, membrane tension, and wave-induced deformation, can still be probed in the laboratory by carefully selecting material properties, fluid depth, and forcing parameters. A central concept in fluid-structure interaction (FSI) modeling is the characteristic length scale,

$$\lambda_c = 2\pi \left(\frac{B}{\rho g} \right)^{1/4}, \quad (1.1)$$

which relates bending stiffness B to gravitational wave forcing ρg and determines whether a floating structure behaves more like a rigid plate or a deformable membrane (Suzuki & Yoshida, 1996; Suzuki et al., 2007; Zhang & Schreier, 2022) (Figure 1.1). By matching the ratio of the sheet length (L) to λ_c in the laboratory to that of full-scale structures, experiments reproduce the relative balance of elastic and hydrodynamic forces, allowing key deformation patterns, damping behavior, and wave-structure interactions to be explored. In this way, Faraday experiments provide a tractable means to study

extreme-flexibility regimes that would otherwise be difficult to isolate at full scale, despite the differences in absolute scales and capillary effects.

Building on the insights gained from dimensionless scaling and characteristic length considerations, this study focuses on how the physical properties of floating flexible sheets govern their hydroelastic response. In particular, sheet thickness is chosen as the primary control parameter, as it governs bending stiffness ($B \sim h^3$) and defines a characteristic length scale (λ_c). Varying thickness systematically modifies the relative magnitude of elastic to hydrodynamic forces, allowing exploration of different hydroelastic regimes relevant to floating structures of various scales. Understanding the role of thickness is therefore key to predicting deformation patterns, damping behavior, and wave–structure interactions across different regimes of flexibility. This motivation leads naturally to the primary research question:

Primary research question: How does the thickness of a Very Flexible free Floating Structure influence its hydroelastic response in Faraday waves?

To explore this question in detail, the following sub-questions are addressed:

- How does sheet thickness modify the dispersion relation of surface waves, and how can the relative contributions of gravity, inertia, and tension be identified?
- How does sheet thickness influence the critical acceleration threshold for wave excitation, and what role do inertia and bending rigidity play in setting this threshold?

To investigate these questions, lab-scale Faraday-wave experiments provide a controlled platform to isolate the effects of sheet thickness on hydroelastic response. Unlike full-scale ocean experiments or rotating tank experiments, Faraday setups allow precise control over wave amplitude, frequency, and fluid properties, enabling systematic exploration of the coupling between fluid motion and membrane flexibility. By matching dimensionless parameters such as the ratio sheet length (L) to the characteristic length scale (λ_c), these experiments reproduce the relevant force balance and deformation regimes observed in full-scale floating photovoltaic structures. Lab-scale experiments using vertically oscillated floating films of varying thicknesses are conducted to isolate the influence of structural flexibility on hydroelastic response.

It is hypothesized that increasing sheet thickness will modify the wave dispersion characteristics, leading to a longer critical wavelength at onset, consistent with observations by (Schreier & Jacobi, 2021). Second, thicker sheets are expected to exhibit a higher critical acceleration threshold for wave excitation due to added bending stiffness and inertia, which enhances hydroelastic damping and increases the energy required for the sheet to respond to wave forcing. Finally, because the wave amplitude is measured at onset and different sheets require different forcing, it is anticipated that increasing thickness will also lead to larger wave amplitudes in the coupled sheet-fluid system.

The remainder of this thesis is organized as follows. Chapter 2 reviews the literature on fluid–structure interactions, Faraday waves, and hydroelastic wave phenomena. Chapter 3 presents the methodology, including the experimental setup, instrumentation, data acquisition and processing techniques, as well as a discussion of measurement accuracy. Chapter 4 reports the experimental results, focusing on wavelength measurements and their repeatability, acceleration thresholds and repeatability, and amplitude responses. Chapter 5 interprets the findings, and compares them to other studies and existing literature. Finally, Chapter 6 summarizes the main conclusions, and Chapter 7 provides recommendations based on the study.

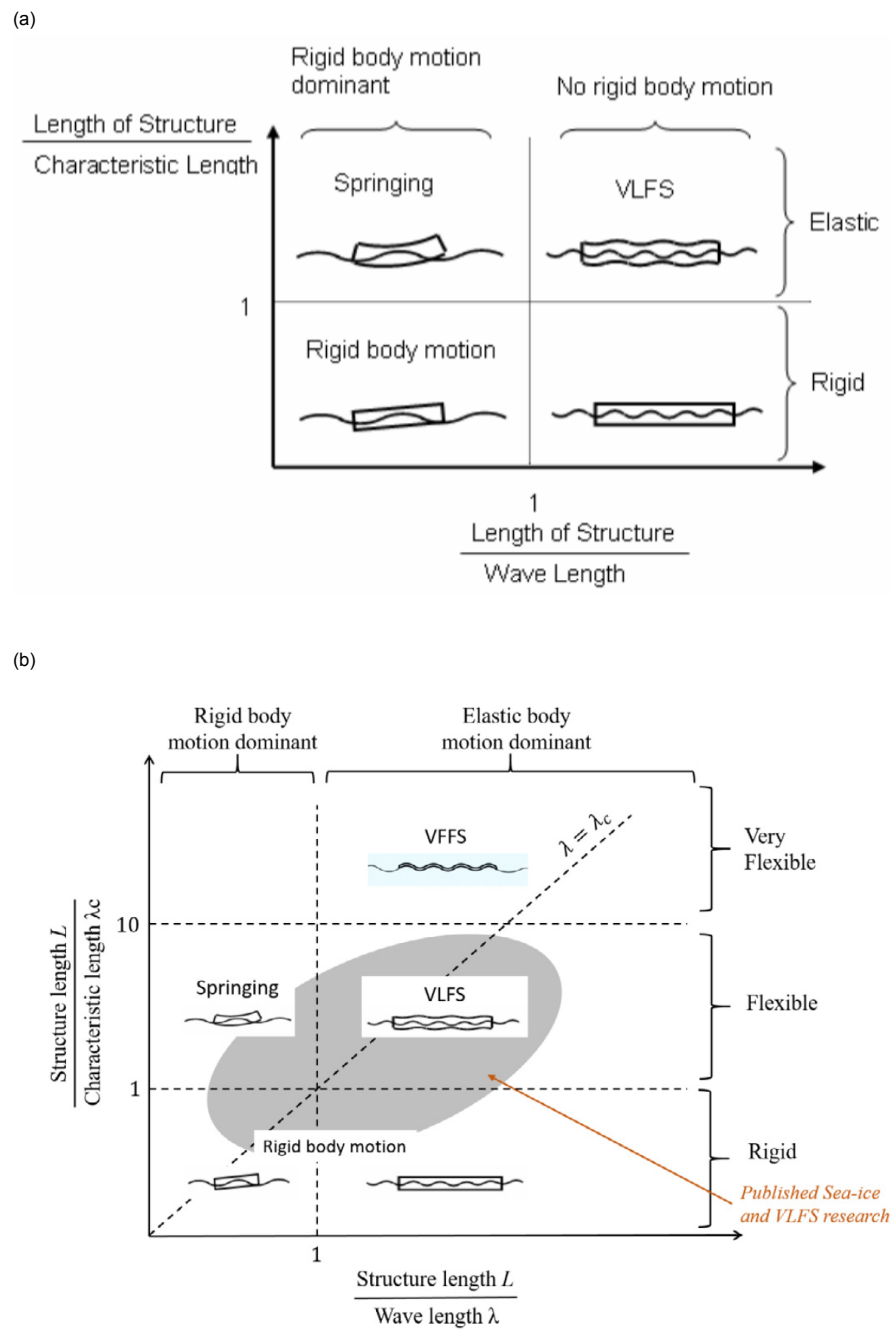


Figure 1.1: Comparison of response diagrams of floating structures using non-dimensional parameters: (a) (Suzuki et al., 2007), (b) (Zhang & Schreier, 2022).

Literature review and theoretical background

Understanding the interaction between thin, flexible structures and fluid surface waves requires insights from multiple overlapping domains, including hydroelastic theory, fluid-structure interactions (FSI), and nonlinear wave mechanics. This chapter also reviews studies on very flexible floating structures (VFFS) and on Faraday wave dynamics, providing a foundation for exploring their combined behavior.

2.1. Motivation from floating photovoltaic systems

Very flexible floating structures have been explored in applied contexts such as floating photovoltaic (FPV) systems, where lightweight sheets or mats are deployed on water surfaces (Acharya & Devraj, 2019; Ramanan et al., 2024). While most FPV systems in practice use stiff, pontoon-based platforms in calm inland waters, thin-membrane designs remain largely experimental.

These extremely flexible sheets experience strong fluid–structure interaction (FSI) under wave forcing, with large deformations and nonlinear responses that are not captured by traditional linear hydroelastic models (Suzuki & Yoshida, 1996). The scarcity of fundamental experimental studies on such systems motivates laboratory investigations into the hydroelastic behavior of thin floating sheets, isolating the effects of structural flexibility, inertia, and tension on wave response.

2.2. Fluid-Structure Interactions with Very Flexible Floating Structures

The interaction between floating structures and surface waves is inherently coupled, involving both fluid dynamics and structural mechanics. At a basic level, surface gravity waves over a uniform water depth h are described by linear wave theory, or Airy waves, with the dispersion relation

$$\omega^2 = gk \tanh(kh), \quad (2.1)$$

where ω is the angular frequency, k the wavenumber, and g gravitational acceleration. A complete derivation can be found in Appendix A. This relation provides a reference for understanding how waves behave in the absence of floating structures.

When an elastic structure floats on the water surface, the classical dispersion relation is modified to account for the additional restoring force from the bending stiffness of the material. For instance, Părau and Dias (2001) derived a dispersion relation for waves beneath a floating ice sheet using Kirchhoff-Love plate theory:

$$\omega^2 = \left(gk + \frac{Bk^5}{\rho} \right) \tanh(kh), \quad (2.2)$$

where B is the bending stiffness of the plate and ρ is the density of the fluid. This form describes flexural-gravity waves, where wave propagation results from the combined effects of gravity and plate

elasticity, and highlights that for thin floating plates, the wavelength depends not only on frequency and water depth but also on mechanical properties. The complete derivation can be found in Appendix E.

For thin, highly flexible membranes, such as those used in floating photovoltaic systems, nonlinear geometric effects can become significant. The Föppl–von Kármán (FvK) plate theory extends classical plate models to account for large deflections, yielding a modified dispersion relation for thin floating films:

$$\omega^2 = \left(gk + \frac{\sigma k^3}{\rho} + \frac{Bk^5}{\rho} \right) \tanh(kh), \quad (2.3)$$

where σ represents an effective surface tension arising from in-plane stresses of the floating layer. This relation captures the combined effects of bending, tension, and gravity, providing a more complete description of wave propagation for thin, flexible membranes. Importantly, it provides a theoretical framework to interpret how variations in sheet thickness and in-plane stress influence the wave patterns observed in the Faraday-wave experiments, linking membrane elasticity and tension to measurable wave properties such as wavelength and propagation characteristics. The full derivation can be found in Appendix F.

This dispersion relation has been employed in previous experimental studies, for example by Ono-dit-Biot et al. (2019) and Deike et al. (2013). Deike et al. (2013) extended the model to include both a static pre-tension term and a dynamic contribution, which depends on the sheet geometry, thickness, material properties, and wave steepness. Their work focused on a pinned membrane with a single thickness, leaving the case of freely floating membranes and the influence of thickness unexplored. This motivates the present study, which systematically investigates how sheet thickness affects the hydroelastic response and dispersion behavior in freely floating membranes.

Similarly, Ono-dit-Biot et al. (2019) compared experimental results for freely floating sheets over a range of thicknesses, but their setup relied on a rotating tank and external airflow to generate waves. This leaves open the question of how freely floating sheets behave under stationary, vertically vibrated conditions, highlighting the need for experiments in a controlled Faraday-wave framework.

More general approaches to fluid-structure interaction, such as two-way coupled simulations combining finite element methods (FEM) for the structure with boundary element methods (BEM) or Navier-Stokes solvers for the fluid, can capture complex behaviors including wave scattering, nonlinear deformation modes, and energy exchange (e.g., Luo et al., 2017; Meylan & Squire, 2002; Scolan & Korobkin, 2001; Zhao et al., 2007). While these methods are powerful, they are computationally intensive and often provide more detail than required when the primary interest is in wavelength shifts and wave selection. In this context, dispersion relation approaches offer a tractable and physically transparent method to predict the influence of structural properties on wave propagation.

While the relations above are well established for steady or linear waves, their extension to systems under time-periodic forcing, such as Faraday waves, is not well established. Understanding these dispersion relations provides a framework to interpret the hydroelastic behavior of thin, flexible floating sheets in the experiments.

2.3. Experimental investigations of Fluid-Structure Interactions

Experimental studies are essential for understanding fluid–structure interaction (FSI), especially for highly deformable floating bodies under unsteady wave forcing. In systems where analytical solutions are difficult or numerical models are not fully validated, physical modeling provides a direct way to capture coupled fluid and structural responses. This section reviews key developments in experimental investigations, grouped by the type of system studied and the measurement techniques employed.

2.3.1. Large-scale hydroelastic models

A key early effort in large-scale hydroelastic modeling was the Mega-Float project, which constructed a 9.75 m long scaled model of a 300 m floating runway to examine elastic responses in waves (Yago & Endo, 1996). Strain gauges and potentiometers were used to track bending and motion, focusing on vertical displacements and structural loads. This study demonstrated how distributed sensing can capture mode shapes and dynamic responses for relatively stiff, long platforms.

2.3.2. Simplified elastic sheets

Simplified elastic sheets have been widely used to study wave propagation and wave-structure coupling, often to mimic ice-wave interactions. Meylan (1994) used pressure probes beneath polypropylene sheets to measure pressure distributions in front of, beneath, and behind the sheet, showing how structural compliance and wave parameters affect the hydrodynamic field. Similarly, Kagemoto et al. (1998) tracked displacements and bending strains along floating elastic strips with optical tracking and strain gauges, demonstrating how low-inertia, high-compliance systems exhibit well-defined modal dynamics under wave loading.

2.3.3. Thin and compliant membranes

For thinner, more compliant structures, inertial effects become secondary to surface tension and viscous damping, requiring high-resolution measurement techniques. Experiments with thin polymeric or elastomeric sheets, such as those by Ono-dit-Biot et al. (2019), used synthetic schlieren imaging to capture full-field deformation without disturbing the sheet itself. Viscous effects are further emphasized in setups using ultra-soft materials like foam or viscoelastic polymers; for instance, Sree et al. (2017) used ultrasound sensors to record vertical displacements of floating PDMS and polypropylene covers, showing significant damping due to viscoelasticity and the role of surface barriers in controlling overwash.

2.3.4. Modern optical measurement techniques

Digital Image Correlation (DIC) has become a popular method for tracking 3D deformations of flexible floating systems. Schreier and Jacobi (2021) applied DIC with stereo cameras and surface dot patterns to reconstruct out-of-plane motion of long, flexible strips with high spatial and temporal fidelity. This approach is particularly effective for capturing subtle local deformations.

2.3.5. Summary and link to present work

Taken together, these studies illustrate the progression of FSI experiments from rigid-body dynamics to ultra-flexible sheets and increasingly precise measurement techniques. Building on this history, the present work employs in-plane Digital Image Correlation combined with synthetic schlieren imaging to capture full-field deformations of highly flexible floating membranes. This combined, non-intrusive approach provides the spatial and temporal resolution required to systematically investigate the influence of sheet thickness, bending, and in-plane tension on hydroelastic wave responses.

2.4. Fundamentals of Faraday waves

Faraday waves, first observed by Michael Faraday in 1831, are standing waves that form on a liquid surface subjected to vertical oscillations. They arise through parametric resonance, where the flat state of the interface becomes unstable beyond a critical forcing amplitude. The onset and properties of these waves depend sensitively on fluid parameters such as viscosity and surface tension, making them a versatile probe of small-scale fluid-structure interactions.

2.4.1. Classical description

The early theoretical description by Benjamin and Ursell (1954) reduces the problem to a Mathieu equation,

$$\frac{\partial^2 \zeta}{\partial T^2} + (p - 2q \cos 2T)\zeta = 0, \quad (2.4)$$

where ζ represents the surface elevation of the fluid at a given wavenumber, p and q are system-dependent parameters, and $T = \omega t/2$ is the dimensionless time based on the driving frequency ω . This formulation captures the essence of parametric instability: harmonic and subharmonic resonances arise depending on how the forcing frequency couples to the natural wave frequency.

2.4.2. Viscous effects and dispersion relation

Real fluids exhibit viscosity, which significantly influences the onset and growth of Faraday instabilities. Kumar and Tuckerman (1994) developed a linear theory using Floquet analysis for two viscous, immiscible fluid layers. In addition to the full Floquet framework, a simpler hydrodynamic model yields

the following approximate dispersion relation for small-amplitude surface waves:

$$\omega^2(k) = \frac{(\rho_1 - \rho_2)gk}{\rho_1 + \rho_2} + \frac{\sigma k^3}{\rho_1 + \rho_2} - \frac{2k^2(\eta_1 + \eta_2)}{\rho_1 + \rho_2}, \quad (2.5)$$

where ρ_i and η_i are the density and dynamic viscosity of fluid i ($i = 1, 2$), and σ is the interfacial surface tension. This relation gives the natural frequency of small-amplitude waves in a viscous fluid, reducing to the classical inviscid dispersion relation when $\eta_i = 0$. For the most commonly observed subharmonic Faraday instability, the parametric resonance condition can be expressed as

$$\frac{\omega_s(k)}{2} \simeq \omega(k), \quad (2.6)$$

where ω_s is the angular frequency of the shaker.

The critical acceleration amplitude a_{crit} for Faraday instability can then be derived via Floquet analysis. Physically, a_{crit} represents the minimum vertical forcing amplitude required to destabilize a flat fluid surface at a given wavenumber k . In the forcing-wavenumber plane, this gives rise to stability tongues: alternating regions of harmonic and subharmonic instability. Subharmonic waves, which oscillate at half the driving frequency, usually dominate the onset of instability. These tongue diagrams provide both the critical acceleration a_{crit} and the preferred wavenumber k_{crit} at instability onset.

Figures 2.1 and 2.2 illustrate examples of these stability tongues. Figure 2.1 shows the classical tongue structure predicted by linear theory for a glycerine-water mixture, while Figure 2.2 compares the theoretical predictions with experimental measurements, highlighting the correspondence between critical accelerations and the selected harmonic (H) and subharmonic (SH) wavenumbers.

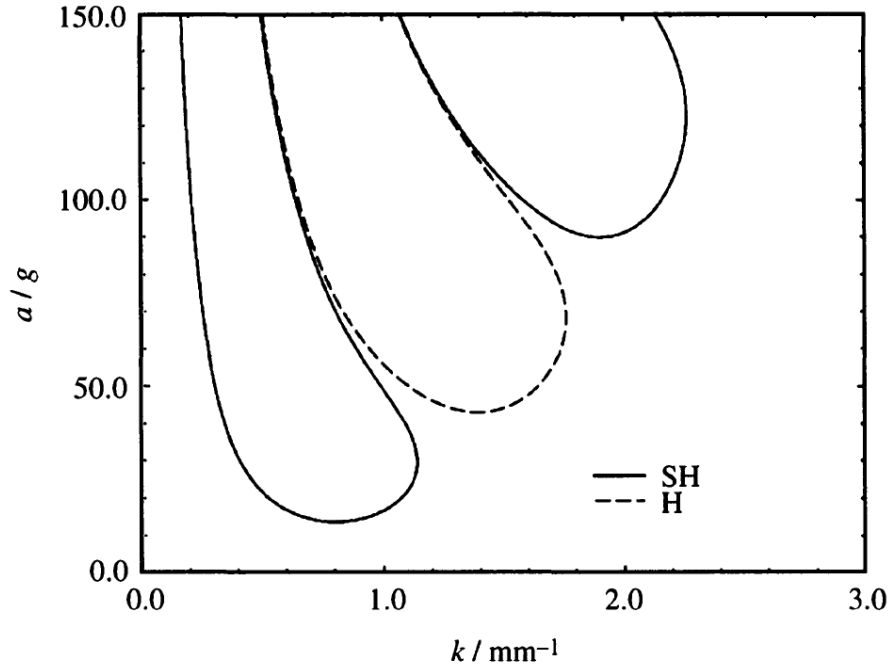


Figure 2.1: Stability boundaries of glycerine–water mixture. Subharmonic (SH) and harmonic (H) tongues alternate (Kumar, 1996).

2.4.3. Elastic sheet extensions

When a thin elastic sheet floats on a fluid surface, the classical Faraday-wave problem is extended to account for the sheet's elasticity and inertia. The governing equations now include the bending stiffness B and the mass per unit area m_A of the sheet, in addition to the usual fluid properties. This formulation, established using Hamiltonian methods and linear stability analysis, allows prediction of modified critical accelerations and wavenumbers in fluid-structure systems.

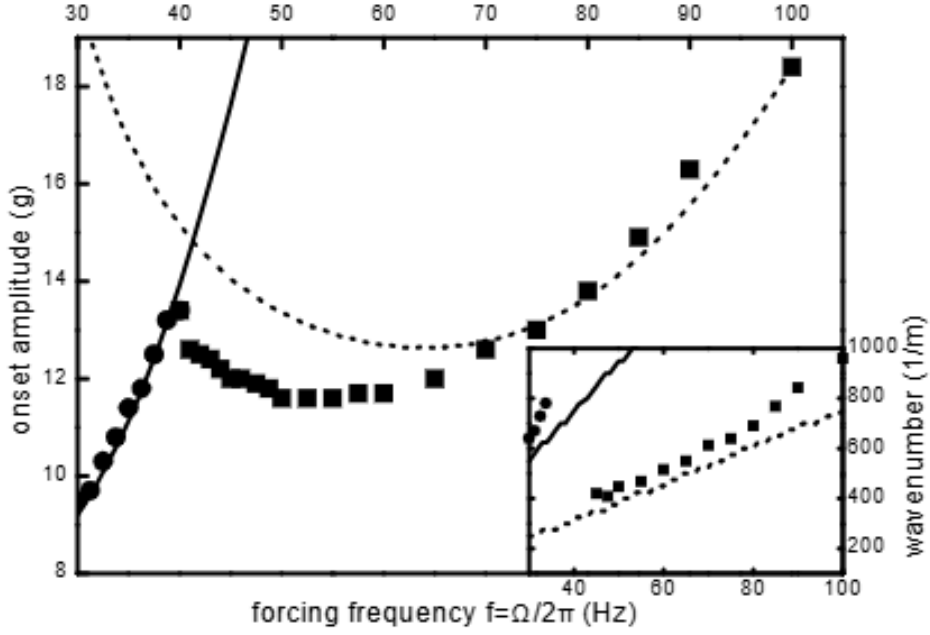


Figure 2.2: Critical acceleration amplitude a_{crit} and critical wavenumbers k_H and k_{SH} for harmonic (circles) and subharmonic (squares) Faraday instability. Symbols: experimental data; lines: theoretical computation (Wagner et al., 1998).

Sardari et al. (2023) derived threshold and dispersion relations of the form

$$a_0 = (k \tanh(kd))^{-1} \left[\delta^2 + \left(\frac{(1 + 2\gamma k \coth(2kd)) \omega^2 - \omega_0^2}{2\omega^2} - \frac{k^4 B}{2\rho g} \right)^2 \right]^{1/2}, \quad (2.7)$$

$$\left(\frac{\omega}{2} \right)^2 = \frac{\rho g k + \sigma k^3 + B k^5}{\rho \tanh(kh) + \frac{2m_A k(1 + e^{4kh})}{(1 + e^{2kh})^2}}. \quad (2.8)$$

Here, δ represents dissipation, and $\gamma = m_A/\rho$ is an effective hydrodynamic thickness, combining the sheet mass per unit area and fluid density. Physically, γ scales with the sheet thickness and density relative to the fluid, with units of length.

2.4.4. Summary and relevance

The theoretical developments reviewed above establish the key ingredients needed to interpret Faraday instabilities in fluids with and without floating elastic sheets. At the classical level, the instability is characterized by a critical acceleration amplitude, a_{crit} , and a selected wavelength, λ_{crit} , both of which follow from the balance between gravity, surface tension, and viscous damping. Extensions to include elastic sheets demonstrate that bending stiffness and sheet inertia further modify these thresholds.

For the present work, Faraday waves are not investigated as a phenomenon in their own right, but rather employed as a diagnostic tool to probe hydroelastic effects in thin, compliant sheets. Systematic variation of sheet thickness allows assessment of how elasticity and inertia influence the onset of instability and the corresponding wave selection.

2.5. Challenges of scaling in laboratory studies

Although Faraday-wave-based setups provide a convenient and controllable environment to study wave-structure interactions at small scales, it is essential to acknowledge the limitations and challenges associated with experimental scaling, particularly when extrapolating results to full-scale floating photovoltaic (FPV) systems.

Conventional model testing in offshore engineering relies on similitude theory to ensure that scaled prototypes replicate the behavior of real systems (Casaburo et al., 2019). Geometric, kinematic, and

dynamic similarities are central to this approach, but their application becomes non-trivial when flexible materials and surface effects are involved.

Froude scaling is commonly employed in wave-structure experiments, as it preserves the balance between gravity and inertial forces. However, for highly flexible systems such as FPV membranes, this approach neglects the influence of elastic and capillary forces, which become increasingly significant at small scales. In particular, surface tension, negligible at full scale, plays a dominant role in the dynamics of small-scale water waves, affecting both wave dispersion and damping characteristics (Stagonas et al., 2011).

The elastic behavior of the floating sheet introduces further complexity. Dynamic similarity for flexible systems requires additional dimensionless parameters beyond the Froude number, such as the Cauchy number, which characterizes the ratio between inertial and elastic forces (Vassalos, 1998). These considerations complicate direct downscaling of FPV systems, especially when attempting to preserve both fluid and structural dynamics.

Geometric scaling of the floating sheet, based on existing full-scale prototypes, provides a first step to maintain realistic aspect ratios. This is complemented by a characteristic length scale associated with the sheet, which is used to ensure that the laboratory model lies within the very flexible floating structures (VFFS) regime. Figure 1.1 illustrates this regime, plotting the structure length normalized by the characteristic length on the vertical axis and the structure length normalized by the wavelength on the horizontal axis. Recent work by Schreier and Jacobi (2021) demonstrated the feasibility of modeling flexible floating structures in wave tanks, highlighting the importance of these non-dimensionalised parameters. Their methodology emphasizes the need for careful scaling of elastic effects. Together, these strategies ensure that the laboratory model captures the dominant physical mechanisms relevant to these thin membrane fluid-structure interactions.

2.6. Summary and knowledge gaps

The reviewed studies collectively demonstrate that hydroelastic interactions of thin sheets with waves have received increasing attention, but each existing approach addresses only part of the problem relevant to very flexible floating structures (VFFS). For instance, Deike et al. (2013) investigated pinned membranes and provided valuable insight into how sheet geometry, thickness, and tension affect wave dynamics. However, their boundary conditions prevent the free-floating behavior that is central to VFFS. In contrast, Ono-dit-Biot et al. (2019) examined freely floating membranes with multiple thicknesses gathering inside on how different thicknesses behave, but their experiments relied on a rotating tank with air-jet-driven forcing needed to create waves. On the other hand, Sardari et al. (2023) studied controlled Faraday-wave forcing on a free floating film, but considered only a single sheet thickness, and the film used is not in the very flexible regime.

Taken together, these studies highlight that no experimental work has yet combined all three essential ingredients: freely floating boundary conditions, controlled Faraday forcing, and systematic variation of sheet thickness deep into the VFFS regime. By systematically varying sheet thickness, the study is able to traverse different hydroelastic regimes, from highly compliant (VFFS) to more rigid behaviour (VLFS). The present study addresses this gap by employing Faraday waves as a diagnostic tool, because they offer well-defined frequency and wavelength characteristics.

3

Methodology

The objective of this study is to determine how the thickness of a floating flexible sheet influences its hydroelastic response to vertical wave forcing. In particular, the study focuses on two aspects. First, how sheet thickness alters the dispersion relation, that is, the relationship between forcing frequency and the observed wavelengths. Second, how it modifies the critical acceleration required for the onset of Faraday waves.

To investigate these aspects, controlled laboratory experiments were performed in which Faraday waves were generated by vertical sinusoidal excitation in a finite-depth fluid layer. Tests were carried out both with and without a floating sheet to isolate the influence of the structure. Sheet thickness was systematically varied to adjust the flexural rigidity and associated characteristic length scale. This enabled comparison across configurations ranging from very flexible floating structures (VFFS) to more rigid systems resembling very large floating structures (VLFS) (See Chapter 5 Figure 5.1 b).

Wave fields were measured using imaging combined with synthetic schlieren, a non-intrusive optical technique that infers surface slopes from refractive distortions of a background dot pattern. This method was selected because it enables full-field reconstruction of wave profiles without physically disturbing the fluid–structure system, unlike intrusive probes or markers that could alter the response of the flexible sheet. The recorded images were processed with digital image correlation and Fourier analysis, which provide quantitative displacement fields and wavelength information with high spatial resolution, making them particularly suitable for capturing subtle variations across different sheet thicknesses.

The excitation conditions were quantified by recording shaker acceleration and displacement using calibrated sensors. Accurate measurement of acceleration is essential, since the onset of Faraday waves is characterized by a critical acceleration threshold, while displacement measurements were essential for calibration purposes.

For reference, the theoretical model of Kumar and Tuckerman (1994), describing Faraday instability between two viscous fluid layers bounded by rigid walls, was used to predict onset thresholds and wavenumbers for the free surface case.

The following sections describe the measurement objectives and target ranges, experimental setup, optical measurement method (synthetic schlieren), analysis techniques, experimental procedure and data treatment, and an assessment of measurement accuracy.

3.1. Measurement Objectives and Target Ranges

To design meaningful experiments, it is essential to define target measurement ranges and accuracies based on theoretical predictions. For this purpose, the linear stability analysis of Kumar and Tuckerman (Kumar & Tuckerman, 1994) is adopted, applied here to a fluid–air configuration where the air layer is treated as infinite and only the fluid depth is varied. Specific fluid choices are detailed in Section 3.2.4.

The model provides the expected critical wavenumber k_{crit} , from which the corresponding critical wavelength λ_{crit} follows, as well as the critical acceleration amplitude a_{crit} at the onset of Faraday instabilities. By evaluating the model across excitation frequencies of 0 Hz to 100 Hz and fluid depths of 5 mm to 25 mm, we obtain the predicted ranges of measurable wave characteristics:

- **Wavelengths:** 4 mm to 161 mm, depending on frequency and fluid depth.
- **Critical accelerations:** approximately 0.03–1.83 g .
- **Excitation frequencies:** Excitation frequencies were chosen to generate wavelengths that could be reliably captured and analyzed within the measurement domain, avoiding cases that would be either too long or too short to provide useful information.

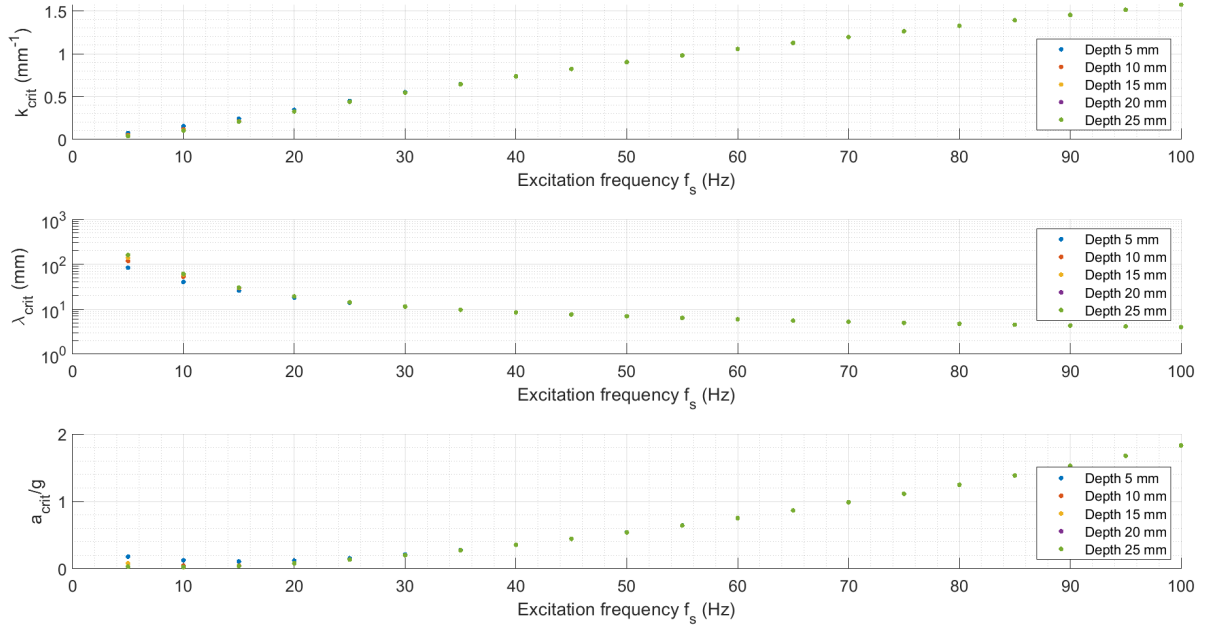


Figure 3.1: Predicted stability characteristics for the silicone oil–air system based on the linear stability analysis of Kumar and Tuckerman (Kumar & Tuckerman, 1994). Shown are the critical wavenumber k_{crit} , wavelength λ_{crit} , and normalized acceleration amplitude a_{crit}/g as functions of excitation frequency, evaluated for fluid depths between 5 mm and 25 mm.

Based on these predictions, the following measurement goals are established:

Spatial resolution To resolve wave patterns within approximately 10% of the predicted wavelength, a target effective spatial resolution of roughly 0.4 mm is desired for the shortest expected waves. Achieving this resolution depends not only on the raw imaging system (camera sensor, lens, and pixel size) but also on processing parameters such as DIC subset size, grid spacing, and subsequent analysis (e.g., Fourier transforms). Consequently, the effective resolution after data analysis may differ from the raw pixel scale. These factors are taken into account in the accuracy assessment presented in Section 3.6.

Temporal resolution Since the study focuses on the spatial characteristics of the standing waves rather than the full temporal evolution within a cycle, it is sufficient to capture images at specific, reproducible phases of the excitation. To capture at least one image per oscillation period of the fluid surface at the maximum excitation frequency of 100 Hz, the camera must acquire images at a minimum rate of 100 fps. Acceleration measurements, however, must resolve the sinusoidal variation within each cycle. To capture at least 5–10 samples per excitation period, the acceleration signal should be acquired at a minimum rate of approximately 500 Hz, with higher rates (up to 1000 Hz) providing improved temporal resolution.

Field of view Wave patterns should span at least 2–3 wavelengths across the imaging area to allow robust characterization of the spatial structure.

These targets establish the baseline measurement requirements, providing quantitative criteria for selecting and evaluating the experimental setup. In the following sections, the chosen equipment and data analysis methods are described, with explicit justification of how they meet the spatial and temporal resolution targets, as well as the accuracy needed to resolve wavelengths and critical accelerations.

3.2. Experimental setup

Experiments are conducted using a vertically vibrated fluid system. The core of the setup consists of a cylindrical glass container (130 mm inner diameter, 30 mm height; Figure 3.2 (ii)), securely mounted on a Brüel & Kjær Vibration Exciter Type 4808 (Figure 3.2 (i)). The shaker is driven by a Brüel & Kjær Power Amplifier Type 2719 and controlled via an NF Electronic Instruments 1930A multifunction synthesizer (frequency accuracy ± 5 ppm), producing sinusoidal vertical oscillations described by

$$z(t) = z_a \sin(2\pi f_s t),$$

where z_a denotes the vertical displacement amplitude and f_s the excitation frequency. The corresponding vertical acceleration is

$$a(t) = -a_a \sin(2\pi f_s t),$$

with the vertical acceleration amplitude $a_a = (2\pi f_s)^2 z_a$. The operating range of the shaker spans 5 Hz to 10 kHz, with a maximum peak-to-peak displacement of 12.7 mm and accelerations up to 71 g.

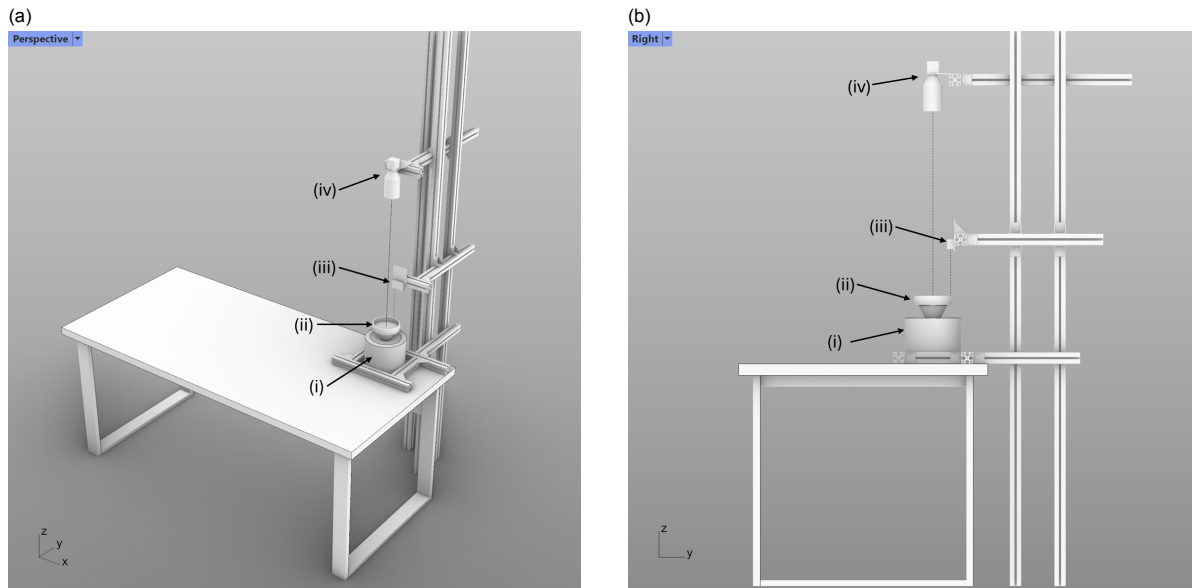


Figure 3.2: Visual representations of the experimental setup: (a) perspective view and (b) right-side view. Key components are labeled as follows: (i) shaker, (ii) cylindrical glass tank, (iii) laser distance meter, and (iv) Basler camera with lens.

3.2.1. Motion control and data acquisition

Shaker motion is continuously monitored in real time using an accelerometer (calibration factor 956 ± 16 mV/g), affixed to the shaker and connected to a PCB Model 482B11 ICP signal conditioner. This arrangement enables precise measurement of the vertical acceleration applied to the fluid system, ensuring accurate control and validation of the excitation amplitude within $\pm 1\%$ of the setpoint.

Complementary measurements of vertical displacement are obtained with an *optoNCDT ILD 1420-200* laser distance sensor (Figure 3.2 (iii)), which offers a 200 mm measurement range, linearity better than 0.08% full-scale output (≤ 160 μm), and repeatability of ± 8 μm .

No specific sampling rate can be set directly on the accelerometer or laser sensor; instead, temporal resolution is controlled via the LabVIEW data acquisition configuration. The acquisition is chosen to

provide roughly 10 samples per excitation cycle, ensuring accurate reconstruction of the excitation waveform and reliable extraction of displacement and acceleration signals across all tested frequencies (see Appendices N and O for validation).

3.2.2. Imaging system

Surface deformation is recorded using a Basler a2A1920-150µm camera (2.3 MP, 1920 × 1200 pixels, up to 150 fps) equipped with a Nikon AF-S NIKKOR 24–85 mm f/3.5–4.5G ED VR lens. The camera is mounted in a fixed top-down orientation, 800 mm above the tank base, covering the full fluid domain. Image acquisition is synchronized with the excitation signal via the sync-out of the multifunction synthesizer routed through a frequency divider, ensuring phase-locked recording. Camera gain and exposure are fixed at 12 and 2000 µs, respectively. The frame rate capability exceeds the minimum requirement of 90 fps, capturing at least one image per cycle at the maximum forcing frequency of 90 Hz.

A speckle pattern (dot diameter 0.25 mm) is printed on transparent sketch paper and affixed to the underside of the tank as an optical reference. Illumination is provided from below by a collimated LED (70 mm diameter) powered by a digitally controlled DC supply (0–30 V, 3 A). Images and videos are acquired using Pylon Viewer (Basler, Germany), with the field of view cropped to 1536 × 1200 pixels to match the illuminated area.

3.2.3. Floating structure preparation, deployment and characterization

To investigate the effects of floating structures, a compliant thin sheet is gently placed on the fluid surface. ELASTOSIL® Film 2030 (Wacker Chemie AG), a transparent, highly elastic silicone elastomer, is used (Figure 3.4a (vii)). Circular samples with a radius of 6 cm (diameter 12 cm) are laser-cut to ensure uniform geometry and to prevent contact with the container walls.

Four nominal thicknesses are tested: $20 \pm 1 \mu\text{m}$, $50.0 \pm 2.5 \mu\text{m}$, $100 \pm 5 \mu\text{m}$, and $200 \pm 10 \mu\text{m}$, consistent with the $\pm 5\%$ manufacturer tolerance. To minimize wrinkling during deployment, films are carefully submerged and released from their carrier sheets underwater, allowing them to settle smoothly onto the fluid interface. Trapped air and surface water are removed prior to measurements.

The material density is $\rho = 1.075 \pm 0.025 \text{ g/cm}^3$, and a Poisson ratio of $\nu = 0.5$ is assumed, consistent with the nearly incompressible behavior of silicone elastomers. The manufacturer-reported Young's modulus, $E = 0.58 \pm 0.02 \text{ MPa}$, based on tensile tests of the 20 µm films (Appendix G.8), is independently verified using a mechanical test based on static wrinkles.

Young's modulus check

To validate the material stiffness and assess the impact of laser cutting, a static wrinkling test is performed. Thin rectangular specimens of ELASTOSIL® Film 2030 are gently compressed on a deionized water layer to induce a wrinkled state. The resulting wrinkle wavelength, governed by the balance of film bending and hydrostatic forces, provides a direct measurement of bending stiffness. According to marginal stability theory Vella et al. (2004), the wavelength λ_c scales as

$$\lambda_c \sim 2\pi \left(\frac{Ed^3}{12(1-\nu^2)\rho g} \right)^{1/4},^1 \quad (3.1)$$

allowing extraction of the Young's modulus E from measured wrinkle wavelengths.

Tests are conducted for both hand-cut and laser-cut films across four thicknesses (d). For each case, wrinkle wavelengths are extracted using the same image-based method later applied to dynamic tests (see Section 3.4.2). The results show good agreement with theoretical predictions using the supplier's reported modulus of $E = 0.58 \pm 0.02 \text{ MPa}$ (Figure 3.3).

No systematic differences are observed between hand-cut and laser-cut samples, confirming that laser cutting does not alter the mechanical properties. This validates the use of laser cutting as a uniform sample preparation method. Based on this, the supplier-provided modulus is used in subsequent calculations of plate bending stiffness B :

$$B = \frac{Ed^3}{12(1-\nu^2)}.$$

¹This equation resembles the one from the Introduction 1, Equation 1.1.

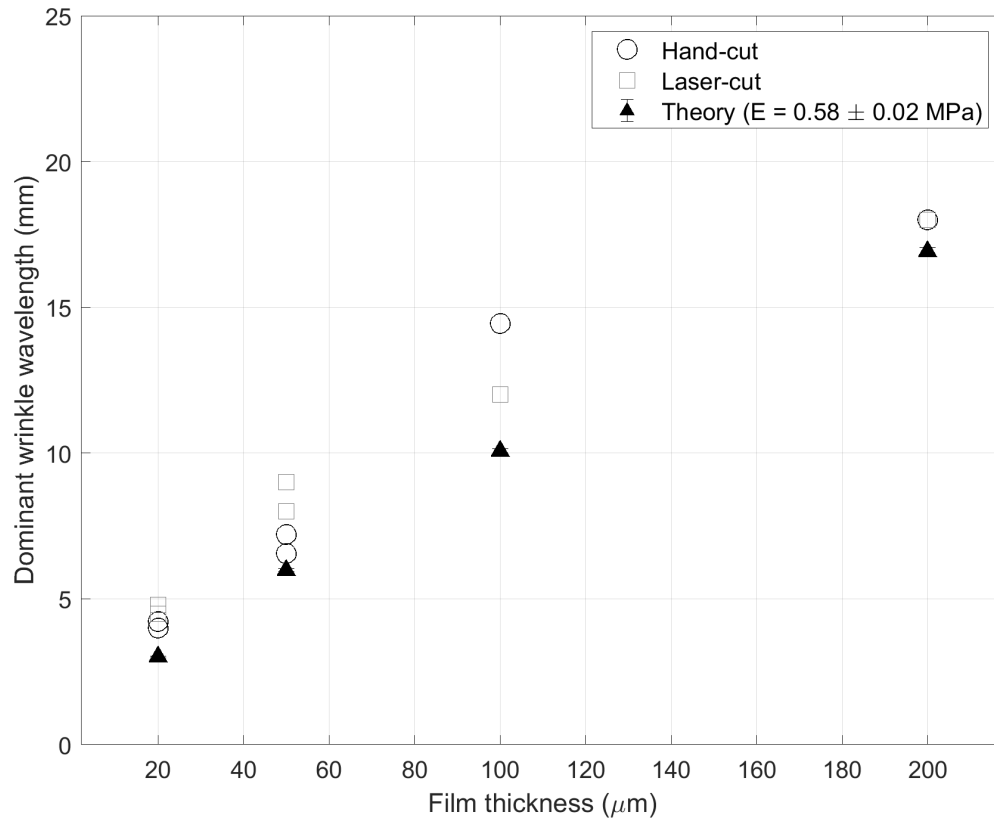


Figure 3.3: Measured wrinkle wavelengths as a function of film thickness for ELASTOSIL® Film 2030. Circles: hand-cut samples; squares: laser-cut samples; triangles: theoretical predictions from Equation 3.1.

3.2.4. Working fluids and tank configuration

Two working fluids are considered in this study: silicone oil (Silicones and More, 5 cSt) and deionized water (Sigma-Aldrich, Product No. 8.48333.9010). Silicone oil is initially chosen because its viscosity and surface tension are stable and relatively insensitive to contamination, making it suitable for reproducible Faraday-type experiments. However, the ELASTOSIL® films sink in silicone oil, preventing floating-structure tests. Consequently, silicone oil is used only in preliminary baseline experiments to validate the experimental setup and analysis procedure. All subsequent floating-sheet experiments are conducted in deionized water, which reliably supports the films.

The laboratory ambient temperature is maintained at $20 \pm 2^\circ\text{C}$, and the fluid properties are summarized in Table 3.1. Air properties are also included in the table for reference in theoretical models discussed in Section 3.4.1.

Table 3.1: Physical properties of the working fluids used in the experiments, measured or reported at 20°C . The table lists the density ρ , dynamic viscosity η , kinematic viscosity $\tilde{\nu}$, surface tension σ , and refractive index n for each fluid. These parameters were used for theoretical predictions and data analysis in the study.

Fluid	ρ [kg/m ³]	η [mPa s]	$\tilde{\nu}$ [mm ² /s]	σ [mN/m]	n [-]
Water	1000	1.00	1.00	72.75	1.33
Silicone oil 5 cSt	910	4.55	5.00	19.70	1.40
Air	1.204	0.0181	15.0	0.00	1.00

The fluid depth is fixed at $h = 10$ mm for all tests, as discussed in Section 3.4.1.

3.3. Optical method: Synthetic Schlieren

The response of both the bare fluid interface and the fluid–sheet system is characterized using a background-oriented imaging technique, commonly known as synthetic schlieren (Moisy et al., 2009). This method monitors the apparent displacement of a background dot pattern as viewed through the refracting fluid interface. Surface waves distort the optical path, producing measurable in-plane displacements of the background pattern, as illustrated schematically in Figure 3.4.

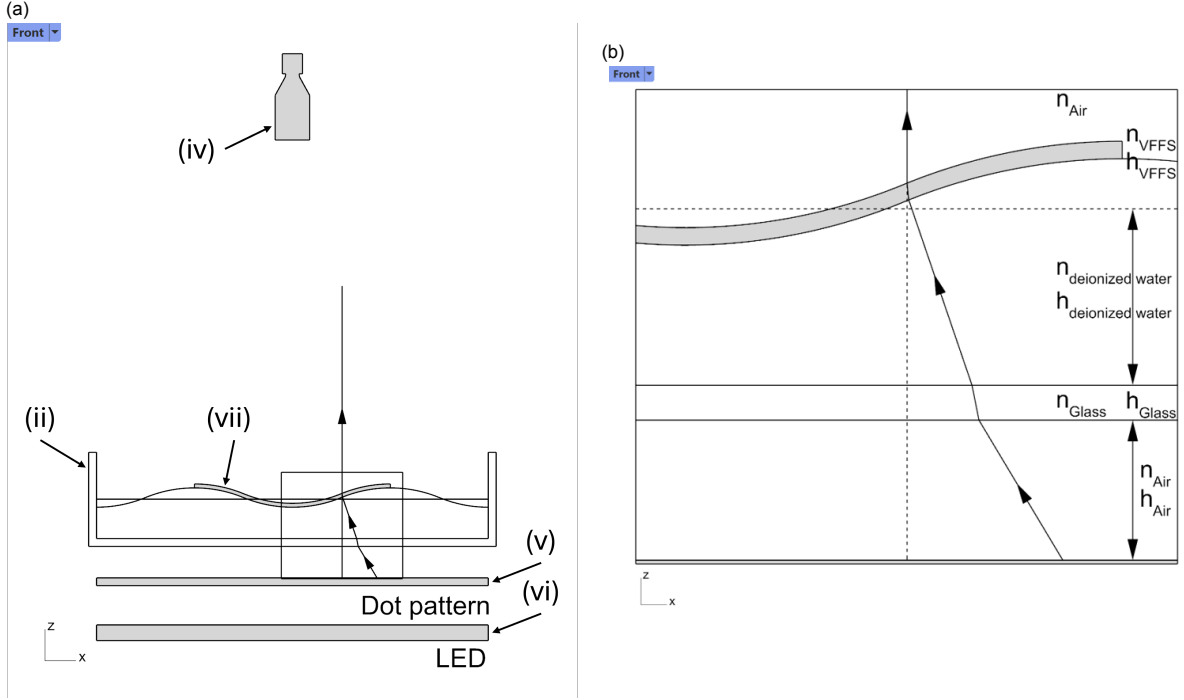


Figure 3.4: Synthetic Schlieren setup used to visualize surface deformation and refraction. (a) Overview of the optical setup, showing key components: (ii) cylindrical glass tank, (iv) Basler camera with lens, (v) dot pattern, (vi) LED, and (vii) floating ELASTOSIL® Film 2030. (b) Magnified view of the region marked in (a), showing the four layers: glass, fluid (deionized water is presented), ELASTOSIL® Film 2030, and air. Dot displacement is used to quantify surface deformation.

In classical synthetic schlieren, these measured displacements can be integrated to reconstruct the full interface elevation field. In this study, however, the primary goal is to determine the dominant surface wavelengths. Since wavelength information is directly encoded in the periodicity of the displacement field, full surface reconstruction is unnecessary. This approach avoids detailed modeling of refractive index gradients and reduces sensitivity to noise. The key assumption is that the observed wave field is stationary and periodic, such that the displacement pattern preserves the wavelength of the underlying surface deformation.

3.3.1. Principle

Each measurement requires at minimum two images: an undisturbed reference image of the background dot pattern and a disturbed image captured during excitation. The displacement field between the two is obtained via digital image correlation (DIC), which divides the images into interrogation windows and tracks the apparent motion of the dot features. These displacements primarily reflect local slope variations of the fluid interface, which are proportional to both the amplitude and spatial characteristics of the surface waves.

3.3.2. Implementation

Image correlation is performed with the open-source packages `Ncorr` (Matlab, version 1.14.0.0) (Blaber et al., 2015) and `OpenPIV` (Python) (Liberzon et al., 2021). Both packages use an interrogation window size of 24 pixels with a 20-pixel overlap, ensuring consistent displacement analysis. `Ncorr` is

applied to free-surface cases (both silicone oil and deionized water), where large dot deformations and occasional dot stretching occur, proving to be more robust under these conditions. `OpenPIV` is used for surfaces covered with ELASTOSIL[®] films, offering faster processing while producing comparable results.

Digital image correlation (DIC) tracks the apparent motion of the speckle pattern by correlating interrogation windows between reference and disturbed images. The chosen window size balances spatial resolution and measurement noise: smaller windows capture finer details but increase noise sensitivity, while larger windows provide smoother fields at the expense of resolving small-scale variations. The 20-pixel overlap ensures continuity between windows; although higher than typical literature recommendations, it produces reliable displacement fields for the chosen pattern density and contrast. A more systematic study of window size and overlap could further optimize accuracy and is suggested as a future recommendation.

Pixel displacements are converted into physical units using calibration factors obtained from reference objects, yielding a scale of 0.06 mm/pixel (see Appendix H).

To ensure well-defined periodicity in the displacement fields, image acquisition is phase-locked to the forcing cycle. The function generator provides two outputs: a sine wave that drives the shaker, producing vertical oscillations of the fluid surface, and a TTL (digital) output that triggers the camera through a frequency divider. The TTL pulse centers determine the instants of camera exposure, and the frequency divider selects every n th excitation cycle. In MATLAB plots, gray rectangles indicate camera exposure windows, and black dots mark the center of each capture.

The vertical motion of the surface is visualized in the *Surface disp* plots, which show the upward and downward displacement of the fluid at each instant. This does not represent the full surface shape but corresponds to the displacement captured via phase-locked acquisition.

Two illustrative examples of subharmonic surface motion (oscillation at half the shaker frequency) are shown in Figures 3.5 and 3.6. In the first example (Figure 3.5), an even frequency divider captures the same phase of the surface oscillation each cycle, indicated by the black dots. In the second example (Figure 3.6), an odd frequency divider results in successive captures at opposite phases (180° apart), alternating between peaks and troughs, which highlights the onset of subharmonic behavior.

This approach demonstrates how the combination of the function generator sine, TTL output, frequency divider, and camera exposure timing enables precise phase-locked acquisition, which is critical for measuring reproducible displacements and analyzing both harmonic and subharmonic wave behavior. Validation of the phase-locking is provided in Appendix I.

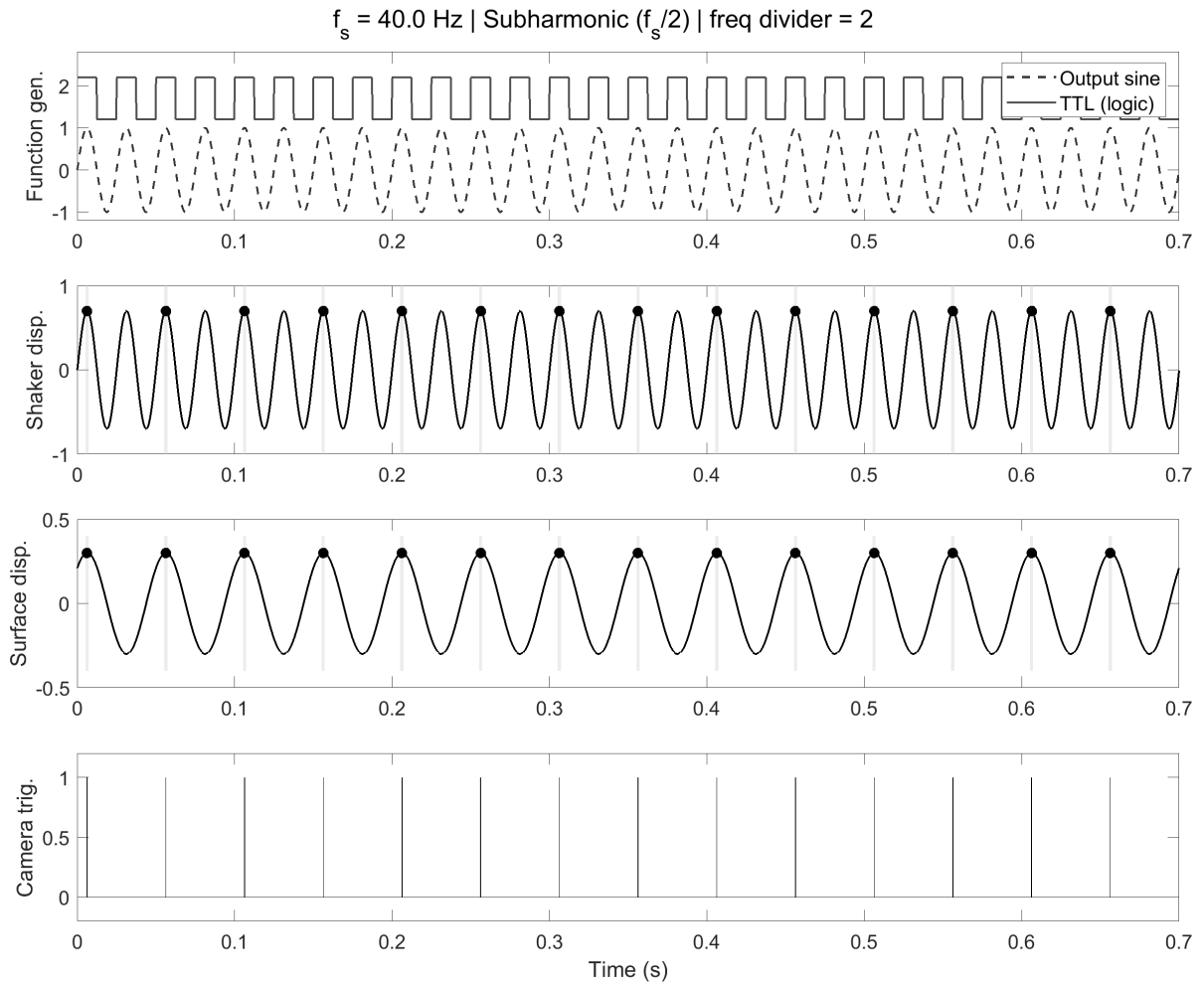


Figure 3.5: Example of phase-locked acquisition of subharmonic surface motion using an even frequency divider value of 2 (simulation). Top graph: function generator output at 40 Hz (dotted line) and TTL trigger signal (solid black line). Second graph: shaker displacement replicating the 40 Hz signal. Third graph: subharmonic surface displacement at 20 Hz. Black dots indicate camera trigger times. Fourth graph: camera trigger signal and camera exposure windows of 2 ms (gray rectangles). This illustrates how an even frequency divider synchronizes image acquisition to the same phase of the surface oscillation.

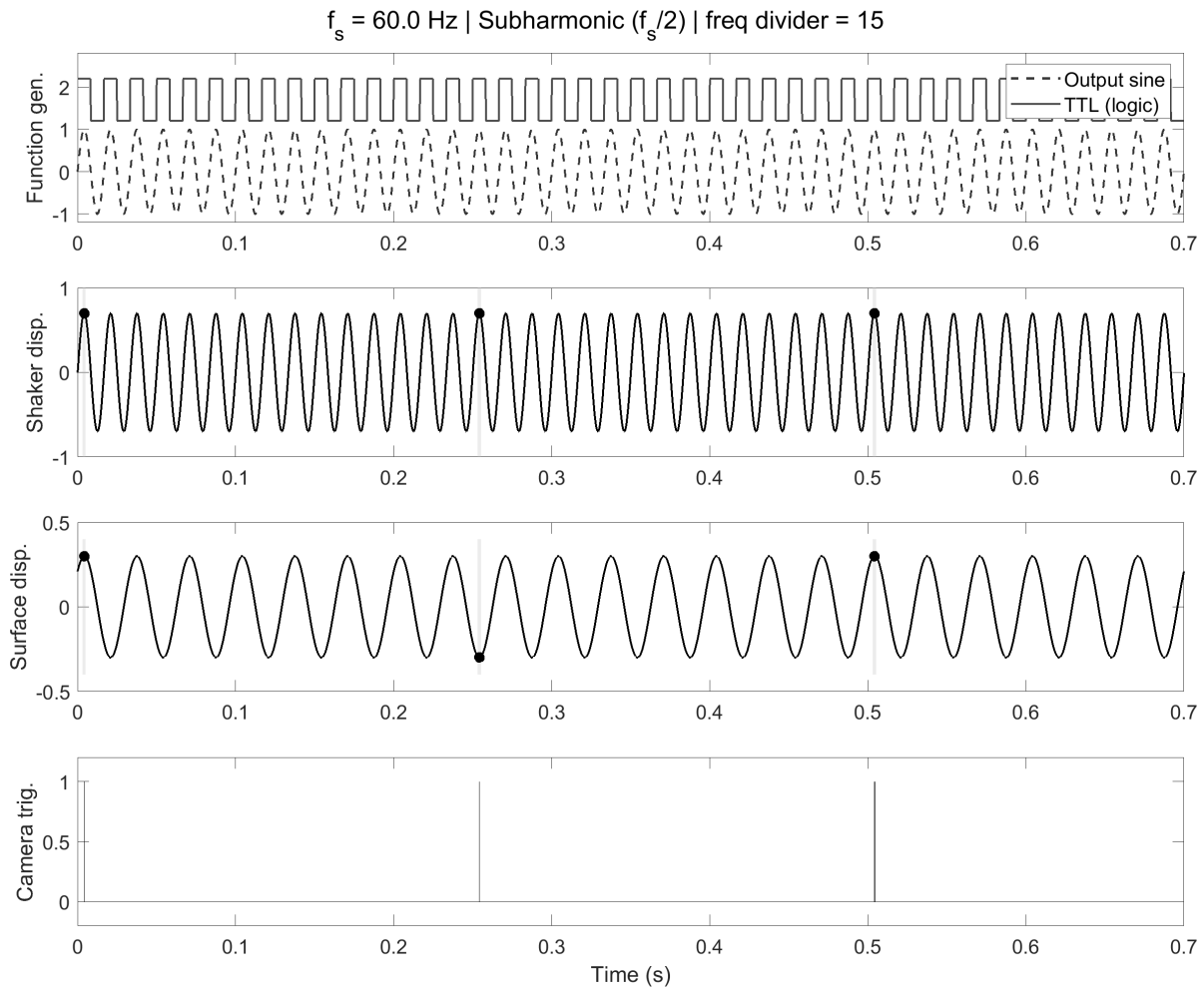


Figure 3.6: Example of phase-locked acquisition of subharmonic surface motion using an odd frequency divider value of 15 (simulation). Top graph: function generator output at 60 Hz (dotted line) and TTL trigger signal (solid black line). Second graph: shaker displacement replicating the 60 Hz signal. Third graph: subharmonic surface displacement at 30 Hz, with successive camera captures occurring at opposite phases (180° apart), alternating between peaks and troughs. Fourth graph: camera trigger signal and camera exposure windows of 2 ms (gray rectangles). This illustrates how an odd frequency divider synchronizes image acquisition to alternate phases of the surface oscillation.

3.4. Analysis methods

3.4.1. Analytical fluid-fluid Faraday instability model

To design and interpret the experiments, reference predictions of wave characteristics were established using a Python implementation of the linear stability analysis developed by Kumar and Tuckerman (Kumar & Tuckerman, 1994). This approach applies Floquet theory to a fluid–fluid system, in the present study, a fluid–air interface, to compute the stability of a flat interface under vertical oscillations. The model provides theoretical estimates of the critical wavenumber k_{crit} , the corresponding critical wavelength λ_{crit} , and the critical acceleration amplitude a_{crit} at the onset of Faraday instabilities.

The implementation requires, for each fluid, the density, dynamic viscosity, fluid layer height, and surface tension (Table 3.1), as well as the excitation frequency of the vertical oscillations. The air layer is treated as effectively infinite. These parameters enable accurate prediction of instability thresholds under the experimental conditions used here.

The model was evaluated over excitation frequencies in the range 0 Hz to 100 Hz and fluid depths between 5 mm to 25 mm. Figure 3.7 shows a representative stability diagram for the deionized water–air system at 30 Hz and 10 mm depth. Red regions indicate subharmonic instability tongues, blue regions indicate harmonic instability, and the black cross marks the critical point of instability.

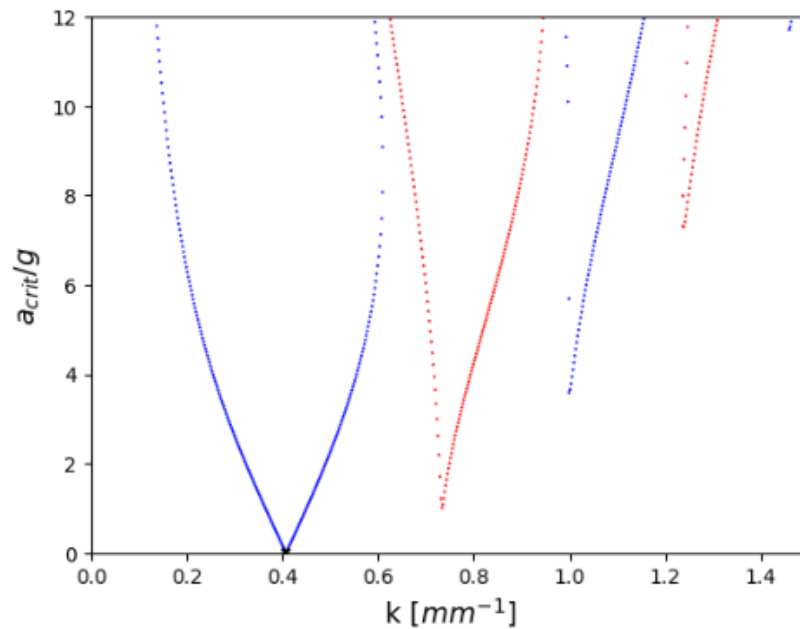


Figure 3.7: Representative stability diagram for the deionized water–air system at 30 Hz excitation frequency and 10 mm fluid depth. Acceleration normalized by g is plotted against wavenumber. Red regions indicate subharmonic instability, blue regions indicate harmonic instability, and the black cross marks the critical point of instability. For this case, the critical values are $a_{\text{crit}} = 0.0301 g$ and $k_{\text{crit}} = 0.407 \text{ 1/mm}$.

Silicone oil, described in Section 3.2.4, was initially used in preliminary tests due to its well-defined rheological properties. Predictions for silicone oil were employed to define measurement targets, including wavelength and acceleration ranges (Section 3.1), and also served as validation for free-surface experiments (dashed lines in Section 4, Figures 4.4–4.6). Although silicone oil could not support floating sheets, these analyses provided a reliable benchmark. The silicone oil predictions are shown in Figure 3.1.

Subsequently, the model was evaluated using deionized water properties to provide validation for free-surface measurements in the main experiments (dashed lines in Section 4, Figures 4.5–4.7), with results shown in Figure 3.8.

Based on Figures 3.8 and 3.1, the fluid depth was fixed at $h = 10 \text{ mm}$ for all tests. Variations in depth have a minor effect on both wavelength and acceleration, and this choice ensures that waves remain within the tank while maintaining consistency across experiments.

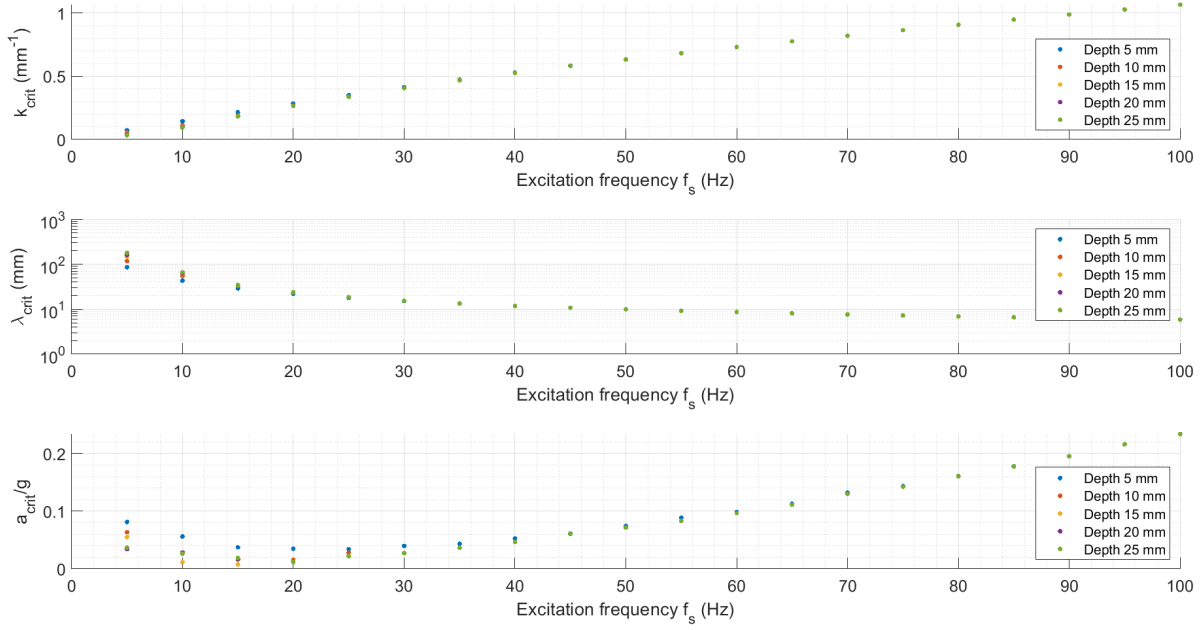


Figure 3.8: Predicted stability characteristics for the silicone oil–air system based on the linear stability analysis of Kumar and Tuckerman (Kumar & Tuckerman, 1994). Shown are the critical wavenumber k_{crit} , wavelength λ_{crit} , and normalized acceleration amplitude a_{crit}/g as functions of excitation frequency, evaluated for fluid depths between 5 mm and 25 mm.

3.4.2. Wavelength derivation

The analysis aims to determine the dominant wavelength of the standing surface waves from image sequences. Several approaches were tested, but only the one described below proved robust and was adopted for all subsequent analyses. The method proceeds in three steps: displacement fields are first extracted from the surface motion, then transformed into an orientation-independent representation, and finally subjected to spectral analysis to identify the dominant wavelength. To make the procedure transparent, it is illustrated step by step using synthetic data, which provide clearer visual examples than experimental images where patterns are less ideal.

Step 1: Displacement extraction The first step is to obtain surface displacements from the image data. Each recording contains a reference image of the quiescent (undeformed) surface (Figure 3.9a) and a frame of the surface under oscillatory forcing (Figure 3.9b). Digital Image Correlation (DIC) is applied frame-by-frame, using the reference image as the baseline. This produces two displacement fields, d_x (Figure 3.9c) and d_y (Figure 3.9d), corresponding to in-plane motion along the x - and y -directions, respectively.

In practice, evaluating multiple frames is important, as a single snapshot may not fully capture the dominant wavelength due to phase-dependent variations in the surface deformation. By analyzing a sequence of frames, the method accounts for temporal fluctuations and ensures a more reliable estimation of the standing wave characteristics.

To illustrate the method more transparently, a synthetic wave field is constructed. An idealized surface height field $\zeta(x, y)$ is prescribed (Figure 3.10) as

$$\zeta(x, y) = \zeta_a \sin\left(\frac{2\pi x}{\lambda}\right) \sin\left(\frac{2\pi y}{\lambda}\right),$$

where ζ_a is the wave amplitude (0.2 mm in the example) and λ is the prescribed wavelength (10 mm in the example). From this known surface, the corresponding displacements d_x and d_y are generated by taking spatial derivatives in the x - and y -directions. The resulting synthetic displacement fields are shown in Figure 3.11. This approach provides clean, noise-free examples that clearly demonstrate the link between a wavy surface and the displacement fields that DIC produces in an experiment.

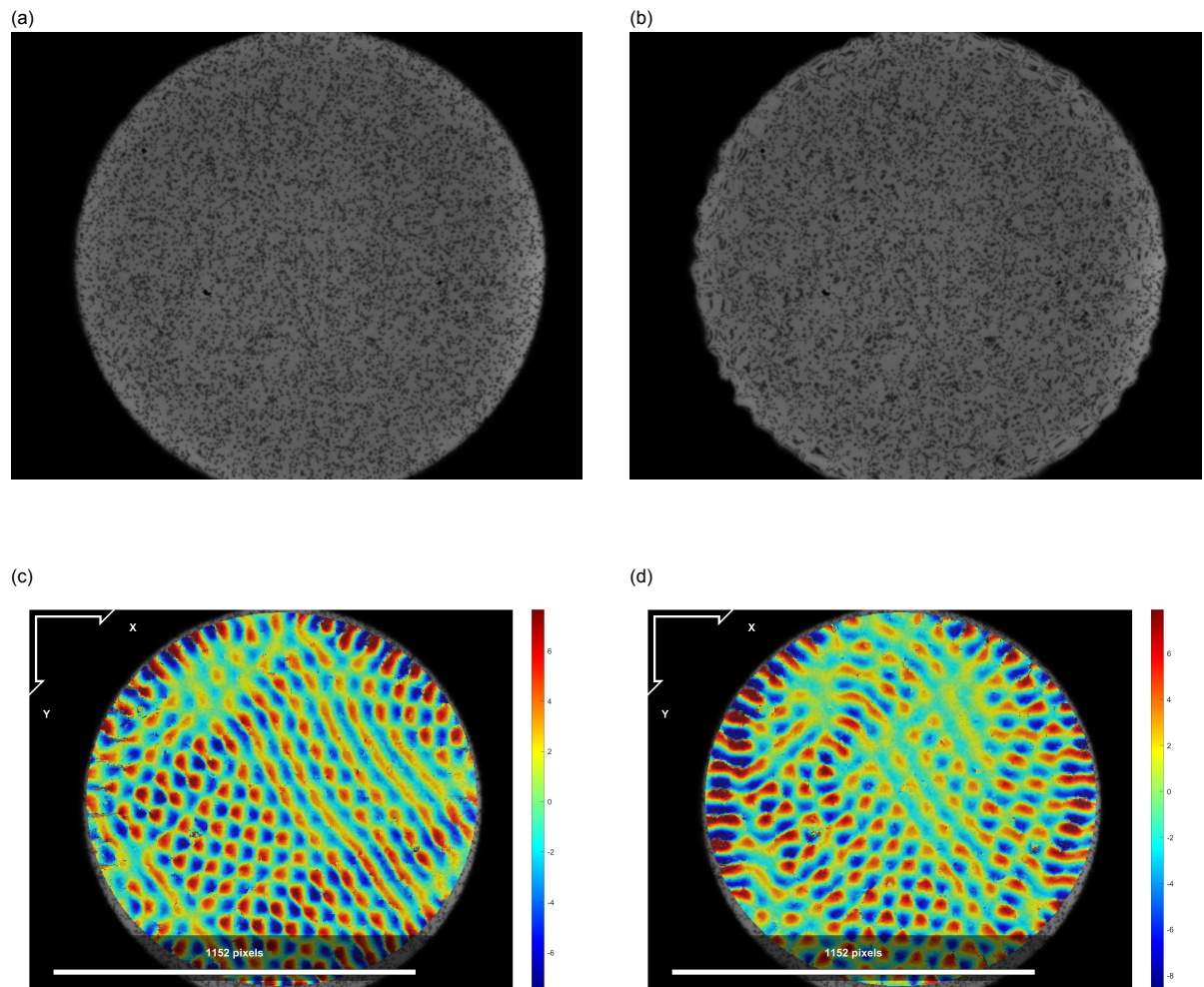


Figure 3.9: Example of DIC workflow for silicone oil at 80 Hz. (a) Reference image, (b) deformed image under oscillation, (c) displacement in x -direction (d_x), (d) displacement in y -direction (d_y). In (c–d), red indicates displacements up to 7 px and blue down to -7 px.

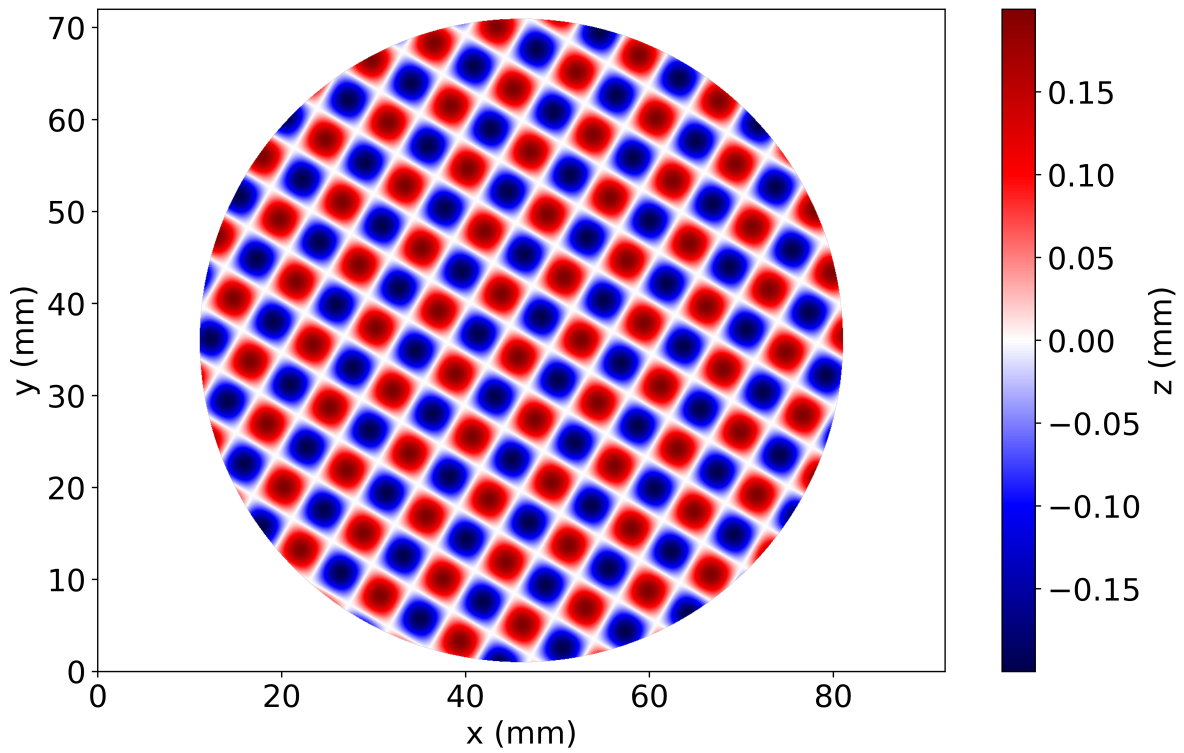


Figure 3.10: Example of a prescribed synthetic surface $\zeta(x, y)$ used for validation. Parameters: wavelength 10 mm, amplitude 0.2 mm, orientation 30° . Color map indicates local surface height.

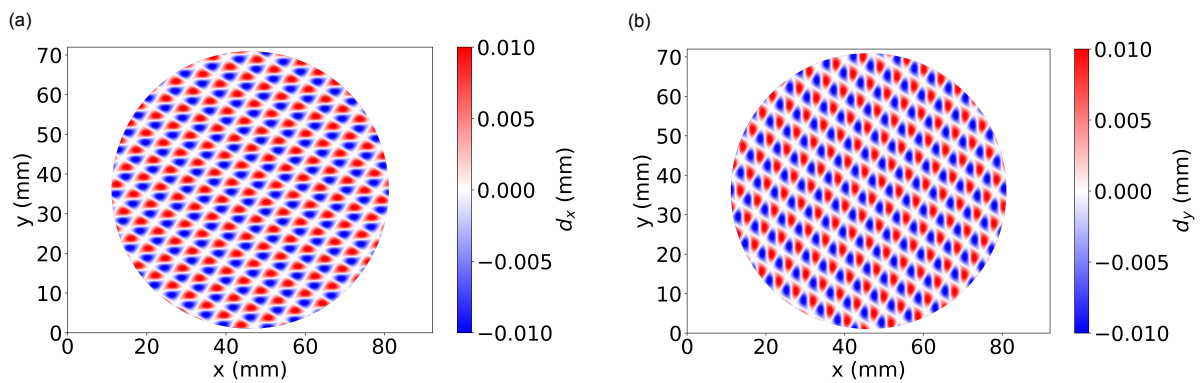


Figure 3.11: Example of synthetic displacement fields derived from the prescribed surface of Figure 3.10. (a) Displacement in the x -direction (d_x), (b) displacement in the y -direction (d_y). These clean, noise-free fields illustrate how the surface height relates to DIC-measured displacements in experiments.

Step 2: Orientation-independent representation Because the wave field inside the circular container does not have a fixed orientation, the two displacement components are combined into a single complex field

$$\tilde{\zeta}(x, y) = \frac{\partial \zeta(x, y)}{\partial x} + i \frac{\partial \zeta(x, y)}{\partial y} = d_x(x, y) + i d_y(x, y),$$

where $\zeta(x, y)$ is the local surface height. This representation preserves both gradient directions simultaneously and enables orientation-agnostic spectral analysis.

The mathematical motivation is that the Fourier transform of the complex gradient field can be expressed as

$$\mathcal{F}\{\tilde{\zeta}(x, y)\} = f_x \mathcal{F}\{\zeta(x, y)\} + i f_y \mathcal{F}\{\zeta(x, y)\} = (f_x + i f_y) \cdot \mathcal{F}\{\zeta(x, y)\}.$$

Taking the modulus yields

$$|\mathcal{F}\{\tilde{\zeta}\}| = \sqrt{f_x^2 + f_y^2} \cdot |\mathcal{F}\{\zeta(x, y)\}| = f_r \cdot |\mathcal{F}\{\zeta(x, y)\}|,$$

where $f_r = \sqrt{f_x^2 + f_y^2}$ is the radial spatial frequency. This operation makes concentric ring structures more prominent in the Fourier domain, which directly correspond to the dominant wavelength.

Step 3: Spectral analysis The final step is to determine the dominant wavelength via spectral analysis. For each frame, the 2D Fourier spectrum of the complex gradient field $\tilde{\zeta}(x, y)$ is computed. In the case of experimental data, multiple frames from the same excitation condition are processed and their spectra are summed. This averaging ensures that transient orientation effects do not bias the result. The resulting 2D spectrum of the silicone oil at 80 Hz is shown in Figure 3.12a. Because only the positive quadrant of the Fourier space is plotted ($f_x \geq 0, f_y \geq 0$), the isotropic ring structure appears as a bright quarter ring near the center of the plot, indicating that the largest Fourier magnitude occurs at a well-defined radial frequency. Taking the radially averaged spectrum (Figure 3.12b) collapses the 2D Fourier information onto a single axis. The peak in this radial spectrum corresponds to the dominant radial spatial frequency f_r , from which the wavelength of the standing wave can be inferred as $\lambda = 1/f_r$. For the silicone oil at 80 Hz, the peak occurs at $f_r = 0.213/\text{mm}$, corresponding to a wavelength of $\lambda = 4.7 \text{ mm}$.

For the synthetic tests, the prescribed surface was rotated (e.g., Figure 3.10) and the spectra from multiple rotations were summed to produce an isotropic distribution that mimics the random orientations encountered in practice. The summed 2D spectrum is shown in Figure 3.12c, and the corresponding radially averaged spectrum in Figure 3.12d. Interestingly, the spectrum exhibits two prominent peaks: the highest peak occurs at $f_r = 0.202/\text{mm}$ (wavelength $\lambda = 4.95 \text{ mm}$), while the secondary peak is located at $f_r = 0.283/\text{mm}$.

A possible explanation is that the analysis detects the most frequently recurring spatial pattern in the displacement fields. In the synthetic surface case, the regions of zero slope (white regions in the displacement maps) occur more regularly than the maxima or minima (red or blue regions), so the Fourier transform emphasizes these repeating intervals. Both crests and troughs correspond to zero slope, meaning that the highest peak effectively measures the distance from crest to trough, i.e., half a wavelength. The second peak, by contrast, occurs at a frequency larger by a factor of $\sqrt{2}$, which most likely corresponds to the diagonal distance between consecutive crests (or troughs) in the checkerboard-like pattern of the rotated synthetic surface. While these features arise in the synthetic case due to its idealized, noise-free structure, they do not appear in experimental data, which lack perfectly square, regular patterns.

This three-step procedure, from displacement extraction via DIC to orientation-independent representation to spectral analysis, provides a robust and reproducible means of determining the governing wavelength. Convergence studies (Appendix J and Appendix K) demonstrate that stable wavelength estimates are obtained after analyzing 180 frames per test, beyond which additional frames do not alter the results. Similarly, a radial binning of 1200 bins is adopted to generate the 2D Fourier spectrum, providing sufficient resolution for identifying the dominant wavelength. These parameters are used consistently for all subsequent analyses. Finally, Section 3.6 discusses the accuracy and limitations of this approach, ensuring transparent and reliable wavelength determination across all experimental cases.

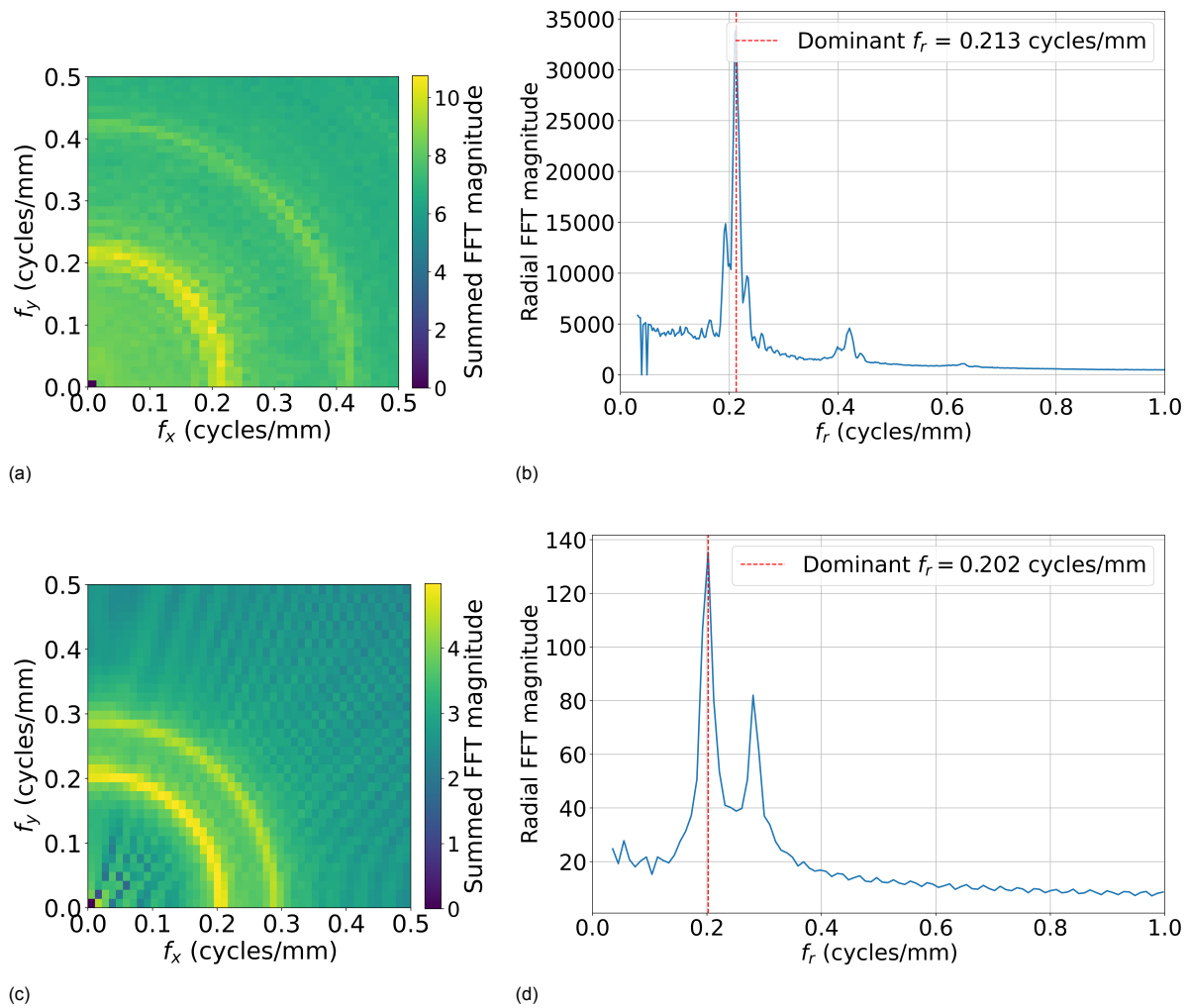


Figure 3.12: (a) Summed 2D Fourier spectrum of silicone oil at 80 Hz. (b) Radial average spectrum of (a), indicating a peak radial spatial frequency $f_r = 0.213/\text{mm}$ (wavelength $\lambda = 4.7 \text{ mm}$). (c) Summed 2D Fourier spectrum of the synthetic surface. (d) Radial average spectrum of (c), indicating peaks at $f_r = 0.202/\text{mm}$ ($\lambda = 4.95 \text{ mm}$) and $f_r = 0.283/\text{mm}$ (diagonal spacing).

3.4.3. Critical acceleration derivation

The goal of this subsection is to determine the critical acceleration, a_{crit} , required to initiate the subharmonic instability in the floating layer. While the original approach aims to infer a_{crit} from the temporal growth of surface displacements at different excitation amplitudes, practical limitations of the method lead to a more direct measurement of the lowest acceleration at which standing waves clearly appear.

Onset time and initial method for critical acceleration The original plan to determine the critical acceleration relies on identifying the time it takes for subharmonic wave motion to appear at a given excitation amplitude. By performing tests at multiple acceleration amplitudes and plotting the inverse of the onset time ($1/t_0$) against acceleration, a linear extrapolation to $1/t_0 = 0$ indicates the acceleration at which the instability would take infinite time to appear, i.e., the critical acceleration.

To detect the onset of the instability, the temporal evolution of the surface displacement is tracked using Digital Image Correlation (DIC). For each frame, the maximum in-plane displacement is extracted from the displacement fields, yielding a time series of displacement magnitudes. These data are then fitted with a logistic growth function

$$f(t) = \frac{\Delta d}{1 + e^{-K(t-t_0)}} + d_0,$$

where Δd is the total displacement change between the plateaus, K is the growth rate, t_0 is the inflection point, and d_0 is the initial displacement. The inflection point t_0 , corresponding to the time of steepest growth in displacement, is taken as the objective onset time of the subharmonic instability.

The derivative of the logistic function,

$$\frac{df(t)}{dt} = \frac{\Delta d K e^{-K(t-t_0)}}{(1 + e^{-K(t-t_0)})^2},$$

reaches its maximum at $t = t_0$,

$$\left. \frac{df(t)}{dt} \right|_{t=t_0} = \frac{\Delta d K}{4}.$$

Figure 3.13 illustrates a simulated example of surface displacement fitted with a logistic curve. In this case, the fitted parameters are $\Delta d = 5.07$ px, $K = 0.24$ /s, $t_0 = 24.93$ s, and $d_0 = 1.95$ px.

However, the logistic growth approach has both theoretical and practical limitations for describing the onset of subharmonic Faraday waves. The standard logistic differential equation,

$$\frac{df}{dt} = Kf - \frac{K}{\Delta d} f^2,$$

assumes monotonic growth toward a positive saturation plateau and does not preserve the odd symmetry of the wave amplitude: negative excursions are treated the same as positive ones, whereas the physical standing-wave system oscillates around zero. A cubic nonlinearity,

$$\frac{df}{dt} = Kf - \frac{K}{\Delta d^2} f^3,$$

restores this symmetry and more accurately reflects the subharmonic dynamics. Because the quadratic logistic model cannot represent negative displacements, the displacement magnitude $|f(t)|$ is used for fitting. Even so, experiments with the floating material reveal that the logistic fit is unreliable: it assumes a well-defined initial plateau and a clear saturation plateau, but the initial plateau is often negligible. Moreover, the inferred onset time t_0 depends strongly on the number of frames included in the fit. Figure 3.14 illustrates this sensitivity for a 100 μ m film at 70 Hz (test 3). As the number of frames in the fitting window increases, the resulting onset time changes, demonstrating that a consistent determination of t_0 is not possible. For these reasons, the logistic method is ultimately not used to quantify the onset of subharmonic motion.

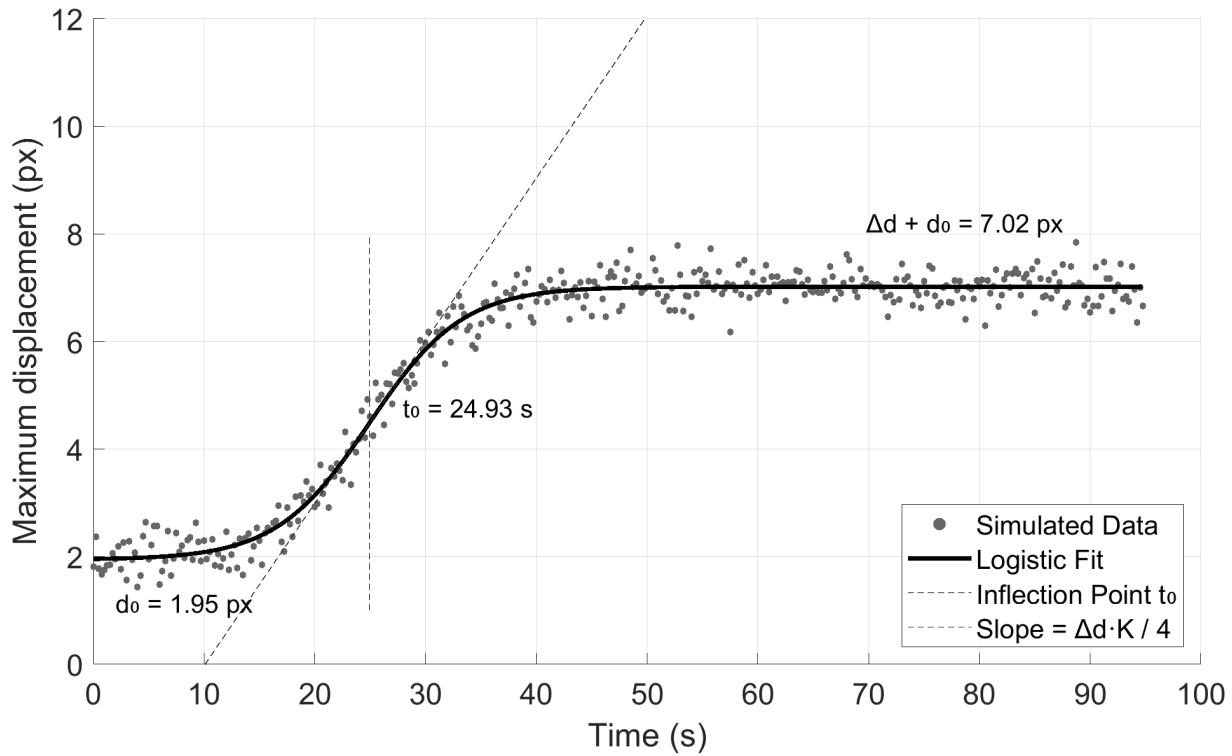


Figure 3.13: Example of simulated surface displacement over time (in pixels) fitted with a logistic growth curve. Displacement data are shown as circles, and the fitted logistic curve is shown as a solid black line. Fitted parameters: total displacement change $\Delta d = 5.07$ px, growth rate $K = 0.24/\text{s}$, inflection point $t_0 = 24.93$ s, and initial displacement $d_0 = 1.95$ px. This illustrates how the onset time of subharmonic instability is determined from the steepest growth in displacement.

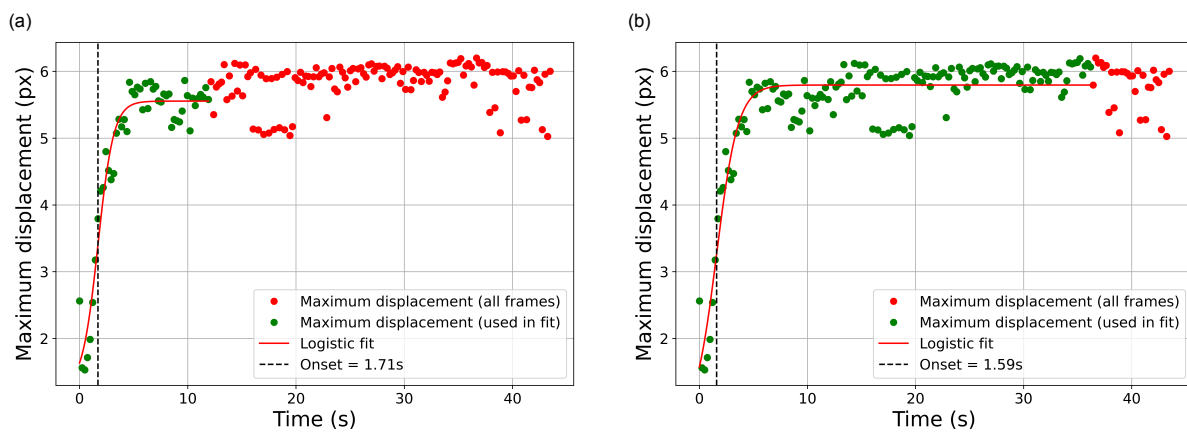


Figure 3.14: Maximum displacement magnitude (px) from in-plane DIC for deionized water covered with a $100\ \mu\text{m}$ floating sheet at 60 Hz. Each time step corresponds to a recorded frame. Green markers indicate the data included in the logistic fit, red markers show all measured points, and the solid red line is the resulting fit. (a) uses 50 frames ($t_0 = 1.71$ s), (b) uses 150 frames ($t_0 = 1.59$ s), showing that when the initial plateau is not clearly present, the estimated onset time depends on the chosen frame range.

Acceleration measurement and practical determination of critical acceleration Instead, the critical acceleration is determined experimentally by observing the appearance of standing waves at sufficiently high excitation amplitudes and performing multiple tests while gradually lowering the acceleration. The lowest acceleration at which waves appear is taken as the critical acceleration.

Acceleration data are recorded using an accelerometer mounted on the shaker. The accelerometer calibration factor, determined in-house, is 956 ± 15 mV/g (Appendix L). For each test, three short time windows are extracted at randomly selected moments in the video to verify the stability of the excitation. The peak-to-peak voltage from each window is converted to acceleration using the calibrated sensitivity, and the final acceleration amplitude assigned to the test is the average of these three measurements.

Preliminary tests (Appendices N and O) confirm that the laser distance meter reliably captures both amplitude and frequency of the shaker's oscillatory motion. Amplitude estimates are consistent across different sampling rates, and a sampling rate approximately ten times higher than the excitation frequency provides the most accurate and stable measurements. These results directly support the temporal resolution requirement outlined in Section 3.1, which specifies capturing at least 5–10 samples per excitation period. The convergence of the experimental tests with this requirement indicates that measuring around ten points per period is sufficient to accurately and reproducibly resolve both displacement and acceleration data.

3.4.4. Surface reconstruction and amplitude estimation

The vertical surface displacement $\zeta(x, y)$ is reconstructed from the in-plane dot-pattern displacements $d_x(x, y)$ and $d_y(x, y)$ obtained via synthetic schlieren measurements described in Section 3.3 (Moisy et al., 2009). Following the small-slope approximation, the apparent in-plane displacements are proportional to the surface gradient:

$$\frac{\partial \zeta}{\partial x} \approx \alpha d_x, \quad \frac{\partial \zeta}{\partial y} \approx \alpha d_y,$$

where

$$\alpha = \frac{n_{\text{air}}}{n_{\text{water}} L_{\text{air}}}$$

is an optical calibration factor depending on the refractive indices and the effective air path length L_{air} (Moisy et al., 2009). In the present setup, the camera–pattern distance is measured as 0.81 m, while the combined water and glass thickness between the pattern and the free surface is approximately 0.02 m, yielding an air path length of

$$L_{\text{air}} = 0.81 - 0.02 = 0.79 \text{ m}, \quad \text{and thus } \alpha \approx 0.95 \text{ for } n_{\text{air}} = 1.00, n_{\text{water}} = 1.333.$$

Moisy et al. (Moisy et al., 2009) reconstructed the surface by minimizing the difference between the measured slope field $\kappa = (\alpha d_x, \alpha d_y)$ and the gradient of a reconstructed surface. This can be expressed mathematically as a least-squares problem:

$$\min_{\zeta(x,y)} \iint \left[\left(\frac{\partial \zeta}{\partial x} - \alpha d_x \right)^2 + \left(\frac{\partial \zeta}{\partial y} - \alpha d_y \right)^2 \right] dx dy,$$

where the integral is taken over the measurement domain. The functional above represents the squared error between the measured slopes and the gradient of the reconstructed surface.

To solve this minimization problem, one can use the Euler-Lagrange equation. For a functional of the form

$$J[\zeta] = \iint f(\partial_x \zeta, \partial_y \zeta) dx dy,$$

the Euler-Lagrange equation is

$$\frac{\partial}{\partial x} \frac{\partial f}{\partial (\partial_x \zeta)} + \frac{\partial}{\partial y} \frac{\partial f}{\partial (\partial_y \zeta)} - \frac{\partial f}{\partial \zeta} = 0.$$

In our case, $f = (\partial_x \zeta - \alpha d_x)^2 + (\partial_y \zeta - \alpha d_y)^2$, so that

$$\frac{\partial f}{\partial(\partial_x \zeta)} = 2(\partial_x \zeta - \alpha d_x), \quad \frac{\partial f}{\partial(\partial_y \zeta)} = 2(\partial_y \zeta - \alpha d_y), \quad \frac{\partial f}{\partial z} = 0$$

Substituting into the Euler-Lagrange equation and dividing through by 2 gives

$$\frac{\partial}{\partial x}(\partial_x \zeta - \alpha d_x) + \frac{\partial}{\partial y}(\partial_y \zeta - \alpha d_y) = 0.$$

Expanding the derivatives leads to

$$\frac{\partial^2 \zeta}{\partial x^2} + \frac{\partial^2 \zeta}{\partial y^2} = \frac{\partial(\alpha d_x)}{\partial x} + \frac{\partial(\alpha d_y)}{\partial y}.$$

This can be compactly written using the Laplace operator as

$$\nabla^2 \zeta(x, y) = \frac{\partial(\alpha d_x)}{\partial x} + \frac{\partial(\alpha d_y)}{\partial y},$$

which is the Poisson equation that we solve numerically to reconstruct the surface elevation $\zeta(x, y)$ from the measured slope field.

In this study, the Poisson equation is solved numerically in Fourier space. This approach ensures that the reconstructed surface is consistent with both x - and y -gradients simultaneously and provides a smooth, least-squares-optimal reconstruction. The Fourier-based solver is naturally suited for a rectangular computational grid, but in this study the measured data are restricted to a circular field of view. Grid points outside this circular region are masked during reconstruction, which does not affect the accuracy of the reconstructed surface inside the measurement region.

To remove systematic slope artefacts (also noted by Moisy et al. (2009)), a best-fit tilted plane is subtracted from $\zeta(x, y)$. Wave amplitudes are then estimated as half the peak-to-trough difference. However this method is sensitive to outliers: a single corrupted displacement vector can introduce spurious maxima or minima, which may dominate the amplitude estimate even if the rest of the field is reconstructed correctly.

For amplitude estimation, this reconstruction is performed on a single representative image rather than a full time series. This contrasts with the wavelength analysis, where the full temporal sequence of surface displacements is used and Fourier-based methods are applied to determine the dominant wavelengths. The single-image approach suffices for order-of-magnitude amplitude estimates but does not capture temporal variations or provide the statistical robustness afforded by time-series analysis.

The objective of this reconstruction is not to provide highly accurate hydroelastic amplitude measurements, but to obtain the correct order of magnitude for wave steepness estimation and wavelength cross-checking. Because the theoretical calibration factor relies on small-angle assumptions and neglects higher-order refraction effects, these amplitudes should be considered approximate; quantitative measurements require direct calibration against a known surface profile.

3.5. Experimental procedure and data treatment

Measurement procedure Before each measurement, the fluid surface is allowed to come to apparent rest, such that no visible surface motion remains. No quantitative verification of this rest condition is performed (see Chapter 7 Section 7.2 for recommendations on how this could be improved). While the surface is settling, the desired excitation frequency and amplitude are set using the multifunction synthesizer. The frequency divider value is adjusted to provide an image acquisition rate of approximately 4 frames per second. This rate is not intended to resolve every oscillation period; instead, taking one image every few excitation cycles makes it possible to record a longer time span with the same total number of frames, while still providing sufficient information to detect the onset of wave motion. Using an odd divider setting ensures that successive images correspond to alternating wave phases, which makes the onset of motion especially visible in the displacement of the dot pattern. For example, a divider value of 15 is used for an excitation frequency of 60 Hz (Figure 3.6).

Once these parameters are established, a reference image of the static surface and the underlying dot pattern is captured. This reference frame serves as a baseline for subsequent displacement calculations. Next, the multifunction synthesizer and video recording system are initiated simultaneously, capturing the surface response over a sequence of 380 frames. The sequence length of 380 frames

is chosen as a practical compromise: long enough to ensure capture of the instability onset and subsequent steady oscillations, while avoiding excessive data storage demands. No dedicated analysis is performed in advance to determine the optimal number of frames. However, a posteriori convergence tests on the wavelength analysis (Appendix J) confirm that stable estimates can be obtained with significantly fewer frames. For onset detection, the exact onset time is not known a priori, so a sufficiently long sequence is necessary to ensure that the instability is reliably captured.

At the end of each run, five additional images are captured at half the excitation frequency (frequency divider value of 2; see Figure 3.5 for an example at 40 Hz). These were initially intended for alternative methods of wavelength determination, but are ultimately excluded from the final analysis because such sparse image sets prove insufficient for a robust spectral estimate. Finally, the shaker acceleration is recorded with an accelerometer. The sampling interval is chosen so that approximately 10 samples are taken per excitation cycle. The complete image–acceleration sequence is repeated three times at random intervals to assess temporal stability and reproducibility without requiring a full time-series analysis. An overview of the acquisition settings, including frequency divider values and sampling intervals, is given in Table 3.2.

Table 3.2: Acquisition settings used in the experiments. For each shaker frequency f_s , the frequency divider value was selected such that the image acquisition rate was close to 4 frames per second. Odd divider values ensure that successive frames correspond to alternating wave phases. The accelerometer sampling interval was adjusted to provide about 10 samples per excitation cycle, as validated in Appendix O.

Shaker frequency f_s [Hz]	Frequency divider value [-]	Accelerometer sampling interval [ms]
20	5	5
30	7	3
40	11	3
50	13	2
60	15	2
70	17	1
80	21	1
90	23	1

Frequency and amplitude variation Systematic variations of excitation frequency and amplitude are carried out for all fluids and material samples. In the silicone oil reference tests (without floating films), frequencies in the range of 20 Hz to 80 Hz are explored in 10 Hz increments, with five discrete amplitude settings tested per frequency. At each frequency, the acceleration is decreased stepwise, starting from high amplitude and progressing toward lower values. The chosen frequency range is guided by the predictions of the linear stability model (Figure 3.1). Frequencies below 20 Hz produce wavelengths exceeding the tank dimensions and the limited field of view imposed by the LED illumination, making reliable measurement impractical. To assess repeatability, each frequency–amplitude combination is repeated three times (see Chapter 4 for a quantitative demonstration of reproducibility).

For deionized water, both reference tests (without floating films) and material tests (with floating films) are performed. Reference tests follow a similar protocol, but here a range of frequencies from 30 Hz to 90 Hz is used, with six amplitude settings per frequency. The lower bound is set higher than for silicone oil to ensure the wavelengths remain fully visible within the field of view, consistent with model predictions (Figure 3.8), while the upper bound is chosen to remain within a range where significant wavelength variation can still be observed. Material samples with thicknesses of $20 \pm 1 \mu\text{m}$, $50.0 \pm 2.5 \mu\text{m}$, $100 \pm 5 \mu\text{m}$, and $200 \pm 10 \mu\text{m}$ are examined over the entire frequency range. To balance testing time with data reliability, only the measurements at 30 Hz, 60 Hz, and 90 Hz are repeated three times. These frequencies are selected to represent the lower, middle, and upper bounds of the operational range, corresponding to wavelengths and critical accelerations predicted by the model. As discussed in Chapter 4, the high consistency observed in these repeated measurements supports the assumption that the system’s behavior at intermediate frequencies and thicknesses is similarly stable.

Data processing and statistical treatment After wavelength extraction (Section 3.4.2), the results are combined and presented as follows. For each excitation frequency, several amplitude tests are conducted. Since Faraday theory predicts that the wavelength depends only on frequency (and not on

forcing amplitude, once the instability is established), the mean wavelength across all amplitude tests at that frequency is calculated. The standard error of the mean (SEM) is used to indicate uncertainty and is plotted together with the mean values. For repeated runs at the same frequency, no additional averaging is performed. Instead, the repetitions are shown side-by-side in the plots to allow a direct visual assessment of reproducibility.

For accelerations, the results of all tests are reported together with their measurement uncertainties, as determined from the accelerometer calibration procedure (see Section 3.6.4). The lowest acceleration at which waves are observed is taken as the critical value, in line with what is defined in Section 3.4.3. Repeatability in acceleration thresholds is likewise assessed by displaying repeated runs next to each other, rather than by statistical averaging.

For amplitude, only the order of magnitude is considered; therefore, the surface profile from a single representative test at 60 Hz is presented for both the free-surface and covered cases.

3.6. Accuracy assessment

The aim of this section is to evaluate whether the experimental setup and data analysis methods meet the measurement goals established in Section 3.1. Specifically, the assessment concerns whether the achieved accuracy is sufficient to reliably determine the onset acceleration and dominant wavelength.

For some components, such as the laser distance meter and accelerometer, the required precision could be anticipated in advance, which allowed the selection of appropriate sensors. For other aspects, particularly the extraction of wavelengths from evolving wave fields, the analysis methods were developed in parallel with the experiments. In these cases, accuracy could only be assessed once the complete processing workflow had been carried out.

The following discussion addresses the main sources of uncertainty in the final setup, with emphasis on liquid depth consistency, sensor performance, and the wavelength extraction procedure. Where possible, uncertainties are quantified and propagated to the derived quantities, enabling an evaluation of whether the measurement goals are satisfied and supporting a robust interpretation of the results.

3.6.1. Liquid depth uncertainty

Each day, a series of tests is performed using fresh liquid, which introduces a degree of uncertainty and non-uniformity in the measurements. Throughout all tests, a target liquid depth of 10 mm is maintained. The required volume V is calculated based on the container dimensions, where the diameter D is 130 mm and the desired liquid height h is 10 mm. The volume is given by

$$V = A \cdot h = \pi \cdot \left(\frac{D}{2}\right)^2 \cdot h = \pi \cdot (6.5 \text{ cm})^2 \cdot 1 \text{ cm} \approx 132.73 \text{ cm}^3 = 0.133 \text{ L}.$$

This volume is measured using a graduated cylinder with an indicated accuracy of ± 10 mL. The liquid height is verified using a ruler with a stated precision of 1 mm. The presence of the meniscus may introduce additional offsets that affect the exact liquid depth. Although both the graduated cylinder and the ruler have specified accuracy limits, measurement precision up to roughly half of the indicated uncertainty is often achievable in practice.

Considering the volume uncertainty as ± 5 mL, the corresponding uncertainty in liquid height δh can be estimated by dividing the volume uncertainty δV by the cross-sectional area A :

$$\delta h = \frac{\delta V}{A} = \frac{5 \text{ cm}^3}{132.73 \text{ cm}^2} \approx 0.0377 \text{ cm} = 0.38 \text{ mm}.$$

This indicates that the uncertainty in volume measurement contributes up to approximately 0.38 mm variation in the liquid height. Based on the preliminary analysis in Section 3.4.1, variations of this magnitude are not expected to significantly affect the measured wavelength or critical acceleration values during the experiments.

3.6.2. Multifunction synthesizer uncertainty

The multifunction synthesizer that is used to drive the shaker has a frequency accuracy of ± 5 ppm (manufacturer specifications, Appendix G.1), ensuring highly stable and precise excitation across all tested frequencies. This level of accuracy guarantees negligible deviation over the experimental timescales and is more than sufficient for the frequency ranges considered in this study.

3.6.3. Laser distance meter uncertainty

The laser distance meter used in this study is specified with two important accuracy parameters: repeatability and linearity (manufacturer specifications, Appendix G.5). The repeatability, defined as $\pm 8 \mu\text{m}$, represents the device's ability to consistently reproduce the same measurement under identical conditions and is an indicator of its short-term precision or noise level. Linearity, specified as $\leq 160 \mu\text{m}$, denotes the maximum deviation of the sensor's output from an ideal linear response over the entire measurement range, representing the maximum systematic error or bias.

Since the focus of this study is on tracking the vertical motion of the shaker platform continuously over time, repeatability is the more relevant parameter. This is because the experiment requires resolving small changes and oscillations in displacement with high temporal resolution, where measurement noise and consistency dominate the accuracy requirements. In contrast, linearity affects the absolute accuracy of displacement measurements over the full range, which is less critical in this context where relative motion and dynamic changes are of primary interest. Therefore, the repeatability value is used to characterize the effective measurement resolution in the analysis.

3.6.4. Accelerometer and acceleration measurement uncertainty

The accelerometer output was recorded through the LabVIEW interface with sampling intervals chosen to yield approximately ten samples per excitation period (Table 3.2). This sampling density provides sufficient temporal resolution for accurate reconstruction of the acceleration waveform, in accordance with the Nyquist–Shannon sampling theorem, which states that a continuous signal can be exactly reconstructed if the sampling rate exceeds twice the highest frequency present in the signal (Shannon, 1949). The sampling strategy was applied consistently across all excitation frequencies to ensure reliable signal acquisition (see Appendices N and O).

The accelerometer is connected to the shaker via a dedicated sensor line integrated into the experimental setup. According to the manufacturer's specifications (Appendix G.6), the device exhibits a maximum DC offset of $\pm 30 \text{ mV}$ and a gain accuracy of $\pm 1\%$. Since no calibration factor was provided by the manufacturer, a dedicated calibration procedure was performed using known excitation parameters, yielding

$$C = (956 \pm 15) \text{ mV/g},$$

which is applied consistently to all subsequent measurements (see Appendix L for details). Measured voltage amplitude V_a is converted to acceleration amplitude a_a in units of g via

$$a_a = \frac{V_a}{C},$$

with combined standard uncertainty

$$\delta a_a = a_a \sqrt{\left(\frac{\delta V_a}{V_a}\right)^2 + \left(\frac{\delta C}{C}\right)^2}.$$

Here, δV_a accounts for the $\pm 1\%$ gain accuracy, and $\delta C = 15 \text{ mV/g}$ represents the calibration uncertainty.

This framework ensures that reported accelerations include both instrumental and calibration uncertainties, providing realistic confidence bounds consistent with GUM and established error propagation approaches.

3.6.5. Uncertainty propagation from images to wavelength

Section 3.4.2 describes the extraction of the dominant wavelength from image sequences via displacement estimation, complex-field representation, and Fourier-domain analysis. The uncertainty at each stage is quantified to determine the resulting wavelength uncertainty in millimetres. This analysis follows the *Guide to the Expression of Uncertainty in Measurement* (GUM) (Joint Committee for Guides in Metrology (JCGM), 2008) and standard error propagation techniques (Bevington & Robinson, D. Keith, 2003; Taylor, 1997), using first-order (linearized) propagation throughout.

²First-order propagation for independent variables V_a and C : $\delta a_a = \sqrt{(\partial a_a / \partial V_a \delta V_a)^2 + (\partial a_a / \partial C \delta C)^2}$ with $\partial a_a / \partial V_a = 1/C$, $\partial a_a / \partial C = -V_a/C^2$.

The processing chain comprises five steps: (i) extraction of displacement fields from the DIC, (ii) formation of the complex displacement amplitude, (iii) Fourier analysis with finite resolution and measurement noise, (iv) radial averaging into bins, and (v) conversion from pixels to physical units.

Uncertainty sources are identified at each stage and, when independent, are combined using the Root-Sum-Square (RSS) rule.

1) DIC displacement fields Digital Image Correlation (DIC) provides the in-plane displacement fields $d_x(x, y)$ and $d_y(x, y)$ on a sampling grid. Each component is subject to Type A uncertainty arising from factors such as image noise, subset size, interpolation, and correlation quality. Several studies have systematically quantified these contributions; in particular, Pan et al. (2010) provide a detailed error budget for two-dimensional DIC, including effects from optics and pattern quality, with typical precisions ranging from 0.01 px–0.05 px under static conditions. A broader review of DIC error sources is also given by Pan (2018).

Type A uncertainties can, in principle, be estimated by comparing repeated measurements of a static target. True static image pairs were not acquired in these experiments; instead, a posteriori “static” tests were attempted using sequences from the oscillating Faraday-wave data. Although these phase-locked image pairs could ideally capture the surface at identical instances, slight rotations and surface evolution introduce apparent displacements of 0.5 px to 1 px, overestimating the Type A uncertainty and not reflecting the intrinsic DIC precision. Details of these attempted static tests are provided in Appendix M.

Given the absence of true static repeats, a literature-based baseline for the DIC uncertainty is adopted. General principles of DIC, including the effects of image quality, subset (window) size, step size, and correlation algorithms on measurement accuracy, are discussed by Sutton et al. (2010). The present study does not systematically investigate the influence of subset or step size on DIC precision due to the lack of dedicated static images. Instead, a representative value from the literature is assumed. Quantitative guidance from Pan (2018) and Pan et al. (2010) reports sub-pixel precisions in the range of 0.01 px to 0.05 px under well-controlled static conditions, with typical values around $\sigma_{\text{DIC}} = 0.02$ px. While no direct benchmarking against other DIC implementations is performed, Ncorr is expected to achieve sub-pixel precision consistent with these ranges. Accordingly, $\sigma_{\text{DIC}} = 0.02$ px is retained as a conservative baseline uncertainty.

2) Complex displacement amplitude The two displacement components are combined into the complex field

$$\tilde{\zeta}(x, y) = d_x(x, y) + i d_y(x, y).$$

Uncertainty in the magnitude $|\tilde{\zeta}(x, y)|$ follows from first-order propagation of independent variables d_x and d_y ³:

$$\delta|\tilde{\zeta}(x, y)| = \frac{1}{|\tilde{\zeta}(x, y)|} \sqrt{(d_x \delta d_x)^2 + (d_y \delta d_y)^2}.$$

In practice, this random variability manifests in the Fourier spectrum as jitter of the spectral peak. Instead of propagating analytically through the Fourier transform, it is represented as a frequency-domain uncertainty, δf_{noise} , directly linked to σ_{DIC} (see below).

3) Fourier analysis and discretisation The Discrete Fourier Transform (DFT), computed here using MATLAB’s Fast Fourier Transform (FFT) algorithm, introduces a frequency-grid spacing of

$$\delta f_{\text{FFT}} = \frac{1}{N s},$$

where N is the number of DIC points per direction and s is the subset step in pixels (Oppenheim & Schaffer, 2010). For the adopted parameters ($N = 295$, $s = 4$ px), this yields $\delta f_{\text{FFT}} = 8.5 \times 10^{-4}$ px⁻¹.

³First-order propagation for independent variables d_x and d_y : $\delta f = \sqrt{(\partial f / \partial d_x \delta d_x)^2 + (\partial f / \partial d_y \delta d_y)^2}$, with $\partial|\tilde{\zeta}| / \partial d_x = d_x / |\tilde{\zeta}|$, $\partial|\tilde{\zeta}| / \partial d_y = d_y / |\tilde{\zeta}|$.

Noise in the displacement field, quantified by the baseline DIC precision σ_{DIC} , produces variance in the Fourier spectrum. Propagating the sub-pixel displacement uncertainty through the FFT, the corresponding contribution to the peak frequency can be estimated as

$$\delta f_{\text{DIC}} \approx \frac{\sigma_{\text{DIC}}}{N_s},$$

giving $\delta f_{\text{DIC}} = 1.7 \times 10^{-5} \text{ px}^{-1}$ for the parameters above. This relation follows from linearized propagation of uncertainty onto the discrete frequency grid defined by the DFT.

4) Radial averaging (binning) To obtain an isotropic spectrum, magnitudes are averaged into N_{bin} concentric annuli between k_{min} and k_{max} . With bin width Δf_{bin} , the assignment of each sample to the bin centre introduces a quantisation uncertainty. Adopting the GUM standard uncertainty for a uniform distribution,

$$\delta f_{\text{rad}} = \frac{\Delta f_{\text{bin}}}{\sqrt{12}}.$$

For $N_{\text{bin}} = 1200$, $k_{\text{min}} = 0.00066 \text{ px}^{-1}$, and $k_{\text{max}} = 0.176 \text{ px}^{-1}$, this gives $\delta f_{\text{rad}} = 4.2 \times 10^{-5} \text{ px}^{-1}$.

5) Conversion to wavelength in millimetres The dominant wavelength in pixels is

$$\lambda_{\text{px}} = \frac{1}{f_{\text{peak}}},$$

where f_{peak} is the peak spatial frequency obtained from the Fourier spectrum.⁴

The uncertainty in λ_{px} is derived from the total frequency uncertainty, combining contributions from FFT discretisation, DIC noise, and radial-bin quantisation as independent sources:

$$\delta f_{\text{px}} = \sqrt{\delta f_{\text{FFT}}^2 + \delta f_{\text{DIC}}^2 + \delta f_{\text{rad}}^2}.$$

Applying first-order propagation for the inverse relation $y = 1/x$ yields

$$\delta \lambda_{\text{px}} = \frac{\delta f_{\text{px}}}{f_{\text{peak}}^2},^5$$

Conversion to physical units is obtained using the pixel size p (in mm/px):

$$\lambda_{\text{mm}} = \lambda_{\text{px}} p.$$

The pixel size calibration sets the physical scale of the measurements. In Ncorr, a line corresponding to a controlled displacement stroke of 5 mm was drawn. Ncorr then calculated the pixel-to-millimetre calibration factor as

$$p \approx 0.060 \text{ mm/px}.$$

From this factor, the stroke length in pixels can be inferred as

$$\text{stroke in pixels} = \frac{5 \text{ mm}}{p} \approx 83.3 \text{ px}.$$

Figures illustrating the calibration procedure are provided in Appendix H.

Each endpoint of the stroke can be located within ± 1 px, resulting in a total positional uncertainty of

$$\Delta_{\text{px,total}} = 1 \text{ px (start)} + 1 \text{ px (end)} = 2 \text{ px}.$$

This uncertainty propagates to the pixel size as

$$\delta p = \frac{\Delta_{\text{px,total}}}{\text{stroke in pixels}} p = \frac{2 \text{ px}}{83.3 \text{ px}} \cdot 0.060 \text{ mm/px} \approx 0.0014 \text{ mm/px}.$$

⁴Some report the wavenumber $k = 2\pi f$ in radians per pixel. Here, f_{peak} is in cycles per pixel, so the inverse directly gives the wavelength in pixels.

⁵First-order propagation for a single variable x : $\delta y = |\partial y / \partial x| \delta x = \delta x / x^2$, with $x = f_{\text{peak}}$, $\delta x = \delta f_{\text{px}}$.

Combining this calibration uncertainty with the wavelength uncertainty in pixels, $\delta\lambda_{\text{px}}$, the total uncertainty in millimetres follows from first-order propagation for the product of independent quantities (Bevington & Robinson, D. Keith, 2003; Joint Committee for Guides in Metrology (JCGM), 2008; Taylor, 1997):

$$\delta\lambda_{\text{mm}} = \sqrt{(p \delta\lambda_{\text{px}})^2 + (\lambda_{\text{px}} \delta p)^2}.$$

To assess how uncertainty propagates across the evaluated wavelength range, Figure 3.15 present a quantitative analysis of wavelength estimation errors. Figure 3.15a shows the measured dominant wavelengths with corresponding absolute uncertainties in millimetres, while Figure 3.15b illustrates the relative error as a percentage of each wavelength.

As expected from the applied uncertainty propagation model, the absolute error increases with wavelength. For instance, the longest wavelength considered, 25 mm, exhibits an uncertainty of approximately ± 8.88 mm, corresponding to a relative error of about 35.5 %. In contrast, the shortest wavelength, 4 mm, shows a much smaller uncertainty of ± 0.25 mm, or roughly 6.1 %. This trend arises from the inverse relationship between spatial frequency and wavelength, where small errors in frequency space, due to FFT resolution and radial binning, become amplified at long wavelengths.

A target accuracy of better than 10 % was set for the shortest resolvable wavelength, 4 mm, which is comfortably met, validating the robustness of the approach for detecting fine-scale periodic features. However, the analysis also highlights an intrinsic limitation: precision degrades for low-frequency components, where spatial resolution and calibration uncertainties have a greater effect.

While the plots illustrate these trends, the full numerical data used to generate them is tabulated in Appendix R. The same uncertainty estimation procedure is directly applicable to the experimental results presented in later chapters, providing a consistent framework for reporting both measured values and their associated confidence.

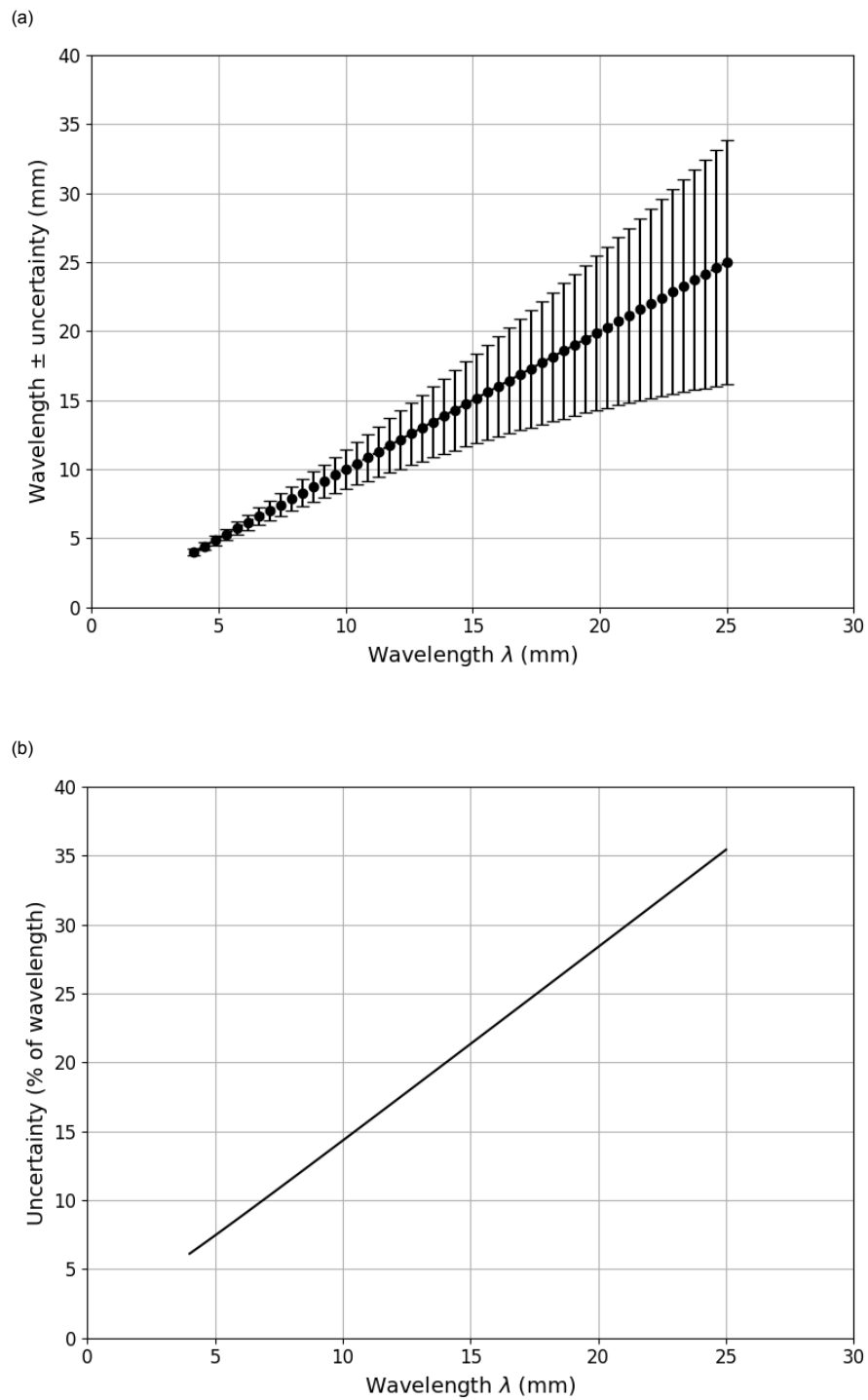


Figure 3.15: Assessment of measurement accuracy for dominant wavelengths. (a) Absolute uncertainty bars for each wavelength. (b) Relative uncertainty expressed as a percentage. Both illustrate how measurement precision depends on the wavelength, with larger wavelengths showing increased uncertainty.

4

Results

This chapter presents the experimental results from two investigations. The first examines the wavelength and dispersion behavior of Faraday surface waves, with particular attention to the influence of floating thin films. To illustrate how the wavelengths are obtained, representative digital image correlation (DIC) outputs are shown at the beginning of the chapter. The second investigation concerns the onset of the Faraday instability, quantifying the minimum vertical acceleration, commonly referred to as the critical acceleration, required to initiate standing waves across a range of excitation frequencies. Finally, DIC output is briefly used again to provide order-of-magnitude estimates of wave amplitudes through surface reconstructions.

4.1. DIC observations

Representative DIC displacement fields at 60 Hz are shown in Figure 4.1 for deionized water and silicone oil, both with a free surface. These fields correspond to the in-plane displacements in the x - and y -directions (orthogonal to each other and lying within the imaging plane). Both the coordinate axes and the displacement magnitudes are expressed in pixels (px), consistent with the image-based nature of the DIC measurements. Maximum displacements of up to nearly 10 px are observed for water and up to 7.5 px for silicone oil. The patterns are largely regular, and it is already apparent that a wavelength or repeating structure can be extracted from these outputs. Throughout this chapter, red corresponds to positive displacements and blue to negative displacements. The in-plane displacements indicate the local slope: strong color intensities correspond to large slopes, while values near zero occur at wave crests and troughs. Although in principle wavelengths could be estimated by measuring the distance between consecutive crests, the patterns are not always perfectly regular (see, for example, Figure 4.3a). To quantify the wavelength systematically, the method described in Section 3.4.2 is applied.

When elastic membranes cover the surface of deionized water, the displacement fields change noticeably with thickness (Figure 4.3). Thinner membranes exhibit more frequent repetitions of white regions (corresponding to crests and troughs), which is consistent with shorter wavelengths. Thicker membranes, by contrast, display broader colored regions with fewer crests and troughs, consistent with longer wavelengths. Again, the precise wavelengths are determined using the systematic method outlined in Section 3.4.2.

At lower excitation frequencies, additional features appear. In tests at 30 Hz with the thinnest membranes (20 μm and 50 μm), small-scale wrinkles can be observed in the DIC displacement fields (Figure 4.2). For the 20 μm membrane, displacements of up to approximately 10 px are reported, while for the 50 μm case, the maximum displacements reach about 7.5 px. The wrinkles are most pronounced for the thinnest membrane, though some irregularities remain visible in the thicker case.

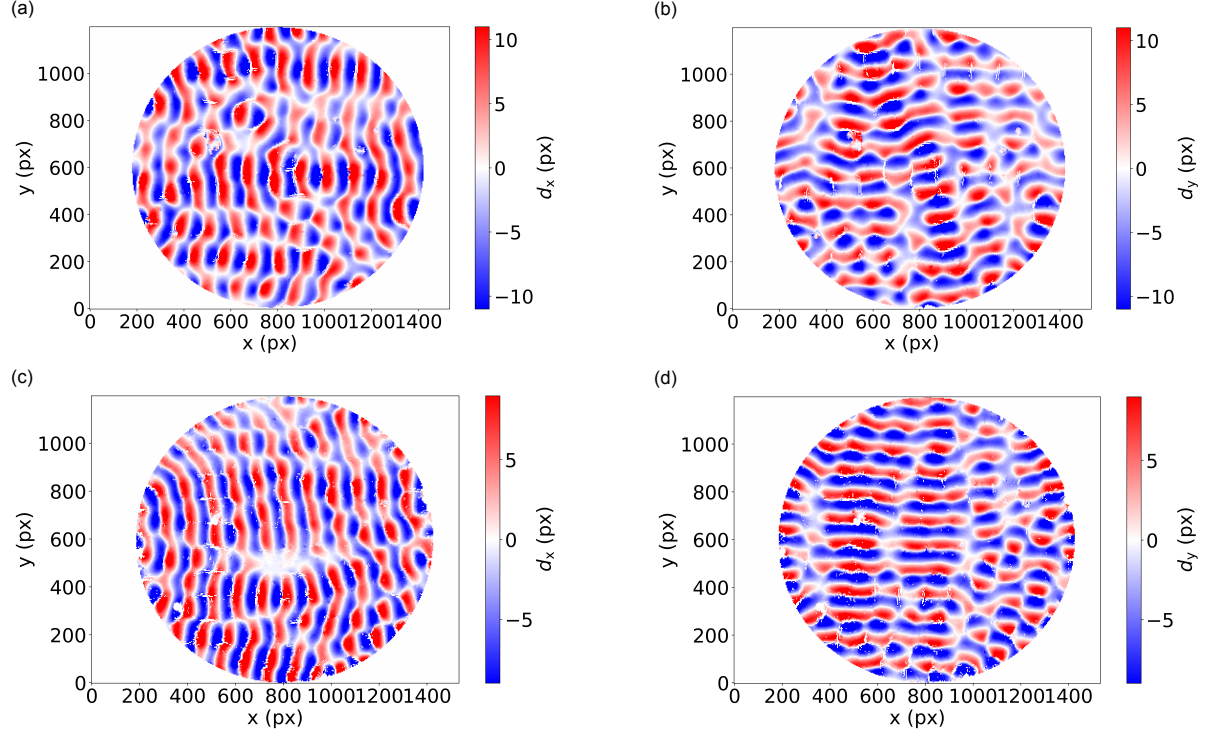


Figure 4.1: Representative DIC displacement fields at 60 Hz, showing deionized water with a free surface (top row) and silicone oil with a free surface (bottom row). (a, c) Displacement in the x -direction (d_x) and (b, d) displacement in the y -direction (d_y).

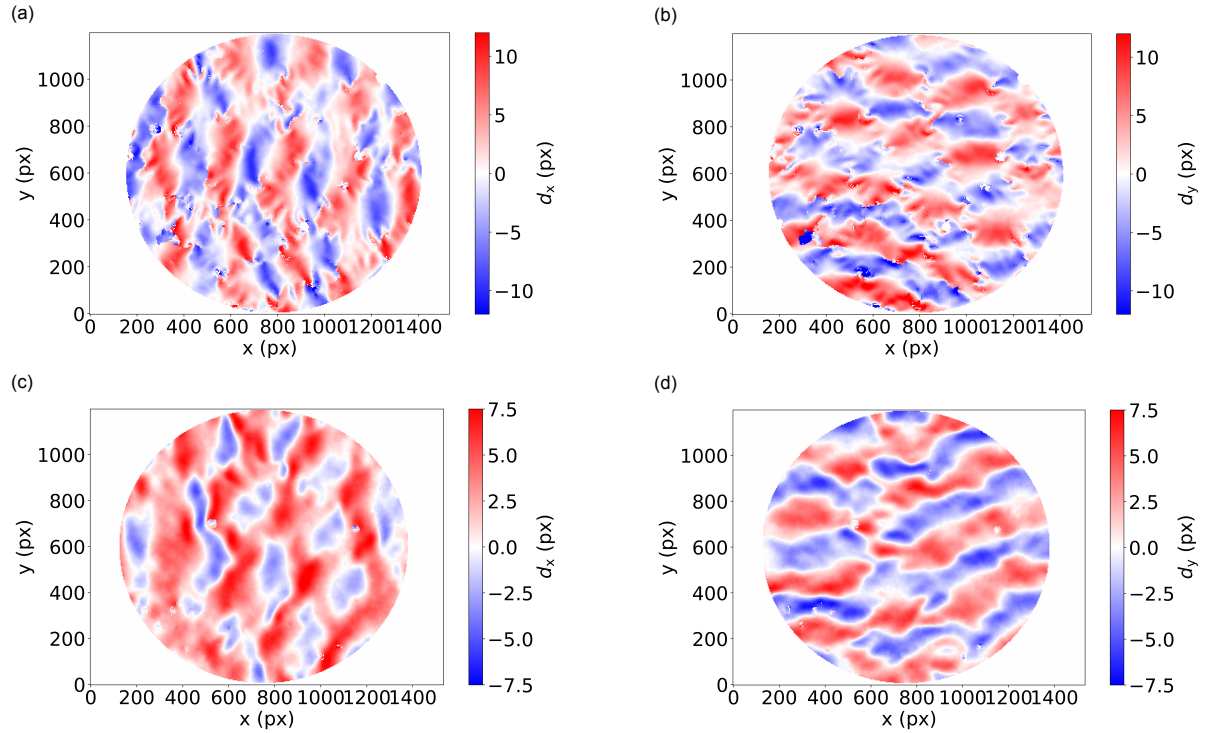


Figure 4.2: Representative DIC displacement fields for deionized water at 30 Hz, covered with elastic membranes of thickness 20 μm (top row) and 50 μm (bottom row). (a, c) Displacement in the x -direction (d_x) and (b, d) displacement in the y -direction (d_y), highlighting localized wrinkle features in the membrane.

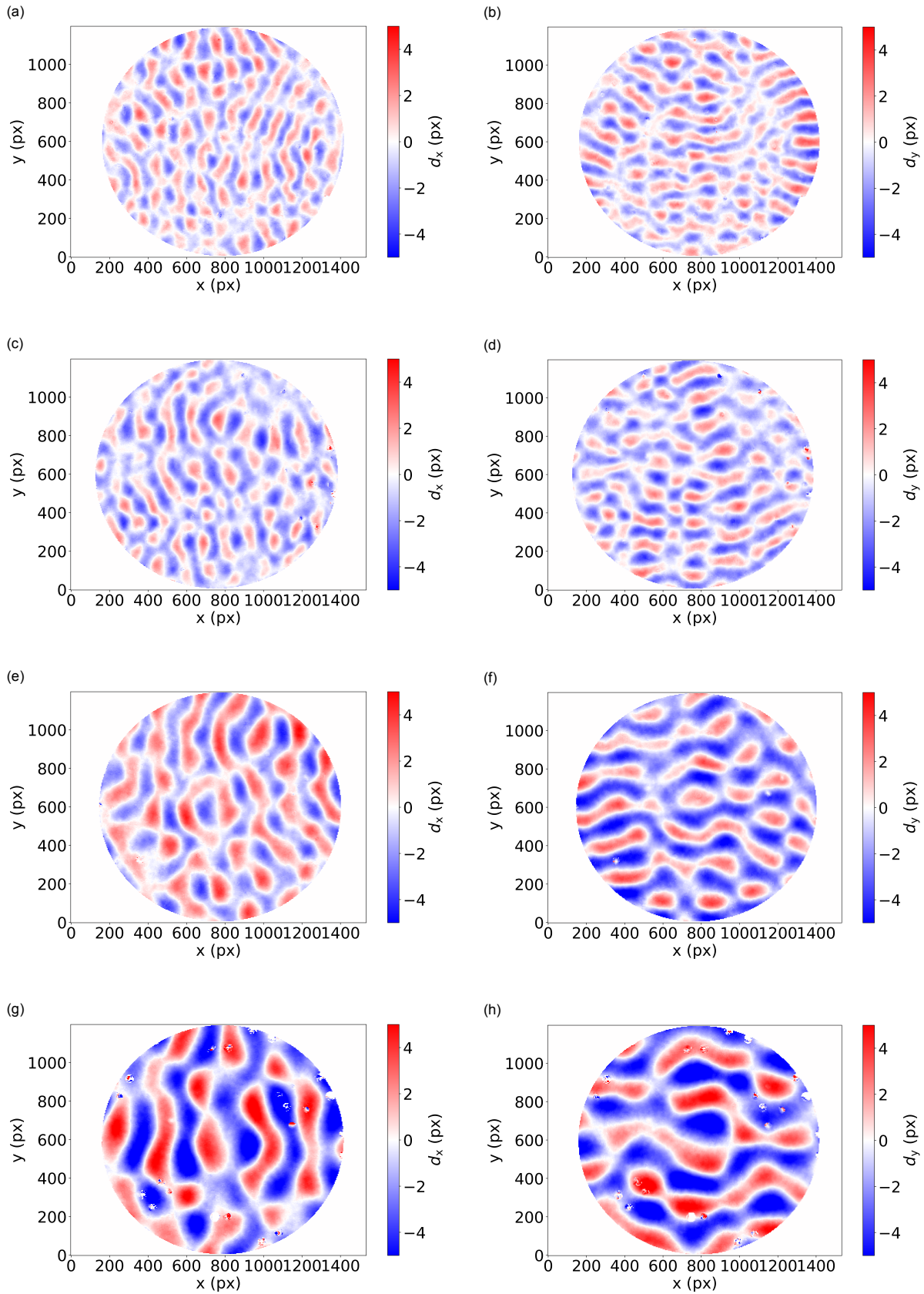


Figure 4.3: Representative displacement fields from DIC measurements for deionized water at 60 Hz, covered by elastic membranes of varying thicknesses: 20 μm , 50 μm , 100 μm , and 200 μm . (a, c, e, g) Displacement in the x -direction (d_x), and (b, d, f, h) displacement in the y -direction (d_y).

4.2. Wavelength measurements

4.2.1. Silicone oil

The wavelengths of Faraday waves in bare (free-surface) silicone oil were measured across a range of excitation frequencies. Figure 4.4 presents the measured values, with error bars indicating the standard error of the mean within each repetition. Each repetition is plotted separately with slight horizontal offsets for clarity. As expected, the wavelength decreases with increasing excitation frequency. Overall, the measurements are highly reproducible: most repetitions at 20 Hz, 50 Hz, and 80 Hz overlap within the reported standard error.

Some larger error bars (specifically for repetitions 1 and 2 at 20 Hz and repetition 1 at 50 Hz) arise from outliers in individual measurements. For instance, in repetition 1 at 20 Hz, the measured wavelengths were 19.5 mm, 18.6 mm, 19.5 mm, 18.6 mm, and 8.2 mm, indicating a clear failure in the wavelength derivation for that single point. Such outliers shift the mean and increase the standard error for the affected repetitions, but they do not change the overall trend. Excluding these anomalous values would bring the repetition means into closer agreement.

Despite these isolated deviations, the data remain in excellent agreement with the theoretical dispersion relation. The theoretical curve, shown as black dashed line in Figure 4.4, is obtained from the linear stability model of Equation 2.5. In this model, the subscripts ₁ and ₂ denote the two fluids, with medium 1 corresponding to the liquid layer and medium 2 to the overlying air; the associated material properties are listed in Table 3.1.

4.2.2. Deionized water

The wavelengths of Faraday waves in deionized water were measured across a range of excitation frequencies, both for the free surface and for surfaces covered with floating films of varying thicknesses 20 μm , 50 μm , 100 μm , and 200 μm . Figure 4.5 shows the measured values, with error bars indicating the standard error of the mean over amplitude measurements within each repetition. Each repetition is shown separately with slight horizontal offsets to illustrate reproducibility.

As observed for silicone oil, the wavelength decreases with increasing excitation frequency for all cases. The free surface measurements show consistent deviations from the theoretical dispersion relation, although the overall trend remains. For floating films, the measured wavelengths generally increase with increasing thickness. In particular, the 20 μm films align closely with the free surface measurements, while thicker films (50 μm –200 μm) exhibit progressively longer wavelengths. Repeat measurements at 30 Hz, 60 Hz, and 90 Hz show good reproducibility, with most values overlapping within the reported standard error.

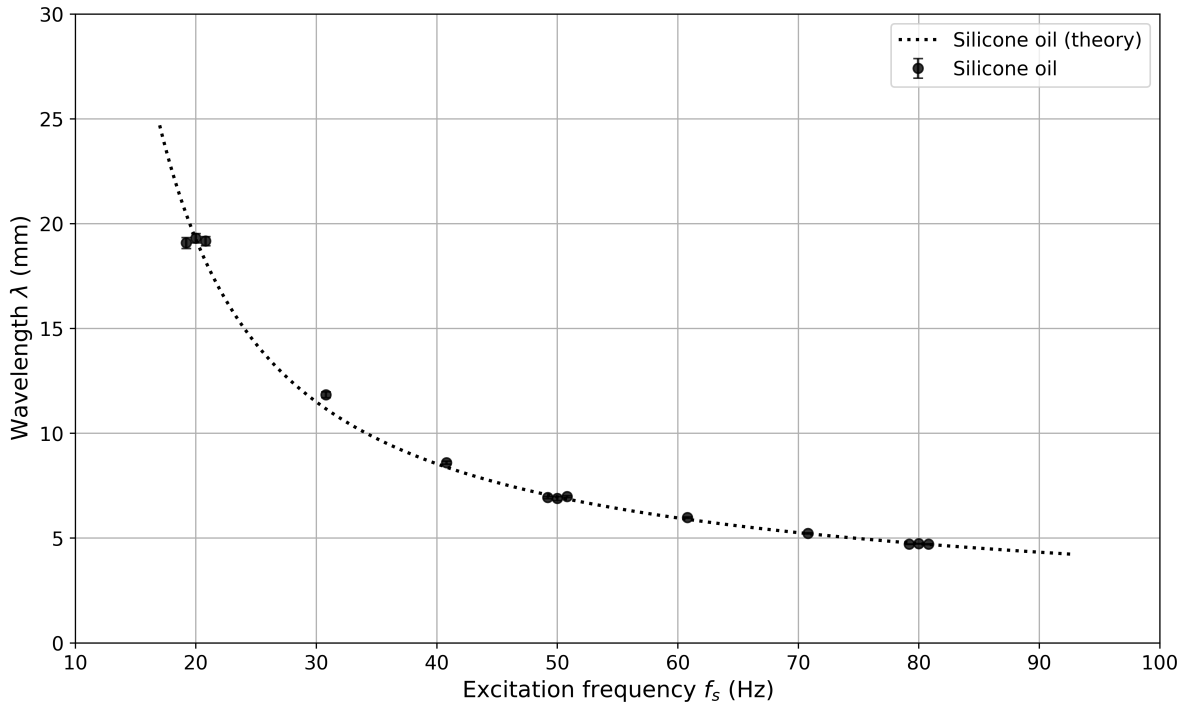


Figure 4.4: Measured wavelengths in bare (free surface) silicone oil as a function of excitation frequency. Error bars indicate the standard error of the mean across amplitude measurements within each repetition. Each repetition is shown separately with slight horizontal offsets. The dashed line shows the theoretical dispersion relation of the free surface case: Equation 2.5.

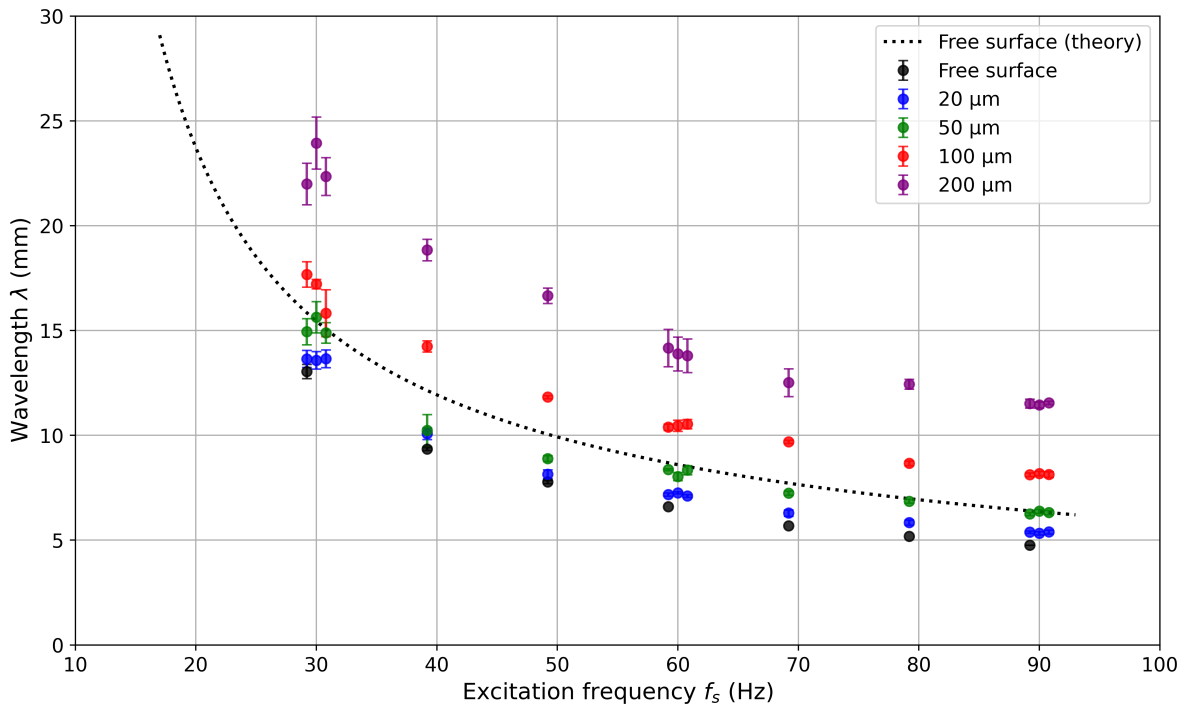


Figure 4.5: Measured wavelengths on deionized water for the free surface and surfaces covered with floating films of various thicknesses. Error bars indicate the standard error of the mean across amplitude measurements within each repetition. Each repetition is shown separately with slight horizontal offsets. Markers are color-coded by film thickness. The dashed line shows the theoretical dispersion relation of the free surface case: Equation 2.5.

4.3. Critical acceleration measurements

4.3.1. Silicone oil

Critical acceleration values for the onset of Faraday waves in silicone oil were measured over a range of excitation frequencies. Figure 4.6 shows the vertical accelerations tested in each run. For each excitation frequency, several acceleration levels were investigated as described in the test matrix, and the lowest acceleration at which subharmonic standing waves were observed was taken as the critical acceleration. Each repetition is displayed with slight horizontal offsets to illustrate reproducibility. Error bars indicate the measurement accuracy of the accelerometer-based determination of acceleration.

The measured critical accelerations are generally close to the theoretical predictions, with values consistently lying slightly above the model curve. A clear trend of increasing critical acceleration with excitation frequency is visible. Repeat measurements at selected frequencies (20 Hz, 50 Hz, and 80 Hz) show good reproducibility.

4.3.2. Deionized water

Critical acceleration values for the onset of Faraday waves in deionized water were measured for the free surface and for surfaces covered with floating films of thicknesses 20 μm , 50 μm , 100 μm , and 200 μm . Figure 4.7 shows the lowest acceleration at which subharmonic standing waves appeared for each frequency, which is taken as the critical acceleration. At each frequency, several acceleration levels were tested, but only the lowest value is presented. Each repetition is displayed with slight horizontal offsets to illustrate reproducibility.

The general trend of increasing critical acceleration with excitation frequency is observed for all cases. Across the different film thicknesses, the critical acceleration generally increases with thickness. Some deviations are notable: the free surface critical acceleration is not consistently lower than that of the thinnest film, lying between the 20 μm and 50 μm film values for frequencies above 60 Hz, and between the 50 μm and 100 μm values for lower frequencies. Additionally, the free surface measurements show large deviations from the theoretical predictions.

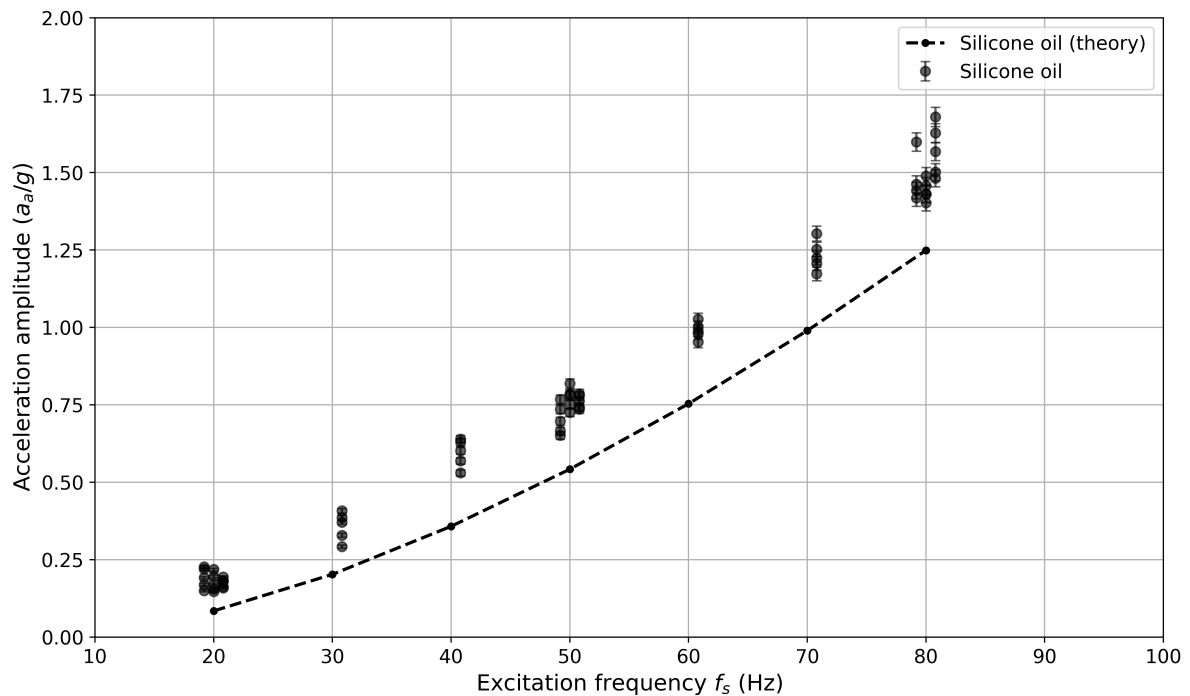


Figure 4.6: Measured accelerations for silicone oil as a function of excitation frequency. Error bars indicate the measurement accuracy. At each frequency, several acceleration levels were tested, with the lowest value at which subharmonic standing waves appeared taken as the critical acceleration. Each repetition is shown separately with slight horizontal offsets to illustrate reproducibility. The dashed line connects the theoretical critical acceleration values obtained with the model discussed in Section 3.4.1.

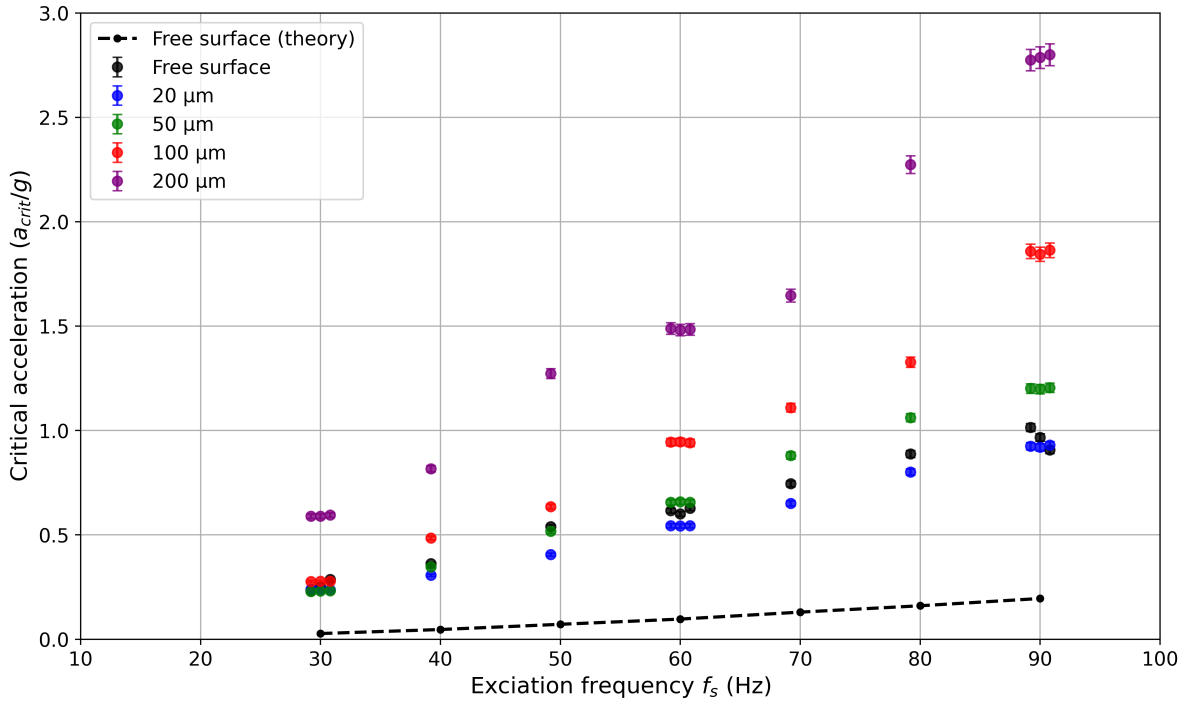


Figure 4.7: Measured critical accelerations for deionized water, both for the free surface and for surfaces covered with floating films of different thicknesses, as a function of excitation frequency. Error bars indicate the measurement accuracy. Each repetition is displayed with slight horizontal offsets to illustrate reproducibility. The dashed line connects the theoretical critical acceleration values obtained with the model discussed in Section 3.4.1.

4.4. Wave amplitude estimates

Figure 4.8 presents representative reconstructed surfaces at 60 Hz for deionized water and silicone oil with free surfaces. The wave amplitudes are approximately 0.25 mm for deionized water and 0.2 mm for silicone oil. These reconstructed surfaces capture the overall vertical displacement of the fluid interface and provide a direct estimate of the wave amplitude.

For deionized water covered with elastic membranes of varying thicknesses, the reconstructed surfaces at 60 Hz (Figure 4.10) indicate that wave amplitude increases with membrane thickness. Specifically, the approximate amplitudes are 0.06 mm for the 20 μm membrane (Figure 4.10a), 0.07 mm for the 50 μm membrane (Figure 4.10b), 0.12 mm for the 100 μm membrane (Figure 4.10c), and 0.21 mm for the 200 μm membrane (Figure 4.10d). These values confirm the trend observed in the DIC displacement fields: thicker membranes produce larger vertical displacements, while the free surface case consistently exhibits the largest amplitudes.

In low-frequency tests at 30 Hz with the thinnest membranes, small-scale wrinkles are visible in the reconstructed surfaces (Figure 4.9), although they are more pronounced in the DIC displacement fields. For the 20 μm membrane (Figure 4.9a), the wrinkle amplitude is approximately 0.25 mm, while for the 50 μm membrane (Figure 4.9b), the wrinkles are less pronounced, with an amplitude of roughly 0.15 mm. These observations highlight that localized surface features may be partially smoothed in the reconstruction process, but the overall amplitude trends remain consistent.

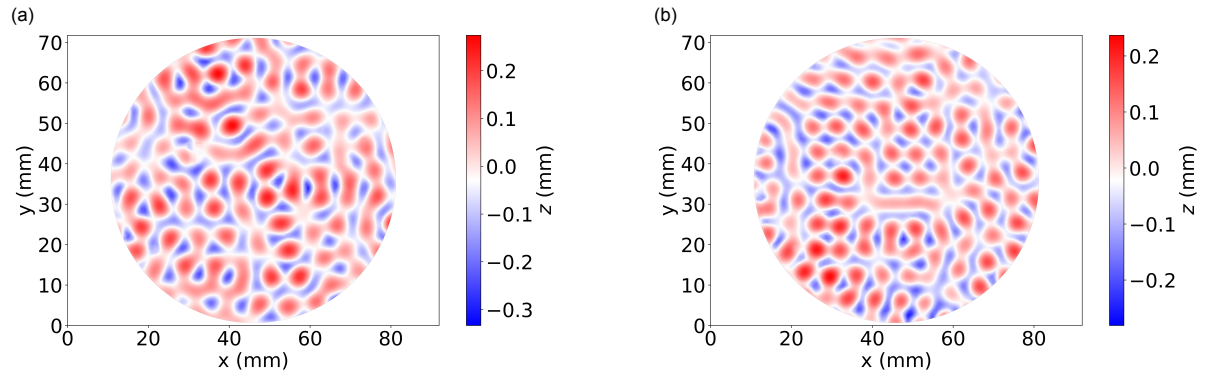


Figure 4.8: Reconstructed surfaces from DIC measurements at 60 Hz for (a) deionized water and (b) silicone oil, both with free surfaces. The figures highlight the overall wave amplitudes of approximately 0.25 mm and 0.2 mm, respectively.

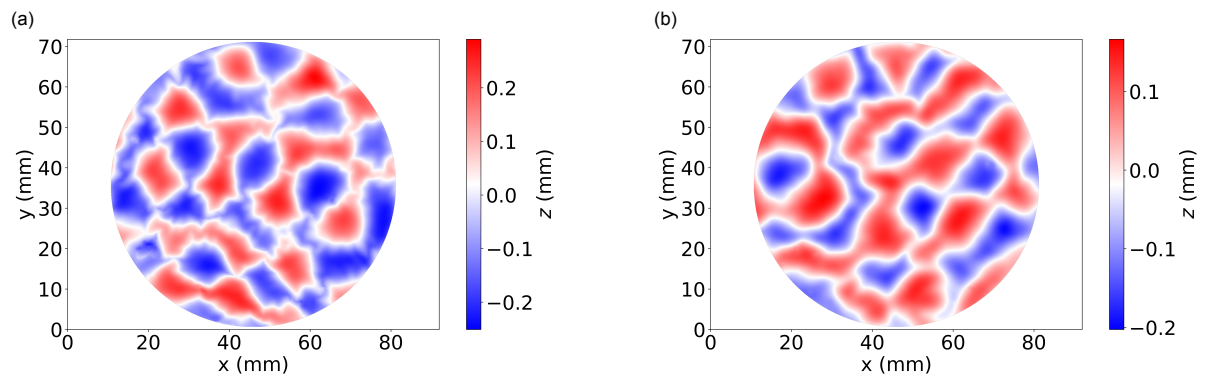


Figure 4.9: Reconstructed surfaces from DIC measurements for deionized water at 30 Hz, covered with elastic membranes of thickness (a) 20 μm and (b) 50 μm . Localized wrinkle features are most pronounced for the thinner membrane.

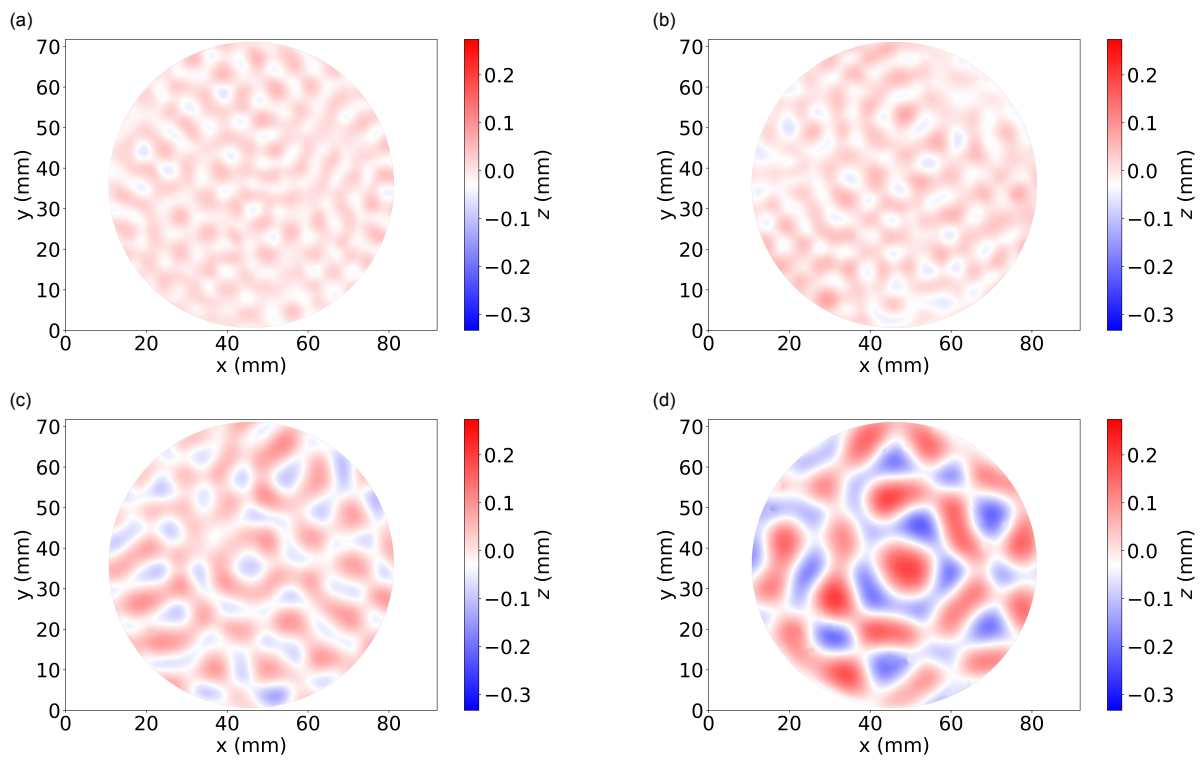


Figure 4.10: Reconstructed surfaces from DIC measurements for deionized water at 60 Hz, covered by elastic membranes of varying thicknesses: (a) 20 μm , (b) 50 μm , (c) 100 μm , and (d) 200 μm .

5.1. Validation with silicone oil

Silicone oil was used to validate the experimental methodology due to its well-characterized and stable properties. Wavelength measurements for repetition 3 were compared against the theoretical dispersion relation for a viscous fluid-air interface (Equation 2.5). By fitting the surface tension, σ , as a free parameter, the best-fit curve yielded $\sigma = 19.47 \text{ mN/m}$, in excellent agreement with the value of 19.7 mN/m reported by the manufacturer. Figure 5.2 shows the mean wavelengths: the solid red line corresponds to the best-fitted curve using dispersion relation 2.5 with variable surface tension σ , while the dashed line represents the theoretical prediction. The close match confirms the accuracy of the setup and the reliability of the analysis methods.

Critical acceleration measurements provide further confirmation of the validity of the experimental methodology. Across the tested frequency range, the measured critical accelerations were consistently higher than the theoretical predictions. This systematic overestimation originates from the applied measurement protocol: instead of maintaining the system at acceleration levels extremely close to the onset for long or indefinite periods, the experiments were conducted at values that reliably produced subharmonic surface patterns within a practical observation time. As a result, the recorded critical accelerations represent slight overestimations of the true onset values. This behavior was anticipated and, importantly, demonstrates that the methodology correctly captures the onset of hydroelastic waves, confirming the reliability of the experimental approach.

Together, the wavelength and critical acceleration results demonstrate that the experimental setup is robust, accurate, and reliable under controlled conditions. The low sensitivity of silicone oil to environmental contaminants such as dust, humidity, and surfactants further enhances the reproducibility of the measurements. Although material-covered experiments could not be performed with silicone oil, these baseline measurements establish confidence in both the experimental setup and the data analysis procedures, thereby providing a solid foundation for the subsequent floating-film investigations.

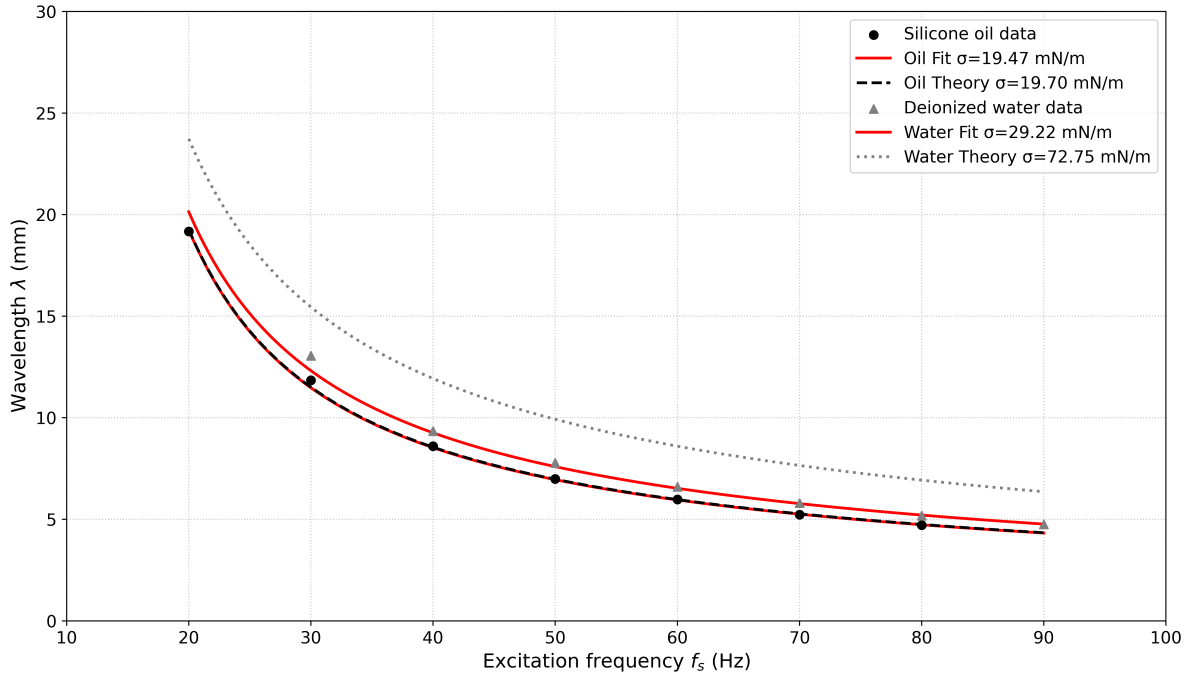


Figure 5.2: Mean wavelengths in free-surface silicone oil and water as a function of excitation frequency. Black circles indicate silicone oil measurements, and the solid red line represents the best-fit dispersion relation for free-surface silicone oil using Equation 2.5 with variable surface tension ($\sigma = 19.47 \text{ mN/m}$). The black dashed line corresponds to the theoretical dispersion relation for silicone oil with the manufacturer's value of $\sigma = 19.7 \text{ mN/m}$. Gray triangles denote deionized water measurements; the solid red line shows the fitted dispersion relation for free-surface deionized water with $\sigma = 29.22 \text{ mN/m}$, and the gray dotted line represents the theoretical water curve using $\sigma = 72.75 \text{ mN/m}$.

5.2. Deviation from theory for free surface deionized water

In contrast to the silicone oil experiments, the measurements conducted with water exhibit more pronounced deviations from theoretical predictions. Given the close agreement observed for silicone oil, a similar level of correspondence was initially expected for water. However, the experimental data reveal significant departures from the theoretical curves.

The experimentally inferred surface tension for the water samples ($\sigma = 29.22$ mN/m) is substantially lower than the intrinsic value of clean water ($\sigma = 72.75$ mN/m), obtained by fitting Equation 2.5 with σ as a free parameter. By fitting Equation 2.5 with surface tension as a free parameter, the best-fit value for the water samples was found to be $\sigma = 29.22$ mN/m. This is substantially lower than the intrinsic surface tension of clean water, $\sigma = 72.75$ mN/m. As illustrated in Figure 5.2, this discrepancy suggests that the interfacial behavior of the experimental water differs from that of ideal, uncontaminated water. Similar observations have been reported in other studies; for example, Ono-dit-Biot et al. (2019) measured an effective surface tension of approximately 50 ± 10 mN/m in experimental water samples. A likely contributing factor is the presence of surface-active contaminants introduced through environmental exposure or handling during the experiments.

Local variations in surface tension generate fluid motion along the interface, a phenomenon known as the Marangoni effect (Rengasamy, 2006). Such flows can stabilize the interface and enhance damping by redistributing momentum and energy. Even trace amounts of surfactants can induce these surface tension gradients, thereby increasing effective viscous damping. In the context of Faraday waves, Daniel et al. (2004) demonstrated that minute surfactant concentrations significantly alter the onset conditions of the instability by modifying both interfacial tension and damping. These effects provide a consistent explanation for the elevated critical accelerations observed in water, which resemble theoretical predictions for a fluid with substantially higher effective viscosity, potentially up to four times that of pure water (Figure 5.3 dotted lines). The increased damping raises the energy threshold required to trigger the Faraday instability, accounting for the experimental observations.

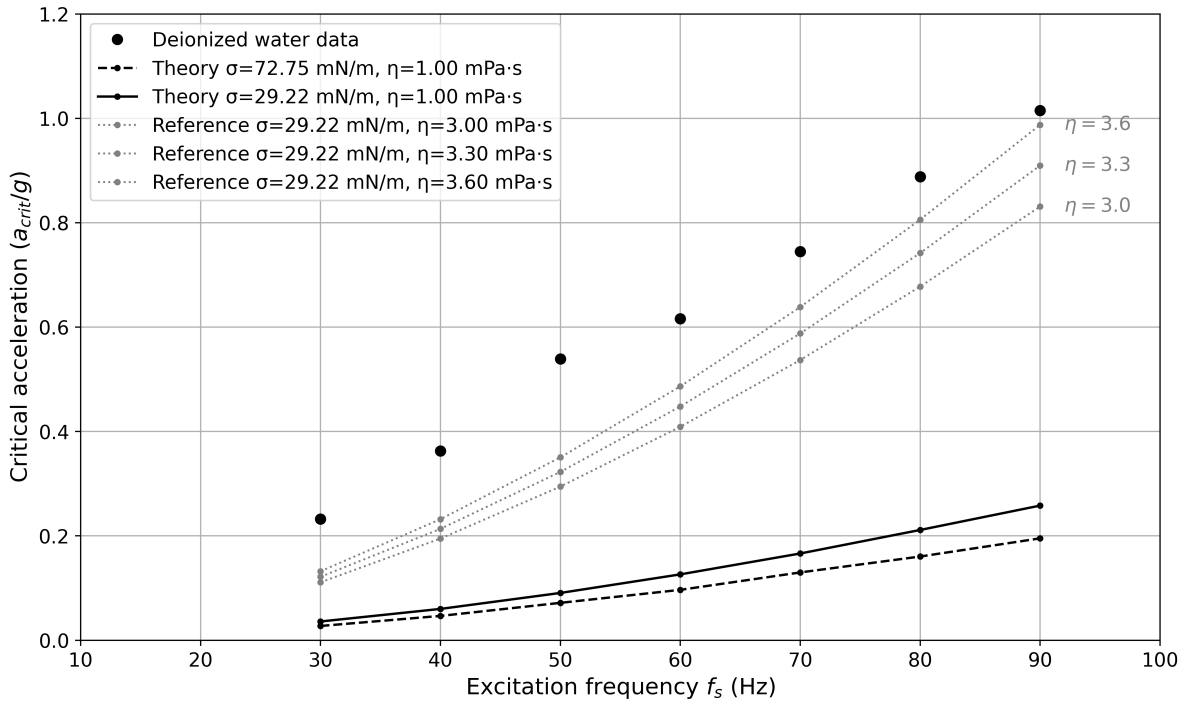


Figure 5.3: Critical acceleration for free-surface deionized water as a function of excitation frequency. Black circles indicate the experimental measurements (lowest acceleration per frequency), and the black dashed line represents the theoretical prediction using the literature water properties ($\sigma = 72.75$ mN/m, $\eta = 0.89$ mPa.s). The solid black line shows the theory curve with the fitted surface tension ($\sigma = 29.22$ mN/m) while keeping the viscosity at the water value. Gray dotted lines indicate reference calculations with the fitted surface tension and different viscosities ($\eta = 3.0$ mPa.s, $\eta = 3.3$ mPa.s, $\eta = 3.6$ mPa.s) to illustrate the influence of viscous damping on the critical acceleration.

Although direct, simultaneous measurements of surface tension and viscosity were not performed during the wave experiments, the results point toward a complex interplay between surface contamination, Marangoni-induced flows, interfacial rheology, and wave-damping mechanisms. These findings underscore the high sensitivity of water-based Faraday wave experiments to environmental conditions and emphasize the importance of maintaining rigorous control over surface cleanliness in future studies.

5.3. Dispersion relation deionized water with floating films

Experimental observations show that the dominant wavelength increases with sheet thickness. This behavior is consistent with the theoretical framework of Ono-dit-Biot et al. (2019), which shows that bending stiffness tends to lengthen hydroelastic waves, while inertia tends to shorten them. In our system, the effect of bending stiffness dominates, particularly for the thicker membranes, explaining the observed wavelength increase with thickness.

For a quantitative comparison, the measured wavelength data were first tested against the non-dissipative dispersion relation for floating sheets on Faraday waves (Equation 2.8) (Sardari et al., 2023). While the relation captures the overall trend, systematic deviations between measured and theoretical wavelengths are evident (Figure 5.4), suggesting the presence of additional physical effects beyond the original model. In their study, Sardari et al. (2023) introduced a damping factor δ to account for discrepancies between experimental and theoretical wavelengths, expressed as $\omega' = \omega(1 - \delta)$, where ω' is the dissipative angular frequency. Applying this approach to our data results in a negative δ (Figure 5.5), which would imply negative damping. Such a correction is unphysical, as it would suggest the experimental waves propagate faster than the theoretical prediction in the absence of dissipation. This observation indicates that the discrepancies are not caused by energy loss, but rather by additional physical effects intrinsic to the floating sheet system.

To capture these effects, the analysis was extended to the Föppl–von Kármán (FvK) framework for elastic membranes. The FvK dispersion relation (Equation 2.3) accounts for contributions from gravity, surface tension, and bending stiffness. In the present system, the bending and gravitational terms are determined by material properties and fluid depth and are not adjustable. The effective in-plane tension in the sheet remains the only practically tunable parameter. The theoretical FvK FSI curves are shown in Figure 5.5 (dashed lines), and, as with the simpler non-dissipative model, measured wavelengths are systematically larger than predicted.

Following the framework proposed by Deike et al. (2013) for membranes with pinned boundaries, the effective tension can be decomposed into a static and a dynamic component that depends on wave steepness, $\epsilon = \zeta_a k$. Applying this framework to freely floating sheets, the total effective tension is expressed as:

$$\sigma_{\text{tot}} = \sigma + \sigma_{\text{add}} = \sigma + cEd(\zeta_a k)^2, \quad (5.1)$$

where σ_{add} represents an additional, dynamic tension component and c is a geometry-dependent factor. By fitting the measured wavelengths using σ_{tot} as a variable, the additional tension required to reconcile the data with the FvK predictions can be inferred. The fitted values are of the expected order of magnitude, though they differ numerically from those reported by Deike et al. (2013) due to differences in sheet geometry and boundary conditions. Table 5.1 highlights this difference: the geometry factor c ranges from 3 to 6 in their study and 0.239–0.369 in the present work. This discrepancy arises primarily from the difference in units (N/m vs. mN/m) and the pinned versus freely floating boundary conditions. Despite this, the ratio of static to dynamic tension and the wave steepness values are comparable, indicating that while absolute values differ, the scaling of dynamic effects is consistent. These results demonstrate that the geometry factor is influenced not only by sheet geometry but also by boundary conditions. Overall, the introduction of an additional tension term provides a plausible explanation for the observed deviations.

To validate this conclusion, the additional tension term was also incorporated as a variable into the non-dissipative Faraday wave dispersion relation. Using this approach instead of the δ correction factor, the fitted σ_{add} values remain consistent with those obtained from the FvK analysis (Figure 5.6), further supporting the robustness of the methodology.

The close agreement between the fitted additional tension values across both the FvK and Faraday FSI frameworks confirms that introducing a dynamic tension component provides a consistent and physically plausible explanation for the observed deviations between theory and experiment. The introduction of σ_{add} accounts for the systematic increase in measured wavelengths relative to the base theoretical model, highlighting the influence of wave-induced tension in the floating sheet.

Table 5.1: Overview of material properties (Young's modulus E [MPa] and film thickness d [mm]), wave properties (wave steepness $\zeta_a k$), tensions (static σ_s [N/m] and additional σ_{add} [N/m]), tension ratio ($\sigma_{\text{add}}/\sigma_s$), and fitted geometry factor c for both the present study and study by Deike et al. (2013).

Case	E [MPa]	d [mm]	$\zeta_a k$	σ_s [N/m]	σ_{add} [N/m]	$\sigma_{\text{add}}/\sigma_s$	c
Deike et al.	1.05	0.350	0.074	4.00	12.0	3.00	6.00
Deike et al.	1.50	0.500	0.074	4.00	12.0	3.00	3.00
Present	0.60	0.020	0.053	0.0289	0.0122	0.42	0.369
Present	0.60	0.050	0.053	0.0289	0.0302	1.05	0.365
Present	0.60	0.100	0.073	0.0289	0.0869	3.01	0.275
Present	0.60	0.200	0.093	0.0289	0.2489	8.62	0.239

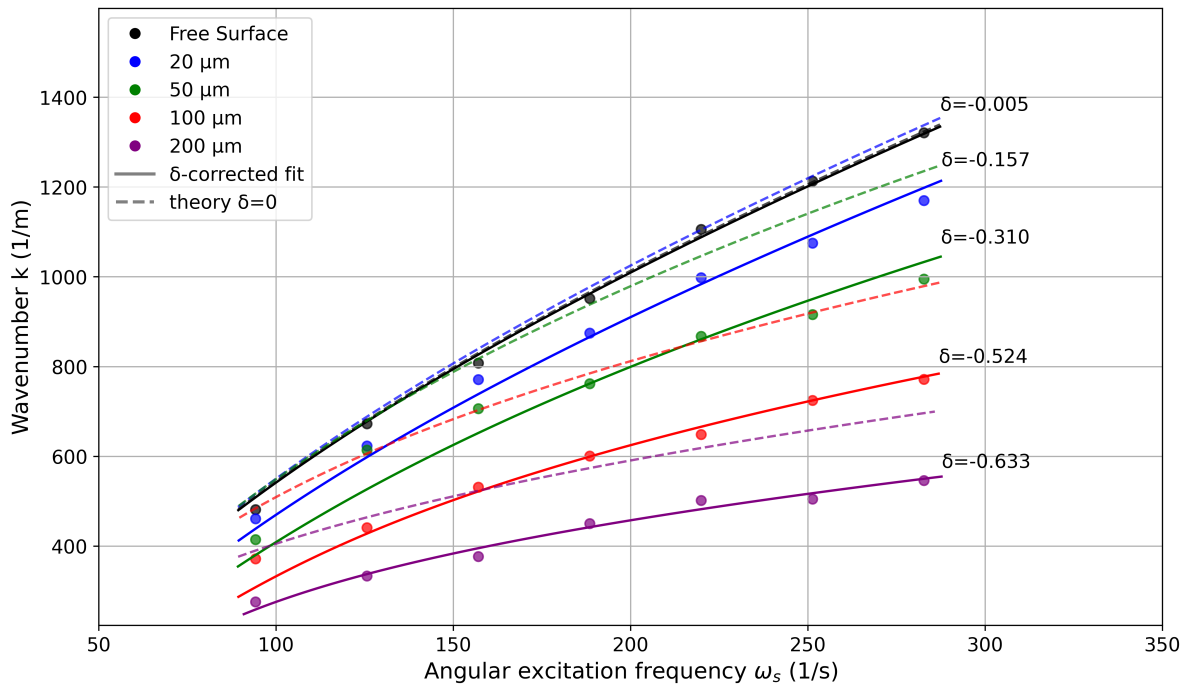


Figure 5.4: Comparison of measured Faraday wave wavelengths with theoretical predictions of the Faraday wave dispersion relation for a fluid–structure interaction (FSI) system (Sardari et al., 2023). Wavenumber k is plotted on the vertical axis and angular excitation frequency ω on the horizontal axis. The dashed line represents the non-dissipative prediction, while the solid line shows the fitted curve including a damping factor δ as a free parameter. Negative fitted values of δ indicate that the discrepancy cannot be explained by dissipation alone, suggesting the presence of additional physical effects beyond simple damping.

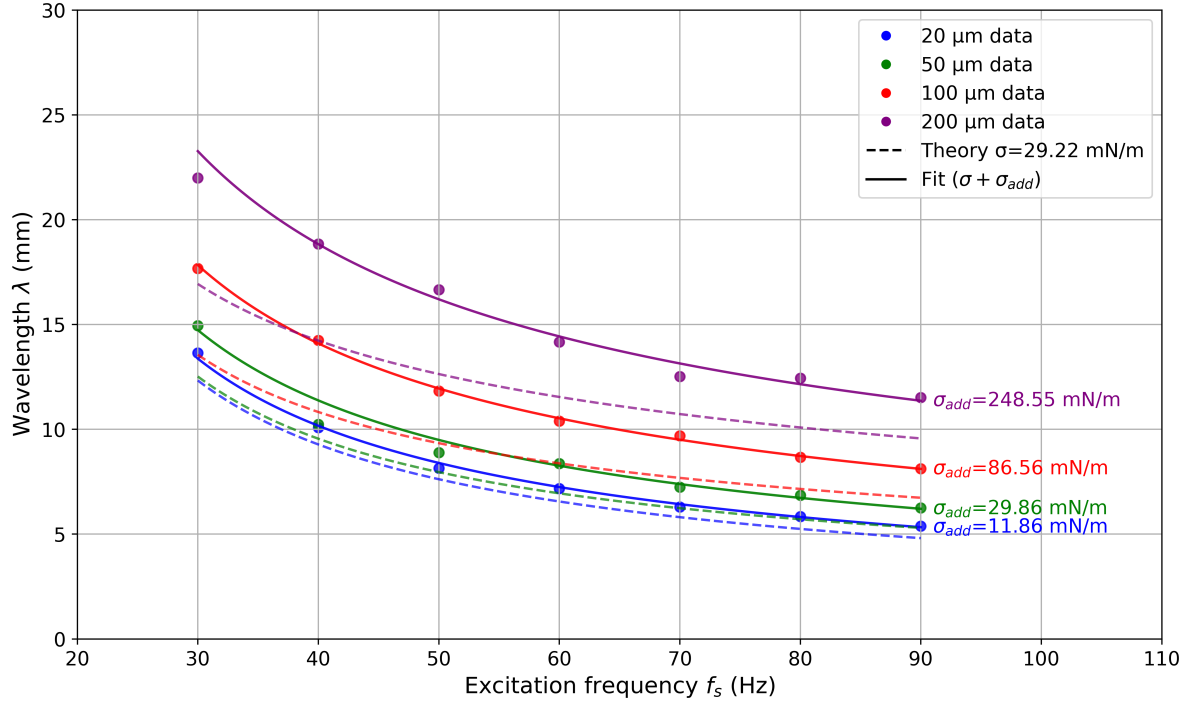


Figure 5.5: Measured wavelengths of free-floating water films as a function of excitation frequency (ω on the horizontal axis, k on the vertical axis). Dashed lines show the theoretical FvK-linear wave dispersion relation with fixed material properties (Equation 2.3), while solid lines correspond to the FvK prediction including the fitted dynamic tension term σ_{add} .

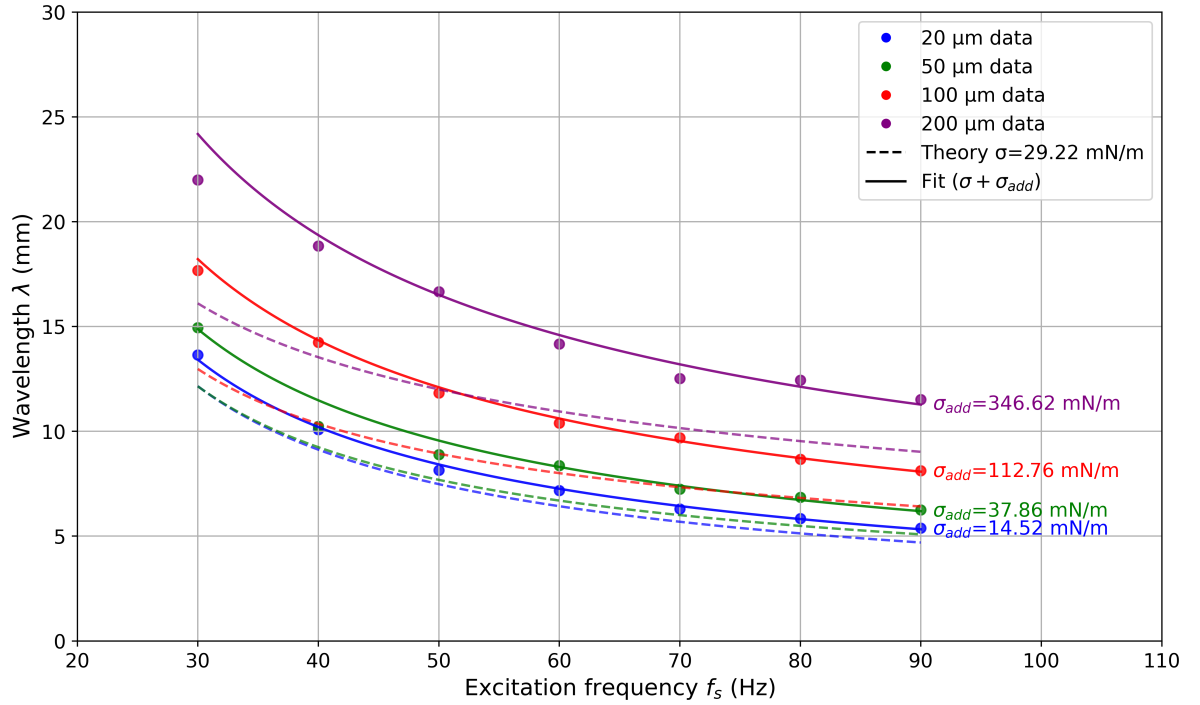


Figure 5.6: Measured wavelengths of free-floating water films as a function of excitation frequency (ω on the horizontal axis, k on the vertical axis), compared with the non-dissipative Faraday FSI dispersion relation (Sardari et al., 2023). Dashed lines represent the theoretical model with surface tension only, while solid lines include the fitted dynamic tension term σ_{add} .

5.4. Wrinkle formation in thin membranes

In the low-frequency excitation regime (30 Hz), the thinnest membranes (20 μm and 50 μm) exhibit localized wrinkling instabilities that break the otherwise smooth fluid-following motion. These wrinkles are clearly visible in the displacement fields of the 20 μm membrane (Figure 5.7), where circular markers highlight the regions of interest. Both the d_x and d_y components reveal the same wrinkle patterns, confirming that the effect is not an artifact of directional measurement.

To quantify the wrinkle scale, a simple line overlay was used to measure the spacing between adjacent crests, with the length calibrated against a known distance in the field of view. This analysis yields a wrinkle wavelength of approximately 3 mm, which aligns well with the theoretical wrinkle wavelength predicted from the static buckling analysis for a 20 μm sheet (Figure 3.3). This agreement provides further evidence that the observed patterns represent genuine mechanical wrinkling rather than experimental noise.

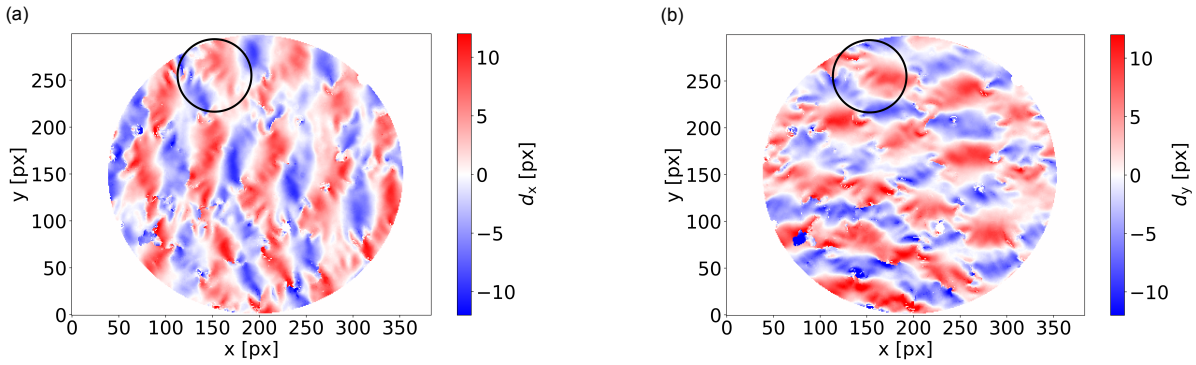


Figure 5.7: Localized wrinkles observed in a 20 μm thick floating membrane under low-frequency excitation (30 Hz). (a) Displacement in the x -direction and (b) displacement in the y -direction highlight localized wrinkle features with measured wavelengths from 2.5 mm to 3.2 mm, consistent with static buckling predictions (Figure 3.3).

This correspondence indicates that, even in a dynamic environment, thin membranes are susceptible to local compressive instabilities similar to those that produce static wrinkles under an applied force. These wrinkles arise from forces not accounted for by the standard FvK or Faraday wave dispersion relations, which assume a smooth, tensioned membrane responding elastically to the fluid motion. While the dynamic tension term $\sigma_{\text{add}} = cEd(\zeta_a k)^2$ successfully describes the *sheet-wide* increase in in-plane tension and the resulting overall wavelength, it does not suppress *localized buckling*.

The spatially selective nature of the wrinkles may be influenced by the flow structure of standing Faraday waves. Following Saddier et al. (2024), standing waves create stagnation points at antinodes where viscous shear is maximal, producing local compressive stresses that can trigger buckling in thin regions. This mechanism provides a plausible explanation for why wrinkles appear only in specific locations, despite σ_{add} acting across the entire sheet.

Overall, the measured wavelengths follow the trends predicted by FvK and Faraday FSI models, but the occurrence of localized wrinkles highlights a subscale mechanical effect that influences local deformation without dominating the overall wave behavior. This distinction reinforces the interpretation that σ_{add} governs large-scale wavelength selection, whereas localized buckling reveals residual compressive instabilities superimposed on the global, tensioned response of the floating membrane.

6

Conclusion

This study aimed to investigate the influence of sheet thickness on the hydroelastic response of very flexible, free-floating membranes under Faraday-wave excitation. Laboratory-scale experiments were conducted using vertically oscillated membranes of varying thicknesses (20 μm to 200 μm) on a water surface. Wavelength, critical acceleration, and wave amplitude were measured and compared to theoretical predictions from established hydroelastic and Faraday-wave models. Free-surface experiments without any floating membranes were first performed using silicone oil to validate the methodology and establish accurate baseline measurements, which were successful. Additional free-surface experiments on deionized water provided a reference for comparison with hydroelastic cases; however, these results deviated from theoretical predictions, likely due to surface contamination and Marangoni effects.

Sheets of thickness 20 μm , 50 μm , and 100 μm were classified as Very Flexible Floating Structures (VFFS). The 200 μm sheet approached the Very Large Floating Structure (VLFS) regime. Analysis showed that increasing thickness leads to longer wavelengths, as expected from the increasing bending stiffness. An additional global tension effect was observed for all thicknesses, likely due to the dynamic behavior of the membranes. For the thinnest sheets at low excitation frequencies, localized wrinkles appeared. These wrinkles were not visible across the entire field of view, but they were fairly repetitive, with wavelengths comparable to those observed in static wrinkle tests used to estimate the Young's modulus. This suggests that the local in-plane tension reaches magnitudes sufficient to induce buckling, reflecting regions of temporary compression induced by the underlying Faraday waves, which locally exceed the buckling threshold of the thin membrane. Such behaviors highlight instabilities not captured by conventional continuum models.

Critical accelerations were observed to increase with sheet thickness. The 100 μm and 200 μm sheets showed significant increases in onset acceleration, whereas the 20 μm and 50 μm sheets exhibited values close to the free surface case. This suggests that thicker sheets, due to their greater mass and bending stiffness, exhibit smaller response amplitudes under the same excitation, while very thin membranes remain highly flexible and easily deformed.

In conclusion, this research demonstrates that sheet thickness is a primary determinant of hydroelastic response in free-floating membranes. Thicker sheets exhibit increased bending stiffness and mass. The growth in bending stiffness dominates over the added inertia, leading to longer wavelengths compared to very thin membranes, while the combined effect of stiffness and mass also results in higher onset accelerations and altered wave amplitudes, reflecting their greater resistance to Faraday-wave excitation. In contrast, very thin sheets remain highly flexible, prone to local instabilities, and influenced by dynamic tension effects. These findings provide experimental evidence for the role of thickness in governing hydroelastic behavior and offer practical insights for the design and modeling of very flexible floating structures, such as offshore floating photovoltaic systems or other thin maritime membranes.

Recommendations

Building on the experience gained during this study, several recommendations can be made to enhance the experimental setup and data quality in future investigations. These are especially relevant for research involving the Faraday instability and floating flexible structures.

7.1. Fluid selection and material compatibility

The results obtained with silicone oil highlight the benefits of using a well-characterized and chemically stable fluid. The high resistance to surface contamination of silicone oil and its predictable interfacial properties contributed to highly reliable results. For future experiments, especially those involving surface-sensitive wave phenomena, it is strongly recommended to use a primary working fluid with similar stability and low susceptibility to airborne contaminants or particulate matter.

However, since silicone oil is not compatible with all floating materials due to buoyancy constraints, a suitable alternative material that remains afloat in such fluids must be identified while retaining transparency and mechanical flexibility. This is especially important if the structure is intended to remain in the very flexible floating structure (VFFS) regime. Finding an appropriate film-fluid combination will be critical for reproducibility and consistency in future studies.

7.2. Imaging methodology and optical setup

In this work, the rest condition of the fluid surface was established visually, which may not exclude small residual motions. Future experiments could implement objective verification methods, such as analyzing pre-run displacement fields from DIC, monitoring accelerometer signals for residual vibrations, or quantifying damping times.

In this work, a major limitation arose from the use of video recordings rather than direct frame capture. While convenient, the video compression process reduced image contrast and resolution, degrading the quality of the Digital Image Correlation (DIC) analysis. For future work, it is strongly recommended to capture individual high-resolution frames directly, which are still triggered in synchronization with the excitation signal and the connected frequency divider. This avoids the pitfalls of decomposing lower-quality video files and maintains full control over both timing and image fidelity.

In this study, phase-locked imaging was employed to ensure consistent displacement measurements across oscillation cycles. The specific phase of image capture in the standing wave was not explicitly controlled beyond avoiding the equilibrium position, which was sufficient for accurate wavelength analysis. For studies interested in specific wave amplitude effects, however, it is recommended to capture images at well-defined phases, such as the absolute peaks or troughs, to determine the true maximum displacement.

A related consideration is the motion of the dot pattern attached to the bottom of the tank, which oscillates vertically along with the shaker. In the present study, this effect was not explicitly accounted for; as it was assumed that the resulting vertical displacements, ranging from approximately 10^{-5} m at high frequencies and low accelerations to 1.5×10^{-4} m at lower frequencies and higher accelerations, are negligible compared to the camera distance of 0.81 m, including the 0.01 m tank thickness. For

similar experiments, it is recommended to estimate or measure this motion at least to ensure that it does not significantly affect the displacement analysis, particularly if the imaging setup or measurement precision differs from the present study.

Illumination should be improved. Although bottom-lighting was used, it was insufficient, requiring adjustments in gain and exposure time in the imaging software (Pylon Viewer), which in theory reduces image quality and introduces noise. Using a stronger light source beneath the tank and/or a camera with an adjustable aperture is recommended to achieve high-contrast, low-noise imaging without the need for excessive gain or long exposure times.

Finally, the appearance of a persistent tilt in reconstructed surfaces highlights potential issues with mechanical and optical alignment. Although the exact cause is not conclusively identified, it is recommended to carefully level both the camera and the experimental table before each set of measurements. Misalignment can affect the accuracy of surface reconstruction and, consequently, the interpretation of wave profiles. Particular attention should be paid to centering the optical axis of the camera above the tank. In the current setup, the camera is not positioned exactly above the center of the cylindrical tank because the field of view is cropped. To ensure the region of interest is correctly captured, the camera must be adjusted, which can potentially introduce a small tilt. Additionally, care should be taken to avoid exciting the eigenfrequencies of the setup, as this can lead to a global displacement of the recorded images relative to the reference frame, introducing artificial displacements that do not reflect actual surface motion.

7.3. Trigger synchronization and measurement procedure

One practical limitation encountered during this study was related to the manual coordination of the experimental start between the shaker and the image acquisition system. Although the camera was reliably triggered via a frequency divider connected to the multifunction synthesizer, this triggering began as soon as the synthesizer was powered on. However, the shaker did not start oscillating immediately. The sinusoidal output to the amplifier had to be manually activated by pressing a separate button. Thus, to start a test, both the shaker activation and the recording trigger in the imaging software (Pylon Viewer) had to be manually synchronized. This procedure introduced some uncertainty in identifying the exact onset time of oscillation. However, since the onset time was not ultimately used in the analysis, this source of uncertainty did not significantly affect the results.

Future experiments would greatly benefit from a dedicated triggering system that simultaneously initiates both the shaker oscillation and the image acquisition. Such synchronization would eliminate timing ambiguities and improve the accuracy of identifying wave onset.

Regarding the determination of the critical acceleration, the procedure described in Chapter 3 was tested and validated on free-surface experiments using silicone oil and water, where it performed satisfactorily. However, when applied to experiments involving floating material films, the same method became unreliable. The fitting approach could not be used effectively, and instead, the smallest measured value was chosen as the critical acceleration. In hindsight, this approach likely underestimated the uncertainty. A more robust protocol would involve measuring the wave response at multiple excitation amplitudes, both above and below the instability threshold. For example, one can incrementally lower the amplitude from a level where standing waves clearly form to a level where no waves are detected, thereby bracketing the critical acceleration between two values. The critical value could then be reported as the midpoint between these amplitudes, with uncertainty estimated as half their difference.

Alternative techniques also exist, such as the method presented by Sardari et al. (2023), which estimates the critical acceleration based on the measured damping rate of the standing waves. Incorporating such approaches would provide more reliable and reproducible threshold measurements in future studies.

7.4. Experimental scope and coverage

The number of frequencies tested (seven) and the repetitions performed were adequate for fitting dispersion relations and assessing repeatability. However, if resources permit, expanding the frequency range could help further validate the theoretical models and capture the transition between different wave regimes. More data points would also reduce uncertainty in fitted parameters.

7.5. Future outlook

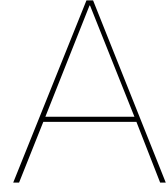
The experimental setup used in this study, based on Faraday-wave excitation of floating membranes, provides a versatile tool for probing hydroelastic behavior under controlled conditions. In this study, the focus was on the dispersion relation and critical acceleration, and experiments were conducted to ensure the onset of Faraday waves for each membrane thickness. As a result, different thicknesses were subjected to different shaker amplitudes, and the response at the same excitation amplitude or wave steepness was not directly compared. Future studies could explore how membranes of varying thickness respond under the same forcing conditions, which would provide additional insight into amplitude-dependent hydroelastic behavior. Additionally, low-frequency, high-amplitude excitation could generate steep waves, offering the opportunity to investigate extreme deformations, localized wrinkling, or even wave breaking in very flexible floating structures. Such investigations could further enhance the fundamental understanding of hydroelastic interactions and provide practical guidance for the design and optimization of thin, flexible floating structures, including offshore floating photovoltaic systems.

Bibliography

- Abidi, I., & Nsaibi, M. (2024). Assessing the impact of renewable energy in mitigating climate change: A comprehensive study on effectiveness and adaptation support. *International Journal of Energy Economics and Policy*. <https://doi.org/10.32479/ijeep.15769>
- Acharya, M., & Devraj, S. (2019). Floating solar photovoltaic (fspv): A third pillar to solar pv sector. *New Delhi, India: The Energy and Resources Institute*.
- Benjamin, T. B., & Ursell, F. J. (1954). The stability of the plane free surface of a liquid in vertical periodic motion. *Proceedings of the Royal Society of London. Series A, Mathematical and Physical Sciences*, 225, 505–515. <https://doi.org/10.1098/rspa.1954.0218>
- Bevington, P. R., & Robinson, D. Keith. (2003). *Data reduction and error analysis for the physical sciences* (3rd ed.). McGraw–Hill.
- Blaber, J., Adair, B., & Antoniou, A. (2015). Ncorr: Open-source 2d digital image correlation matlab software. *Experimental Mechanics*, 55(6), 1105–1122. <https://doi.org/10.1007/s11340-015-0009-1>
- Casaburo, A., Petrone, G., Franco, F., & De Rosa, S. (2019). A review of similitude methods for structural engineering. *Applied Mechanics Reviews*, 71(3), 030802. <https://doi.org/10.1115/1.4043787>
- Chu, E., & Tarazano, D. L. (2017). A brief history of solar panels. *Smithsonian Magazine*. <https://www.smithsonianmag.com/sponsored/brief-history-solar-panels-180972006/>
- Claus, R., & López, M. (2022). Key issues in the design of floating photovoltaic structures for the marine environment. *Renewable and Sustainable Energy Reviews*, 164, 112502. <https://doi.org/https://doi.org/10.1016/j.rser.2022.112502>
- Daniel, S., Kalso, E., & Li, M.-C. (2004). The onset acceleration for surfactant-covered faraday waves. *Physics of Fluids*, 16(5), 1346–1350. <https://doi.org/10.1063/1.1668632>
- Deike, L., Bacri, J.-C., & Falcon, E. (2013). Nonlinear waves on the surface of a fluid covered by an elastic sheet. *Journal of Fluid Mechanics*, 733, 394–413. <https://doi.org/10.1017/jfm.2013.379>
- Gerritsma, J. (n.d.). Hydromechanica 4 - golven [Technical University Delft].
- Joint Committee for Guides in Metrology (JCGM). (2008). *Evaluation of measurement data — guide to the expression of uncertainty in measurement (gum)* (tech. rep. No. JCGM 100:2008). Bureau International des Poids et Mesures (BIPM).
- Kagemoto, H., Fujino, M., & Murai, M. (1998). Theoretical and experimental predictions of the hydroelastic response of a very large floating structure in waves. *Applied Ocean Research*, 20(3), 135–144. [https://doi.org/https://doi.org/10.1016/S0141-1187\(98\)00017-0](https://doi.org/https://doi.org/10.1016/S0141-1187(98)00017-0)
- Kumar, K. (1996). Linear theory of faraday instability in viscous liquids. *Proceedings: Mathematical, Physical and Engineering Sciences*, 452(1948), 1113–1126. Retrieved January 7, 2025, from <http://www.jstor.org/stable/52892>
- Kumar, K., & Tuckerman, L. S. (1994). Parametric instability of the interface between two fluids. *Journal of Fluid Mechanics*, 279, 49–68. <https://doi.org/10.1017/S0022112094003812>
- Lamb, H. (1932). *Hydrodynamics* (6th). Cambridge University Press.
- Lamb, H. (1945). *Hydrodynamics*. Dover Publications. <http://uf.catalog.fcla.edu/uf.jsp?st=UF021537409&ix=pm&l=0&V=D&pm=1>
- Liberzon, A., et al. (2021). Openpiv-python (v0.23.4). <https://doi.org/10.5281/zenodo.4409178>
- Luo, Y., Wu, J., & Zhang, J. (2017). Hydroelastic response of a very large floating structure using a bem-fem coupling approach. *Ocean Engineering*, 130, 526–536. <https://doi.org/10.1016/j.oceaneng.2016.11.030>
- Marouani, I. (2024). Contribution of renewable energy technologies in combating phenomenon of global warming and minimizing ghg emissions. *Clean energy science and technology*, 2(2), 164–164. <https://doi.org/10.18686/cest.v2i2.164>
- Meylan, M. H., & Squire, V. A. (2002). The response of ice floes to ocean waves. *Ocean Engineering*, 29(3), 347–359. [https://doi.org/10.1016/S0029-8018\(01\)00043-4](https://doi.org/10.1016/S0029-8018(01)00043-4)

- Meylan, M. H. (1994). *The behaviour of sea ice in ocean waves* [Doctoral dissertation, University of Otago]. <https://ourarchive.otago.ac.nz/handle/10523/12836>
- Miles, J. W., & Henderson, D. (1990). Parametrically forced surface waves. *Annual Review of Fluid Mechanics*, 22(1), 143–165. <https://doi.org/10.1146/annurev.fl.22.010190.001043>
- Moisy, F., Rabaud, M., & Salsac, K. (2009). A synthetic schlieren method for the measurement of the topography of a liquid interface. *Experiments in Fluids*, 46, 1021–1036. <https://doi.org/10.1007/s00348-008-0608-z>
- Oliveira-Pinto, S., & Stokkermans, J. (2020). Marine floating solar plants: An overview of potential, challenges, and feasibility [Research Article, Paper 202010. Received 25/02/2020; Accepted 03/06/2020; Published online 26/11/2020]. *Proceedings of the Institution of Civil Engineers – Maritime Engineering*, 173(4), 120–135. <https://doi.org/10.1680/jmaen.2020.10>
- Ono-dit-Biot, J.-C., Trejo, M., Loukiantcheko, E., Lauch, M., Raphaël, E., Dalnoki-Veress, K., & Salez, T. (2019). Hydroelastic wake on a thin elastic sheet floating on water. *Phys. Rev. Fluids*, 4, 014808. <https://doi.org/10.1103/PhysRevFluids.4.014808>
- Oppenheim, A. V., & Schaffer, R. W. (2010). *Discrete-time signal processing* (3rd ed.). Pearson.
- Pan, B. (2018). Digital image correlation for surface deformation measurement: Historical developments, recent advances and future goals. *Measurement Science and Technology*, 29(8), 083001. <https://doi.org/10.1088/1361-6501/aac504>
- Pan, B., Qian, K., Xie, H., & Asundi, A. (2010). A realistic error budget for two-dimensional digital image correlation. *Optics and Lasers in Engineering*, 48(10), 999–1006. <https://doi.org/10.1016/j.optlaseng.2010.02.005>
- Părău, E., & Dias, F. (2001). Waves due to a steadily moving load on a floating ice plate. In A. King & Y. Shikhmurzaev (Eds.), *Proceedings of the iutam symposium on free surface flows* (pp. 229–236, Vol. 62). Springer, Dordrecht. https://doi.org/10.1007/978-94-010-0796-2_28
- Ramanan, C., Lim, K. H., Kurnia, J. C., Roy, S., Bora, B. J., & Medhi, B. J. (2024). Towards sustainable power generation: Recent advancements in floating photovoltaic technologies. *Renewable and Sustainable Energy Reviews*, 194, 114322. <https://doi.org/https://doi.org/10.1016/j.rser.2024.114322>
- Rengasamy, R. S. (2006). *Thermal and moisture transport in fibrous materials* [Surface Tension]. CRC Press.
- Saddier, L., Palotai, A., Aksil, M., Tsamados, M., & Berhanu, M. (2024). Breaking of a floating particle raft by water waves. *Physical Review Fluids*, 9(9), 094302.
- Sahu, A., Yadav, N., & Sudhakar, K. (2016). Floating photovoltaic power plant: A review. *Renewable and Sustainable Energy Reviews*, 66, 815–824. <https://doi.org/10.1016/j.rser.2016.08.038>
- Sardari, V., Bahmani, L., & Maleki, M. (2023). Faraday waves in a low-viscosity fluid covered with a floating elastic sheet [Preprint, dated July 11, 2023].
- Schreier, S., & Jacobi, G. (2021). Experimental investigation of wave interaction with a thin floating sheet. *International Journal of Offshore and Polar Engineering*, 31(04), 435–444.
- Scolan, Y. M., & Korobkin, A. A. (2001). Water impact on an elastic plate. *Journal of Sound and Vibration*, 245(3), 493–515. [https://doi.org/10.1016/S0022-460X\(00\)00085-9](https://doi.org/10.1016/S0022-460X(00)00085-9)
- Shannon, C. E. (1949). Communication in the presence of noise. *Proceedings of the IRE*, 37(1), 10–21. <https://doi.org/10.1109/jrproc.1949.232969>
- Squire, V. A. (2008). Synergies between vlf hydroelasticity and sea ice research. *International Journal of Offshore and Polar Engineering*, 18(4), 241–253. <https://publications.isope.org/journals/ijope-18-4/abst-18-4-p241-JC-431-Squire.pdf>
- Sree, D. K., Law, A. W.-K., & Shen, H. H. (2017). An experimental study on the interactions between surface waves and floating viscoelastic covers [Recent Advances on Wave Motion in Fluids and Solids]. *Wave Motion*, 70, 195–208. <https://doi.org/https://doi.org/10.1016/j.wavemoti.2016.08.003>
- Stagonas, D., Warbrick, D., Müller, G., & Magagna, D. (2011). Surface tension effects on energy dissipation by small scale, experimental breaking waves. *Coastal Engineering*, 58(9), 826–836. <https://doi.org/10.1016/j.coastaleng.2011.05.009>
- Sutton, M. A., Schreier, H. W., & Orteu, J.-J. (2010). *Image correlation for shape, motion and deformation measurements: Basic concepts, theory and applications*. Springer.
- Suzuki, H., & Yoshida, K. (1996). Design flow and strategy for safety of very large floating structure. *Proceedings of International Workshop on Very Large Floating Structures (VLFS)*, 21–27.

- Suzuki, H. (2005). Overview of megafloat: Concept, design criteria, analysis, and design [Very Large Floating Structures]. *Marine Structures*, 18(2), 111–132. <https://doi.org/https://doi.org/10.1016/j.marstruc.2005.07.006>
- Suzuki, H., Riggs, H., Fujikubo, M., Shugar, T., Seto, H., Yasuzawa, Y., Bhattacharya, B., Hudson, D., & Shin, H. (2007). Very large floating structures. *International Conference on Offshore Mechanics and Arctic Engineering*, 42681, 391–442.
- Taylor, J. R. (1997). *An introduction to error analysis: The study of uncertainties in physical measurements* (2nd ed.). University Science Books.
- Trapani, K., Millar, D. L., & Smith, H. C. (2013). Novel offshore application of photovoltaics in comparison to conventional marine renewable energy technologies. *Renewable Energy*, 50, 879–888. <https://doi.org/10.1016/j.renene.2012.08.043>
- Trapani, K., & Santafé, M. R. (2014). A review of floating photovoltaic installations: 2007–2013. *Progress in Photovoltaics: Research and Applications*, 22(1), 1–16. <https://doi.org/10.1002/pip.2466>
- United Nations. (2024). What is renewable energy? [Accessed: 2024-12-20]. <https://www.un.org/en/climatechange/what-is-renewable-energy>
- Vassalos, D. (1998). Physical modelling and similitude of marine structures. *Ocean Engineering*, 26(2), 111–123. [https://doi.org/https://doi.org/10.1016/S0029-8018\(97\)10004-X](https://doi.org/https://doi.org/10.1016/S0029-8018(97)10004-X)
- Vella, D., Aussillous, P., & Mahadevan, L. (2004). Elasticity of an interfacial particle raft. *Europhysics Letters*, 68(2), 212. <https://doi.org/10.1209/epl/i2004-10202-x>
- Wagner, C., Müller, H. W., & Knorr, K. (1998). Faraday waves on a viscoelastic liquid. *Physical Review Letters*, 83(2), 308–311. <https://doi.org/10.1103/PhysRevLett.83.308>
- World Meteorological Organization. (2023). Provisional state of the global climate 2023 [Accessed on 20 December 2024]. <https://wmo.int/files/provisional-state-of-global-climate-2023>
- World Meteorological Organization. (2025a). Global annual to decadal climate update: Likelihood of at least one year between 2025 and 2029 exceeding the 2024 record [Accessed via news reporting on WMO forecasts by AMS 'State of the Climate' report, 2025].
- World Meteorological Organization. (2025b). Wmo confirms 2024 as warmest year on record at about 1.55 °c above pre-industrial level [Accessed: 2025-08-19].
- Wu, H., & West, S. R. (2024). Co-optimisation of wind and solar energy and intermittency for renewable generator site selection. *Heliyon*, 10(5). <https://doi.org/10.1016/j.heliyon.2024.e26891>
- Yago, K., & Endo, H. (1996). On the hydroelastic response of box-shaped floating structure with shallow draft. *Journal of the Society of Naval Architects of Japan*, 1996(180), 341–352. https://doi.org/10.2534/jjasnaoe1968.1996.180_341
- Zeng, L., Korobkin, A., Ni, B., & Xue, Y. (2021). Hydroelastic waves propagating in an ice-covered channel. *Journal of Fluid Mechanics*, 886, A18. <https://doi.org/10.1017/jfm.2019.1042>
- Zhang, M., & Schreier, S. (2022). Review of wave interaction with continuous flexible floating structures. *Ocean Engineering*, 264, 112404. <https://doi.org/https://doi.org/10.1016/j.oceaneng.2022.112404>
- Zhao, M., An, G. K., & Wu, Y. (2007). Hydroelastic analysis of flexible floating interconnected structures. *Ocean Engineering*, 34(11-12), 1516–1531. <https://doi.org/10.1016/j.oceaneng.2007.01.003>



Derivation of the linear gravity wave dispersion relation

A.1. Finite depth

The derivation of the linear wave theory presented in this section follows the material from the course *MT2433 Scheepsbewegingen* (2021-2022) (Gerritsma, n.d.). The analysis considers cylindrical waves propagating in the x -direction over a fluid layer of finite depth. The fluid is assumed to be non-viscous, incompressible, and homogeneous. In linear wave theory, it is further assumed that the wave amplitude is small compared to the wavelength, resulting in a small steepness parameter. Under this condition, nonlinear terms in the governing equations, which are of the same order as the square of the steepness, can be neglected. This allows for a linearized treatment of the governing equations and boundary conditions. A typical wave profile for such cylindrical waves is shown in Figure A.1.

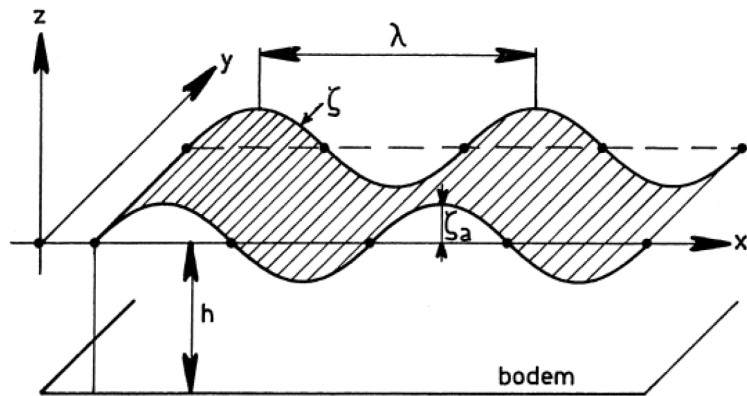


Figure A.1: Cylindrical waves.

A.1.1. Wave velocity potential

The velocity potential $\phi(x, z, t)$ of the wave must satisfy the Laplace equation:

$$\frac{\partial^2 \phi}{\partial x^2} + \frac{\partial^2 \phi}{\partial y^2} + \frac{\partial^2 \phi}{\partial z^2} = 0. \quad (\text{A.1})$$

The water velocity in the x , y , and z -directions is defined as follows, respectively:

$$u = \frac{\partial \phi}{\partial x} \quad (\text{A.2})$$

$$v = \frac{\partial \phi}{\partial y} = 0 \quad (\text{A.3})$$

$$w = \frac{\partial \phi}{\partial z}. \quad (\text{A.4})$$

Since $\frac{\partial^2 \phi}{\partial y^2} = 0$, the Laplace equation A.1 simplifies to:

$$\frac{\partial^2 \phi}{\partial x^2} + \frac{\partial^2 \phi}{\partial z^2} = 0. \quad (\text{A.5})$$

For a simple wave with small steepness, the wave profile resembles a sine or cosine. In this context, the wave potential is written as follows:

$$\phi(x, z, t) = \xi(z) \sin(kx - \omega t), \quad (\text{A.6})$$

where $\xi(z)$ is an unknown function of variable z , as it is known from experience that the water motion in a wave is also a function of the vertical distance from the water surface. The minus sign in the sine indicates that a displacement of the wave surface with velocity $c_w = \frac{\omega}{k}$ is considered in the direction of the positive x -axis. The choice of this propagation direction is arbitrary. Substituting the expression for the wave velocity potential A.6 into the simplified Laplace equation A.5 yields:

$$\frac{d^2 \xi(z)}{dz^2} - k^2 \xi(z) = 0. \quad (\text{A.7})$$

With the solution:

$$\xi(z) = C_1 e^{kz} + C_2 e^{-kz}. \quad (\text{A.8})$$

Thus, the velocity potential is written as:

$$\phi = (C_1 e^{kz} + C_2 e^{-kz}) \sin(kx - \omega t). \quad (\text{A.9})$$

To determine the constants C_1 and C_2 , as well as the ratio $\frac{\omega}{k}$, the following boundary conditions are considered.

Seabed boundary condition The vertical velocity at the seabed is zero, as shown in Figure A.2. From $\frac{\partial \phi}{\partial z} = 0$ for $z = -h$, it follows from equation A.9 that

$$(kC_1 e^{-kh} - kC_2 e^{kh}) \sin(kx - \omega t) = 0 \quad (\text{A.10})$$

$$C_1' e^{-kh} - C_2' e^{kh} = 0 \quad (\text{A.11})$$

With a mathematical trick, we can write:

$$C_1' e^{-kh} = C_2' e^{kh} = \frac{C}{2}. \quad (\text{A.12})$$

Then:

$$C_1' = \frac{C}{2} e^{kh} \quad \text{and} \quad C_2' = \frac{C}{2} e^{-kh}. \quad (\text{A.13})$$

Substituting these into the general expression for $\xi(z)$ (A.8), we get:

$$\xi(z) = \frac{C}{2} (e^{k(h+z)} + e^{-k(h+z)}) = C \cosh k(h+z). \quad (\text{A.14})$$

Thus, the velocity potential becomes:

$$\phi(x, z, t) = C \cosh k(h+z) \sin(kx - \omega t). \quad (\text{A.15})$$

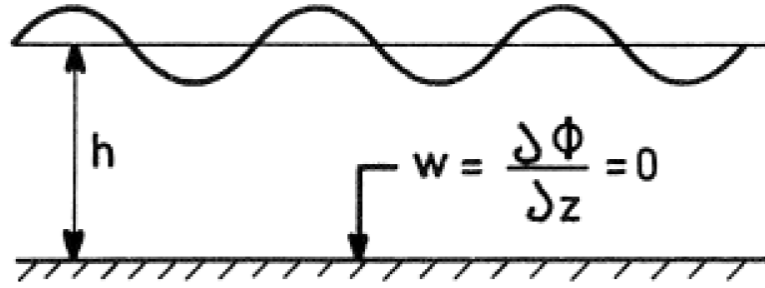


Figure A.2: Seabed boundary condition.

Dynamic free surface boundary condition The pressure at the perturbed fluid surface, located at $z = \zeta(x, y, t)$, is equal to the atmospheric pressure P_0 . This requirement defines the dynamic boundary condition at the free surface (see Figure A.3). The Bernoulli equation for unsteady flow is given by:

$$\frac{\partial \phi}{\partial t} + \frac{1}{2}(u^2 + v^2 + w^2) + \frac{P}{\rho} + gz = C, \quad (\text{A.16})$$

where u , v , and w are defined in equations A.2-A.4. In the case where wave crests are parallel to the y -axis, we have $v = 0$. For waves with small steepness, the quadratic terms $u^2 + v^2 + w^2$ represent a nonlinear contribution to the Bernoulli equation. Since the wave steepness ϵ is small ($\epsilon \ll 1$), the effects of these nonlinear terms are also small (proportional to ϵ^2) and can be neglected in first-order theory. This simplification is part of the linearization process used in small-amplitude wave theory. With these assumptions, the linearized Bernoulli equation becomes:

$$\frac{\partial \phi}{\partial t} + \frac{P}{\rho} + gz = C. \quad (\text{A.17})$$

The constant C can be found by assuming that when the wave is not yet generated (i.e., the fluid is at rest), the constant can be determined by substituting $\frac{\partial \phi}{\partial t} = 0$ and $z = \zeta = 0$, yielding $C = \frac{P_0}{\rho}$. For the free fluid surface, the following condition applies:

$$\frac{\partial \phi}{\partial t} + \frac{P_0}{\rho} + g\zeta = \frac{P_0}{\rho}, \quad \text{for } z = \zeta. \quad (\text{A.18})$$

Since the term $\frac{P_0}{\rho}$ appears on both sides, it can be eliminated, resulting in:

$$\frac{\partial \phi}{\partial t} + g\zeta = 0, \quad \text{for } z = \zeta. \quad (\text{A.19})$$

The potential at the free surface $z = \zeta$ can be developed using a Taylor series expansion. It is important to note that the vertical displacement ζ is small compared to the depth of the fluid (i.e., $\zeta \ll h$). This assumption means that the same approximation for the potential at $z = \zeta$ applies for $z = 0$, as the displacement is small relative to the depth. The Taylor series expansion for $\phi(x, z, t)$ about $z = 0$ (the undisturbed surface) is written as:

$$\phi(x, z, t) = \phi(x, 0, t) + \zeta \left(\frac{\partial \phi(x, 0, t)}{\partial z} \right)_{z=0} + O(\zeta^2). \quad (\text{A.20})$$

This is based on the fact that ζ is small, so higher-order terms are negligible. The time derivative of ϕ is:

$$\frac{\partial \phi}{\partial t} = \left(\frac{\partial \phi(x, 0, t)}{\partial z} \right)_{z=0} + O(\zeta^2). \quad (\text{A.21})$$

Thus, in the linearized form, the equation A.18 becomes:

$$\frac{\partial \phi}{\partial t} + g\zeta = 0 \quad \text{at } z = 0. \quad (\text{A.22})$$

From this, the wave displacement ζ can be derived in terms of ϕ .

$$\zeta = -\frac{1}{g} \frac{\partial \phi}{\partial t} \quad \text{at } z = 0. \quad (\text{A.23})$$

With ϕ (A.15), we get:

$$\zeta = \frac{\omega C}{g} \cosh(kh) \cos(kx - \omega t) = \zeta_a \cos(kx - \omega t). \quad (\text{A.24})$$

Finally, using this expression for ζ , we obtain the potential ϕ as:

$$\phi = \frac{\zeta_a g}{\omega} \frac{\cosh(k(h+z))}{\cosh(kh)} \sin(kx - \omega t). \quad (\text{A.25})$$

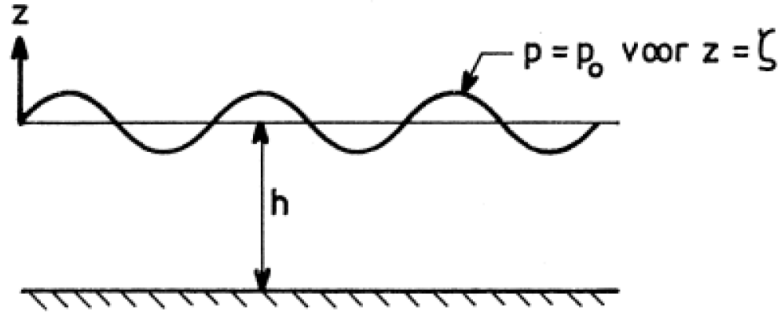


Figure A.3: Dynamic free surface boundary condition.

Kinematic boundary condition The relationship between the wave number k and the angular frequency ω follows from the boundary condition that the vertical velocity of a water particle at the free surface must be equal to the vertical velocity of the surface itself. This is a kinematic boundary condition. From the equation of the free surface $z = \zeta(x, t)$, we have:

$$\frac{dz}{dt} = \frac{\partial \zeta}{\partial t} + u \frac{\partial \zeta}{\partial x}. \quad (\text{A.26})$$

The second term in this expression is of second-order smallness because both the velocity u and the slope of the water surface are small due to the assumption that the wave steepness is small, as shown in Figure A.4. Therefore, after linearization, we get:

$$\frac{dz}{dt} = \frac{\partial \zeta}{\partial t} \quad \text{at the free surface } z = \zeta. \quad (\text{A.27})$$

Now, the vertical velocity of a water particle is given by $\frac{\partial \phi}{\partial z}$, so at the surface $z = 0$, we have:

$$\frac{\partial \phi}{\partial z} = \frac{\partial \zeta}{\partial t} \quad \text{for } z = 0. \quad (\text{A.28})$$

Hereby, we assumed that $z = 0$ is similar to $z = \zeta$ based on the linearization that we formulated before in Equation A.21. By differentiating the dynamic boundary condition (A.22) with respect to time, we obtain:

$$\frac{\partial^2 \phi}{\partial t^2} + g \frac{\partial \zeta}{\partial t} \quad \text{for } z = 0. \quad (\text{A.29})$$

Using expression (A.28) and some rearranging of the terms leads to:

$$\frac{\partial \phi}{\partial z} + \frac{1}{g} \frac{\partial^2 \phi}{\partial t^2} \quad \text{for } z = 0. \quad (\text{A.30})$$

This equation is called the Cauchy-Poisson condition. It is a linear equation in only one variable, ϕ . Substituting the wave velocity potential expression (A.25) into this boundary condition at the free surface (the Cauchy-Poisson condition) gives the dispersion relation:

$$\frac{\partial \phi(z=0)}{\partial z} = Ck \sinh(kh) \sin(kx - \omega t) \quad (\text{A.31})$$

$$\frac{\partial^2 \phi(z=0)}{\partial t^2} = C\omega^2 \cosh(kh) \sin(kx - \omega t) \quad (\text{A.32})$$

$$\omega^2 = kg \tanh(kh). \quad (\text{A.33})$$

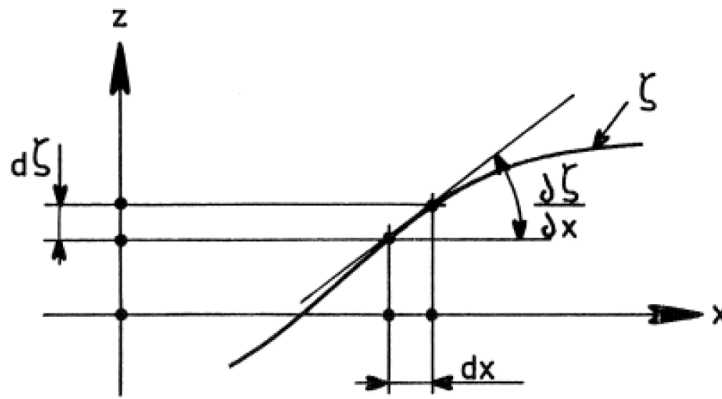


Figure A.4: Kinematic free surface boundary condition.

B

Derivation of the linear capillary wave dispersion relation

B.1. Finite depth

The derivation of the linear capillary wave theory presented here has been established with the help of Lamb (1932) and Lamb (1945). The same velocity potential as derived in the dispersion relation for finite-depth linear gravity waves (see Appendix A) is used. The fluid is assumed to be incompressible, inviscid, and homogeneous. To apply linear theory, the wave steepness, defined as the ratio of wave height to wavelength, is considered small. This allows for the neglect of higher-order nonlinear terms in the governing equations. In the Bernoulli pressure formulation, gravity effects are neglected since surface tension primarily governs the dynamics of capillary waves.

Dynamic free surface boundary condition The fluid pressure $P(r, t)$ acting on the sheet is calculated by assuming an incompressible and irrotational flow. In the region above the sheet, the fluid velocity is described by the potential $\phi(r, z, t)$, which satisfies Laplace's equation:

$$\nabla^2 \phi = 0, \quad (\text{B.1})$$

where $r = (x, y)$ denotes the horizontal in-plane coordinates. The pressure on the sheet is given by a derivation of the linearized Bernoulli equation A.17:

$$\frac{\partial \phi}{\partial t} + \frac{P_0}{\rho} + gz = -\frac{(P + P_0)}{\rho}. \quad (\text{B.2})$$

Solving this for P leaves us:

$$P = -\rho \frac{\partial \phi}{\partial t} \Big|_{z=0} - \rho g \zeta, \quad (\text{B.3})$$

where ρ is the density of the fluid and g is the acceleration due to gravity. But for capillary waves the assumption is made that gravity can be neglected. Thus this simplifies to

$$P = -\rho \frac{\partial \phi}{\partial t} \Big|_{z=0}. \quad (\text{B.4})$$

Kinematic boundary condition The kinematic boundary condition relates the vertical displacement of the beam to the fluid velocity at the surface. The kinematic boundary condition is:

$$\frac{\partial \zeta}{\partial t} = \frac{\partial \phi}{\partial z} \Big|_{z=0}. \quad (\text{B.5})$$

We assume a solution for the velocity potential $\phi(r, z, t)$, which satisfies Laplace's equation:

$$\phi = \frac{\zeta_a g}{\omega} \frac{\cosh(k(h+z))}{\cosh(kh)} \sin(kx - \omega t). \quad (\text{B.6})$$

Taking the derivative of ϕ with respect to z and evaluating at $z = 0$:

$$\left. \frac{\partial \phi}{\partial z} \right|_{z=0} = \frac{\zeta_a g}{\omega} \frac{k \sinh(kh)}{\cosh(kh)} \sin(kx - \omega t). \quad (\text{B.7})$$

Thus, the kinematic boundary condition becomes:

$$\frac{\partial \zeta}{\partial t} = \frac{\zeta_a}{\omega} \frac{k \sinh(kh)}{\cosh(kh)} \sin(kx - \omega t). \quad (\text{B.8})$$

To find the expression for ζ , we integrate with respect to time t :

$$\zeta(r, t) = \int \frac{\zeta_a g}{\omega} \frac{k \sinh(kh)}{\cosh(kh)} \sin(kx - \omega t) dt. \quad (\text{B.9})$$

This integration gives:

$$\zeta(r, t) = -\frac{\zeta_a g}{\omega^2} \frac{k \sinh(kh)}{\cosh(kh)} \cos(kx - \omega t) + f(r), \quad (\text{B.10})$$

where $f(r)$ is an arbitrary function of the spatial coordinates r representing the initial condition. To satisfy the initial condition $\zeta(r, t = 0) = 0$, we set $f(r) = 0$. Thus, the displacement becomes:

$$\zeta(r, t) = -\frac{\zeta_a g}{\omega^2} \frac{k \sinh(kh)}{\cosh(kh)} \cos(kx - \omega t). \quad (\text{B.11})$$

Pressure condition at the common surface The fluid pressure is now discontinuous at a surface of separation, so we have

$$P = \sigma \left(\frac{1}{R_1} + \frac{1}{R_2} \right), \quad (\text{B.12})$$

where R_1 and R_2 are the principal radii of curvature and σ is the surface tension. In our case, there is only one principal radius of curvature, as a monochromatic wave is considered, so $R_2 = 0$. The radius of curvature R_1 is approximated by the inverse of the second derivative of the surface elevation ζ . Setting this equal to the pressure formulation obtained from the dynamic free surface boundary condition gives

$$\sigma \left(\frac{\partial^2 \zeta}{\partial x^2} \right) = -\rho \left. \frac{\partial \phi}{\partial t} \right|_{z=0}. \quad (\text{B.13})$$

First, calculate the time derivative of ϕ :

$$\frac{\partial \phi}{\partial t} = -\frac{\zeta_a g}{\omega} \frac{\cosh(k(h+z))}{\cosh(kh)} \omega \cos(kx - \omega t). \quad (\text{B.14})$$

Evaluating at $z = 0$, this becomes:

$$\left. \frac{\partial \phi}{\partial t} \right|_{z=0} = -\zeta_a g \cos(kx - \omega t). \quad (\text{B.15})$$

The second space derivative of $\zeta(r, t)$:

$$\frac{\partial^2 \zeta(r, t)}{\partial x^2} = \frac{\zeta_a g}{\omega^2} \frac{k^3 \sinh(kh)}{\cosh(kh)} \cos(kx - \omega t). \quad (\text{B.16})$$

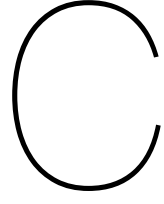
This leaves us to

$$\sigma \frac{\zeta_a g}{\omega^2} \frac{k^3 \sinh(kh)}{\cosh(kh)} \cos(kx - \omega t) = \rho \zeta_a g \cos(kx - \omega t). \quad (\text{B.17})$$

Multiplying both terms with ω^2 and dividing by $\cos(kx - \omega t)$, g , and ζ_a

$$\sigma k^3 \tanh(kh) = \rho \omega^2 \quad (\text{B.18})$$

$$\omega^2 = \frac{\sigma k^3}{\rho} \tanh(kh). \quad (\text{B.19})$$



Derivation of the linear gravity-capillary wave dispersion relation

C.1. Finite depth

The derivation of the linear gravity-capillary wave theory presented here has been established with the help of Lamb (1932) and Lamb (1945). The fluid is assumed to be incompressible, inviscid, and homogeneous, and the wave motion is analyzed under the assumption of small wave steepness, allowing linearization of the governing equations. The velocity potential used in this derivation is the same as the one derived for the dispersion relation of finite-depth linear gravity waves (see Appendix A). In contrast to the capillary wave dispersion derivation, gravity effects are not neglected in the case of gravity-capillary waves, as both surface tension and gravity contribute to the wave dynamics.

Dynamic free surface boundary condition The fluid pressure $P(r, t)$ acting on the sheet is calculated by assuming an incompressible and irrotational flow. In the region above the sheet, the fluid velocity is described by the potential $\phi(r, z, t)$, which satisfies Laplace's equation:

$$\nabla^2 \phi = 0, \quad (\text{C.1})$$

where $r = (x, y)$ denotes the horizontal in-plane coordinates. The pressure on the sheet is given by a derivation of the linearized Bernoulli equation A.17:

$$\frac{\partial \phi}{\partial t} + \frac{P_0}{\rho} + gz = -\frac{(P + P_0)}{\rho}. \quad (\text{C.2})$$

Solving this for P leaves us:

$$P = -\rho \frac{\partial \phi}{\partial t} \Big|_{z=0} - \rho g \zeta, \quad (\text{C.3})$$

where ρ is the density of the fluid and g is the acceleration due to gravity. Now for gravity-capillary waves it is not allowed to neglect the gravity effects.

Kinematic boundary condition The kinematic boundary condition relates the vertical displacement of the beam to the fluid velocity at the surface. The kinematic boundary condition is:

$$\frac{\partial \zeta}{\partial t} = \frac{\partial \phi}{\partial z} \Big|_{z=0}. \quad (\text{C.4})$$

We assume a solution for the velocity potential $\phi(r, z, t)$, which satisfies Laplace's equation:

$$\phi = \frac{\zeta_a g}{\omega} \frac{\cosh(k(h+z))}{\cosh(kh)} \sin(kx - \omega t). \quad (\text{C.5})$$

Taking the derivative of ϕ with respect to z and evaluating at $z = 0$:

$$\left. \frac{\partial \phi}{\partial z} \right|_{z=0} = \frac{\zeta_a g}{\omega} \frac{k \sinh(kh)}{\cosh(kh)} \sin(kx - \omega t). \quad (\text{C.6})$$

Thus, the kinematic boundary condition becomes:

$$\frac{\partial \zeta}{\partial t} = \frac{\zeta_a}{\omega} \frac{k \sinh(kh)}{\cosh(kh)} \sin(kx - \omega t). \quad (\text{C.7})$$

To find the expression for ζ , we integrate with respect to time t :

$$\zeta(r, t) = \int \frac{\zeta_a g}{\omega} \frac{k \sinh(kh)}{\cosh(kh)} \sin(kx - \omega t) dt. \quad (\text{C.8})$$

This integration gives:

$$\zeta(r, t) = -\frac{\zeta_a g}{\omega^2} \frac{k \sinh(kh)}{\cosh(kh)} \cos(kx - \omega t) + f(r), \quad (\text{C.9})$$

where $f(r)$ is an arbitrary function of the spatial coordinates r representing the initial condition. To satisfy the initial condition $\zeta(r, t = 0) = 0$, we set $f(r) = 0$. Thus, the displacement becomes:

$$\zeta(r, t) = -\frac{\zeta_a g}{\omega^2} \frac{k \sinh(kh)}{\cosh(kh)} \cos(kx - \omega t). \quad (\text{C.10})$$

Pressure condition at the common surface The fluid pressure is now discontinuous at a surface of separation so we have

$$P = \sigma \left(\frac{1}{R_1} + \frac{1}{R_2} \right), \quad (\text{C.11})$$

where, R_1 and R_2 are the principle radii of curvature and σ the surface tension. In our case there is only one principle radius of curvature as a monochromatic wave is considered so $R_2 = 0$. The radius of curvature R_1 is approximated with the inverse of the second derivative of surface elevation ζ . Setting this equal to the pressure formulation obtained from the dynamics boundary condition gives

$$\sigma \left(\frac{\partial^2 \zeta}{\partial x^2} \right) = -\rho \left. \frac{\partial \phi}{\partial t} \right|_{z=0} - \rho g \zeta. \quad (\text{C.12})$$

First, calculate the time derivative of ϕ :

$$\frac{\partial \phi}{\partial t} = -\frac{\zeta_a g}{\omega} \frac{\cosh(k(h+z))}{\cosh(kh)} \omega \cos(kx - \omega t). \quad (\text{C.13})$$

Evaluating at $z = 0$, this becomes:

$$\left. \frac{\partial \phi}{\partial t} \right|_{z=0} = -\zeta_a g \cos(kx - \omega t). \quad (\text{C.14})$$

The second space derivative of $\zeta(r, t)$:

$$\frac{\partial^2 \zeta(r, t)}{\partial x^2} = \frac{\zeta_a g}{\omega^2} \frac{k^3 \sinh(kh)}{\cosh(kh)} \cos(kx - \omega t). \quad (\text{C.15})$$

This leaves us to

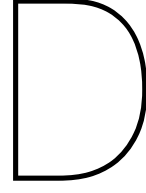
$$\sigma \frac{\zeta_a g}{\omega^2} \frac{k^3 \sinh(kh)}{\cosh(kh)} \cos(kx - \omega t) = \rho \zeta_a g \cos(kx - \omega t) - \rho g \frac{\zeta_a g}{\omega^2} \frac{k \sinh(kh)}{\cosh(kh)} \cos(kx - \omega t). \quad (\text{C.16})$$

Multiplying both terms with ω^2 and dividing by $\cos(kx - \omega t)$, g , and ζ_a results in

$$\sigma k^3 \tanh(kh) + \rho k g \tanh(kh) = \rho \omega^2 \quad (\text{C.17})$$

$$\omega^2 = \frac{\sigma k^3}{\rho} \tanh(kh) + kg \tanh(kh) \quad (\text{C.18})$$

$$\omega^2 = \left(\frac{\sigma k^3}{\rho} + kg \right) \tanh(kh). \quad (\text{C.19})$$



Derivation of the fluid–structure dispersion relation based on Euler-Bernoulli beam theory and linear gravity wave theory

D.1. Finite depth

The derivation of the fluid–structure interaction presented here combines Euler–Bernoulli beam theory with the velocity potential derived for finite-depth linear gravity waves (see Appendix A). The velocity potential satisfies Laplace’s equation and includes depth dependence, which alters the resulting dispersion relation compared to the infinite-depth approximations.

The Euler–Bernoulli beam theory is applied to model the bending behavior of slender elastic beams subjected to fluid loading. This theory assumes that the beam is homogeneous, isotropic, and linearly elastic, with small deflections such that geometric nonlinearities can be neglected. The beam is also considered slender, meaning its length is much greater than its cross-sectional dimensions, which allows the deformation to be governed primarily by bending. Shear deformation and axial stretching are ignored.

Furthermore, the cross-sections of the beam are assumed to remain plane and perpendicular to the neutral axis during deformation, implying no twisting or warping. The material’s Young’s modulus E and the second moment of area I are taken as constant along the beam’s length. These assumptions make the Euler–Bernoulli model suitable for analyzing long, thin structures where bending dominates the response to dynamic fluid forces.

D.1.1. Governing equation

The mechanical behavior of an Euler-Bernoulli beam is governed by the following fourth-order partial differential equation:

$$EI\nabla_r^4\zeta - \rho_e d \frac{\partial^2 \zeta}{\partial t^2} = P + P_{\text{ext}}, \quad (\text{D.1})$$

where E is the Young’s modulus of the beam, I is the second moment of area of the beam’s cross-section, ρ_e is the density of the beam material, and d is the thickness of the beam. The pressures P and P_{ext} are exerted on the sheet, with P representing the hydrodynamic pressure from the fluid and P_{ext} representing an external perturbation (e.g. an air jet), which is assumed to be zero here. The operator ∇_r^4 denotes the biharmonic operator in the in-plane coordinates $r = (x, y)$, i.e. $\nabla_r^4 = \left(\frac{\partial^2}{\partial x^2} + \frac{\partial^2}{\partial y^2} \right)^2$.

Dynamic free surface Boundary Condition The external pressure $P(r, t)$ acting on the sheet is calculated using the dynamic boundary condition, assuming incompressible and irrotational flow. The

fluid velocity is described by the potential $\phi(r, z, t)$, which satisfies Laplace's equation:

$$\nabla^2 \phi = 0. \quad (\text{D.2})$$

Using the linearized Bernoulli equation for the pressure acting on the sheet:

$$\frac{\partial \phi}{\partial t} + \frac{P_0}{\rho} + gz = \frac{(P + P_0)}{\rho}. \quad (\text{D.3})$$

Solving for P , we get:

$$P = \rho \frac{\partial \phi}{\partial t} \Big|_{z=0} + \rho g \zeta, \quad (\text{D.4})$$

where ρ is the fluid density, and g is the acceleration due to gravity.

Kinematic boundary condition The kinematic boundary condition relates the vertical displacement of the beam to the fluid velocity at the surface. The kinematic boundary condition is:

$$\frac{\partial \zeta}{\partial t} = \frac{\partial \phi}{\partial z} \Big|_{z=0}. \quad (\text{D.5})$$

We assume a solution for the velocity potential $\phi(r, z, t)$, which satisfies Laplace's equation:

$$\phi = \frac{\zeta_a g}{\omega} \frac{\cosh(k(h+z))}{\cosh(kh)} \sin(kx - \omega t). \quad (\text{D.6})$$

Taking the derivative of ϕ with respect to z and evaluating at $z = 0$:

$$\frac{\partial \phi}{\partial z} \Big|_{z=0} = \frac{\zeta_a g}{\omega} \frac{k \sinh(kh)}{\cosh(kh)} \sin(kx - \omega t). \quad (\text{D.7})$$

Thus, the kinematic boundary condition becomes:

$$\frac{\partial \zeta}{\partial t} = \frac{\zeta_a}{\omega} \frac{k \sinh(kh)}{\cosh(kh)} \sin(kx - \omega t). \quad (\text{D.8})$$

To find the expression for ζ , we integrate with respect to time t :

$$\zeta(r, t) = \int \frac{\zeta_a g}{\omega} \frac{k \sinh(kh)}{\cosh(kh)} \sin(kx - \omega t) dt. \quad (\text{D.9})$$

This integration gives:

$$\zeta(r, t) = -\frac{\zeta_a g}{\omega^2} \frac{k \sinh(kh)}{\cosh(kh)} \cos(kx - \omega t) + f(r), \quad (\text{D.10})$$

where $f(r)$ is an arbitrary function of the spatial coordinates r representing the initial condition. To satisfy the initial condition $\zeta(r, t = 0) = 0$, we set $f(r) = 0$. Thus, the displacement becomes:

$$\zeta(r, t) = -\frac{\zeta_a g}{\omega^2} \frac{k \sinh(kh)}{\cosh(kh)} \cos(kx - \omega t). \quad (\text{D.11})$$

Pressure acting on the Beam The fluid pressure $P(r, t)$ acting on the beam can be determined using the dynamic boundary condition. From the linearized Bernoulli equation:

$$\frac{\partial \phi}{\partial t} + \frac{P_0}{\rho} + gz = \frac{(P + P_0)}{\rho}, \quad (\text{D.12})$$

where P_0 is the ambient pressure, ρ is the fluid density, and g is the acceleration due to gravity. Solving for P , we find:

$$P = \rho \frac{\partial \phi}{\partial t} \Big|_{z=0} + \rho g \zeta. \quad (\text{D.13})$$

First, calculate the time derivative of ϕ :

$$\frac{\partial \phi}{\partial t} = -\frac{\zeta_a g}{\omega} \frac{\cosh(k(h+z))}{\cosh(kh)} \omega \cos(kx - \omega t). \quad (D.14)$$

Evaluating at $z = 0$, this becomes:

$$\frac{\partial \phi}{\partial t} \Big|_{z=0} = -\zeta_a g \cos(kx - \omega t). \quad (D.15)$$

Substituting this result and the expression for $\zeta(r, t)$ into the pressure equation, gives:

$$P = \rho (-\zeta_a g \cos(kx - \omega t)) + \rho g \left(-\frac{\zeta_a g}{\omega^2} \frac{k \sinh(kh)}{\cosh(kh)} \cos(kx - \omega t) \right). \quad (D.16)$$

Simplifying the terms:

$$P = -\rho g \zeta_a \cos(kx - \omega t) - \rho g \frac{\zeta_a g}{\omega^2} \frac{k \sinh(kh)}{\cosh(kh)} \cos(kx - \omega t). \quad (D.17)$$

D.1.2. Dispersion relation

We now calculate the terms in the Euler-Bernoulli beam equation D.1 and derive the dispersion relation.

Bending term: $EI \nabla_r^4 \zeta$ The fourth spatial derivative of ζ is:

$$\frac{\partial^4 \zeta}{\partial x^4} = -\frac{\zeta_a g}{\omega^2} \frac{k^5 \sinh(kh)}{\cosh(kh)} \cos(kx - \omega t). \quad (D.18)$$

Thus, the bending term is:

$$EI \nabla_r^4 \zeta = -EI k^5 \frac{\zeta_a g}{\omega^2} \frac{\sinh(kh)}{\cosh(kh)} \cos(kx - \omega t). \quad (D.19)$$

Inertia term: $\rho_e d \frac{\partial^2 \zeta}{\partial t^2}$ The second time derivative of ζ is:

$$\frac{\partial^2 \zeta}{\partial t^2} = -\frac{\zeta_a g}{\omega^2} \frac{k \sinh(kh)}{\cosh(kh)} \omega^2 \cos(kx - \omega t). \quad (D.20)$$

Thus, the inertia term becomes:

$$\rho_e d \frac{\partial^2 \zeta}{\partial t^2} = -\rho_e d \zeta_a g k \frac{\sinh(kh)}{\cosh(kh)} \cos(kx - \omega t). \quad (D.21)$$

Pressure term: P The external pressure P acting on the beam is:

$$P = -\left(\rho g \zeta_a + \rho g \frac{\zeta_a g}{\omega^2} \frac{k \sinh(kh)}{\cosh(kh)} \right) \cos(kx - \omega t). \quad (D.22)$$

Substituting the bending, inertia, and pressure terms into the Euler-Bernoulli equation D.1:

$$-EI k^5 \frac{\zeta_a g}{\omega^2} \frac{\sinh(kh)}{\cosh(kh)} \cos(kx - \omega t) + \rho_e d \zeta_a g k \frac{\sinh(kh)}{\cosh(kh)} \cos(kx - \omega t) = -\left(\rho g \zeta_a + \rho g \frac{\zeta_a g}{\omega^2} \frac{k \sinh(kh)}{\cosh(kh)} \right) \cos(kx - \omega t). \quad (D.23)$$

Simplifying, multiplying each term with ω^2 , and dividing each term by $g, \zeta_a, \cos(kx - \omega t)$ gives

$$-EI k^5 \frac{\sinh(kh)}{\cosh(kh)} + \rho_e d k \omega^2 \frac{\sinh(kh)}{\cosh(kh)} = -\left(\rho \omega^2 + \rho g k \frac{\sinh(kh)}{\cosh(kh)} \right). \quad (D.24)$$

Further simplifying results to

$$-EI k^5 \tanh(kh) + \rho_e dk \omega^2 \tanh(kh) - \rho g k \tanh(kh) = -\rho \omega^2 \quad (\text{D.25})$$

even further simplifying to

$$\omega^2 = \left(\frac{EI k^5}{\rho} - \frac{\rho_e dk \omega^2}{\rho} + gk \right) \tanh(kh). \quad (\text{D.26})$$

By multiplying each term by $\frac{\text{kg}}{\text{kg}}$, we are effectively multiplying by 1, which does not change the outcome. This makes the expression more intuitive:

$$\omega^2 = \left(\frac{EI k^5}{\rho g k} - \frac{\rho_e dk \omega^2}{\rho g k} + \frac{gk}{gk} \right) kg \tanh(kh) \quad (\text{D.27})$$

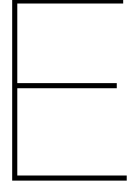
where

$$k_p = \left(\frac{\rho g}{EI} \right)^{\frac{1}{4}} \quad (\text{D.28})$$

$$\omega_0 = \sqrt{\frac{\rho g}{\rho_e d}}. \quad (\text{D.29})$$

Using these definitions, the dispersion relation simplifies to

$$\omega^2 = \left(1 - \left(\frac{\omega}{\omega_0} \right)^2 + \left(\frac{k}{k_p} \right)^4 \right) kg \tanh(kh). \quad (\text{D.30})$$



Derivation of the fluid–structure dispersion relation based on Kirchhoff-Love beam theory and linear gravity wave theory

E.1. Finite depth

The derivation of the fluid–structure interaction presented here combines Kirchhoff–Love plate theory with the velocity potential derived for finite-depth linear gravity waves (see Appendix A). The plate is assumed to be thin, homogeneous, isotropic, and linearly elastic, with small vertical deflections allowing for linearization. Shear deformation and rotary inertia are neglected, consistent with the assumptions of Kirchhoff–Love theory. The fluid is modeled as incompressible, inviscid, and irrotational, and the wave steepness is assumed small enough to ignore nonlinear terms. The use of the depth-dependent velocity potential modifies the resulting dispersion relation by explicitly incorporating the effect of finite fluid depth.

E.1.1. Governing equation

The mechanical system of the elastic sheet is governed by the Kirchhoff-love plate equation, which simplifies to the following form:

$$B\nabla_r^4\zeta + \rho_e d \frac{\partial^2 \zeta}{\partial t^2} = P + P_{\text{ext}}, \quad (\text{E.1})$$

where B is the bending stiffness of the sheet, and ρ_e is the sheet's density. The first term accounts for the bending and the second term represents the solid inertia. The pressures P and P_{ext} are exerted on the sheet, with P representing a hydrostatic pressure and P_{ext} representing an external perturbation (e.g. an air jet), assumed to be zero here.

Dynamic free surface boundary condition The fluid pressure $P(r, t)$ acting on the sheet is calculated by assuming an incompressible and irrotational flow. In the region above the sheet, the fluid velocity is described by the potential $\phi(r, z, t)$, which satisfies Laplace's equation:

$$\nabla^2 \phi = 0. \quad (\text{E.2})$$

The pressure on the sheet is given by a derivation of the linearized Bernoulli equation A.17:

$$\frac{\partial \phi}{\partial t} + \frac{P_0}{\rho} + gz = -\frac{(P + P_0)}{\rho}. \quad (\text{E.3})$$

Solving this for P leaves us:

$$P = -\rho \frac{\partial \phi}{\partial t} \Big|_{z=0} - \rho g \zeta, \quad (\text{E.4})$$

where ρ is the density of the fluid and g is the acceleration due to gravity.

Kinematic boundary condition The kinematic boundary condition relates the vertical displacement of the beam to the fluid velocity at the surface. The kinematic boundary condition is:

$$\frac{\partial \zeta}{\partial t} = \frac{\partial \phi}{\partial z} \Big|_{z=0}. \quad (\text{E.5})$$

We assume a solution for the velocity potential $\phi(r, z, t)$, which satisfies Laplace's equation:

$$\phi = \frac{\zeta_a g}{\omega} \frac{\cosh(k(h+z))}{\cosh(kh)} \sin(kx - \omega t). \quad (\text{E.6})$$

Taking the derivative of ϕ with respect to z and evaluating at $z = 0$:

$$\frac{\partial \phi}{\partial z} \Big|_{z=0} = \frac{\zeta_a g}{\omega} \frac{k \sinh(kh)}{\cosh(kh)} \sin(kx - \omega t). \quad (\text{E.7})$$

Thus, the kinematic boundary condition becomes:

$$\frac{\partial \zeta}{\partial t} = \frac{\zeta_a}{\omega} \frac{k \sinh(kh)}{\cosh(kh)} \sin(kx - \omega t). \quad (\text{E.8})$$

To find the expression for ζ , we integrate with respect to time t :

$$\zeta(r, t) = \int \frac{\zeta_a g}{\omega} \frac{k \sinh(kh)}{\cosh(kh)} \sin(kx - \omega t) dt. \quad (\text{E.9})$$

This integration gives:

$$\zeta(r, t) = -\frac{\zeta_a g}{\omega^2} \frac{k \sinh(kh)}{\cosh(kh)} \cos(kx - \omega t) + f(r), \quad (\text{E.10})$$

where $f(r)$ is an arbitrary function of the spatial coordinates r representing the initial condition. To satisfy the initial condition $\zeta(r, t = 0) = 0$, we set $f(r) = 0$. Thus, the displacement becomes:

$$\zeta(r, t) = -\frac{\zeta_a g}{\omega^2} \frac{k \sinh(kh)}{\cosh(kh)} \cos(kx - \omega t). \quad (\text{E.11})$$

Pressure acting on the beam The fluid pressure $P(r, t)$ acting on the beam can be determined using the dynamic boundary condition. From the linearized Bernoulli equation:

$$\frac{\partial \phi}{\partial t} + \frac{P_0}{\rho} + gz = \frac{(P + P_0)}{\rho}, \quad (\text{E.12})$$

where P_0 is the ambient pressure, ρ is the fluid density, and g is the acceleration due to gravity. Solving for P , we find:

$$P = \rho \frac{\partial \phi}{\partial t} \Big|_{z=0} + \rho g \zeta. \quad (\text{E.13})$$

First, calculate the time derivative of ϕ :

$$\frac{\partial \phi}{\partial t} = -\frac{\zeta_a g}{\omega} \frac{\cosh(k(h+z))}{\cosh(kh)} \omega \cos(kx - \omega t). \quad (\text{E.14})$$

Evaluating at $z = 0$, this becomes:

$$\frac{\partial \phi}{\partial t} \Big|_{z=0} = -\zeta_a g \cos(kx - \omega t). \quad (\text{E.15})$$

Substituting this result and the expression for $\zeta(r, t)$ into the pressure equation, gives:

$$P = \rho (-\zeta_a g \cos(kx - \omega t)) + \rho g \left(-\frac{\zeta_a g}{\omega^2} \frac{k \sinh(kh)}{\cosh(kh)} \cos(kx - \omega t) \right). \quad (\text{E.16})$$

Simplifying the terms:

$$P = -\rho g \zeta_a \cos(kx - \omega t) - \rho g \frac{\zeta_a g}{\omega^2} \frac{k \sinh(kh)}{\cosh(kh)} \cos(kx - \omega t). \quad (\text{E.17})$$

E.1.2. Dispersion relation

We now calculate the terms in the Kirchoff-Love plate equation E.1 and derive the dispersion relation.

Bending term: $EI \nabla_r^4 \zeta$ The fourth spatial derivative of ζ is:

$$\frac{\partial^4 \zeta}{\partial x^4} = -\frac{\zeta_a g}{\omega^2} \frac{k^5 \sinh(kh)}{\cosh(kh)} \cos(kx - \omega t). \quad (\text{E.18})$$

Thus, the bending term is:

$$B \nabla_r^4 \zeta = -B k^5 \frac{\zeta_a g}{\omega^2} \frac{\sinh(kh)}{\cosh(kh)} \cos(kx - \omega t). \quad (\text{E.19})$$

Inertia term: $\rho_e d \frac{\partial^2 \zeta}{\partial t^2}$ The second time derivative of ζ is:

$$\frac{\partial^2 \zeta}{\partial t^2} = -\frac{\zeta_a g}{\omega^2} \frac{k \sinh(kh)}{\cosh(kh)} \omega^2 \cos(kx - \omega t). \quad (\text{E.20})$$

Thus, the inertia term becomes:

$$\rho_e d \frac{\partial^2 \zeta}{\partial t^2} = -\rho_e d \zeta_a g k \frac{\sinh(kh)}{\cosh(kh)} \cos(kx - \omega t). \quad (\text{E.21})$$

But as explained in the assumptions this term will be omitted.

Pressure term: P The external pressure P acting on the beam is:

$$P = -\left(\rho g \zeta_a + \rho g \frac{\zeta_a g}{\omega^2} \frac{k \sinh(kh)}{\cosh(kh)} \right) \cos(kx - \omega t). \quad (\text{E.22})$$

Substituting the bending, inertia, and pressure terms into the Kirchoff-Love equation E.1:

$$-B k^5 \frac{\zeta_a g}{\omega^2} \frac{\sinh(kh)}{\cosh(kh)} \cos(kx - \omega t) = -\left(\rho g \zeta_a + \rho g \frac{\zeta_a g}{\omega^2} \frac{k \sinh(kh)}{\cosh(kh)} \right) \cos(kx - \omega t). \quad (\text{E.23})$$

Simplifying, multiplying each term by ω^2 , and dividing each term by g , ζ_a , and $\cos(kx - \omega t)$ gives

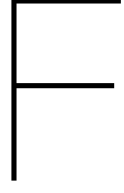
$$-B k^5 \frac{\sinh(kh)}{\cosh(kh)} = -\left(\rho \omega^2 + \rho g k \frac{\sinh(kh)}{\cosh(kh)} \right), \quad (\text{E.24})$$

which can be further simplified to

$$-B k^5 \tanh(kh) - \rho g k \tanh(kh) = -\rho \omega^2, \quad (\text{E.25})$$

and even further to

$$\omega^2 = \left(\frac{E I k^5}{\rho} + g k \right) \tanh(kh). \quad (\text{E.26})$$



Derivation of the fluid–structure dispersion relation based on Föppl–von Kármán plate theory and linear gravity wave theory

F.1. Finite depth

This derivation follows the approach outlined by Ono-dit-Biot et al. (2019). The system consists of a thin elastic sheet floating on an incompressible, inviscid, and irrotational fluid of finite depth. The wave amplitudes are assumed to be small relative to the wavelength, allowing linearization of the governing equations. The vertical displacement of the sheet is described by $z = \zeta(r, t)$, where $r = (x, y)$ are the horizontal coordinates and t denotes time. The membrane is assumed to be a thin film, such that mass-related inertia can be neglected. Furthermore, the Cauchy stress tensor σ_c is treated as a scalar that represents a uniform surface tension σ . The velocity potential used for the fluid motion is the one derived in the dispersion relation for finite-depth linear gravity waves (see Appendix A).

F.1.1. Governing equation

The mechanical system of the elastic sheet is governed by the Föppl–von Kármán equation, which simplifies to the following form:

$$B\nabla_r^4\zeta - \sigma\nabla_r^2\zeta + \rho_e d \frac{\partial^2\zeta}{\partial t^2} = P + P_{\text{ext}}, \quad (\text{F.1})$$

where B is the bending stiffness of the sheet, σ is the surface tension, and ρ_e is the density of the sheet. The first term accounts for the bending, the second term for the tension, and the third term represents the solid inertia. The pressures P and P_{ext} are exerted on the sheet, with P representing a hydrostatic pressure and P_{ext} representing an external perturbation (e.g. an air jet), assumed to be zero here.

Dynamic free surface boundary condition The fluid pressure $P(r, t)$ acting on the sheet is calculated by assuming an incompressible and irrotational flow. In the region above the sheet, the fluid velocity is described by the potential $\phi(r, z, t)$, which satisfies Laplace's equation:

$$\nabla^2\phi = 0. \quad (\text{F.2})$$

The pressure on the sheet is given by a derivation of the linearized Bernoulli equation A.17:

$$\frac{\partial\phi}{\partial t} + \frac{P_0}{\rho} + gz = -\frac{(P + P_0)}{\rho}. \quad (\text{F.3})$$

Solving this for P leaves us:

$$P = -\rho \frac{\partial \phi}{\partial t} \Big|_{z=0} - \rho g \zeta, \quad (\text{F.4})$$

where ρ is the density of the fluid and g is the acceleration due to gravity.

Kinematic boundary condition The kinematic boundary condition relates the vertical displacement of the beam to the fluid velocity at the surface. The kinematic boundary condition is:

$$\frac{\partial \zeta}{\partial t} = \frac{\partial \phi}{\partial z} \Big|_{z=0}. \quad (\text{F.5})$$

We assume a solution for the velocity potential $\phi(r, z, t)$, which satisfies Laplace's equation:

$$\phi = \frac{\zeta_a g}{\omega} \frac{\cosh(k(h+z))}{\cosh(kh)} \sin(kx - \omega t). \quad (\text{F.6})$$

Taking the derivative of ϕ with respect to z and evaluating at $z = 0$:

$$\frac{\partial \phi}{\partial z} \Big|_{z=0} = \frac{\zeta_a g}{\omega} \frac{k \sinh(kh)}{\cosh(kh)} \sin(kx - \omega t). \quad (\text{F.7})$$

Thus, the kinematic boundary condition becomes:

$$\frac{\partial \zeta}{\partial t} = \frac{\zeta_a}{\omega} \frac{k \sinh(kh)}{\cosh(kh)} \sin(kx - \omega t). \quad (\text{F.8})$$

To find the expression for ζ , we integrate with respect to time t :

$$\zeta(r, t) = \int \frac{\zeta_a g}{\omega} \frac{k \sinh(kh)}{\cosh(kh)} \sin(kx - \omega t) dt. \quad (\text{F.9})$$

This integration gives:

$$\zeta(r, t) = -\frac{\zeta_a g}{\omega^2} \frac{k \sinh(kh)}{\cosh(kh)} \cos(kx - \omega t) + f(r), \quad (\text{F.10})$$

where $f(r)$ is an arbitrary function of the spatial coordinates r representing the initial condition. To satisfy the initial condition $\zeta(r, t = 0) = 0$, we set $f(r) = 0$. Thus, the displacement becomes:

$$\zeta(r, t) = -\frac{\zeta_a g}{\omega^2} \frac{k \sinh(kh)}{\cosh(kh)} \cos(kx - \omega t). \quad (\text{F.11})$$

Pressure acting on the beam The fluid pressure $P(r, t)$ acting on the beam can be determined using the dynamic boundary condition. From the linearized Bernoulli equation:

$$\frac{\partial \phi}{\partial t} + \frac{P_0}{\rho} + gz = \frac{(P + P_0)}{\rho}, \quad (\text{F.12})$$

where P_0 is the ambient pressure, ρ is the fluid density, and g is the acceleration due to gravity. Solving for P , we find:

$$P = \rho \frac{\partial \phi}{\partial t} \Big|_{z=0} + \rho g \zeta. \quad (\text{F.13})$$

First, calculate the time derivative of ϕ :

$$\frac{\partial \phi}{\partial t} = -\frac{\zeta_a g}{\omega} \frac{\cosh(k(h+z))}{\cosh(kh)} \omega \cos(kx - \omega t). \quad (\text{F.14})$$

Evaluating at $z = 0$, this becomes:

$$\frac{\partial \phi}{\partial t} \Big|_{z=0} = -\zeta_a g \cos(kx - \omega t). \quad (\text{F.15})$$

Substituting this result and the expression for $\zeta(r, t)$ into the pressure equation, gives:

$$P = \rho (-\zeta_a g \cos(kx - \omega t)) + \rho g \left(-\frac{\zeta_a g}{\omega^2} \frac{k \sinh(kh)}{\cosh(kh)} \cos(kx - \omega t) \right). \quad (\text{F.16})$$

Simplifying the terms:

$$P = -\rho g \zeta_a \cos(kx - \omega t) - \rho g \frac{\zeta_a g}{\omega^2} \frac{k \sinh(kh)}{\cosh(kh)} \cos(kx - \omega t). \quad (\text{F.17})$$

F.1.2. Dispersion relation

We now calculate the terms in the Föppl–von Kármán plate equation F.1 and derive the dispersion relation.

Bending term: $B \nabla_r^4 \zeta$ The fourth spatial derivative of ζ is:

$$\frac{\partial^4 \zeta}{\partial x^4} = -\frac{\zeta_a g}{\omega^2} \frac{k^5 \sinh(kh)}{\cosh(kh)} \cos(kx - \omega t). \quad (\text{F.18})$$

Thus, the bending term is:

$$B \nabla_r^4 \zeta = -B k^5 \frac{\zeta_a g}{\omega^2} \frac{\sinh(kh)}{\cosh(kh)} \cos(kx - \omega t). \quad (\text{F.19})$$

Stress term: $-\sigma \nabla_r^2 \zeta$ The second spatial derivative of $\zeta(r, t)$ is:

$$\frac{\partial^2 \zeta}{\partial x^2} = \frac{\zeta_a g}{\omega^2} \frac{k^3 \sinh(kh)}{\cosh(kh)} \cos(kx - \omega t), \quad (\text{F.20})$$

which gives the tension term:

$$-\sigma \nabla_r^2 \zeta = -\sigma \frac{\zeta_a g}{\omega^2} \frac{k^3 \sinh(kh)}{\cosh(kh)} \cos(kx - \omega t). \quad (\text{F.21})$$

Inertia term: $\rho_e d \frac{\partial^2 \zeta}{\partial t^2}$ The second time derivative of ζ is:

$$\frac{\partial^2 \zeta}{\partial t^2} = -\frac{\zeta_a g}{\omega^2} \frac{k \sinh(kh)}{\cosh(kh)} \omega^2 \cos(kx - \omega t). \quad (\text{F.22})$$

Thus, the inertia term becomes:

$$\rho_e d \frac{\partial^2 \zeta}{\partial t^2} = -\rho_e d \zeta_a g k \frac{\sinh(kh)}{\cosh(kh)} \cos(kx - \omega t). \quad (\text{F.23})$$

But as explained in the assumptions this term will be omitted.

Pressure term: P The external pressure P acting on the beam is:

$$P = -\left(\rho g \zeta_a + \rho g \frac{\zeta_a g}{\omega^2} \frac{k \sinh(kh)}{\cosh(kh)} \right) \cos(kx - \omega t). \quad (\text{F.24})$$

Substituting the bending, inertia, and pressure terms into the Föppl–von Kármán plate equation F.1:

$$-B k^5 \frac{\zeta_a g}{\omega^2} \frac{\sinh(kh)}{\cosh(kh)} \cos(kx - \omega t) - \sigma \frac{\zeta_a g}{\omega^2} \frac{k^3 \sinh(kh)}{\cosh(kh)} \cos(kx - \omega t) = -\left(\rho g \zeta_a + \rho g \frac{\zeta_a g}{\omega^2} \frac{k \sinh(kh)}{\cosh(kh)} \right) \cos(kx - \omega t). \quad (\text{F.25})$$

Simplifying, multiplying each term by ω^2 , and dividing each term by g , ζ_a , and $\cos(kx - \omega t)$ gives

$$-Bk^5 \frac{\sinh(kh)}{\cosh(kh)} - \sigma k^3 \frac{\sinh(kh)}{\cosh(kh)} = -\left(\rho \omega^2 + \rho g k \frac{\sinh(kh)}{\cosh(kh)} \right), \quad (\text{F.26})$$

which can be further simplified to

$$-Bk^5 \tanh(kh) - \sigma k^3 \tanh(kh) - \rho g k \tanh(kh) = -\rho \omega^2, \quad (\text{F.27})$$

and finally to

$$\omega^2 = \left(\frac{Bk^5}{\rho} + \frac{\sigma k^3}{\rho} + gk \right) \tanh(kh). \quad (\text{F.28})$$

F.2. Full Cauchy stress tensor

This section presents an extended derivation of the fluid-structure dispersion relation by incorporating the full two-dimensional Cauchy stress tensor, σ_{ij} , in the thin elastic sheet model. Unlike previous derivations where the stress tensor was simplified as a scalar surface tension, here all in-plane stress components are included. Specifically, this means that both normal stresses σ_{xx} and σ_{yy} , which act along the x - and y -directions respectively, as well as the shear stress σ_{xy} (and by symmetry σ_{yx}), are retained in the formulation. It is important to note that the general Cauchy stress tensor, denoted σ_C elsewhere in this report, is a three-dimensional tensor describing stresses in all spatial directions. For the thin plate approximation considered here, σ_{ij} represents the full 2D in-plane Cauchy stress tensor.

The underlying assumptions remain consistent with earlier sections: the system consists of a thin elastic sheet floating on an incompressible, inviscid, and irrotational fluid with small-amplitude waves, allowing for linearization. This approach considers the fluid to have finite depth, and the velocity potential is explicitly dependent on this finite depth, which modifies the resulting dispersion relation and fluid-structure interaction behavior.

F.2.1. Governing equation

The mechanical system of the elastic sheet is governed by the Föppl–von Kármán equation, which simplifies to the following form:

$$B\nabla_r^4\zeta - \nabla_r \cdot (\sigma_{ij} \cdot \nabla_r \zeta) + \rho_e d \frac{\partial^2 \zeta}{\partial t^2} = P + P_{\text{ext}}, \quad (\text{F.29})$$

where B is the bending stiffness of the sheet, σ_{ij} is the 2D stress tensor of the sheet, and ρ_e is the density of the sheet. The first term accounts for the bending, the second term for the internal stress, and the third term represents the solid inertia. The pressures P and P_{ext} are exerted on the sheet, with P representing a hydrostatic pressure and P_{ext} representing an external perturbation (e.g. an air jet), assumed to be zero here.

Kinematic boundary condition The kinematic boundary condition relates the vertical displacement of the beam to the fluid velocity at the surface. The kinematic boundary condition is:

$$\frac{\partial \zeta}{\partial t} = \frac{\partial \phi}{\partial z} \Big|_{z=0}. \quad (\text{F.30})$$

We assume a solution for the velocity potential $\phi(r, z, t)$, which satisfies Laplace's equation:

$$\phi = \frac{\zeta_a g}{\omega} \frac{\cosh(k(h+z))}{\cosh(kh)} \sin(kx - \omega t). \quad (\text{F.31})$$

Taking the derivative of ϕ with respect to z and evaluating at $z = 0$:

$$\frac{\partial \phi}{\partial z} \Big|_{z=0} = \frac{\zeta_a g}{\omega} \frac{k \sinh(kh)}{\cosh(kh)} \sin(kx - \omega t). \quad (\text{F.32})$$

Thus, the kinematic boundary condition becomes:

$$\frac{\partial \zeta}{\partial t} = \frac{\zeta_a}{\omega} \frac{k \sinh(kh)}{\cosh(kh)} \sin(kx - \omega t). \quad (\text{F.33})$$

To find the expression for ζ , we integrate with respect to time t :

$$\zeta(r, t) = \int \frac{\zeta_a g}{\omega} \frac{k \sinh(kh)}{\cosh(kh)} \sin(kx - \omega t) dt. \quad (\text{F.34})$$

This integration gives:

$$\zeta(r, t) = -\frac{\zeta_a g}{\omega^2} \frac{k \sinh(kh)}{\cosh(kh)} \cos(kx - \omega t) + f(r), \quad (\text{F.35})$$

where $f(r)$ is an arbitrary function of the spatial coordinates r representing the initial condition. To satisfy the initial condition $\zeta(r, t = 0) = 0$, we set $f(r) = 0$. Thus, the displacement becomes:

$$\zeta(r, t) = -\frac{\zeta_a g}{\omega^2} \frac{k \sinh(kh)}{\cosh(kh)} \cos(kx - \omega t). \quad (\text{F.36})$$

Pressure acting on the beam The fluid pressure $P(r, t)$ acting on the beam can be determined using the dynamic boundary condition. From the linearized Bernoulli equation:

$$\frac{\partial \phi}{\partial t} + \frac{P_0}{\rho} + gz = \frac{(P + P_0)}{\rho}, \quad (\text{F.37})$$

where P_0 is the ambient pressure, ρ is the fluid density, and g is the acceleration due to gravity. Solving for P , we find:

$$P = \rho \frac{\partial \phi}{\partial t} \Big|_{z=0} + \rho g \zeta. \quad (\text{F.38})$$

First, calculate the time derivative of ϕ :

$$\frac{\partial \phi}{\partial t} = -\frac{\zeta_a g}{\omega} \frac{\cosh(k(h+z))}{\cosh(kh)} \omega \cos(kx - \omega t). \quad (\text{F.39})$$

Evaluating at $z = 0$, this becomes:

$$\frac{\partial \phi}{\partial t} \Big|_{z=0} = -\zeta_a g \cos(kx - \omega t). \quad (\text{F.40})$$

Substituting this result and the expression for $\zeta(r, t)$ into the pressure equation, gives:

$$P = \rho (-\zeta_a g \cos(kx - \omega t)) + \rho g \left(-\frac{\zeta_a g}{\omega^2} \frac{k \sinh(kh)}{\cosh(kh)} \cos(kx - \omega t) \right). \quad (\text{F.41})$$

Simplifying the terms:

$$P = -\rho g \zeta_a \cos(kx - \omega t) - \rho g \frac{\zeta_a g}{\omega^2} \frac{k \sinh(kh)}{\cosh(kh)} \cos(kx - \omega t). \quad (\text{F.42})$$

F.2.2. Dispersion relation

We now calculate the terms in the Föppl–von Kármán plate equation F.29 and derive the dispersion relation.

Bending term: $B \nabla_r^4 \zeta$ The fourth spatial derivative of ζ is:

$$\frac{\partial^4 \zeta}{\partial x^4} = -\frac{\zeta_a g}{\omega^2} \frac{k^5 \sinh(kh)}{\cosh(kh)} \cos(kx - \omega t). \quad (\text{F.43})$$

Thus, the bending term is:

$$B \nabla_r^4 \zeta = -B k^5 \frac{\zeta_a g}{\omega^2} \frac{\sinh(kh)}{\cosh(kh)} \cos(kx - \omega t). \quad (\text{F.44})$$

Stress term: $-\nabla_r \cdot (\sigma_{ij} \cdot \nabla_r \zeta)$ The stress σ_{ij} tensor has a general form:

$$\sigma_{ij} = \begin{pmatrix} \sigma_{xx} & \sigma_{xy} \\ \sigma_{xy} & \sigma_{yy} \end{pmatrix}. \quad (\text{F.45})$$

First, compute the gradient of ζ :

$$\nabla_r \zeta = \begin{pmatrix} \frac{\partial \zeta}{\partial x} \\ \frac{\partial \zeta}{\partial y} \end{pmatrix}. \quad (\text{F.46})$$

Next, apply the stress tensor to the gradient:

$$\sigma_{ij} \cdot \nabla_r \zeta = \begin{pmatrix} \sigma_{xx} & \sigma_{xy} \\ \sigma_{xy} & \sigma_{yy} \end{pmatrix} \cdot \begin{pmatrix} \frac{\partial \zeta}{\partial x} \\ \frac{\partial \zeta}{\partial y} \end{pmatrix} = \begin{pmatrix} \sigma_{xx} \frac{\partial \zeta}{\partial x} + \sigma_{xy} \frac{\partial \zeta}{\partial y} \\ \sigma_{xy} \frac{\partial \zeta}{\partial x} + \sigma_{yy} \frac{\partial \zeta}{\partial y} \end{pmatrix}. \quad (\text{F.47})$$

Now, take the divergence of this vector:

$$\nabla_r \cdot (\sigma_{ij} \cdot \nabla_r \zeta) = \frac{\partial}{\partial x} \left(\sigma_{xx} \frac{\partial \zeta}{\partial x} + \sigma_{xy} \frac{\partial \zeta}{\partial y} \right) + \frac{\partial}{\partial y} \left(\sigma_{xy} \frac{\partial \zeta}{\partial x} + \sigma_{yy} \frac{\partial \zeta}{\partial y} \right). \quad (\text{F.48})$$

Expanding the derivatives:

$$\nabla_r \cdot (\sigma_{ij} \cdot \nabla_r \zeta) = \sigma_{xx} \frac{\partial^2 \zeta}{\partial x^2} + \sigma_{xy} \frac{\partial^2 \zeta}{\partial x \partial y} + \sigma_{xy} \frac{\partial^2 \zeta}{\partial y \partial x} + \sigma_{yy} \frac{\partial^2 \zeta}{\partial y^2}. \quad (\text{F.49})$$

Since the mixed derivatives are equal, we combine them:

$$\nabla_r \cdot (\sigma_{ij} \cdot \nabla_r \zeta) = \sigma_{xx} \frac{\partial^2 \zeta}{\partial x^2} + 2\sigma_{xy} \frac{\partial^2 \zeta}{\partial x \partial y} + \sigma_{yy} \frac{\partial^2 \zeta}{\partial y^2}. \quad (\text{F.50})$$

Thus, the stress term is:

$$-\nabla_r \cdot (\sigma_{ij} \cdot \nabla_r \zeta) = - \left(\sigma_{xx} \frac{\partial^2 \zeta}{\partial x^2} + 2\sigma_{xy} \frac{\partial^2 \zeta}{\partial x \partial y} + \sigma_{yy} \frac{\partial^2 \zeta}{\partial y^2} \right). \quad (\text{F.51})$$

The second spatial derivatives of $\zeta(r, t)$ are:

$$\frac{\partial^2 \zeta}{\partial x^2} = \frac{\zeta_a g}{\omega^2} \frac{k^3 \sinh(kh)}{\cosh(kh)} \cos(kx - \omega t) \quad (\text{F.52})$$

$$\frac{\partial^2 \zeta}{\partial x \partial y} = 0 \quad (\text{F.53})$$

$$\frac{\partial^2 \zeta}{\partial y^2} = 0 \quad (\text{F.54})$$

leaving us with a stress term

$$-\nabla_r \cdot (\sigma_{ij} \cdot \nabla_r \zeta) = -\sigma_{xx} \frac{\zeta_a g}{\omega^2} \frac{k^3 \sinh(kh)}{\cosh(kh)} \cos(kx - \omega t). \quad (\text{F.55})$$

Inertia term: $\rho_e d \frac{\partial^2 \zeta}{\partial t^2}$ The second time derivative of ζ is:

$$\frac{\partial^2 \zeta}{\partial t^2} = -\frac{\zeta_a g}{\omega^2} \frac{k \sinh(kh)}{\cosh(kh)} \omega^2 \cos(kx - \omega t). \quad (\text{F.56})$$

Thus, the inertia term becomes:

$$\rho_e h \frac{\partial^2 \zeta}{\partial t^2} = -\rho_e d \zeta_a g k \frac{\sinh(kh)}{\cosh(kh)} \cos(kx - \omega t). \quad (\text{F.57})$$

But as explained in the assumptions this term will be omitted.

Pressure term: P The external pressure P acting on the beam is:

$$P = - \left(\rho g \zeta_a + \rho g \frac{\zeta_a g}{\omega^2} \frac{k \sinh(kh)}{\cosh(kh)} \right) \cos(kx - \omega t). \quad (\text{F.58})$$

Substituting the bending, inertia, and pressure terms into the Föppl–von Kármán plate equation F.29:

$$-Bk^5 \frac{\zeta_a g}{\omega^2} \frac{\sinh(kh)}{\cosh(kh)} \cos(kx - \omega t) - \sigma_{xx} \frac{\zeta_a g}{\omega^2} \frac{k^3 \sinh(kh)}{\cosh(kh)} \cos(kx - \omega t) = - \left(\rho g \zeta_a + \rho g \frac{\zeta_a g}{\omega^2} \frac{k \sinh(kh)}{\cosh(kh)} \right) \cos(kx - \omega t). \quad (\text{F.59})$$

Simplifying, multiplying each term by ω^2 , and dividing each term by g , ζ_a , and $\cos(kx - \omega t)$ gives

$$-Bk^5 \frac{\sinh(kh)}{\cosh(kh)} - \sigma_{xx} k^3 \frac{\sinh(kh)}{\cosh(kh)} = - \left(\rho \omega^2 + \rho g k \frac{\sinh(kh)}{\cosh(kh)} \right), \quad (\text{F.60})$$

which can be further simplified to

$$-Bk^5 \tanh(kh) - \sigma_{xx} k^3 \tanh(kh) - \rho g k \tanh(kh) = -\rho \omega^2, \quad (\text{F.61})$$

and finally to

$$\omega^2 = \left(\frac{Bk^5}{\rho} + \frac{\sigma_{xx} k^3}{\rho} + gk \right) \tanh(kh). \quad (\text{F.62})$$

F.3. Oblique waves incidence

This section extends the previous formulation by considering oblique wave incidence. Instead of assuming a monochromatic linear wave traveling parallel to the x -axis, we now consider a plane wave impinging on the floating structure at an angle. The same fluid–structure interaction framework is used, with the elastic sheet modeled by Föppl–von Kármán plate theory and the fluid assumed to be incompressible, inviscid, and irrotational. The wave remains of small amplitude, allowing for linearization, but the direction of wave propagation introduces anisotropy in the response and modifies the dispersion relation accordingly.

F.3.1. Governing equation

The mechanical system of the elastic sheet is governed by the Föppl–von Kármán equation, which simplifies to the following form:

$$B\nabla_r^4\zeta - \nabla_r \cdot (\sigma_{ij} \cdot \nabla_r \zeta) + \rho_e h \frac{\partial^2 \zeta}{\partial t^2} = P + P_{\text{ext}}, \quad (\text{F.63})$$

where B is the bending stiffness of the sheet, σ_{ij} is the 2D stress tensor of the sheet, and ρ_e is the density of the sheet. The first term accounts for the bending, the second term for the internal stress, and the third term represents the solid inertia. The pressures P and P_{ext} are exerted on the sheet, with P representing a hydrostatic pressure and P_{ext} representing an external perturbation (e.g. an air jet), assumed to be zero here.

Kinematic boundary condition The kinematic boundary condition relates the vertical displacement of the beam to the fluid velocity at the surface. The kinematic boundary condition is:

$$\frac{\partial \zeta}{\partial t} = \frac{\partial \phi}{\partial z} \Big|_{z=0}. \quad (\text{F.64})$$

We assume a solution for the velocity potential $\phi(r, z, t)$, which satisfies Laplace's equation:

$$\phi = \frac{\zeta_a g}{\omega} \frac{\cosh(k(h+z))}{\cosh(kh)} \sin(k_x x + k_y y - \omega t). \quad (\text{F.65})$$

with $k^2 = k_x^2 + k_y^2$. Taking the derivative of ϕ with respect to z and evaluating at $z = 0$:

$$\frac{\partial \phi}{\partial z} \Big|_{z=0} = \frac{\zeta_a g}{\omega} \frac{k \sinh(kh)}{\cosh(kh)} \sin(k_x x + k_y y - \omega t). \quad (\text{F.66})$$

Thus, the kinematic boundary condition becomes:

$$\frac{\partial \zeta}{\partial t} = \frac{\zeta_a}{\omega} \frac{k \sinh(kh)}{\cosh(kh)} \sin(k_x x + k_y y - \omega t). \quad (\text{F.67})$$

To find the expression for ζ , we integrate with respect to time t :

$$\zeta(r, t) = \int \frac{\zeta_a g}{\omega} \frac{k \sinh(kh)}{\cosh(kh)} \sin(k_x x + k_y y - \omega t) dt. \quad (\text{F.68})$$

This integration gives:

$$\zeta(r, t) = -\frac{\zeta_a g}{\omega^2} \frac{k \sinh(kh)}{\cosh(kh)} \cos(k_x x + k_y y - \omega t) + f(r), \quad (\text{F.69})$$

where $f(r)$ is an arbitrary function of the spatial coordinates r representing the initial condition. To satisfy the initial condition $\zeta(r, t = 0) = 0$, we set $f(r) = 0$. Thus, the displacement becomes:

$$\zeta(r, t) = -\frac{\zeta_a g}{\omega^2} \frac{k \sinh(kh)}{\cosh(kh)} \cos(k_x x + k_y y - \omega t). \quad (\text{F.70})$$

Pressure acting on the beam The fluid pressure $P(r, t)$ acting on the beam can be determined using the dynamic boundary condition. From the linearized Bernoulli equation:

$$\frac{\partial \phi}{\partial t} + \frac{P_0}{\rho} + gz = \frac{(P + P_0)}{\rho}, \quad (\text{F.71})$$

where P_0 is the ambient pressure, ρ is the fluid density, and g is the acceleration due to gravity. Solving for P , we find:

$$P = \rho \frac{\partial \phi}{\partial t} \Big|_{z=0} + \rho g \zeta. \quad (\text{F.72})$$

First, calculate the time derivative of ϕ :

$$\frac{\partial \phi}{\partial t} = -\frac{\zeta_a g \cosh(k(h+z))}{\omega \cosh(kh)} \omega \cos(k_x x + k_y y - \omega t). \quad (\text{F.73})$$

Evaluating at $z = 0$, this becomes:

$$\frac{\partial \phi}{\partial t} \Big|_{z=0} = -\zeta_a g \cos(k_x x + k_y y - \omega t). \quad (\text{F.74})$$

Substituting this result and the expression for $\zeta(r, t)$ into the pressure equation, gives:

$$P = \rho (-\zeta_a g \cos(k_x x + k_y y - \omega t)) + \rho g \left(-\frac{\zeta_a g}{\omega^2} \frac{k \sinh(kh)}{\cosh(kh)} \cos(k_x x + k_y y - \omega t) \right). \quad (\text{F.75})$$

Simplifying the terms:

$$P = -\rho g \zeta_a \cos(k_x x + k_y y - \omega t) - \rho g \frac{\zeta_a g}{\omega^2} \frac{k \sinh(kh)}{\cosh(kh)} \cos(k_x x + k_y y - \omega t). \quad (\text{F.76})$$

F.3.2. Dispersion relation

We now calculate the terms in the Föppl–von Kármán plate equation F.63 and derive the dispersion relation.

Bending term: $B \nabla_r^4 \zeta$ The fourth derivative of ζ in the horizontal plane is:

$$\nabla_r^4 \zeta = \frac{\partial^4 \zeta}{\partial x^4} + \frac{\partial^4 \zeta}{\partial y^4}. \quad (\text{F.77})$$

The fourth spatial derivatives of ζ with respect to x and y are:

$$\frac{\partial^4 \zeta}{\partial x^4} = -\frac{\zeta_a g}{\omega^2} k_x^4 \frac{k \sinh(kh)}{\cosh(kh)} \cos(k_x x + k_y y - \omega t) \quad (\text{F.78})$$

$$\frac{\partial^4 \zeta}{\partial y^4} = -\frac{\zeta_a g}{\omega^2} k_y^4 \frac{k \sinh(kh)}{\cosh(kh)} \cos(k_x x + k_y y - \omega t) \quad (\text{F.79})$$

Combining these results gives

$$\nabla_r^4 \zeta = -\frac{\zeta_a g}{\omega^2} \frac{k \sinh(kh)}{\cosh(kh)} \cos(k_x x + k_y y - \omega t) (k_x^4 + k_y^4) \quad (\text{F.80})$$

Assuming $k^2 = k_x^2 + k_y^2$, the bending term becomes:

$$B \nabla_r^4 \zeta = -B k^5 \frac{\zeta_a g}{\omega^2} \frac{\sinh(kh)}{\cosh(kh)} \cos(k_x x + k_y y - \omega t). \quad (\text{F.81})$$

Stress term: $-\nabla_r \cdot (\sigma_{ij} \cdot \nabla_r \zeta)$ The stress σ_{ij} tensor has a general form:

$$\sigma_{ij} = \begin{pmatrix} \sigma_{xx} & \sigma_{xy} \\ \sigma_{xy} & \sigma_{yy} \end{pmatrix}. \quad (\text{F.82})$$

First, compute the gradient of ζ :

$$\nabla_r \zeta = \begin{pmatrix} \frac{\partial \zeta}{\partial x} \\ \frac{\partial \zeta}{\partial y} \end{pmatrix}. \quad (\text{F.83})$$

Next, apply the stress tensor to the gradient:

$$\sigma_{ij} \cdot \nabla_r \zeta = \begin{pmatrix} \sigma_{xx} & \sigma_{xy} \\ \sigma_{xy} & \sigma_{yy} \end{pmatrix} \cdot \begin{pmatrix} \frac{\partial \zeta}{\partial x} \\ \frac{\partial \zeta}{\partial y} \end{pmatrix} = \begin{pmatrix} \sigma_{xx} \frac{\partial \zeta}{\partial x} + \sigma_{xy} \frac{\partial \zeta}{\partial y} \\ \sigma_{xy} \frac{\partial \zeta}{\partial x} + \sigma_{yy} \frac{\partial \zeta}{\partial y} \end{pmatrix}. \quad (\text{F.84})$$

Now, take the divergence of this vector:

$$\nabla_r \cdot (\sigma_{ij} \cdot \nabla_r \zeta) = \frac{\partial}{\partial x} \left(\sigma_{xx} \frac{\partial \zeta}{\partial x} + \sigma_{xy} \frac{\partial \zeta}{\partial y} \right) + \frac{\partial}{\partial y} \left(\sigma_{xy} \frac{\partial \zeta}{\partial x} + \sigma_{yy} \frac{\partial \zeta}{\partial y} \right). \quad (\text{F.85})$$

Expanding the derivatives:

$$\nabla_r \cdot (\sigma_{ij} \cdot \nabla_r \zeta) = \sigma_{xx} \frac{\partial^2 \zeta}{\partial x^2} + \sigma_{xy} \frac{\partial^2 \zeta}{\partial x \partial y} + \sigma_{xy} \frac{\partial^2 \zeta}{\partial y \partial x} + \sigma_{yy} \frac{\partial^2 \zeta}{\partial y^2}. \quad (\text{F.86})$$

Since the mixed derivatives are equal, we combine them:

$$\nabla_r \cdot (\sigma_{ij} \cdot \nabla_r \zeta) = \sigma_{xx} \frac{\partial^2 \zeta}{\partial x^2} + 2\sigma_{xy} \frac{\partial^2 \zeta}{\partial x \partial y} + \sigma_{yy} \frac{\partial^2 \zeta}{\partial y^2}. \quad (\text{F.87})$$

Thus, the stress term is:

$$-\nabla_r \cdot (\sigma_{ij} \cdot \nabla_r \zeta) = - \left(\sigma_{xx} \frac{\partial^2 \zeta}{\partial x^2} + 2\sigma_{xy} \frac{\partial^2 \zeta}{\partial x \partial y} + \sigma_{yy} \frac{\partial^2 \zeta}{\partial y^2} \right). \quad (\text{F.88})$$

The second spatial derivatives of $\zeta(r, t)$ are:

$$\frac{\partial^2 \zeta}{\partial x^2} = \frac{\zeta_a g}{\omega^2} k_x^2 \frac{k \sinh(kh)}{\cosh(kh)} \cos(k_x x + k_y y - \omega t) \quad (\text{F.89})$$

$$\frac{\partial^2 \zeta}{\partial x \partial y} = \frac{\zeta_a g}{\omega^2} k_x k_y \frac{k \sinh(kh)}{\cosh(kh)} \cos(k_x x + k_y y - \omega t) \quad (\text{F.90})$$

$$\frac{\partial^2 \zeta}{\partial y^2} = \frac{\zeta_a g}{\omega^2} k_y^2 \frac{k \sinh(kh)}{\cosh(kh)} \cos(k_x x + k_y y - \omega t) \quad (\text{F.91})$$

leaving us with a stress term

$$\begin{aligned} -\nabla_r \cdot (\sigma_{ij} \cdot \nabla_r \zeta) = & - \left(\sigma_{xx} \frac{\zeta_a g}{\omega^2} k_x^2 \frac{k \sinh(kh)}{\cosh(kh)} \cos(k_x x + k_y y - \omega t) \right. \\ & + 2\sigma_{xy} \frac{\zeta_a g}{\omega^2} k_x k_y \frac{k \sinh(kh)}{\cosh(kh)} \cos(k_x x + k_y y - \omega t) \\ & \left. + \sigma_{yy} \frac{\zeta_a g}{\omega^2} k_y^2 \frac{k \sinh(kh)}{\cosh(kh)} \cos(k_x x + k_y y - \omega t) \right) \end{aligned} \quad (\text{F.92})$$

$$-\nabla_r \cdot (\sigma_{ij} \cdot \nabla_r \zeta) = - \frac{\zeta_a g}{\omega^2} \frac{k \sinh(kh)}{\cosh(kh)} \cos(k_x x + k_y y - \omega t) \left(\sigma_{xx} k_x^2 + 2\sigma_{xy} k_x k_y + \sigma_{yy} k_y^2 \right). \quad (\text{F.93})$$

Inertia term: $\rho_e h \frac{\partial^2 \zeta}{\partial t^2}$ The second time derivative of ζ is:

$$\frac{\partial^2 \zeta}{\partial t^2} = -\frac{\zeta_a g}{\omega^2} \frac{k \sinh(kh)}{\cosh(kh)} \omega^2 \cos(k_x x + k_y y - \omega t). \quad (\text{F.94})$$

Thus, the inertia term becomes:

$$\rho_e h \frac{\partial^2 \zeta}{\partial t^2} = -\rho_e h \zeta_a g k \frac{\sinh(kh)}{\cosh(kh)} \cos(k_x x + k_y y - \omega t). \quad (\text{F.95})$$

But, as explained in the assumptions, this term will be omitted.

Pressure term: P The external pressure P acting on the beam is:

$$P = -\left(\rho g \zeta_a + \rho g \frac{\zeta_a g}{\omega^2} \frac{k \sinh(kh)}{\cosh(kh)} \right) \cos(k_x x + k_y y - \omega t). \quad (\text{F.96})$$

Substituting the bending, inertia, and pressure terms into the Föppl–von Kármán plate equation F.63:

$$\begin{aligned} & -Bk^5 \frac{\zeta_a g}{\omega^2} \frac{\sinh(kh)}{\cosh(kh)} \cos(k_x x + k_y y - \omega t) \\ & -\frac{\zeta_a g}{\omega^2} \frac{k \sinh(kh)}{\cosh(kh)} \cos(k_x x + k_y y - \omega t) (\sigma_{xx} k_x^2 + 2\sigma_{xy} k_x k_y + \sigma_{yy} k_y^2). \end{aligned} \quad (\text{F.97})$$

$$= -\left(\rho g \zeta_a + \rho g \frac{\zeta_a g}{\omega^2} \frac{k \sinh(kh)}{\cosh(kh)} \right) \cos(k_x x + k_y y - \omega t)$$

Simplifying, multiplying each term with ω^2 , and dividing each term by g , ζ_a , $\cos(k_x x + k_y y - \omega t)$ gives

$$-Bk^5 \frac{\sinh(kh)}{\cosh(kh)} - \frac{k \sinh(kh)}{\cosh(kh)} (\sigma_{xx} k_x^2 + 2\sigma_{xy} k_x k_y + \sigma_{yy} k_y^2) = -\left(\rho \omega^2 + \rho g k \frac{\sinh(kh)}{\cosh(kh)} \right). \quad (\text{F.98})$$

Further simplifying results to

$$-Bk^5 \tanh(kh) - k \tanh(kh) (\sigma_{xx} k_x^2 + 2\sigma_{xy} k_x k_y + \sigma_{yy} k_y^2) - \rho g k \tanh(kh) = -\rho \omega^2. \quad (\text{F.99})$$

even further simplifying to

$$\omega^2 = \left(\frac{Bk^5}{\rho} + \frac{k (\sigma_{xx} k_x^2 + 2\sigma_{xy} k_x k_y + \sigma_{yy} k_y^2)}{\rho} + gk \right) \tanh(kh). \quad (\text{F.100})$$

F.3.3. Special cases

Wave propagating along the x-Axis ($k_y = 0$): When the wave propagates only along the x -axis, the wave vector in the y -direction, k_y , is zero. In this case, the stress terms involving k_x and k_y simplify, and the dispersion relation becomes:

$$\omega^2 = \left(\frac{Bk^5}{\rho} + \frac{\sigma_{xx} k_x^3}{\rho} + gk \right) \tanh(kh). \quad (\text{F.101})$$

This represents the frequency of the wave propagation along the x -axis and corresponds to the formulation that was derived earlier.

Isotropic Stress Behavior: $\sigma_{xy} = 0$ and $\sigma_{xx} = \sigma_{yy} = \sigma$ When the shear stress σ_{xy} is zero and the normal stresses in the x - and y -directions are equal, the material exhibits isotropic stress behavior. In this case, the normal stresses are identical in both directions, leading to a symmetric distribution of stress. This simplification implies that the wave propagation is influenced equally by the normal stress in both the x - and y -directions. The equation becomes:

$$\omega^2 = \left(\frac{Bk^5}{\rho} + \frac{\sigma k^3}{\rho} + gk \right) \tanh(kh). \quad (\text{F.102})$$



Device and Material Specifications

Table G.1: Overview of equipment and materials used

Item	Manufacturer	Model	Appendix Ref.
Function generator	NF Electronic Instruments	1930A	G.1
Frequency divider	–	Custom (0–10 kHz, 8–10 V in)	–
DC power supply	Tenma	72-10480 (0–30 V, 3 A)	G.2
Vibration exciter	Brüel & Kjær	Type 4808	G.3
Power amplifier	Brüel & Kjær	Type 2719	G.4
Camera	Basler	aoA1920-150 µm	–
Camera lens	Nikon	AF-S NIKKOR 24–85 mm f/3.5–4.5G ED VR	–
Laser distance sensor	Micro-Epsilon	optoNCDT ILD 1420-200	G.5
DAQ interface	National Instruments	USB-6211	-
ICP signal conditioner	PCB Piezotronics	Model 482B11	G.6
Silicone oil	Silicones and More	5 cSt	G.7
Deionized water	Sigma-Aldrich	8.48333	-
ELASTOSIL® Film 2030	Wacker Chemie (AG)	20, 50, 100, 200 µm thickness	G.8

G.1. Function generator NF Electronics Instruments 1930A

1.4 Rating

1.4.1 Electrical Rating

Waveform	\sim , \wedge , \sqcap , \nearrow , \searrow , DC only					
Oscillation mode	Continuous (CONT)	Continuous oscillation				
	Burst (BURST)	N wave oscillation by trigger signal (N: integer) N = 1 to 65536				
	Gate (GATE)	Integer wave oscillation by trigger signal				
Frequency	Waveforms and frequency ranges	\sim , \sqcap (Duty factor is fixed to 50%)		0.1mHz to 1.2 MHz		
		\wedge , \nearrow , \searrow , \sqcap (Duty factor is variable from 5 to 95%)		0.1mHz to 100kHz		
	Display	Max. 11 digits, Resolution 0.1 mHz (constant)				
	Accuracy	$\pm 5 \times 10^{-6}$ (± 5 ppm)				
	Stability	$\pm 2 \times 10^{-6}$ /Year (± 2 ppm/Year)				
	Setting in terms of cycle period	Setting range	840ns to 10000s			
		Display	Max. 6 digits, Min. resolution 10ns			
		Oscillated by frequency of reciprocal of setting period (cut away 0.1 mHz or less.)				
Output characteristics (Function output)	Max. output	AC only	30Vp-p/Open, 15Vp-p/50 Ω			
		DC only	± 15 V/open, ± 7.5 V/50 Ω			
	Display (Open value)	Output range mode: Auto (AUTO)				
		AC	Vp-p	Max. 3 digits	Min. resolution	0.01mVp-p
			Vrms			0.01mVrms
			dBV			0.1dBV (Constant)
				Max. 3 digits + minus sign		
		DC		Max. 3 digits + minus sign, Min. resolution 0.01mV		
		Output range mode: Fixed (FXD)				
		AC (Vp-p only)		Max. 4 digits, Min. resolution 10mVp-p (Constant)		
	DC		Max. 4 digits + minus sign Min. resolution 10mV (Constant)			

G.2. DC power supply Tenma 72-10480 (0–30 V, 3 A)

Single Bench DC Power Supply **TENMA**TM



Features:

- Complete digital control
- 10mV / 1mA resolution
- Low noise and ripple
- CV / CC constant voltage and constant current mode
- OCP and OVP settings, constant protection mode
- 5 sets of parameters can be stored and recalled
- Output switch control
- Power-off memory function
- Keyboard lock function

Specifications:

Voltage Range / Current Range	0 - 30V / 0 - 3A
Load Regulation	Voltage : $\leq 0.01\%$ +2mV / Current : $\leq 0.1\%$ +5mA
Line Regulation	Voltage : $\leq 0.01\%$ +3mV / Current : $\leq 0.1\%$ +3mA
Setup Resolution	Voltage : 10mV / Current : 1mA
Setup Accuracy (25°C $\pm 5^\circ\text{C}$)	Voltage : $\leq 0.5\%$ +20mV / Current : $\leq 0.5\%$ +5mA
Ripple (20Hz - 20MHz)	Voltage : $\leq 1\text{mVrms}$ / Current : $\leq 3\text{mA}_{\text{rms}}$
Temp. Coefficient	Voltage : $\leq 100\text{ppm}$ +10mV / Current : $\leq 100\text{ppm}$ +5mA
Read Back Accuracy	Voltage : 10mV / Current : 1mA
Read Back Temp. Coefficient	Voltage : $\leq 100\text{ppm}$ +10mV / Current : $\leq 100\text{ppm}$ +5mA
Reaction Time (10% Rated load)	Voltage : $\leq 100\text{mS}$ / Current : $\leq 100\text{mS}$
Operation Environment	Indoor use Altitude : $\leq 2,000\text{m}$ Ambient temperature : $0^\circ\text{C} \sim 40^\circ\text{C}$ Relative humidity : $\leq 80\%$
Weight and Dimension	3.5kg / 110mm(W) \times 156mm(H) \times 260mm(D)
Storage Environment	Ambient temperature : -10°C to $+70^\circ\text{C}$ Relative humidity : $\leq 70\%$
Accessories	User manual, UK Power cord (1.2m), Euro Power cord (1.2m)

Note: Input Voltage : 230V $\pm 10\%$

Part Number Table

Description	Part Number
DC Power Supply, Bench, Single, 3A, 30V	72-10480

Important Notice : This data sheet and its contents (the "Information") belong to the members of the Premier Farnell group of companies (the "Group") or are licensed to it. No licence is granted for the use of it other than for information purposes in connection with the products to which it relates. No licence of any intellectual property rights is granted. The Information is subject to change without notice and replaces all data sheets previously supplied. The Information supplied is believed to be accurate but the Group assumes no responsibility for its accuracy or completeness, any error in or omission from it or for any use made of it. Users of this data sheet should check for themselves the Information and the suitability of the products for their purpose and not make any assumptions based on information included or omitted. Liability for loss or damage resulting from any reliance on the Information or use of it (including liability resulting from negligence or where the Group was aware of the possibility of such loss or damage arising) is excluded. This will not operate to limit or restrict the Group's liability for death or personal injury resulting from its negligence. Tenma is the registered trademark of the Group. © Premier Farnell Limited 2016.

G.3. Vibration exciter Brüel & Kjær Type 4808

BRÜEL & KJÆR® Modal and Measurement Exciters

Vibration Exciter Type 4808

Uses

- General vibration testing
- Mechanical impedance and mobility measurements
- Experimental modal analysis
- Accelerometer calibration

Features

- Force rating: 112 N (25 lbf) sine peak, 187 N (42 lbf) with cooling
- Frequency range: 5 Hz to 10 kHz
- First axial resonance frequency: 10 kHz
- Maximum displacement: 12.7 mm (0.5 in) peak-to-peak with over-travel stops
- Maximum bare table acceleration: 700 m/s² (71 g)
- Rugged construction
- Robust rectilinear guidance system
- Low cross motion and low distortion
- Highly damped axial, transverse and flexural resonances
- Replaceable inserts for moving element protection
- Optimized performance using Power Amplifier Type 2719
- High-quality cable with 4-pin Neutrik® speakON® connectors included for connection to Type 2719

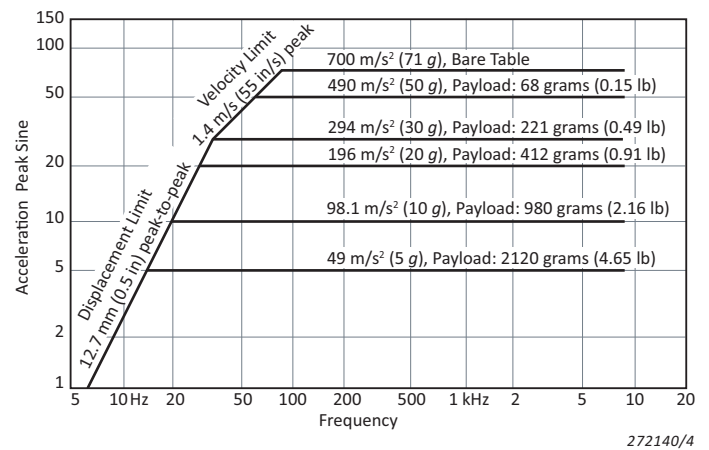


Description

Vibration Exciter Type 4808 is a high-quality, compact exciter with a permanent magnetic field. It is designed for long, trouble-free operation and has a force rating of 112 N (25 lbf), enabling relatively heavy loads to be excited to high g levels. Power Amplifier Type 2719 (180 VA) has been designed specifically to drive Type 4808, but Type 4808 can also be driven by any amplifier up to a maximum input current of 15 A RMS without assisted cooling.

The moving element is supported by a robust rectilinear guidance system consisting of grouped radial and transverse flexures in a unique construction. The flexures are made from a bonded sandwich of spring steel and a damping elastomer, providing a clean acceleration waveform with low cross motion and low distortion characteristics.

Fig. 1 Sine performance curves for Vibration Exciter Type 4808 for operation without assisted cooling



COMPLIANCE WITH STANDARDS



The CE marking is the manufacturer's declaration that the product meets the requirements of the applicable EU directives



RCM mark indicates compliance with applicable ACMA technical standards – that is, for telecommunications, radio communications, EMC and EME



China RoHS mark indicates compliance with administrative measures on the control of pollution caused by electronic information products according to the Ministry of Information Industries of the People's Republic of China



WEEE mark indicates compliance with the EU WEEE Directive

Temperature: According to IEC 60068–2–1 & IEC 60068–2–2

Operating Temperature: 5 to 40 °C (41 to 104 °F)

Storage Temperature: –25 to +70 °C (–13 to +158 °F)

Humidity: According to IEC 60068–2–3

Damp Heat: 93% RH (non-condensing at 40 °C (104 °F))

SPECIFICATIONS

Rated Force:

• Without assisted air cooling: 112 N (25 lbf) sine peak

• With assisted air cooling: 187 N (42 lbf) sine peak

Frequency Range: 5 Hz to 10 kHz bare table

Axial Resonant Frequency: 10 kHz bare table

Max. Bare Table Acceleration: 700 m/s² (71 g)

Max. Displacement: 12.7 mm (0.5 in) peak-to-peak

Max. Velocity: 1.4 m/s (55 in/s)

Dynamic Weight of Moving Element: 160 grams (0.35 lb)

Static Flexure Stiffness: 5.6 N/mm (32 lbf/in)

Maximum Input Current: 15 A RMS (with assisted air cooling 25 A RMS)

Current-to-Force Ratio:

• Coils in Parallel: approximately 0.16 A/F (sine peak)

• Coils in Series: approximately 0.08 A/F (sine peak)

Stray Magnetic Field:

• 20×10^{-3} Tesla at table face

• 8×10^{-3} Tesla at 12.7 mm (0.5 in) above table face

Coil Impedance: Approximately 0.8 Ω at 500 Hz with bare table and coils in parallel

Table Diameter: 62.5 mm (2.45 in)

Fastening Thread: 5 × 5/16" – 18 UNC for M5 and 10–32 UNF inserts. 1 central insert plus 4 equi-spaced on circle of \varnothing 50.8 mm

WEIGHT AND DIMENSIONS

Weight: 35 kg (77.1 lb)

Diameter: 215 mm (8.46 in)

Height: 200 mm (7.87 in)

Type 4808 Vibration Exciter

Includes the following accessories:

- AQ-0649-D-050: Cable with two 4-pin Neutrik speakON connectors, length 5 m (16.4 ft), for connection to Type 2719
- 10 × YS-0810: Thread inserts (M5)
- 10 × YS-0811: Thread inserts (10–32 UNF)
- 1 × QA-0061: Insert Mounting Tool
- 2 × YM-2002: Blanking Plugs

Optional Accessories

TRUNNION

WA-0309 Trunnion

POWER AMPLIFIER

Type 2719 Power Amplifier (180 VA)

STINGERS

Note: Other stingers are available, please ask your sales representative.

WZ-0066

Nylon Stinger Kit

- 10 × stingers, length 50 mm
- 10 × stingers, length 120 mm

UA-1596

Five 2.5 mm Push/Pull Steel Stingers, including:

- 10 × adaptors, diameter 2.5 mm to 10–32 UNF
- 5 × steel rods, length 200 mm, diameter 2.5 mm
- 10 × fastening screws

UA-1597

Five 3.0 mm Push/Pull Steel Stingers, including:

- 10 × adaptors, diameter 3.0 mm to 10–32 UNF
- 5 × steel rods, length 200 mm, diameter 3.0 mm
- 10 × fastening screws

FORCE TRANSDUCERS AND IMPEDANCE HEAD

Type 8230 CCLD Force Transducer (+44/–44 N range)

Type 8230-001 CCLD Force Transducer (+220/–220 N range)

Type 8230-002 CCLD Force Transducer (+2200/–2200 N range)

Type 8230-003 CCLD Force Transducer (+22000/–2200 N range)

Type 8230-C-003 Charge Force Transducer (+22200/–2200 N range)

Type 8231-C Charge Force Transducer (+110000/–2200 N range)

Type 8001 Impedance Head

STUD AND BUSHING ADAPTORS

UA-0125 Mounting Equipment (including isolated studs YP-0150 and non-isolated studs YQ-2960)

UA-2052 Set of 10 Stud Adaptors, 10–32 UNF to ¼"–28 UNF

UA-2054 Set of 20 Bushing Adaptors, 10–32 UNF to ¼"–28 UNF

CABLES

AQ-0649

Cable with two 4-pin Neutrik speakON connectors, available in different lengths from 5 m (16.4 ft) to 40 m (131.2 ft)



Skodsborgvej 307 · DK-2850 Nærum · Denmark
Telephone: +45 77 41 20 00 · Fax: +45 45 80 14 05
www.bksv.com · info@hbkworl.com
Local representatives and service organizations worldwide

To learn more about all HBK offerings, please visit hbkworl.com

Although reasonable care has been taken to ensure the information in this document is accurate, nothing herein can be construed to imply representation or warranty as to its accuracy, currency or completeness, nor is it intended to form the basis of any contract. Content is subject to change without notice – contact HBK for the latest version of this document.

Brüel & Kjær and all other trademarks, service marks, trade names, logos and product names are the property of Hottinger Brüel & Kjær A/S or a third-party company.

G.4. Power amplifier Brüel & Kjær Type 2719

BRÜEL & KJÆR® Power Amplifiers

Power Amplifier Type 2719

Power Amplifier Type 2719 has been designed to drive small vibration exciters, particularly Vibration Exciter Type 4808, which has a force rating of 112 N (25 lbf) sine peak, and Vibration Exciter Type 4809, which has a force rating of 45 N (10 lbf) sine peak.

Type 2719 provides a flat frequency response and low harmonic distortion over a wide frequency range and has extensive control and monitoring capabilities.

The power amplifier can operate in voltage or current mode with low and high output impedance, respectively.

Uses

- Drives Vibration Exciter Type 4808
- Drives Vibration Exciter Type 4809 safely to full rating
- General purpose power amplifier for small vibration exciters requiring up to 180 VA in 0.8 Ω

Features

- 180 VA power output capacity in 0.8 Ω
- Adjustable RMS output-current limit



- Low or high output impedance (voltage/current mode)
- Low distortion over wide frequency range
- Extensive built-in protection, including interlock
- LEDs on front panel showing distortion (clipped output signal), temperature overload, current overload, output signal phase (0° or 180°), operating mode (current or voltage), interlock and power status
- Liquid crystal display (LCD) showing output current and voltage
- Monitor output connectors (voltage and current) on back panel

Description

Power Amplifier Type 2719 has a usable frequency range from DC to 100 kHz. The power output capacity is 180 VA into a 0.8 Ω exciter or resistive load, in the frequency range DC to 15 kHz (± 0.5 dB). The maximum voltage gain is 14 dB. The harmonic content of the output is very small as heavy negative feedback is used. The instrument can tolerate temperature and supply-line variations while maintaining excellent stability. Two output modes are selectable via the front panel. The power output stage is directly coupled to the output, and hence to the connected vibration exciter. A current-limiting circuit prevents excessive instantaneous output current peaks. During operation, the voltage, current levels and waveforms can be inspected at the monitor outputs on the back panel or RMS readings can be obtained from the LCD.

Type 2719 consists of an input stage (both AC-coupled and direct), a preamplifier, a power amplifier and various warning and safety circuits with indication lights (LEDs). The LCD shows output current and output voltage. The amplifier can be used as a voltage generator with low output impedance and a flat voltage frequency response, or as a current generator with high output impedance and a flat current frequency response.

Protection

Power Amplifier Type 2719 features extensive protection circuits for itself and the connected vibration exciter. When triggered, the protection circuits disconnect the input signal and light an LED, indicating the reason for instrument shutdown.

Overload protection against excessive coil current is provided by setting the RMS output current between 1 A and 15 A. This feature enables Type 2719 to safely drive vibration exciters with different maximum current ratings. The signal to the exciter is switched off if the preset current limit is exceeded.

The power output stage is protected by a temperature sensing safety device to prevent output transistor temperatures that exceed design limits and lead to transistor failure. When triggered, the temperature protection circuit blocks the amplifier input signal.

Further protection is provided by an interlock relay that disconnects the input if the operator switches between voltage mode and current mode during operation of Type 2719. Resetting is performed by simply turning the amplifier gain control fully anticlockwise. Dedicated LED indicators advise you of the current operating mode and any distortion when excessive signal levels saturate the preamplifier and cause distortion of the output waveform. The instrument remains operative in this condition.

COMPLIANCE WITH STANDARDS



The CE marking is the manufacturer's declaration that the product meets the requirements of the applicable EU directives



RCM mark indicates compliance with applicable ACMA technical standards – that is, for telecommunications, radio communications, EMC and EME



China RoHS mark indicates compliance with administrative measures on the control of pollution caused by electronic information products according to the Ministry of Information Industries of the People's Republic of China



WEEE mark indicates compliance with the EU WEEE Directive

Safety, EMC Emission and Immunity: According to relevant standards:

- EN/IEC 61010–1, ANSI/UL 61010–1
- EN/IEC 61000–6–2
- EN/IEC 61000–6–4
- CISPR32 Class A limit
- FCC Rules Part 15
- EN/IEC 61326

Temperature: According to IEC 60068–2–1 and IEC 60068–2–2

- Operating temperature: +5 to +40 °C (41 to 104 °F)
- Storage temperature: –25 to +70 °C (–13 to 158 °F)

Humidity: According to IEC 60068–2–78, Damp Heat: 93% RH (non-condensing at 40 °C (104 °F))

Mechanical: Non-operating according to:

- IEC 60068–2–6
- IEC 60068–2–27
- IEC 60068–2–29

Reliability: According to MIL–HDBK 217 F, GB (Part-stress)

Enclosure: According to IEC 60529

POWER OUTPUT CAPACITY

- 180 VA into a 0.8 Ω exciter or resistive load, at 25 °C and nominal mains voltage
- 144 VA into a 1 Ω exciter or resistive load, at 40 °C or at 10% above nominal mains voltage

Connector: 4-pin Neutrik® speakON® (back panel)

OUTPUT VOLTAGE CAPACITY

12 V RMS, DC to 15 kHz

OUTPUT CURRENT CAPACITY

7.5 A RMS at or below 5 Hz

15 A RMS, 40 Hz to 10 kHz

12 A RMS at 15 kHz

FREQUENCY RANGE

Full Capacity: 40 Hz to 10 kHz

Reduced Capacity: DC to 100 kHz

FREQUENCY RESPONSE

Typical small signal response in low impedance mode:

- DC Input: DC to 15 kHz ±0.5 dB; DC to 100 kHz ±3 dB
- AC Input: 15 Hz to 15 kHz ±0.5 dB

INPUT IMPEDANCE

>10 kΩ

DC STABILITY

Less than 50 mV drift from 0 V for ±10% variation of mains supply from nominal, and for 10 to 40 °C (50 to 104 °F) variation in ambient temperature

CONTROLS

Power on/off

Continuously variable gain control, 0 to Cal. (14 dB) with integral reset

Continuously variable current limit control 1 to 15 A (RMS)

Switch for voltage mode or current mode operation

Switch for phase inversion (0° or 180°) between input and output

INDICATOR LAMPS (LEDs)

Power on

Distortion

Temperature overload

Current overload

Phase shift (0° or 180°)

Mode (Voltage or Current)

Interlock

MULTIFUNCTION DISPLAY (LCD)

Voltage (RMS) read-out accuracy ±2%

Current (RMS) read-out accuracy ±2%

PROTECTION

Input signal is removed and an indicator lamp is lit when the following parameters exceed preset limits:

- Driver Coil Current – true RMS adjustable limit 1 to 15 A (RMS)
- Power Transistor Temperature
- Heat Sink Temperature
- Output Signal Distortion – no shutdown

OTHER FEATURES

Electronic peak current limiting

MONITOR OUTPUT

Voltage: 0.1 V/V ±2%

Current: 0.1 V/A ±2%

Connectors: 2 separate BNC sockets (back panel)

POWER REQUIREMENTS

Single phase 100, 120, 230 V RMS, ±10%. Approx. 400 VA at full load

Appliance inlet with fuse holder and voltage selector (back panel)

FUSES

100 V or 120 V: T 8 A slow blow

230 V: T 4 A slow blow

DIMENSIONS

Height: 88 mm (3.5 in), equivalent to 2 RU (rack unit)

Width: 482.6 mm (19 in) with flanges for standard 19 inch rack mounting

Depth: 450 mm (17.7 in)

WEIGHT

15.9 kg (35.0 lb)

Ordering Information

Type 2719 **Power Amplifier**

Includes the following:

- Mains cable

OPTIONAL ACCESSORIES

AQ-0649-D-050 Cable, two 4-pin Neutrik speakON connectors, length 5 m (16.4 ft), for driving Vibration Exciter Type 4808 (included with Type 4808)

WL-1325-D-050 Cable, 4-pin Neutrik SpeakON connector to two banana plugs, length 5 m (16.4 ft), for driving Vibration Exciter Type 4809 (included with Type 4809)

Note: Cables are available in different lengths.

Skodsborgvej 307 · DK-2850 Nærum · Denmark
Telephone: +45 77 41 20 00 · Fax: +45 45 80 14 05
www.bksv.com · info@hbkworl.com
Local representatives and service organizations worldwide

To learn more about all HBK offerings, please visit hbkworl.com

Although reasonable care has been taken to ensure the information in this document is accurate, nothing herein can be construed to imply representation or warranty as to its accuracy, currency or completeness, nor is it intended to form the basis of any contract. Content is subject to change without notice – contact HBK for the latest version of this document.

Brüel & Kjær and all other trademarks, service marks, trade names, logos and product names are the property of Hottinger Brüel & Kjær A/S or a third-party company.



G.5. Micro-Epsilon optoNCDT ILD 1420-200 laser distance sensor

3.3 Technical Data ILD1420

Model	ILD1420-10	ILD1420-25	ILD1420-50	ILD1420-100	ILD1420-200	ILD1420-500
Measuring range	10 mm	25 mm	50 mm	100 mm	200 mm	500 mm
Start of measuring range	20 mm	25 mm	35 mm	50 mm	60 mm	100 mm
Mid of measuring range	25 mm	37.5 mm	60 mm	100 mm	160 mm	350 mm
End of measuring range	30 mm	50 mm	85 mm	150 mm	260 mm	600 mm
Measuring rate ¹	6 adjustable stages: 8 kHz / 4 kHz / 2 kHz / 1 kHz / 0.5 kHz / 0.25 kHz					
Linearity ²	≤ ±8 μm	≤ ±20 μm	≤ ±40 μm	≤ ±80 μm	≤ ±160 μm	≤±500 μm ... ≤±1000 μm
	≤ ±0.08 % FSO					≤ ±0,1 ... 0,2 % FSO
Repeatability ³	0.5 μm	1 μm	2 μm	4 μm	8 μm	20 ... 40 μm
Temperature stability ⁴	±0.015 % FSO/K			±0.01 % FSO/K		
Light spot diameter ⁵ (±10 %)	SMR	90 x 120 μm	100 x 140 μm	90 x 120 μm	750 x 1100 μm	
	MMR	45 x 40 μm	120 x 130 μm	230 x 240 μm		
	EMR	140 x 160 μm	390 x 500 μm	630 x 820 μm		
	smallest ø	45 x 40 μm with 24 mm	55 x 50 μm with 31 mm	70 x 65 μm with 42 mm	-	
Light source	Semiconductor laser < 1 mW, 670 nm (red)					
Laser class	Class 2 in accordance with IEC 60825-1: 2014					
Permissible ambient light ⁶	50,000 lx			30,000 lx	10,000 lx	
Supply voltage	11 ... 30 VDC					
Power consumption	< 2 W (24 V)					
Signal input	1 x HTL laser on/off; 1 x HTL multifunction input: trigger in, zero setting, mastering, teach					
Digital interface ⁷	RS422 (16 bit) / EtherCAT / PROFINET / EtherNet/IP					
Analog output ⁸	4 ... 20 mA / 1 ... 5 V with cable PCF1420-3/U (16 bit; freely scalable within the measuring range)					

Functional Principle, Technical Data

Model	ILD1420-10	ILD1420-25	ILD1420-50	ILD1420-100	ILD1420-200	ILD1420-500
Switching output	1 x error output: npn, pnp, push pull					
Connection	integrated cable 3 m, open ends, minimum bending radius 30 mm (fixed installation) or integrated pigtail 0.3 m with 12-pin M12 connector (see accessories for suitable connection cable)					
Mounting	Screw connection via two mounting holes					
Temperature range	Operation	0 ... +50 °C (+32 ... +122 °F) (non-condensing)				
	Storage	-20 ... +70 °C (-4 ... +158 °) (non-condensing)				
Shock (DIN EN 60068-2-27)	15 g / 6 ms in 3 axes, 1000 shocks each					
Vibration (DIN EN 60068-2-6)	20 g / 20 ... 500 Hz in 3 axes, 2 directions and 10 cycles each					
Protection class (DIN EN 60529) ⁹	IP67					
Material	Aluminium housing					
Weight	approx. 60 g (incl. pigtail), approx. 145 g (incl. cable)					
Control and display elements ¹⁰	Select button: zero, teach, factory setting; web interface for setup: selectable presets, peak selection, video signal, freely selectable averaging possibilities, data reduction, setup management; 2 x color LEDs for power/status					

[1] Factory setting 2 kHz, modifying the factory setting requires the IF2001/USB converter (see accessories); for models with laser class 1 the maximum measuring rate is 4 kHz

[2] FSO = Full Scale Output; the specified data apply to white, diffuse reflecting surfaces (Micro-Epsilon reference ceramic for ILD sensors)

[3] Measuring rate 2 kHz, median 9

[4] The specified value is only achieved by mounting on a metallic sensor holder. Good heat dissipation from the sensor to the holder must be ensured.

[5] $\pm 10\%$; SMR = Start of measuring range; MMR = Mid of measuring range; EMR = End of measuring range

[6] Illuminant: light bulb


[7] For EtherCAT, PROFINET and EtherNet/IP, connection via interface module is required (see accessories)

[8] For models with laser class 1 the D/A conversion is done with 12 bit

[9] Models with laser class 1 have the protection class IP65

[10] Access to web interface requires connection to PC via IF2001/USB (see accessories)

G.6. PCB Piezotronics Model 482B11 ICP signal conditioner

Model Number 482B11		LINE POWERED SIGNAL CONDITIONER FOR ICP® SENSORS		Revision: E ECN #: 40512	
Performance		ENGLISH	SI	OPTIONAL VERSIONS	
Channels		1	1	Optional versions have identical specifications and accessories as listed for the standard model except where noted below. More than one option may be used.	
Voltage Gain(± 1 %)		x1 x10 x100	x1 x10 x100		
High Frequency Response(-5 %)(Gain x1)		85 kHz	85 kHz		
High Frequency Response(-5 %)(Gain x10)		85 kHz	85 kHz		
High Frequency Response(-5 %)(Gain x100)		60 kHz	60 kHz		
Fault/Bias Monitor/Meter(meter)		24 VDC FS	24 VDC FS		
Environmental					
Temperature Range		+30 to +130 °F	-1.1 to +54.4 °C		
Electrical					
AC Power(50-400Hz)		105 to 125 VAC	105 to 125 VAC	[1]	
AC Power		0.25 amps	0.25 amps		
Excitation Voltage(To Sensor)		+24 VDC	+24 VDC		
DC Offset(Maximum)		± 30 mV	± 30 mV		
Constant Current Excitation(To Sensor)		2 to 20 mA	2 to 20 mA	[2]	
Discharge Time Constant		3 sec	3 sec		
Spectral Noise(1 Hz)		4.3 µV/√Hz	-107 dB	NOTES: [1] Unit set to 230 VAC when ordered as model F482B11. [2] User adjustable, factory set at 4 mA (± 0.5 mA).	
Spectral Noise(10 Hz)		1.3 µV/√Hz	-118 dB		
Spectral Noise(100 Hz)		0.37 µV/√Hz	-129 dB		
Spectral Noise(1 kHz)		0.16 µV/√Hz	-136 dB		
Spectral Noise(10 kHz)		0.12 µV/√Hz	-138 dB		
Broadband Electrical Noise(1 to 10,000 Hz)(Gain x1)		29 µV	-91 dB		
Spectral Noise(1 Hz)		31 µV/√Hz	-90 dB		
Spectral Noise(10 Hz)		13 µV/√Hz	-98 dB		
Spectral Noise(100 Hz)		3.7 µV/√Hz	-109 dB		
Spectral Noise(1 kHz)		1.8 µV/√Hz	-115 dB		
Spectral Noise(10 kHz)		0.80 µV/√Hz	-122 dB		
Broadband Electrical Noise(1 to 10,000 Hz)(Gain x10)		198 µV	-74 dB		
Spectral Noise(1 Hz)		274 µV/√Hz	-78 dB		
Spectral Noise(10 Hz)		126 µV/√Hz	-88 dB		
Spectral Noise(100 Hz)		39 µV/√Hz	-96 dB		
Spectral Noise(1 kHz)		15 µV/√Hz	-104 dB		
Spectral Noise(10 kHz)		6.6 µV/√Hz	-113 dB		
Broadband Electrical Noise(1 to 10,000 Hz)(Gain x100)		2.2 mV	-71 dB		
Physical				SUPPLIED ACCESSORIES: Model 017AXX Power Cord (1)	
Electrical Connector(Input, sensor)		BNC Jack	BNC Jack		
Electrical Connector(Output)		BNC Jack	BNC Jack		
Size (Height x Width x Depth)		4.3 in x 1.8 in x 6.0 in	109.2 mm x 45.7 mm x 152.4 mm		
Weight		2 lb	907.2 gm		
All specifications are at room temperature unless otherwise specified. In the interest of constant product improvement, we reserve the right to change specifications without notice. ICP® is a registered trademark of PCB Group, Inc.					
<div><div><div>Phone: 716-684-0001 Fax: 716-684-0987 E-Mail: info@pcb.com</div></div></div>					

G.7. Silicone oil 5 cSt

TDS - Silicone Oil

Description

Silicone oils are polydimethylsiloxanes available in different viscosities.

Application

- Release agent.
Used purely or as a part of a compounded formula **Silicone Oil** provides a non-toxic, non-carbonising mould release for rubber, plastics and metal die-castings.
- Anti-foam agent.
Very small quantities of the fluid are very effective as a foam control agent, especially in non aqueous systems.
- Mechanical fluid.
The very high viscosity-index, the thermal and chemical stability, shear-breakdown resistance and the rubber compatibility as well as the compressibility make this fluid outstanding for mechanical and hydraulic uses.
- Lubricant.
The fluid provides excellent lubricating properties for most plastic and elastomeric surfaces.
Lubricity with metals depends upon the possible combinations such as P.T.F.E., MoS₂ and other lubricity improvers.
- In polishes and chemical specialties.
Silicone oil is used in most automobile and furniture polishes for its ease of application, high gloss with a minimum rubbing and durable water repellent film.
- In electrical and electronic equipment. Because of the excellent dielectric properties silicone oil is widely used as an insulating and damping fluid.

Features

- Little change in physical properties over a wide temperature range.
- The fluids are thermally stable at 150°C for extended time intervals.
- Excellent water repellency.
- Low surface tension. The fluid readily wets clean surfaces to impart water repellency and release characteristics.
- Low toxicity.

Benefits

- Good foam builder
- Imparts soft silky feel to the hair
- Ensures smooth wet shaving foams
- Nonirritant to skin

Warranty: The information given in this product data sheet are believed to be fully accurate. However, Nedform BV shall not be liable for its content and make no warranty with respect thereto. For additional information we request you to contact Nedform BV visit our web-site: www.nedform.com



Moulding and Casting Solutions

Typical Data

Viscosity, Cst	Flashpoint, °C COC	Freezing point, °C	Specific gravity, 25 °C	Surface tension, mN/m	Refrac. index at 25 °C
0,65	-4	-67	0,760	15,9	1,375
1	40	-85	0,816	17,4	1,382
2	48	-90	0,830	18,1	1,387
3	62	-100	0,900	18,9	1,392
5	136	-65	0,910	19,7	1,397
10	162	-65	0,930	20,1	1,399
20	230	-60	0,950	20,6	1,400
50	280	-55	0,959	20,7	1,402
100	>300	-55	0,965	20,9	1,403
200	>300	-50	0,970	21,0	1,403
300	>300	-50	0,970	21,1	1,403
350	>300	-50	0,970	21,1	1,403
500	>300	-50	0,970	21,1	1,403
1000	>300	-50	0,970	21,2	1,403
5000	>300	-50	0,975	21,4	1,403
10000	>300	-50	0,975	21,5	1,403
12500	>300	-50	0,975	21,5	1,403
30000	>320	-50	0,975	21,5	1,403
60000	>300	-50	0,975	21,5	1,403
100000	>300	-50	0,976	21,5	1,404
300000	>300	-45	0,976	21,5	1,404
500000	>300	-40	0,976	21,5	1,404

Shelf life and storage

ATTENTION: Before handling, read product information, Product Safety Data Sheets and container labels for safe use, and any physical and/or health hazard information.

G.8. ELASTOSIL® Film 2030

ULTRATHIN SILICONE FILM FOR HIGH-PRECISION SOLUTIONS

A New Product Form for Silicone Elastomers

ELASTOSIL® Film from WACKER is an ultrathin, high-precision film of crosslinked silicone rubber that is available in various layer thicknesses from 20 µm to > 400 µm and is manufactured under clean-room conditions entirely without solvents. The unique patent-registered manufacturing process produces immaculate, high-precision silicone film with a defined thickness that is impossible by other production processes. The maximum thickness variation across the film width is ±5%. This precision, combined with the proven properties of silicone rubber opens up potential applications that were hardly conceivable until now, and could certainly not be realized on an industrial scale.

ELASTOSIL® Film is especially impressive for its durability. Its outstanding dielectric properties, Young's modulus and rebound resilience remain constant over a wide range of temperatures and frequencies, as well as over millions of load cycles. Moreover, ELASTOSIL® Film is chemically inert and suitable for food contact. Like all silicone elastomers, ELASTOSIL® Film is characterized by selective permeability for gases and water vapor.

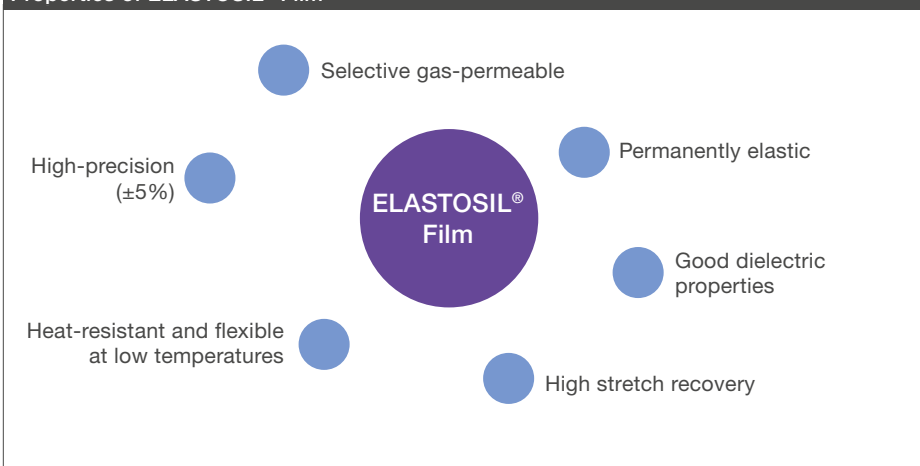
Diverse Applications

ELASTOSIL® Film is ideal for use as a dielectric precision layer in innovative, future-oriented electronics applications: so-called EAPs (electroactive polymers), especially in:

- Actuator technology ("artificial muscles")
- Electricity generation ("energy harvesting")
- Smart sensors

With its typical silicone properties, ELASTOSIL® Film can also be used in food packaging, technical textiles and an extremely wide variety of industrial applications.

Properties of ELASTOSIL® Film



For applications in the medical sector and for wound dressing, ask about our biocompatible SILPURAN® Film.

Form of Delivery and Processing

ELASTOSIL® Film

- Produced under cleanroom conditions, currently on a pilot scale, at a width of 250 mm
- Available as sheet or roll stock on a support film, from which it can be easily stripped off for further processing
- Can be processed by conventional die-cutting or laser techniques
- Can be permanently and reliably bonded using silicone adhesive. Different grades are available for different applications. Ask us, and we will recommend one that is optimum for your application.

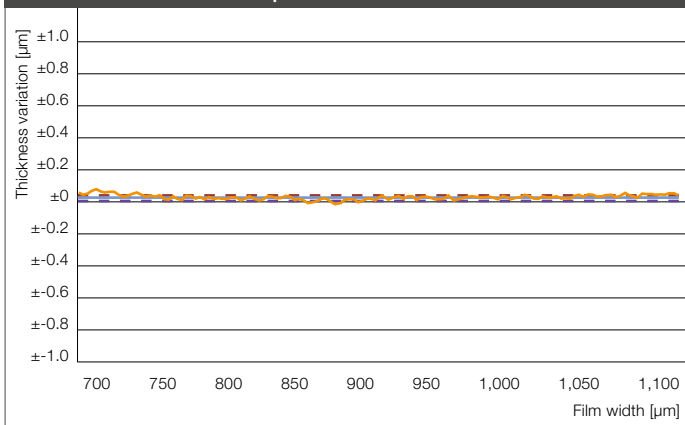
ELASTOSIL® Film 2030 Product Data

Starting material	Addition-curing silicone rubber
Layer thickness	20 µm – 400 µm
Shore A (DIN ISO 7619-1)	27
Elongation at break (ISO 527-3)	450%
Tear strength (ASTM D624 B)	10 N/mm
Glass transition temperature (Tg)	-126 °C
Operating range	-45 °C to 200 °C
Gas permeability (selectivity)	CO ₂ /N ₂ 10:1
Water vapor permeability (JIS 1099 A1)	3,000 g/m ² /24 h at 20 µm 1,200 g/m ² /24 h at 50 µm 800 g/m ² /24 h at 100 µm
Compression set, 22 h, 100 °C (ISO 815-B)	5%
Permittivity ε _r	2.8
Dielectric strength (VDE 0303)	80 – 100 V/µm
Volume resistivity (IEC 60093)	10 ¹⁴ Ω·cm
Suitable for food contact (BfR/FDA) ¹	Yes

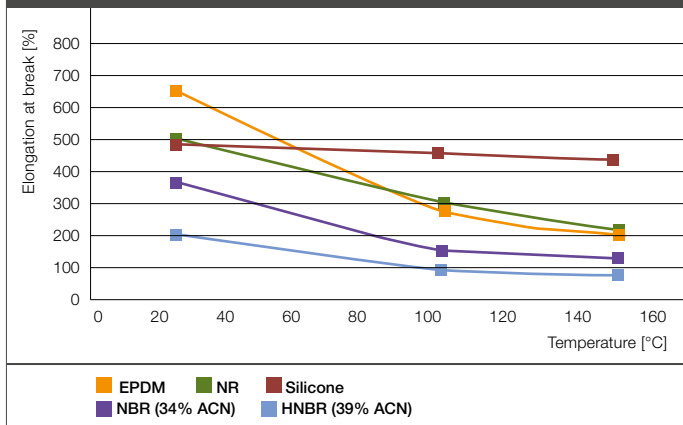
¹ BfR recommendation:
„XV. Silicones“ / FDA CFR 21 § 177.2600
„Rubber articles intended f. repeated use“

These figures are only intended as a guide and should not be used in preparing specifications.

Surface Precision of a 20 µm Thick ELASTOSIL® Film



Heat Resistance of Various Elastomers



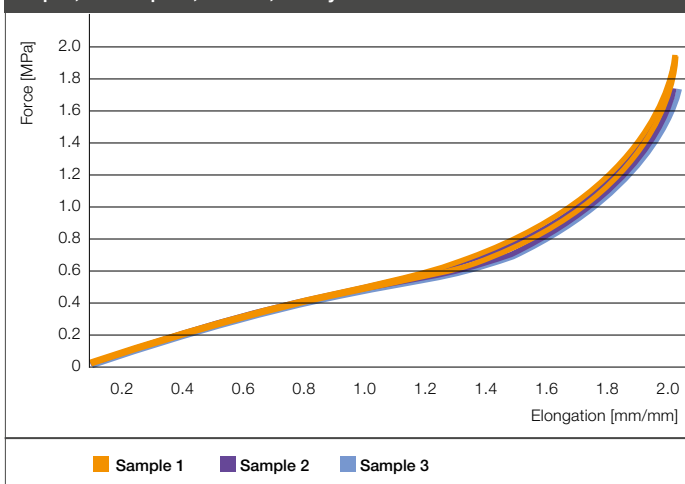
Thickness Precision

The ELASTOSIL® Film process produces films that are a fraction of the thickness of a human hair with state-of-art film thickness uniformity.

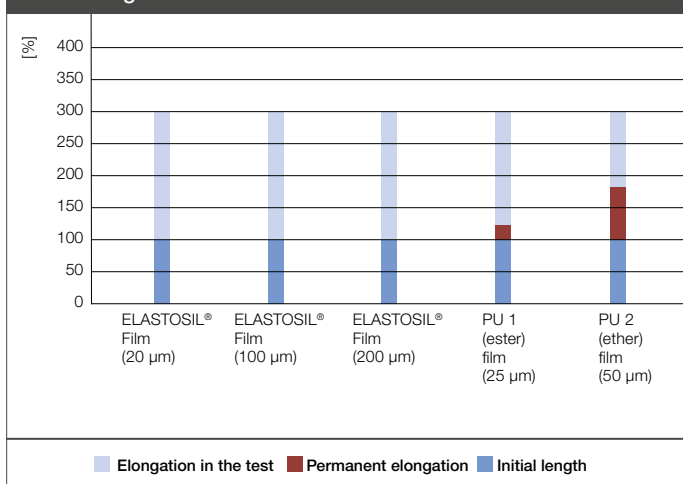
Elongation at Break

Silicones high elongation at break remains practically constant over a wide temperature range.

Stress-Strain Curve of ELASTOSIL® Film
20 µm, 3 Samples, 1.0 Hz, 10 Cycles



Stretch Recovery of ELASTOSIL® Film and PU Film after 24 h at 300% Elongation



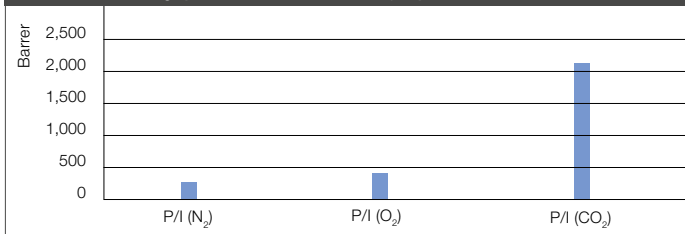
Elasticity and Resilience

ELASTOSIL® Film is highly elastic – permanently.

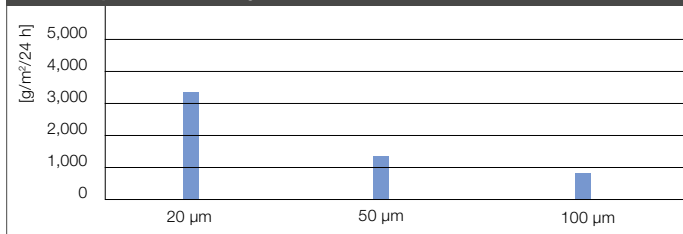
Stretch Recovery

Compared to other materials, silicone, and therefore ELASTOSIL® Film, has excellent elastic recovery.

Gas Permeability (ELASTOSIL® Film 20 µm) ISO 15105-1



Water-Vapor Permeability of ELASTOSIL® Film

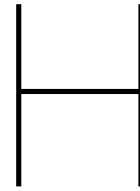


Gas Permeability and Selectivity

ELASTOSIL® Film is water repellent but selectively permeable to gases. This permeability is significantly higher than that of other polymers.

Water-Vapor Permeability

The water-vapor permeability of ELASTOSIL® film depends on the layer thickness.



Camera calibration

H.1. Silicon oil setup

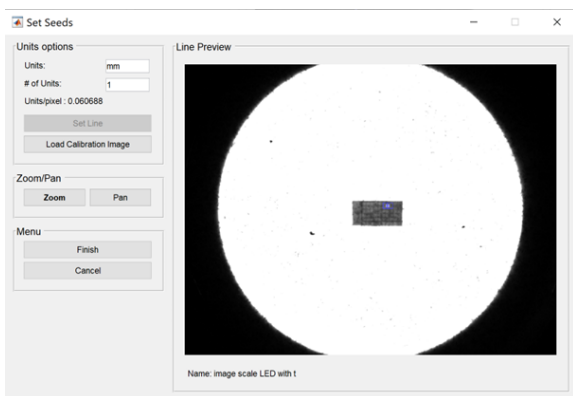


Figure H.1: General view of the scaling calibration over 1 mm horizontally for the silicon oil setup.

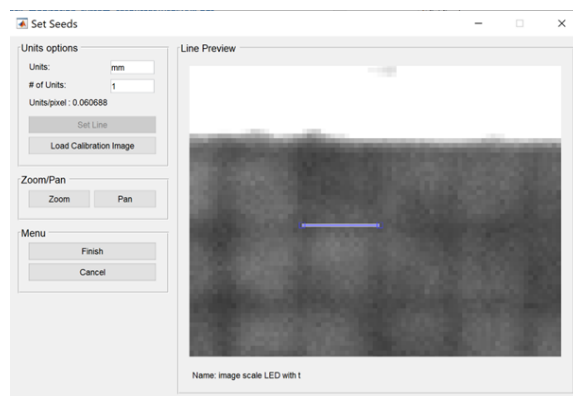


Figure H.2: Zoomed-in view of the scaling calibration over 1 mm horizontally for the silicon oil setup.

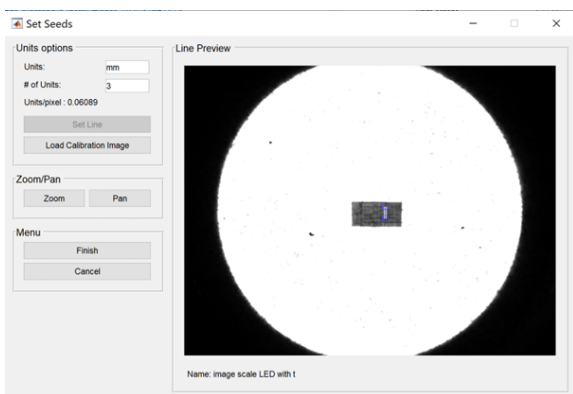


Figure H.3: General view of the scaling calibration over 3 mm vertically for the silicon oil setup.

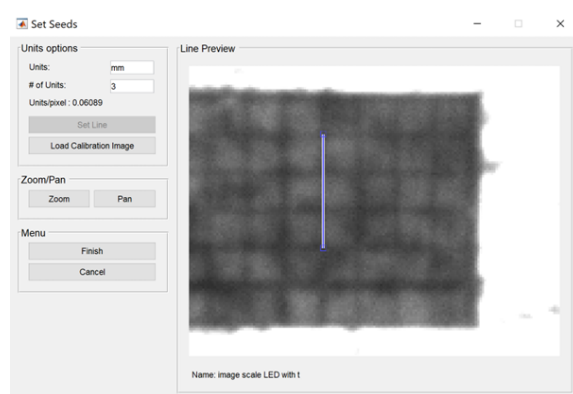


Figure H.4: Zoomed-in view of the scaling calibration over 3 mm vertically for the silicon oil setup.

H.2. Deionized water setup

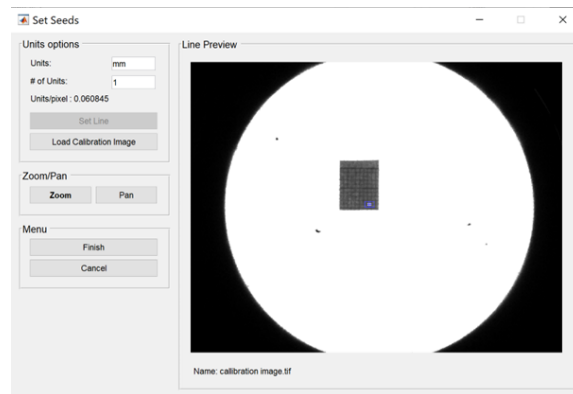


Figure H.5: General view of the scaling calibration over 1 mm horizontally for the deionized water setup.

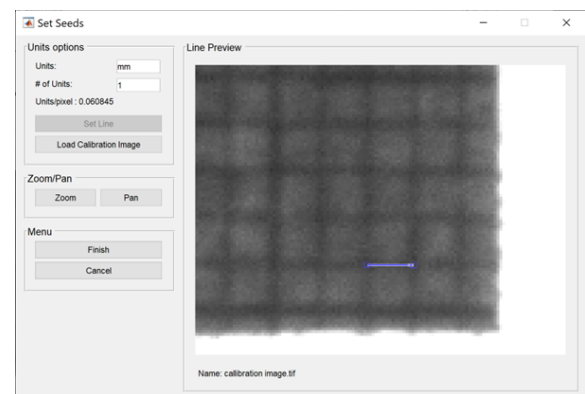


Figure H.6: Zoomed-in view of the scaling calibration over 1 mm horizontally for the deionized water setup.

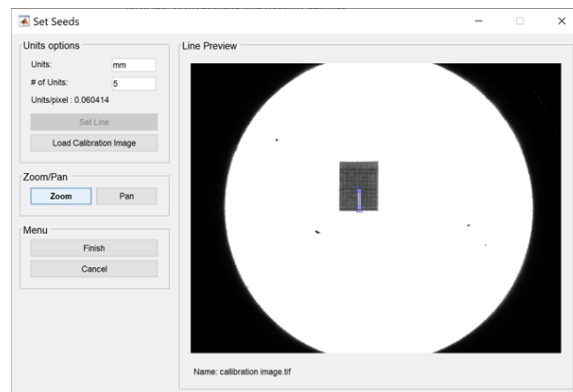


Figure H.7: General view of the scaling calibration over 5 mm vertically for the deionized water setup.

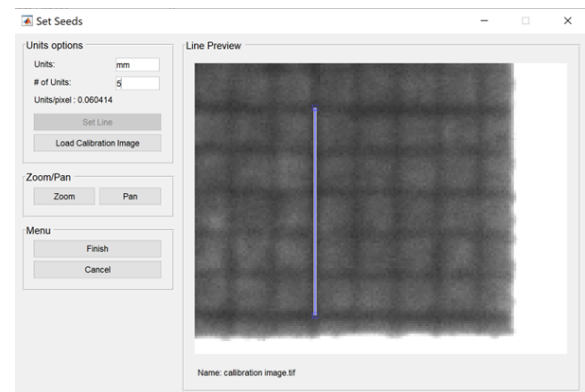


Figure H.8: Zoomed-in view of the scaling calibration over 5 mm vertically for the deionized water setup.

Validation of phase-locked imaging

Preliminary tests were conducted to verify both the digital image correlation (DIC) workflow and the phase-locked camera triggering. A small test case was considered, with the shaker operating at 80 Hz and a frequency divider set to 2, such that the camera captured only the peak surface displacements.

First, the reference image of the dot pattern (Figure I.1a) was correlated with itself. As expected, the resulting displacement fields showed near-zero in-plane motion (Figure I.3a, b ⁶), confirming correct DIC operation.

Next, five consecutive peak images (Figure I.1b–f) were correlated against the reference. The resulting x - and y -displacement fields (Figure I.2a–j ⁶) were highly consistent, indicating stable oscillatory behavior at reproducible phases.

To explicitly test phase-locking, the first peak frame was used as the reference and the subsequent peak frame as the current image. The maximum displacement difference between these two frames remained below 1 px (Figure I.4a–d ⁶), and the majority of displacements were near zero. For context, the displacements relative to the reference image ranged from –6 px to 6 px, so a variation of 0.6 px demonstrates excellent synchronization between camera triggering and surface oscillation.

These results confirm that the imaging system captures images at reproducible phases of the oscillatory motion, ensuring that the measured in-plane displacements accurately reflect the underlying surface wave pattern.

⁶Displacement values are reported in pixels; the calibration factor is 0.06 mm/px.

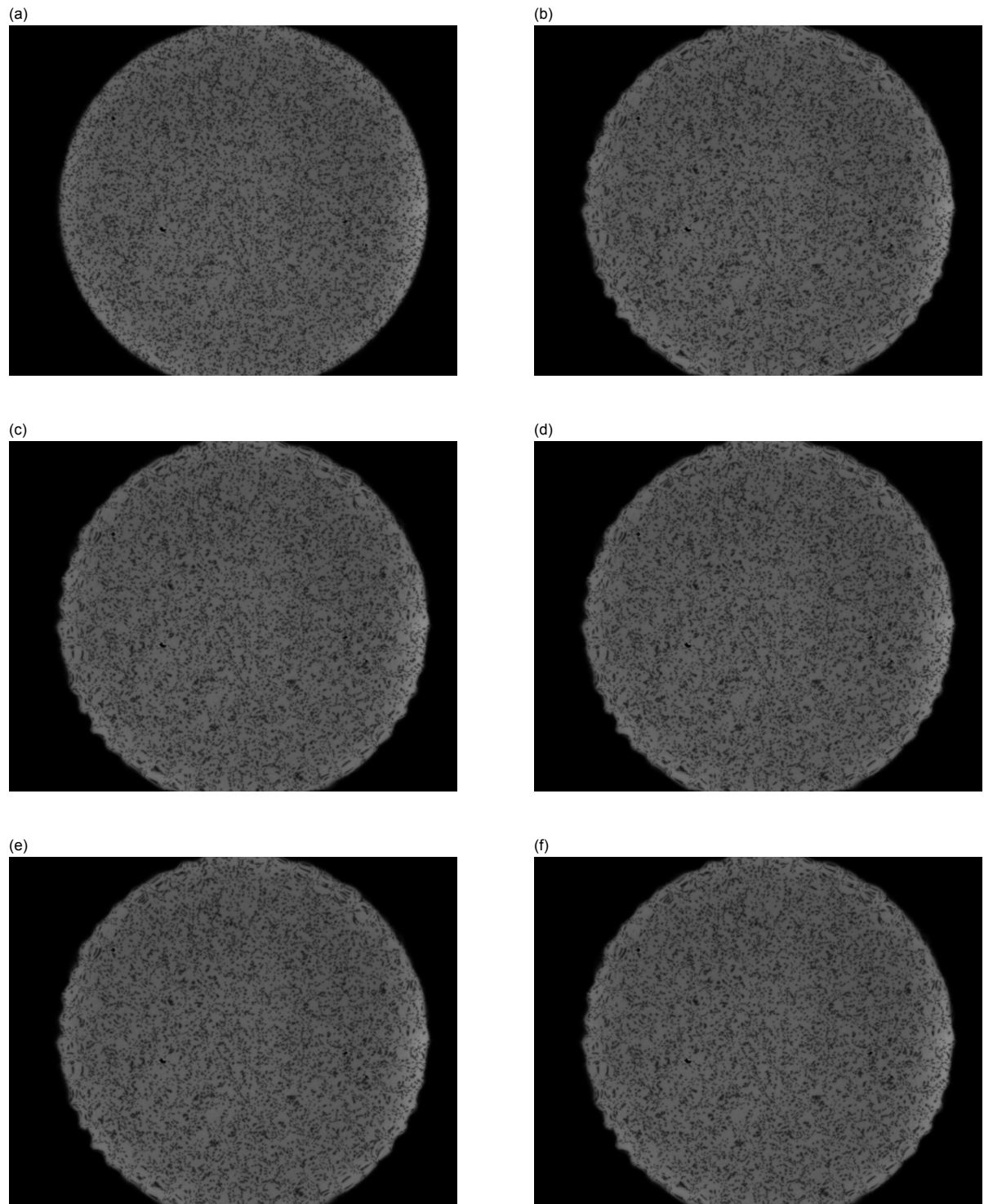


Figure I.1: Example images for silicone oil at 80 Hz showing (a) reference, (b, c, d, e, f) deformed image.

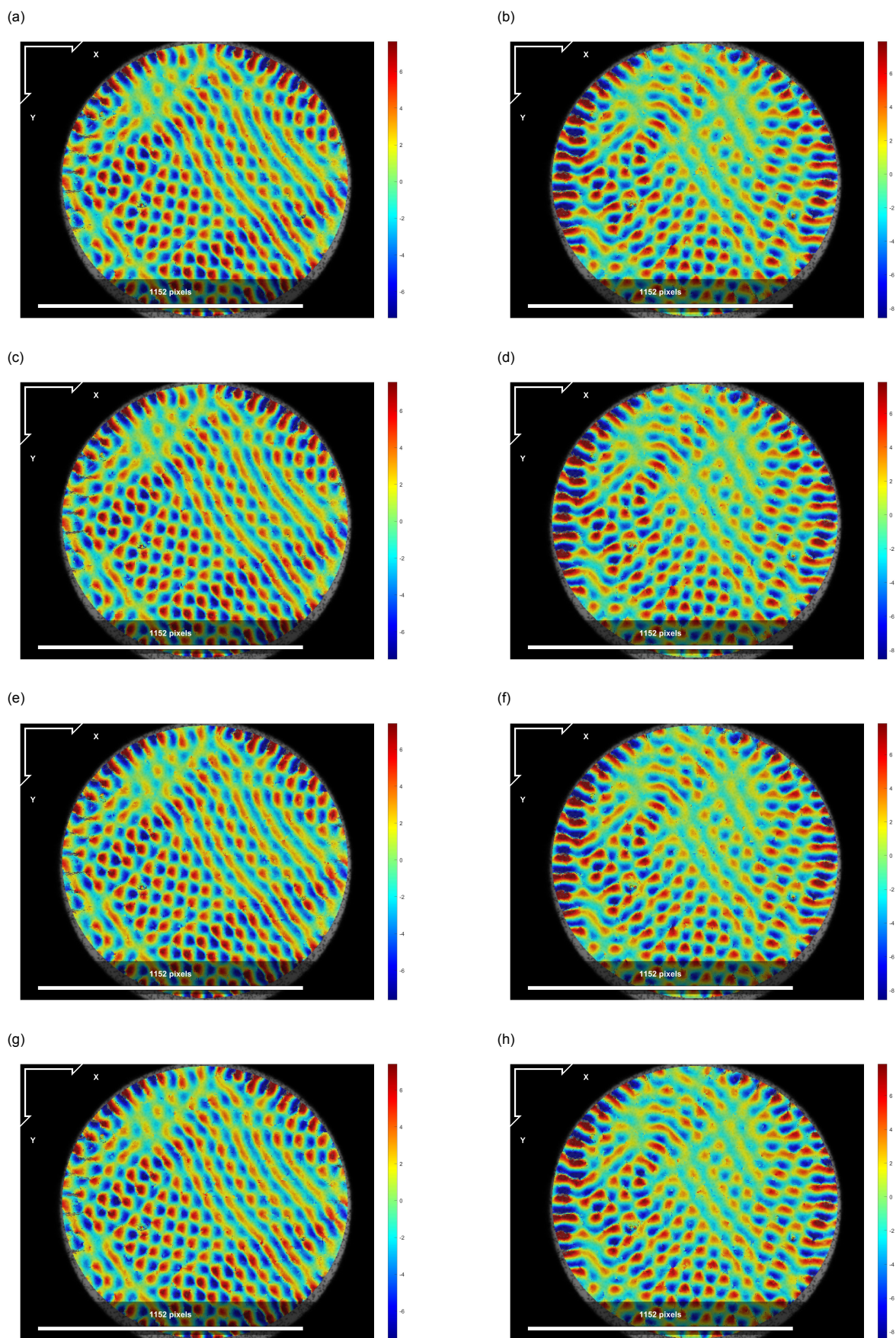


Figure I.2: Examples of DIC output for silicone oil at 80 Hz showing the displacement fields in (a, c, e, g, i) x -direction and (b, d, f, h, j) y -direction.

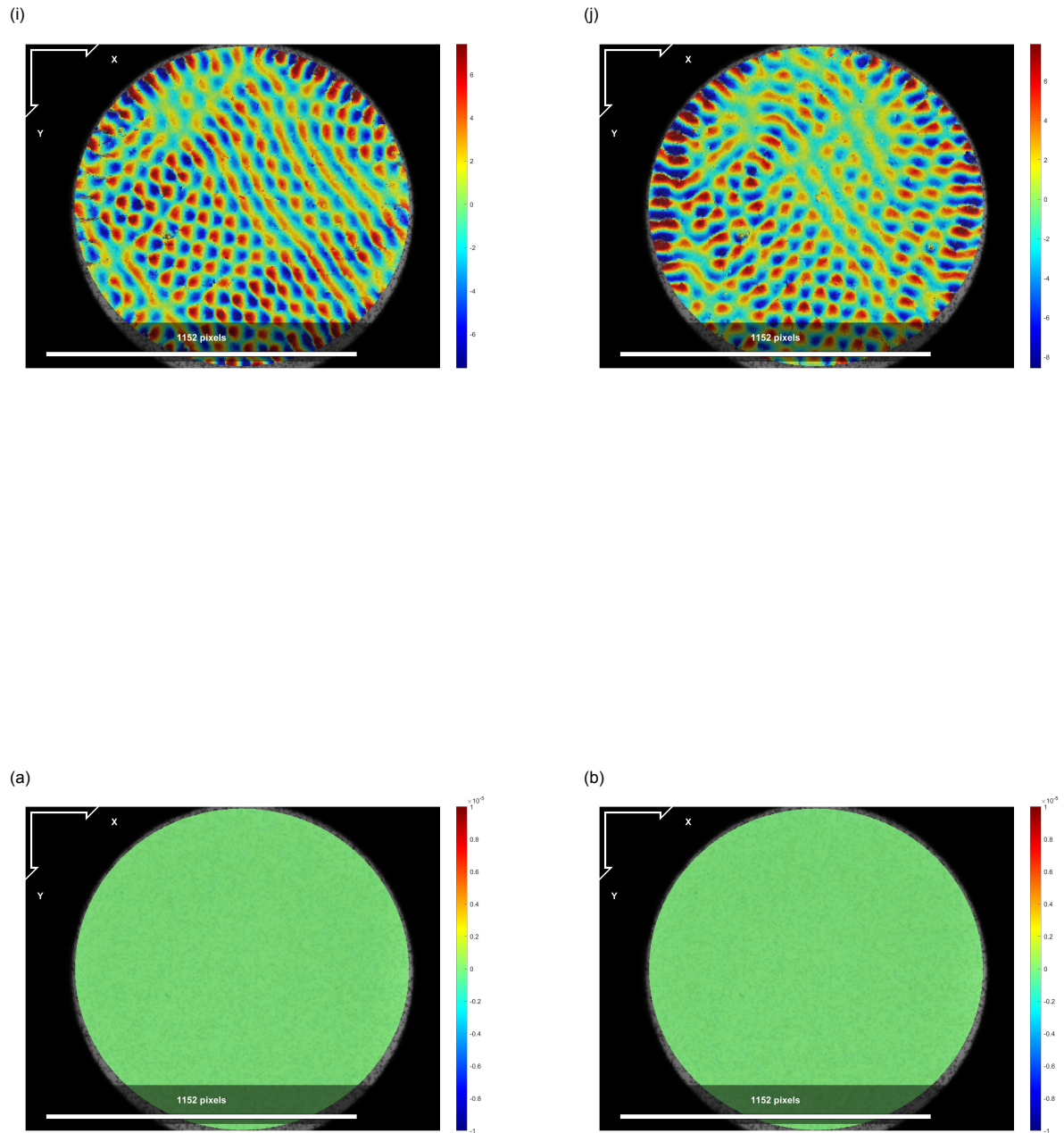


Figure I.3: DIC output showing zero displacement when correlating the reference image with itself for silicone oil at 80 Hz. Subfigures (a) show d_x , and (b) show d_y .

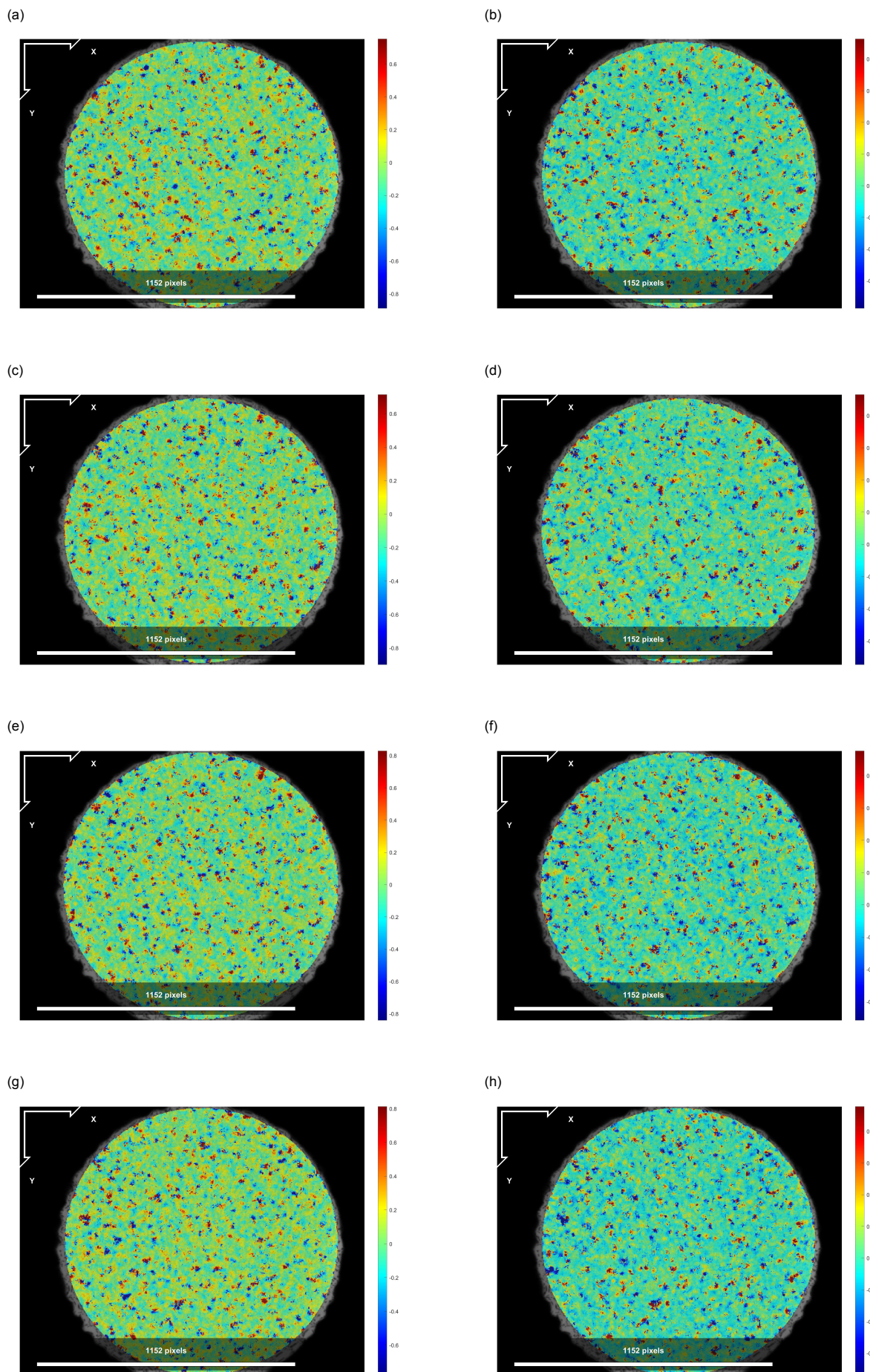


Figure I.4: DIC output showing displacement differences between consecutive peak frames for silicone oil at 80 Hz. Subfigures (a, c, e, g) show d_x , and (b, d, f, h) show d_y .



Convergence study: wavelength stabilization

A convergence study was conducted to determine the minimum number of video frames required to reliably extract the dominant wavelength. The motivation is to reduce computational effort during Digital Image Correlation (DIC) analysis by avoiding unnecessary processing of the full video length.

J.1. Test setup

Experiments were carried out for five configurations: deionized water without a surface film, and film-covered configurations with nominal thicknesses of 20, 50, 100, and 200 μm . For each case, the excitation frequency was fixed at 60 Hz, and the lowest amplitude setting was selected, as it typically results in the slowest development of the instability and thus represents the most challenging scenario for early wavelength determination.

DIC analysis was performed over the entire duration of each video. The dominant wavelength was then calculated using the procedure described in Section 3.4.2. To assess the effect of frame count on the stability of the wavelength estimation, the analysis was repeated for increasing numbers of frames, using subsets of the video in increments of 5 frames (i.e., using the first 5, 10, 15 frames, and so on).

J.2. Results

Figure J.1 shows how the derived dominant wavelength evolves as a function of the number of frames included in the analysis for the 200 μm m case. Initially, the wavelength fluctuates due to transient wave patterns excited during the early stages of instability, such as concentric waves that differ from the final governing pattern. As more frames are included, the calculated wavelength stabilizes and converges toward a consistent value, indicating that the system has reached its characteristic behavior. Similar convergence behavior is observed for the other configurations, which are presented in Section J.4.

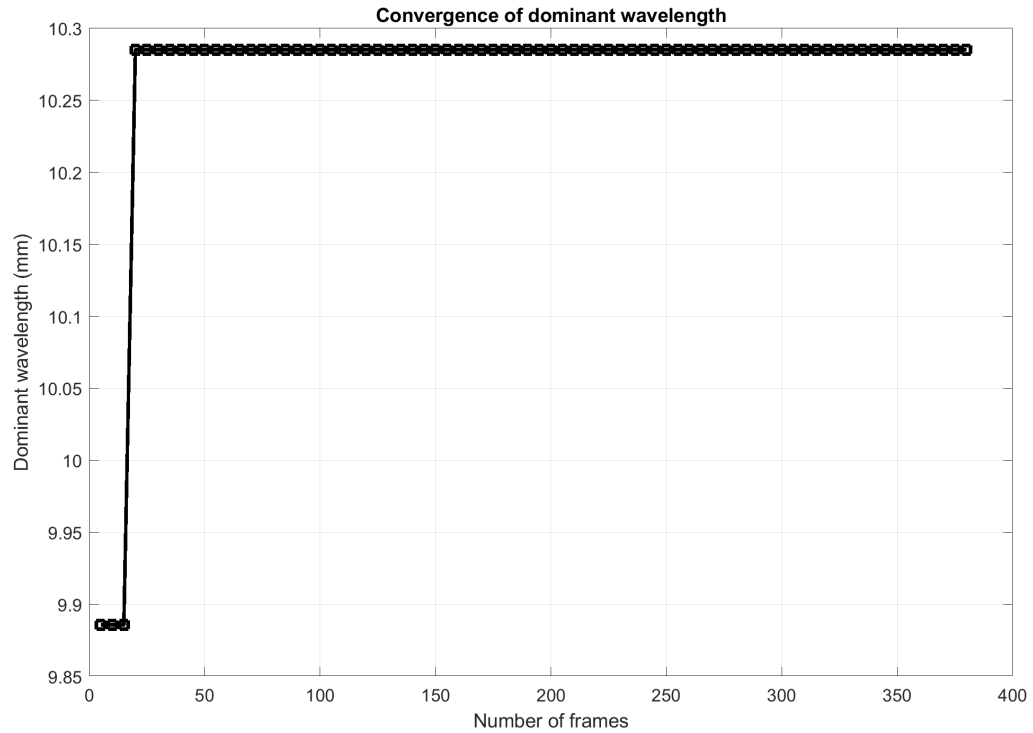


Figure J.1: Convergence of the dominant wavelength as a function of frame count for the 200 μm film-covered configuration at 60 Hz excitation.

J.3. Discussion and conclusion

The study shows that in most cases, the dominant wavelength can be accurately determined using fewer frames than the full video length. Therefore, to improve efficiency without compromising accuracy, it was decided to limit the DIC analysis to the first 180 frames in all experiments. This frame count ensures that the governing wavelength is captured while avoiding the influence of early transient effects and minimizing computational cost.

J.4. Figures

J.4.1. Deionized water at 60 Hz

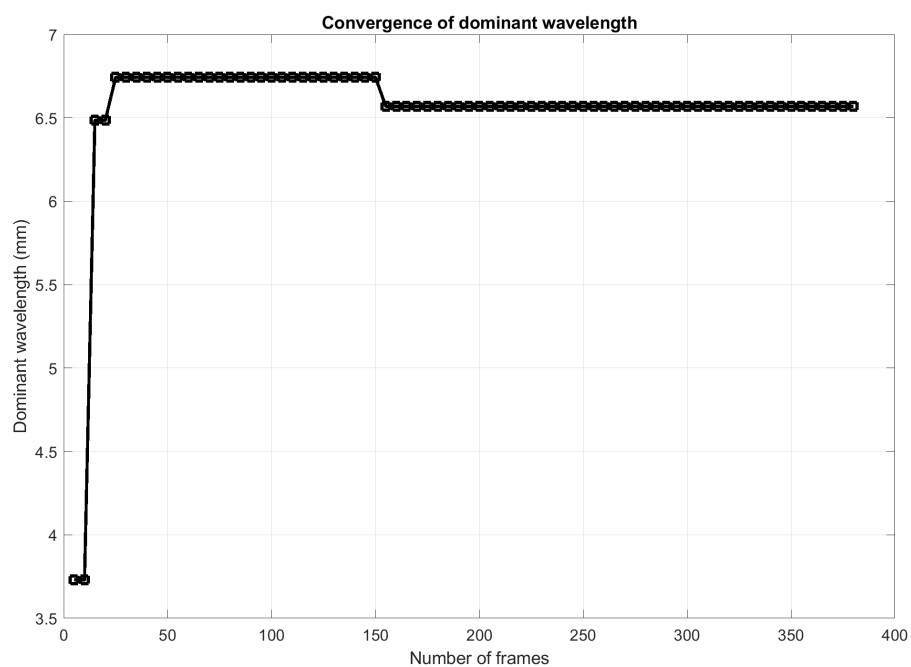


Figure J.2: Convergence of the dominant wavelength as a function of frame count for the uncovered configuration at 60 Hz excitation.

J.4.2. Deionized water with 20 μm floating film at 60 Hz

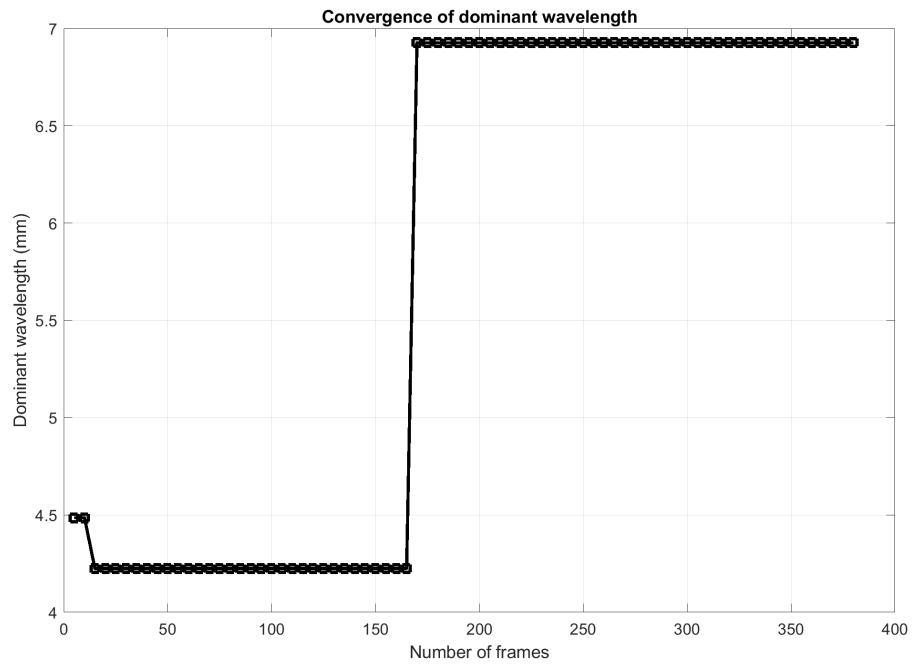


Figure J.3: Convergence of the dominant wavelength as a function of frame count for the 20 μm film-covered configuration at 60 Hz excitation.

J.4.3. Deionized water with 50 μm floating film at 60 Hz

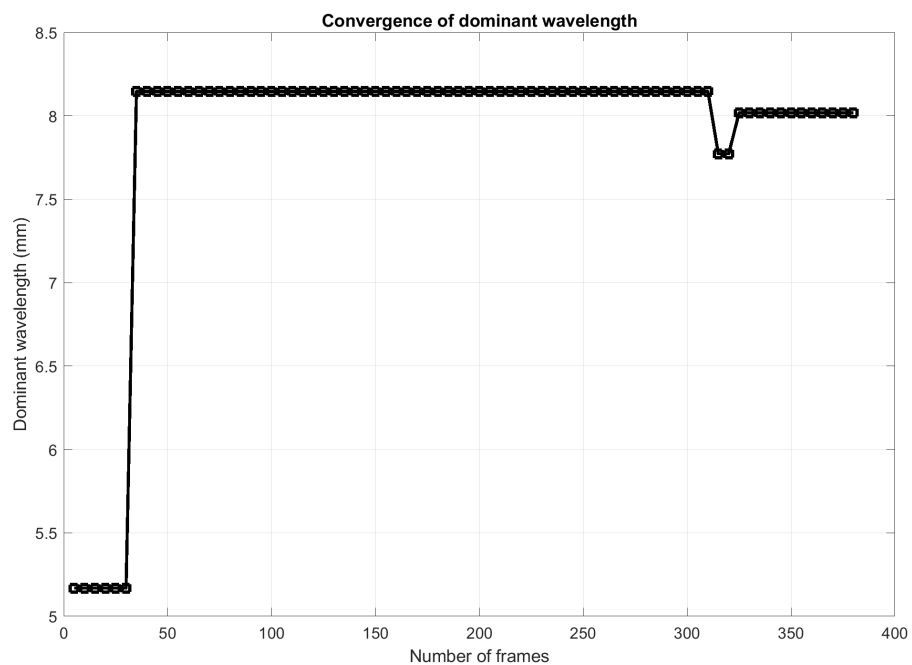


Figure J.4: Convergence of the dominant wavelength as a function of frame count for the 50 μm film-covered configuration at 60 Hz excitation.

J.4.4. Deionized water with 100 μm floating film at 60 Hz

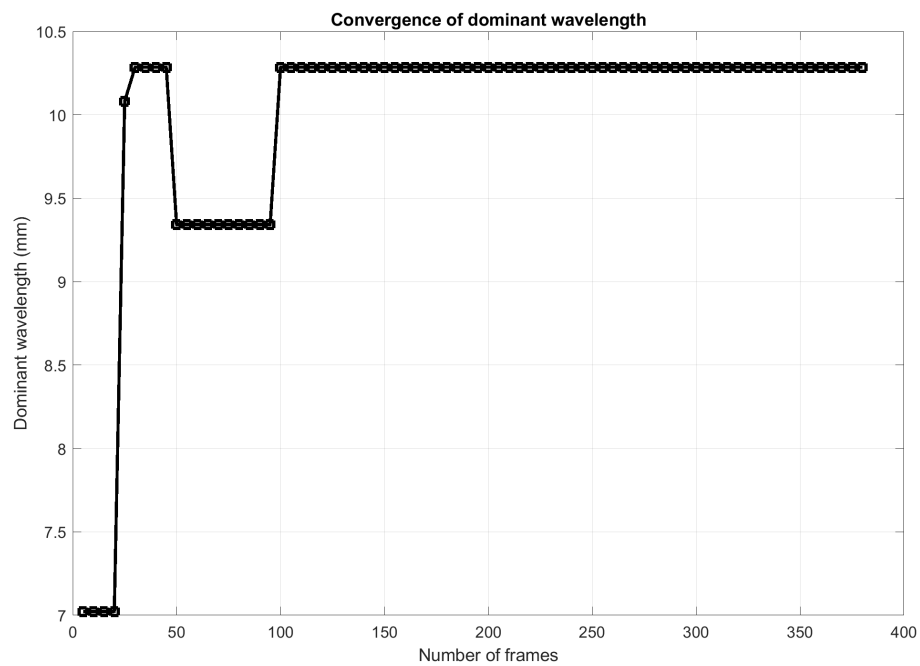
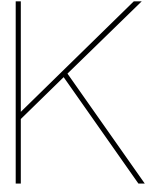


Figure J.5: Convergence of the dominant wavelength as a function of frame count for the 100 μm film-covered configuration at 60 Hz excitation.



Convergence study: radial bin size

A convergence study was conducted to assess the influence of the number of radial bins used during the radial averaging of the two-dimensional Fourier spectrum. This evaluation is essential to identify an optimal bin count that provides accurate wavelength estimation without introducing artifacts or unnecessary computational burden. The trade-off lies in avoiding undersampling (too few bins, leading to poor spectral resolution) and oversampling (too many bins, leading to noise amplification and spurious peaks).

K.1. Test setup

The study was performed across the same experimental conditions as those used in the wavelength stabilization analysis. For each test case, the dominant wavelength was computed by sweeping the number of radial bins from 25 to 3000 in increments of 25.

K.2. Results

Figure K.1 illustrates the behavior of the dominant wavelength as a function of the number of radial bins for the test case involving a 200 μm film at 60 Hz excitation frequency (lowest amplitude setting). The plot reveals a distinct trend: the estimated wavelength decreases with increasing bin number, gradually approaching a stable value. This asymptotic behavior suggests that higher radial resolution enables more precise detection of the dominant spatial frequency component.

However, beyond approximately 1300 bins, a discontinuous shift is observed in the dominant wavelength. This likely indicates the emergence of secondary spectral peaks, which may correspond to nearby frequency components or numerical noise being misidentified as dominant due to oversampling. Thus, using excessively high bin counts can lead to erroneous identification of the governing wavelength. Comparable convergence trends were observed for the other test cases, and the corresponding results are presented in Section K.4.

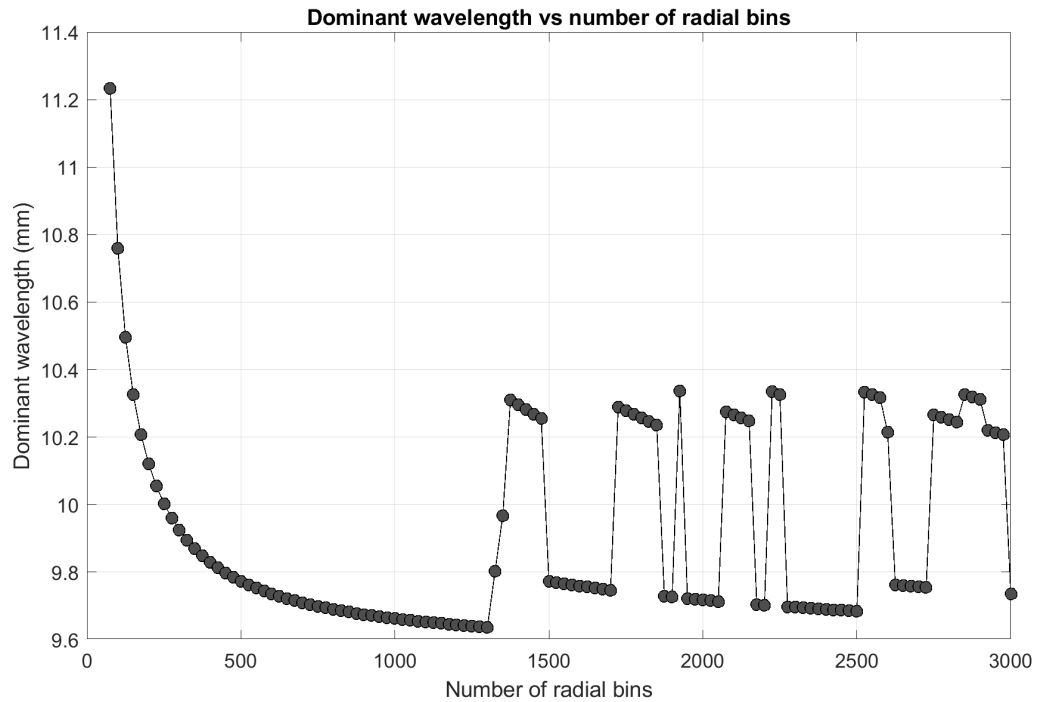


Figure K.1: Convergence of the dominant wavelength as a function of radial bin count for the 200 μm film-covered configuration at 60 Hz excitation.

K.3. Discussion and Conclusion

This convergence analysis demonstrates that a radial bin count of approximately 1200 offers a reasonable balance between spectral resolution and computational efficiency. Beyond this threshold, improvements in resolution become marginal, while the risk of misidentifying the dominant wavelength increases.

Moreover, this study highlights the importance of bin size selection in spectral averaging procedures. While increasing bin counts improves spectral localization, it also introduces sensitivity to minor variations and side-lobes in the power spectrum, which can lead to the erroneous attribution of non-dominant features as governing.

Therefore, for subsequent analyses, a bin count of 1200 is recommended as a robust and conservative choice, ensuring both computational practicality and accurate wavelength estimation across the tested conditions.

K.4. Figures

K.4.1. Deionized water at 60 Hz

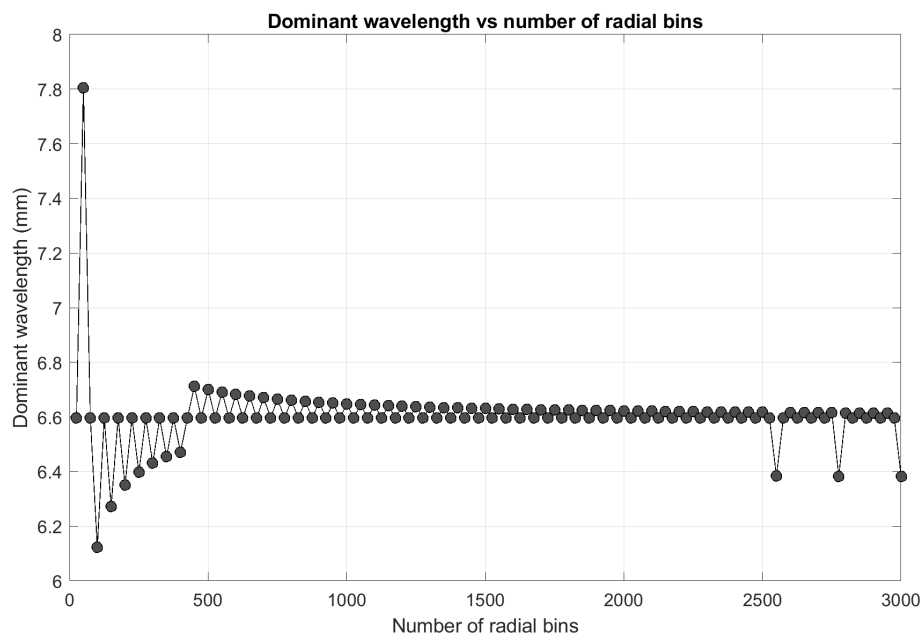


Figure K.2: Convergence of the dominant wavelength as a function of radial bin count for the uncovered configuration at 60 Hz excitation.

K.4.2. Deionized water with 20 μm floating film at 60 Hz

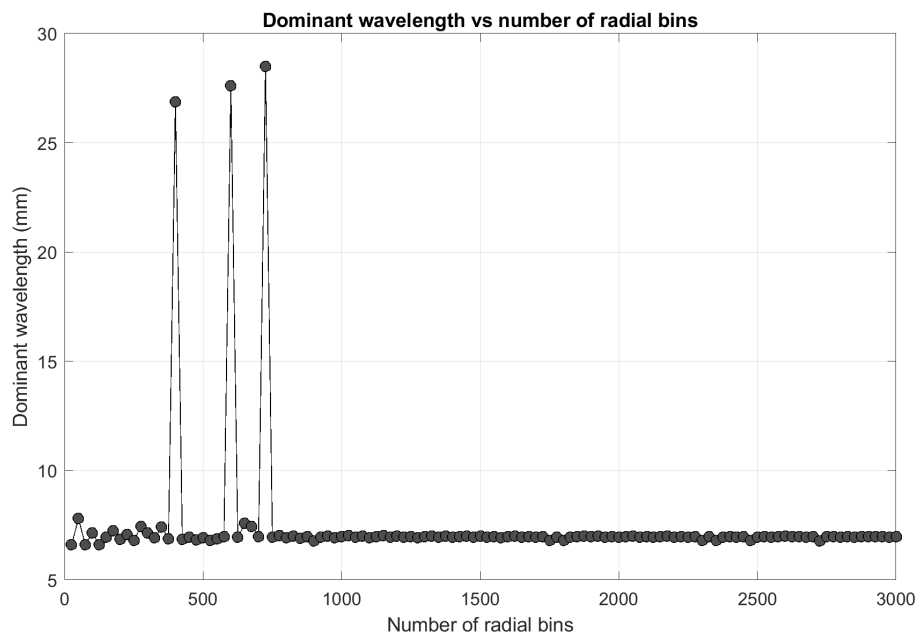


Figure K.3: Convergence of the dominant wavelength as a function of radial bin count for the 20 μm film-covered configuration at 60 Hz excitation.

K.4.3. Deionized water with 50 μm floating film at 60 Hz

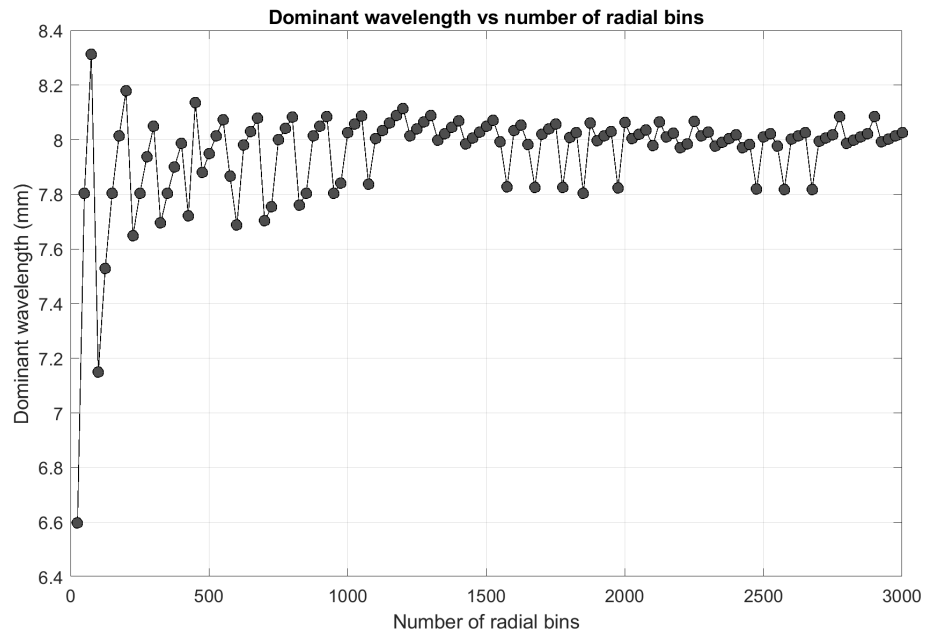


Figure K.4: Convergence of the dominant wavelength as a function of radial bin count for the 50 μm film-covered configuration at 60 Hz excitation.

K.4.4. Deionized water with 100 μm floating film at 60 Hz

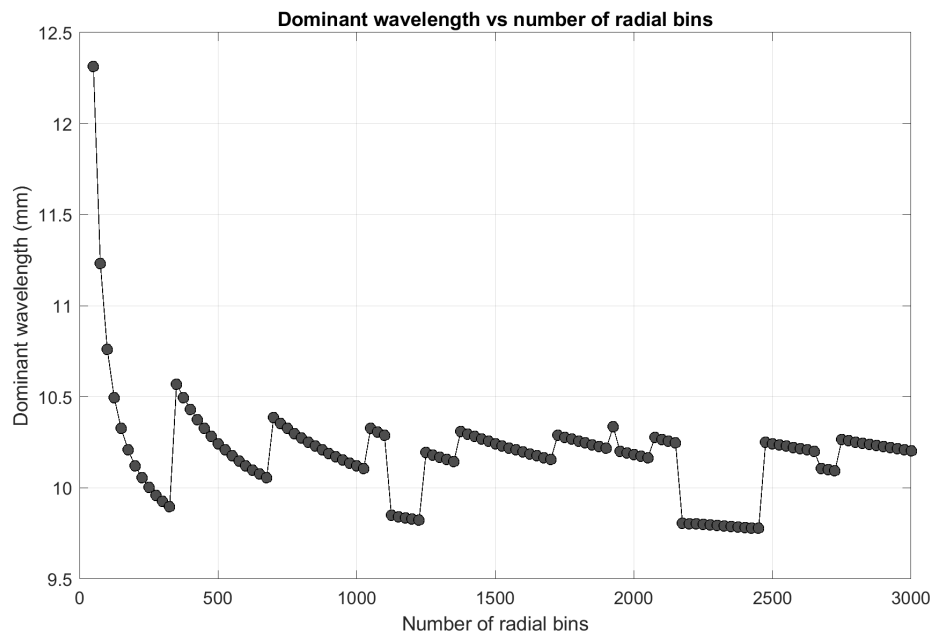
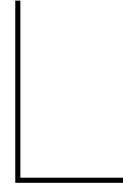


Figure K.5: Convergence of the dominant wavelength as a function of radial bin count for the 100 μm film-covered configuration at 60 Hz excitation.



Accelerometer calibration

To accurately determine the shaker acceleration in units of g, a short calibration test was conducted. The goal was to establish the relationship between the accelerometer's voltage output and actual acceleration, expressed in mV/g. Since no factory calibration data were available, this in-house calibration allowed a direct mapping based on controlled sinusoidal motion.

L.1. Test setup

Calibration was performed at excitation frequencies of 5, 25, and 50 Hz, each with several displacement amplitudes. A signal generator and amplifier drove the shaker with an empty glass tank mounted on top. The displacement of the tank edge was measured using a laser distance meter (repeatability: $\pm 8 \mu\text{m}$), while the acceleration was recorded using an accelerometer mounted to the shaker's internal structure (accuracy: $\pm 1\%$). Data acquisition was done via a National Instruments DAQ and LabVIEW script, recording around 2000 points per run with approximately 10 samples per oscillation cycle. Each run was performed three times to ensure repeatability and assess consistency across repeated measurements.

The vertical displacement amplitude z_a was extracted via Fourier analysis. Assuming sinusoidal motion, the theoretical vertical acceleration amplitude a_a was computed as:

$$a_a = \omega^2 z_a = (2\pi f)^2 z_a,$$

where f is the excitation frequency. This calculated acceleration in m/s^2 was compared to the accelerometer amplitude output voltage V_a , and the calibration factor C in mV/g was then obtained as:

$$C = \frac{V_a}{a_a/g} = \frac{V_a \cdot g}{a_a},$$

with $g = 9.81 \text{ m/s}^2$.

L.2. Calibration accuracy

To evaluate the accuracy of the acceleration and the resulting calibration factor, uncertainties in all relevant quantities were taken into account. Acceleration amplitude a_a in units of g is calculated using the vertical displacement amplitude z_a (in m), excitation frequency f (in Hz), and gravitational acceleration $g = 9.81 \text{ m/s}^2$, via

$$a_a = \frac{z_a \cdot (2\pi f)^2}{g}.$$

The uncertainty in acceleration, δa_a , is determined using first-order (linearized) error propagation, following the *Guide to the Expression of Uncertainty in Measurement* (GUM) (Joint Committee for Guides in Metrology (JCGM), 2008) and standard error propagation methods (Bevington & Robinson, D. Keith, 2003; Taylor, 1997).

For a function $a_a(z_a, f)$ of independent variables z_a and f , the linearized uncertainty is given by:

$$\delta a_a = \sqrt{\left(\frac{\partial a_a}{\partial z_a} \delta z_a\right)^2 + \left(\frac{\partial a_a}{\partial f} \delta f\right)^2}.$$

The partial derivatives with respect to z_a and f are

$$\frac{\partial a_a}{\partial z_a} = \frac{(2\pi f)^2}{g}, \quad \frac{\partial a_a}{\partial f} = \frac{8\pi^2 z_a f}{g}.$$

Substituting these into the general formula yields the explicit expression:

$$\delta a_a = \sqrt{\left(\frac{(2\pi f)^2 \delta z_a}{g}\right)^2 + \left(\frac{8\pi^2 z_a f \delta f}{g}\right)^2}.$$

Here, $\delta z_a = 8 \mu\text{m}$ reflects the repeatability of the laser displacement sensor, and $\delta f = 5 \text{ ppm} \times f$ is based on the frequency synthesizer's specified accuracy.

The calibration factor C in mV/g is computed as

$$C = \frac{V_a}{a_a},$$

where V_a is the measured voltage amplitude output from the accelerometer.

For a function $C(V_a, a_a)$ of independent variables V_a and a_a , the uncertainty is given by

$$\delta C = \sqrt{\left(\frac{\partial C}{\partial V_a} \delta V_a\right)^2 + \left(\frac{\partial C}{\partial a_a} \delta a_a\right)^2}.$$

The partial derivatives are

$$\frac{\partial C}{\partial V_a} = \frac{1}{a_a}, \quad \frac{\partial C}{\partial a_a} = -\frac{V_a}{a_a^2},$$

leading to the explicit expression

$$\delta C = \sqrt{\left(\frac{\delta V_a}{a_a}\right)^2 + \left(\frac{V_a \delta a_a}{a_a^2}\right)^2}.$$

The voltage uncertainty δV_a was estimated based on the specified accuracy of 1 % of the measured accelerometer value (manufacturer specifications, Appendix ??). Combining these contributions provides an upper bound for the accuracy of the calibration factor, consistent with GUM principles (Joint Committee for Guides in Metrology (JCGM), 2008).

L.3. Results

The collected data can be visualized by plotting the voltage amplitude on the y -axis against the vertical displacement on the x -axis. As shown in Figure L.1, a clear linear trend is observed among the data points corresponding to the same excitation frequency. Using the previously established relationship, the acceleration values were computed, allowing for a second representation where voltage is plotted against acceleration, as illustrated in Figure L.2. The data from both 25 Hz and 50 Hz exhibit similar trends, though they are not perfectly identical. This discrepancy is further analyzed in Figure L.3, where the mV/g calibration factor is calculated for each frequency case and presented in a scatter plot. The plot reveals some dispersion between points within similar frequency ranges. According to the datasheet of the accelerometer (manufacturer specifications, Appendix G.6), the accuracy of the voltage gain is specified as $\pm 1 \%$, yet this alone cannot fully account for the observed variance. The datasheet also details spectral noise and broadband electrical noise, but their magnitudes are significantly smaller than the measured variance, suggesting that they are unlikely to be the primary cause. Additionally, the datasheet indicates the presence of a DC offset of up to $\pm 30 \text{ mV}$, which was

particularly noticeable in the 5 Hz data. Since the peak voltage values at this frequency were relatively small, the offset introduces a potential source of error, raising concerns about the significance and reliability of the 5 Hz measurements.

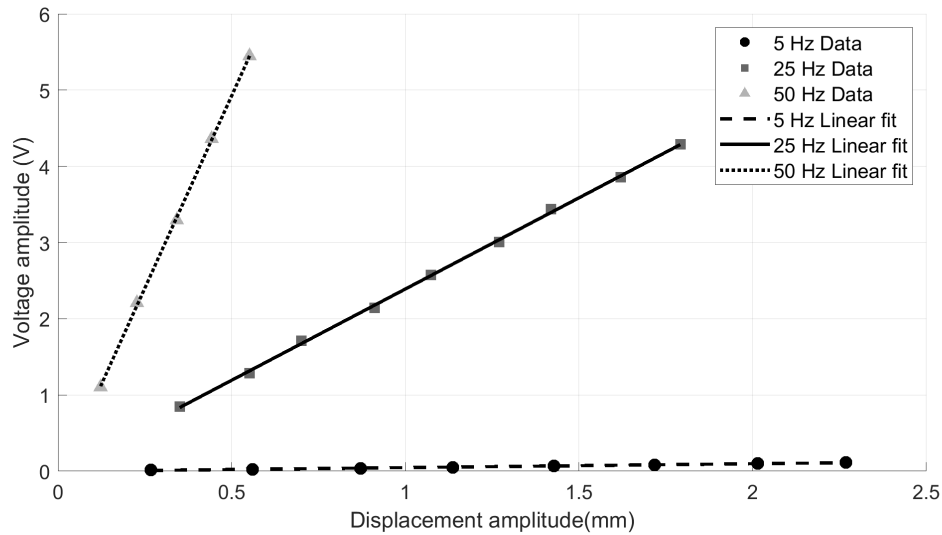


Figure L.1: Trendline analysis of voltage amplitude vs. displacement. Experimental data points are shown with distinct markers, and fitted trendlines indicate the voltage response across different frequency groups.

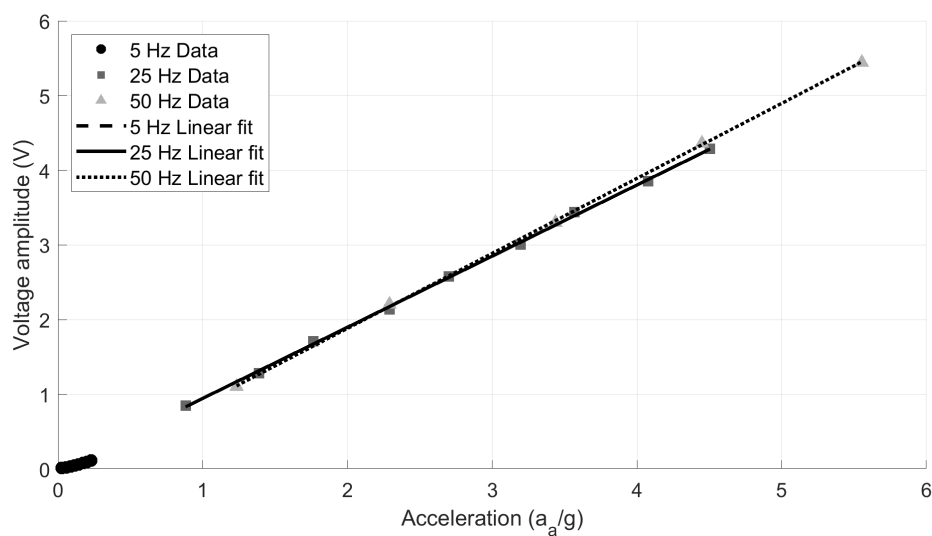


Figure L.2: Trendline analysis of voltage amplitude vs. acceleration. Experimental data points are shown with distinct markers, and fitted trendlines indicate the voltage response across different frequency groups.

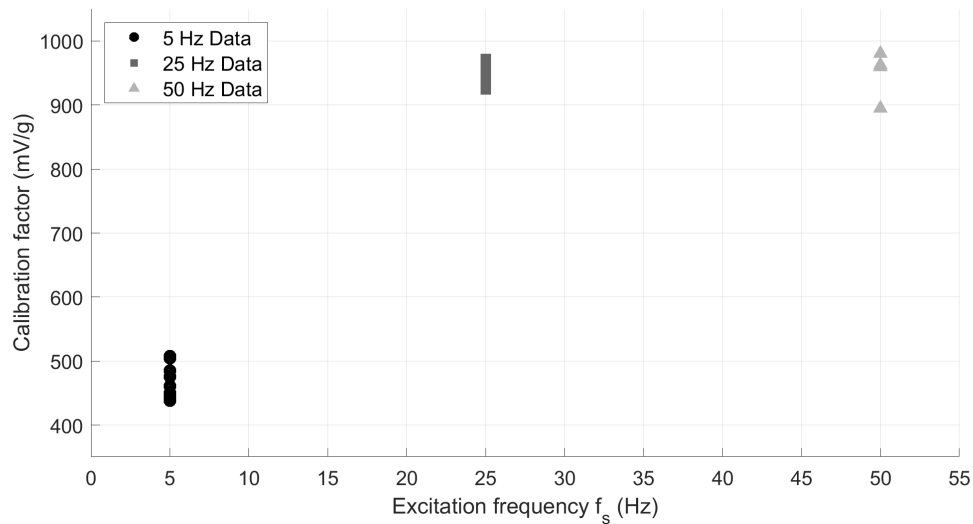


Figure L.3: Scatter plot of accelerometer calibration: mV/g vs. frequency. Distinct markers indicate different frequency groups (5, 25, and 50 Hz).

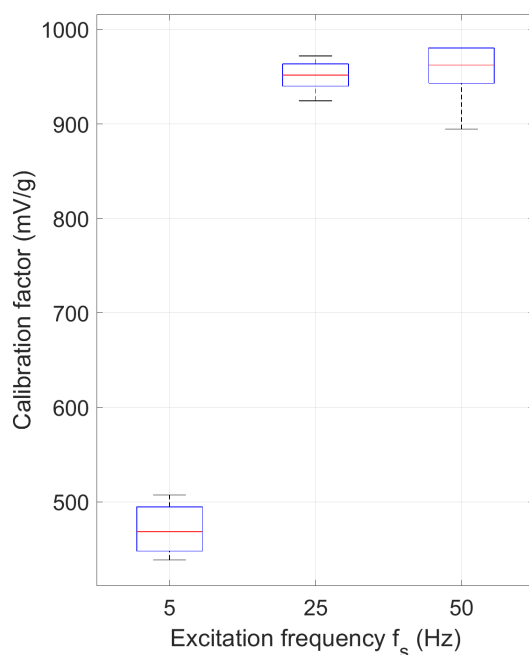


Figure L.4: Repetition 1 (5, 25, and 50 Hz).

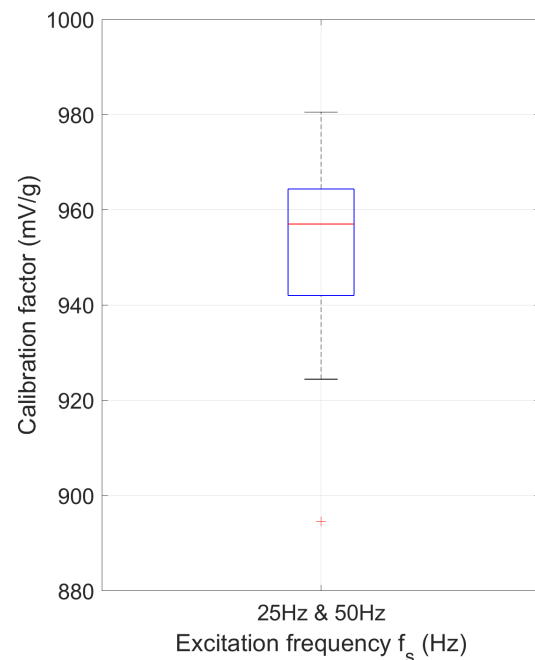


Figure L.5: Repetition 1 (25 and 50 Hz).

Figure L.4 shows that at low frequencies the values clearly deviate from the trend shown by higher frequencies. The measured voltages are below the DC offset, as specified in the specs sheet of the accelerometer. At each frequency, the different tests were presented in a boxplot for repetition one. The data from both 25 Hz and 50 Hz seem to correspond pretty well. So we can combine the data into one boxplot as presented in Figure L.5.

L.3.1. Check repeatability

As outlined in the test setup, each test scenario was repeated three times to assess repeatability. The boxplots shown in Figures L.6, L.7, and L.8 illustrate the results of these repetitions for excitation frequencies of 25 Hz and 50 Hz. The consistency across all three repetitions confirms the high

repeatability of the measurements. Consequently, the derived calibration factor of 956 ± 15 mV/g can be considered reliable.

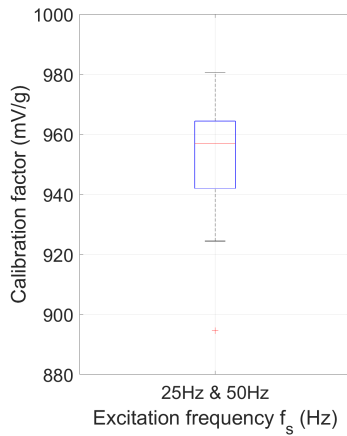


Figure L.6: Repetition 1

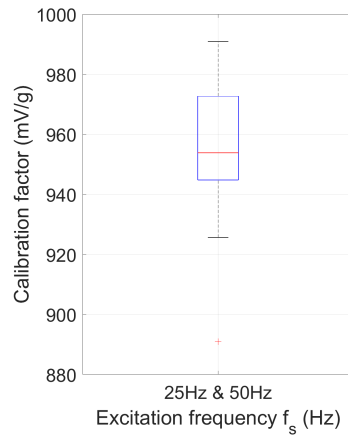


Figure L.7: Repetition 2

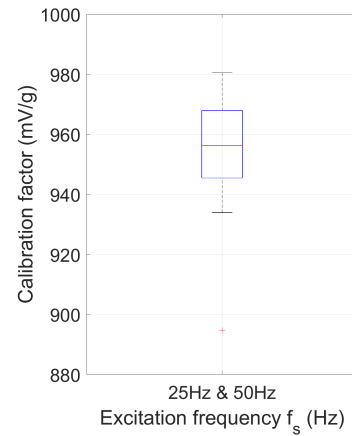


Figure L.8: Repetition 3

L.4. Accelerometer calibration data

L.4.1. Overview measured data repetition 1

Table L.1: Measurement results at 5 Hz, including displacement, voltage, and calibration with associated uncertainties and relative percentage errors.

Displacement (mm)	Error (%)	Voltage (V)	Error (%)	Calibration (mV/g)	Error (%)
0.267 20	2.99	0.013 64	1.00	507.40	3.16
0.560 67	1.43	0.025 40	1.00	450.20	1.74
0.871 67	0.92	0.038 46	1.00	438.61	1.36
1.136 70	0.70	0.050 96	1.00	445.61	1.22
1.428 00	0.56	0.066 24	1.00	461.10	1.15
1.717 10	0.47	0.082 19	1.00	475.75	1.10
2.014 90	0.40	0.098 30	1.00	484.92	1.08
2.269 00	0.35	0.115 22	1.00	504.73	1.06

Table L.2: Measurement results at 25 Hz, including displacement, voltage, and calibration with associated uncertainties and relative percentage errors.

Displacement (mm)	Error (%)	Voltage (V)	Error (%)	Calibration (mV/g)	Error (%)
0.350 42	2.28	0.850 00	1.00	964.40	2.49
0.551 91	1.45	1.283 30	1.00	924.46	1.76
0.700 84	1.14	1.713 30	1.00	971.95	1.52
0.911 09	0.88	2.141 00	1.00	934.30	1.33
1.073 20	0.75	2.577 00	1.00	954.69	1.25
1.270 30	0.63	3.009 60	1.00	941.96	1.18
1.419 20	0.56	3.438 60	1.00	963.31	1.15
1.620 70	0.49	3.856 20	1.00	945.99	1.12
1.791 50	0.45	4.289 00	1.00	951.85	1.10

Table L.3: Measurement results at 50 Hz, including displacement, voltage, and calibration with associated uncertainties and relative percentage errors.

Displacement (mm)	Error (%)	Voltage (V)	Error (%)	Calibration (mV/g)	Error (%)
0.122 64	6.52	1.103 80	1.00	894.60	6.60
0.227 77	3.51	2.205 30	1.00	962.37	3.65
0.341 66	2.34	3.297 60	1.00	959.34	2.55
0.442 40	1.81	4.363 80	1.00	980.44	2.07
0.551 91	1.45	5.444 40	1.00	980.51	1.76



DIC noise

M.1. Uncertainty in DIC Measurements

Part of the uncertainty in the wavelength determination arises from the accuracy of the DIC measurements. The DIC algorithm inherently introduces noise, and it is desirable to quantify this contribution in order to include it in the overall uncertainty budget. A common approach is to acquire multiple images under static conditions, compare the resulting displacement fields, and derive an associated standard deviation, σ_{DIC} . In the present study, no true static images are acquired, so alternative approaches are explored. However, all attempts are complicated by the dynamic nature of the surface, and no perfectly static comparisons are obtained.

An initial approach focuses on the direct influence of DIC on the peak in the complex two-dimensional frequency domain. This is investigated by analyzing the last 50 frames of a test in which the Faraday-wave onset occurs very early. In principle, each phase-locked frame should capture the same wavelength (independent of capturing alternating positions of the standing wave; odd frequency divider setting), allowing the comparison of the dominant spatial frequency. For each of these frames, the complex Fourier-domain representation is computed, and the peaks are compared (Figure M.1). This analysis yields an estimated uncertainty in the frequency peak of

$$\delta f_{\text{DIC}} \approx 1.4 \times 10^{-4} \text{ px}^{-1},$$

corresponding to an approximate

$$\sigma_{\text{DIC}} \sim 0.2 \text{ px}.$$

Another approach involves comparing consecutive images that are phase-locked at the same phase (this can be either consecutive images captured with even frequency divider settings or by skipping one image each time when using odd frequency divider settings). This comparison can be performed in two ways: (i) by running DIC on both the first and second images relative to a common static reference image, and then subtracting the resulting displacement fields, or (ii) by directly comparing the first and second consecutive images using the DIC software.

As an example of the first method, Figure M.3 shows the d_x and d_y displacement fields obtained by referencing the first two consecutive phase-locked images to the same static reference, as well as the difference fields derived from their subtraction. The standard deviations between the frames are

$$\sigma_{\Delta d_x} = 0.189 \text{ px}, \quad \sigma_{\Delta d_y} = 0.185 \text{ px}.$$

However, inspection of the difference plots (Figure M.3e and f) reveals that large deviations are associated with regions where DIC fails, for instance due to air bubbles trapped beneath the sheet. Consequently, this approach does not provide a reliable representation of the intrinsic DIC noise, and it is difficult to filter such artifacts consistently across all image sequences.

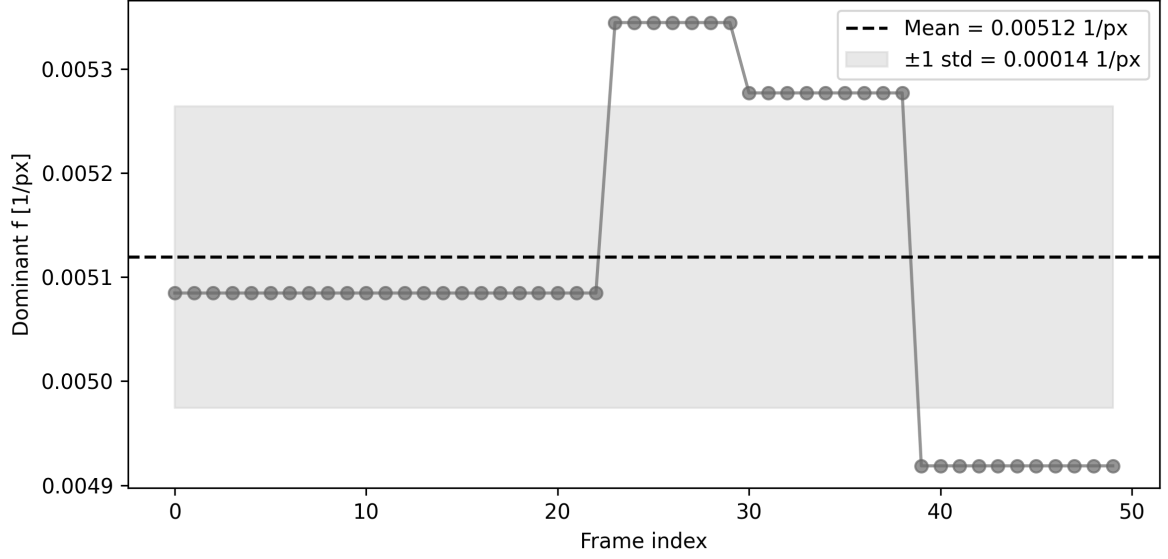


Figure M.1: Dominant spatial frequency f extracted from the complex 2D frequency domain for each frame (dots). Mean frequency across all frames (dashed line) and one standard deviation (shaded area) are also shown.

Finally, an example of the second approach, in which the first and second consecutive phase-locked images are directly compared, is considered. Figure M.2 shows the d_x and d_y displacement fields obtained from this direct comparison, reflecting the intrinsic standard deviation of displacements between consecutive images more directly. The standard deviations between the frames are

$$\sigma_{\Delta d_x} = 0.092 \text{ px}, \quad \sigma_{\Delta d_y} = 0.094 \text{ px}.$$

While these results provide a more representative estimate of the intrinsic DIC noise, the absence of truly static image sequences prevents a definitive separation of algorithmic noise from physical motion of the free surface. Consequently, these analyses illustrate the scale of DIC-related variability in the present experiments, whereas the uncertainty adopted in the main text is based on literature benchmarks (Pan, 2018; Pan et al., 2010).

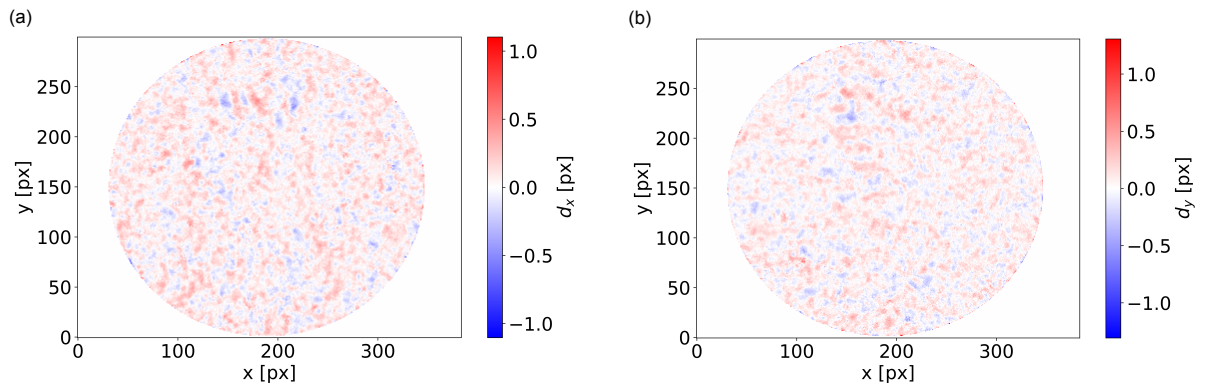


Figure M.2: Example of consecutive-frame DIC comparison, where the first dynamic frame serves as the reference and the second phase-locked frame is compared to it. Panel (a) shows the d_x displacement field and panel (b) the d_y displacement field.⁷

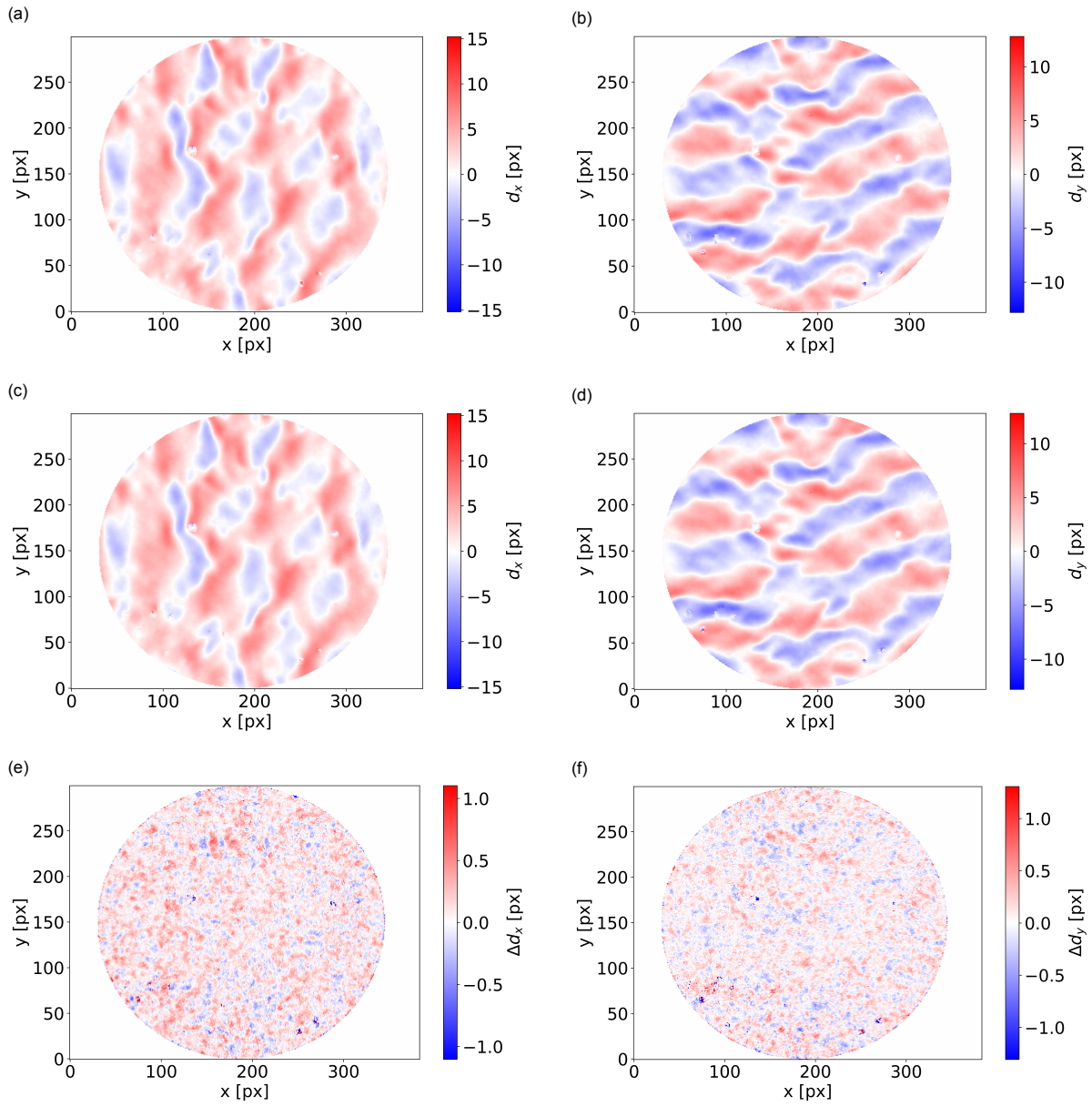
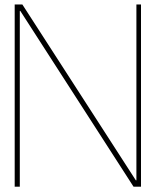


Figure M.3: Example of consecutive-frame DIC comparison using a static reference image. Panels (a–b) show the d_x and d_y displacement fields for the first phase-locked frame, panels (c–d) show the corresponding fields for the second frame, and panels (e–f) present the difference fields Δd_x and Δd_y obtained by subtraction.⁸



Signal extraction from laser distance measurements

The aim of this test is to evaluate whether the analog displacement signal from the laser distance meter can be accurately digitized and analyzed. Specifically, we seek to determine if the dominant frequency and amplitude of the shaker motion can be extracted using Fourier analysis. Additionally, we assess which sampling interval provides the most accurate estimation of the excitation frequency.

N.1. Test setup

The multifunction synthesizer and amplifier were used to excite the shaker at a constant frequency of 5 Hz with a large displacement amplitude to ensure clear motion. The laser distance meter captured displacement over time, and data acquisition was performed using a LabVIEW script.

Measurements were taken at various sampling intervals: 1, 2, 5, 10, 20, and 40 ms. To demonstrate the analysis process, the 20 ms case is discussed in detail. First, the raw displacement data was centered around zero. Because the time steps between measurements were not exactly uniform, the average time step was calculated and used for the Fourier transform. Amplitudes were estimated by taking half the difference between the maximum and minimum displacement within each oscillation cycle, and then averaging across all cycles.

N.2. Results

Figure N.1 shows the centered displacement data and its Fourier transform at a 20 ms sampling interval. A clear spectral peak at approximately 5 Hz confirms that the laser system successfully captured the excitation frequency.

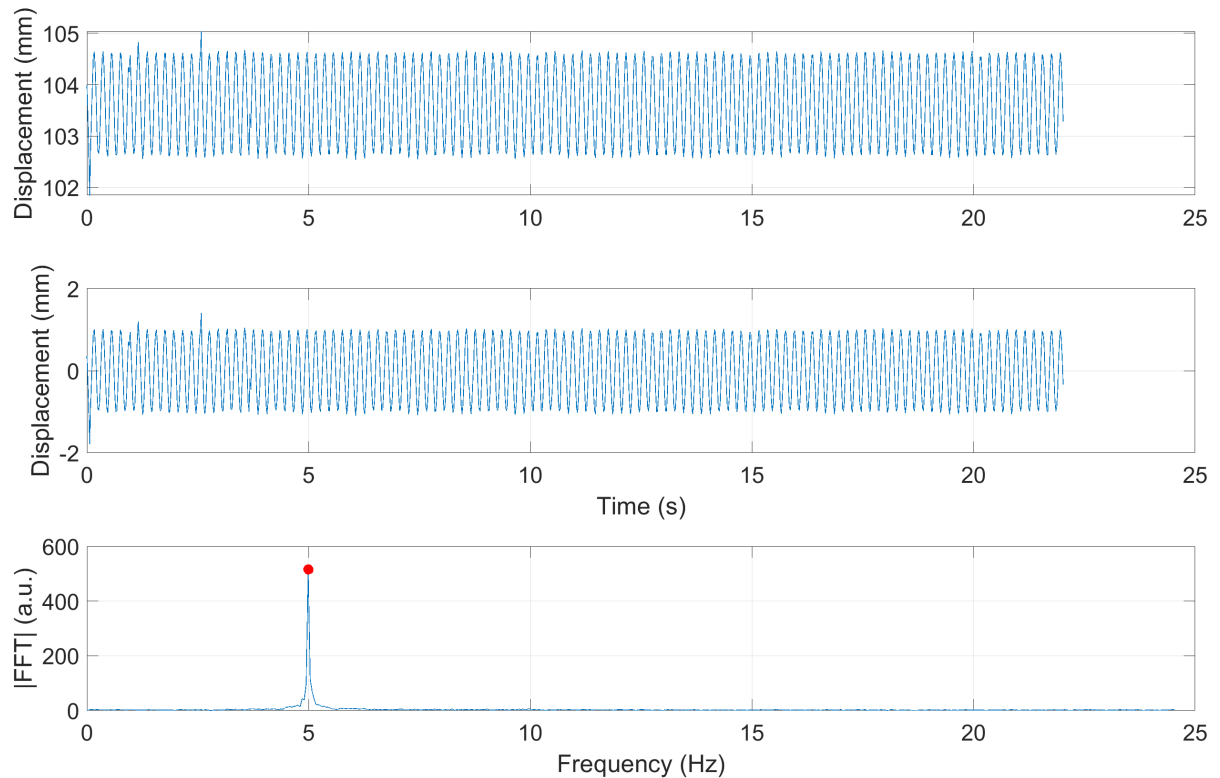


Figure N.1: Measured displacement, centered signal, and Fourier transform at 20 ms sampling interval.

Table N.1 summarizes the derived fundamental frequency and estimated amplitude for each sampling interval.

Table N.1: Derived fundamental frequency and estimated amplitude from laser distance meter measurements at various sampling intervals for a 5 Hz signal. A sampling interval of 20 ms (sampling frequency 50 Hz) provides the best accuracy in capturing the signal frequency, corresponding to 10 samples per cycle.

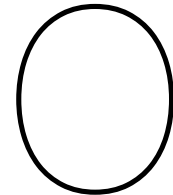
Sampling interval (ms)	Fundamental frequency (Hz)	Estimated amplitude (mm)
1	4.853	1.045
2	4.915	1.034
5	4.960	1.029
10	5.028	1.008
20	4.991	0.999
40	4.990	0.951

N.3. Discussion and conclusion

The results indicate that the laser distance meter can reliably capture both the amplitude and frequency of the oscillatory motion of the shaker. A pronounced peak at 5 Hz in the Fourier spectrum validates the accuracy of the frequency extraction. Furthermore, amplitude estimates remain consistent across different sampling intervals, though slight variations are present.

The sampling interval plays a significant role in frequency resolution. Sampling at a rate approximately ten times higher than the excitation frequency yields the most accurate and stable results. Sampling rates lower than this threshold may introduce artifacts or reduce accuracy, while significantly higher rates do not noticeably improve precision in this case.

Overall, the test confirms that the laser sensor is suitable for digitizing analog displacement signals and allows accurate extraction of key signal parameters.



Signal Extraction from Accelerometer Measurements

The objective of this test is to confirm whether analog voltage output from the accelerometer can be digitized correctly, and whether the excitation frequency and corresponding voltage amplitude can be reliably extracted using Fourier analysis. Furthermore, the test evaluates the impact of sampling interval on the accuracy of the frequency estimation.

O.1. Test setup

The accelerometer was mounted on the shaker, which was again excited at 5 Hz using the same synthesizer. Data acquisition was carried out via a self-developed LabVIEW script at multiple sampling intervals: 1, 2, 5, 10, 20, and 40 ms.

The acquired voltage data was centered around zero to enhance oscillatory visualization. A Fourier transform was applied using the average time step (due to slight timing inconsistencies in acquisition). Voltage amplitudes were estimated by calculating half of the peak-to-peak value for each oscillation cycle, and then averaging over all cycles.

O.2. Results

Figure O.1 presents the centered accelerometer data and its frequency spectrum for a sampling interval of 20 ms. As expected, a peak around 5 Hz confirms that the accelerometer signal correctly reflects the excitation frequency.

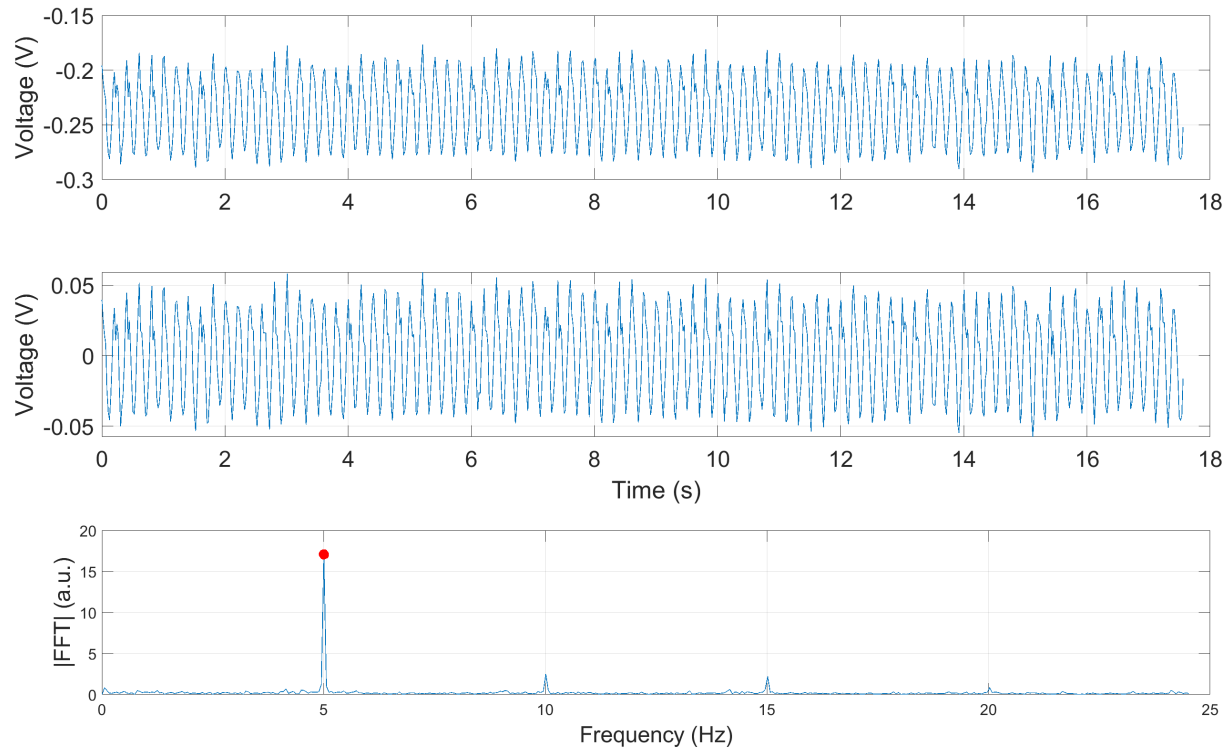


Figure O.1: Measured voltage, centered signal, and Fourier transform at 20 ms sampling interval.

Table O.1 provides the derived frequency and voltage amplitude across all tested sampling intervals.

Table O.1: Derived fundamental frequency and estimated amplitude from accelerometer measurements at various sampling intervals for a 5 Hz signal. A sampling interval of 20 ms (sampling frequency 50 Hz) provides the best accuracy in capturing the signal frequency, corresponding to 10 samples per cycle.

Sampling interval (ms)	Fundamental frequency (Hz)	Estimated amplitude (V)
1	4.969	0.052
2	4.948	0.055
5	4.966	0.051
10	5.017	0.049
20	5.006	0.044
40	4.984	0.040

O.3. Discussion and Conclusion

The results demonstrate that the accelerometer effectively captures the voltage variations associated with the oscillations of the shaker. The frequency content extracted via Fourier transform closely matches the known excitation frequency, validating the integrity of the analog-to-digital conversion process.

As with the laser measurements, sampling interval significantly affects accuracy. Sampling at or above ten times the excitation frequency ensures minimal distortion and accurate parameter extraction. Below this threshold, small deviations become more pronounced. Voltage amplitude estimates also decrease slightly at lower sampling rates, likely due to under-sampling and loss of waveform detail.

In conclusion, the accelerometer setup performs reliably for extracting dynamic properties of oscillatory motion, provided that an adequate sampling rate is maintained.

P

Measured displacement at different sample intervals

Sample interval 1 ms

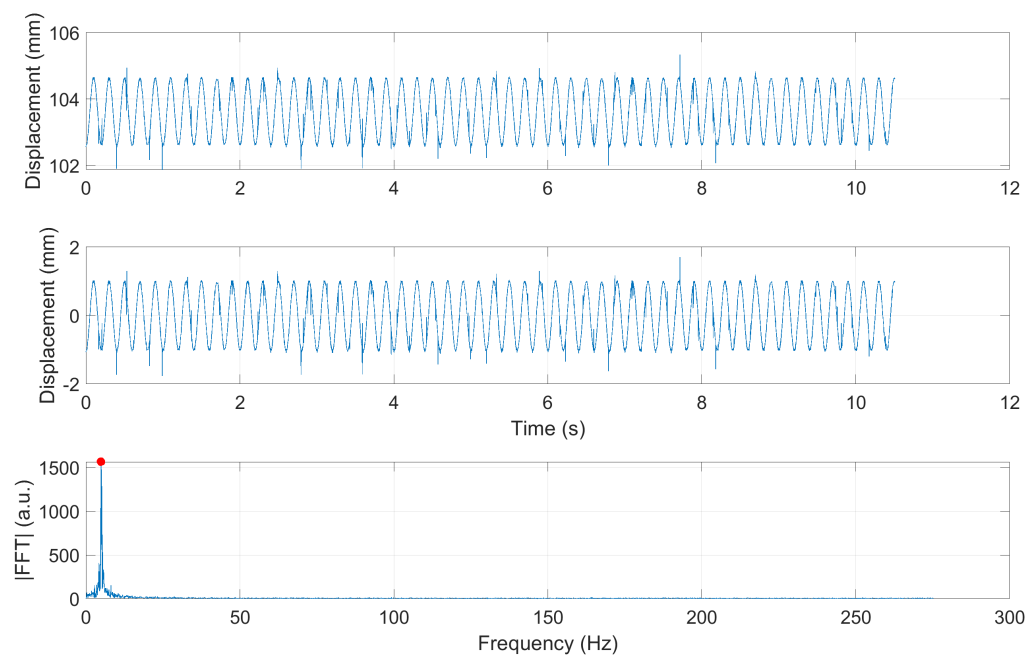


Figure P.1: Measured displacement, centered signal, and Fourier transform at 1 ms sampling interval..

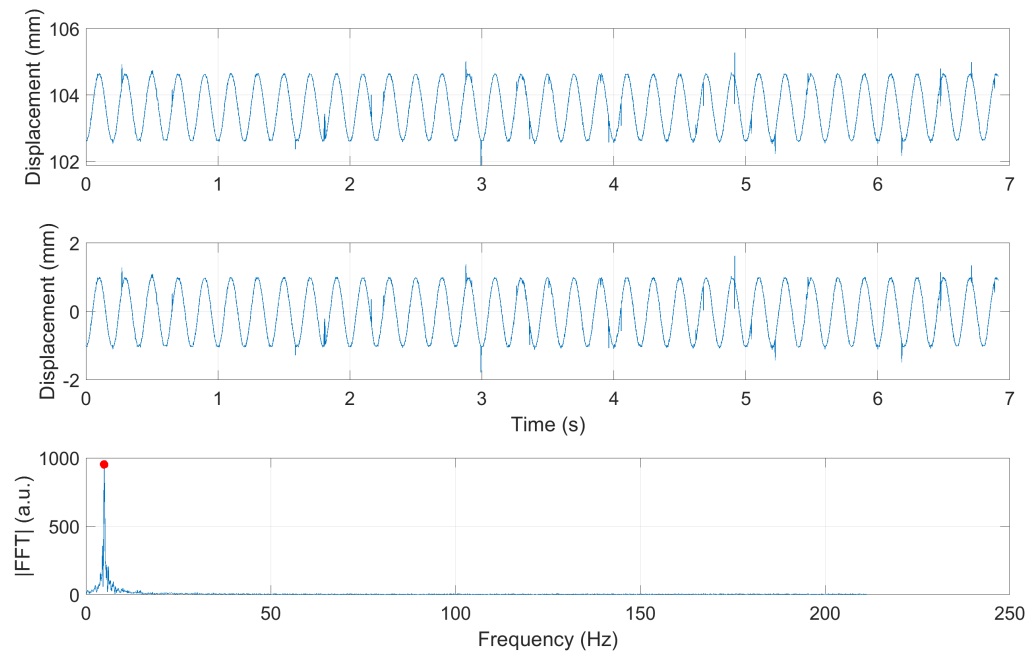
Sample interval 2 ms

Figure P.2: Measured displacement, centered signal, and Fourier transform at 2 ms sampling interval.

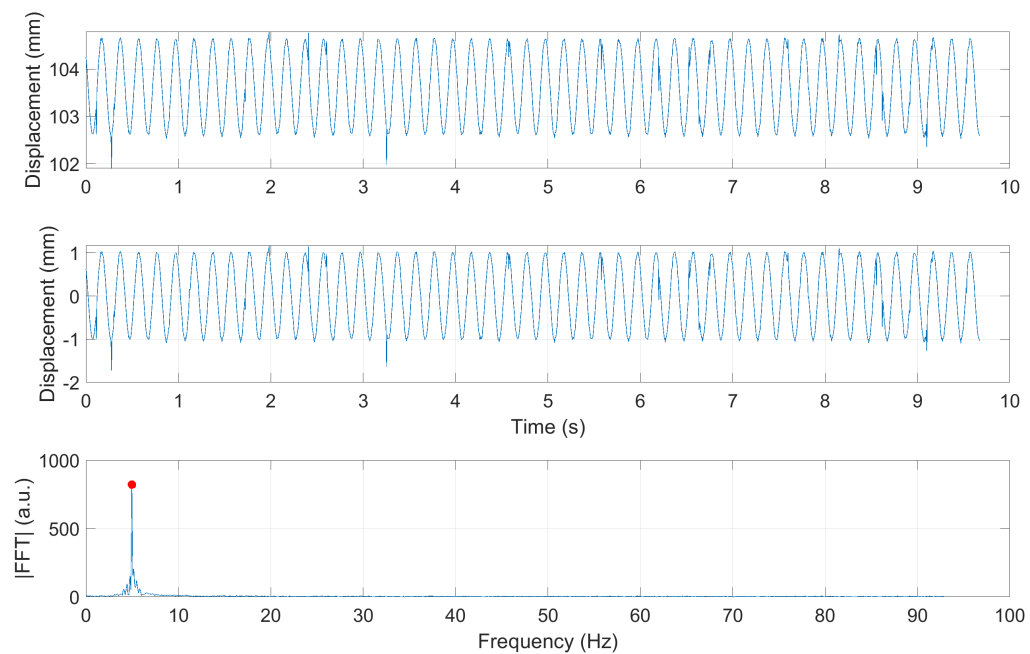
Sample interval 5 ms

Figure P.3: Measured displacement, centered signal, and Fourier transform at 5 ms sampling interval.

Sample interval 10 ms

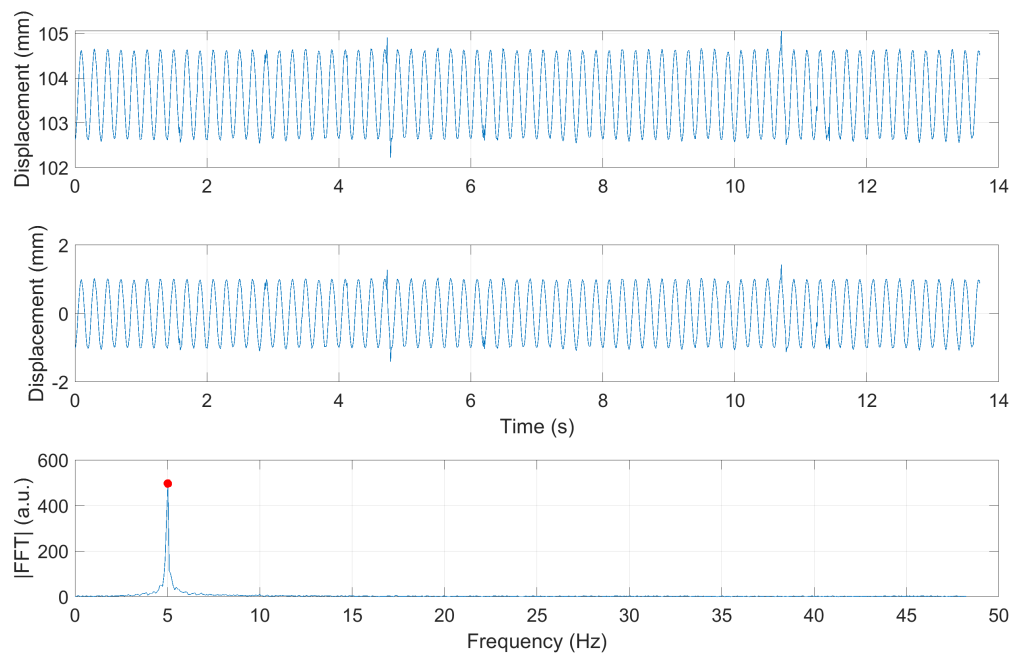


Figure P.4: Measured displacement, centered signal, and Fourier transform at 10 ms sampling interval.

Sample interval 20 ms

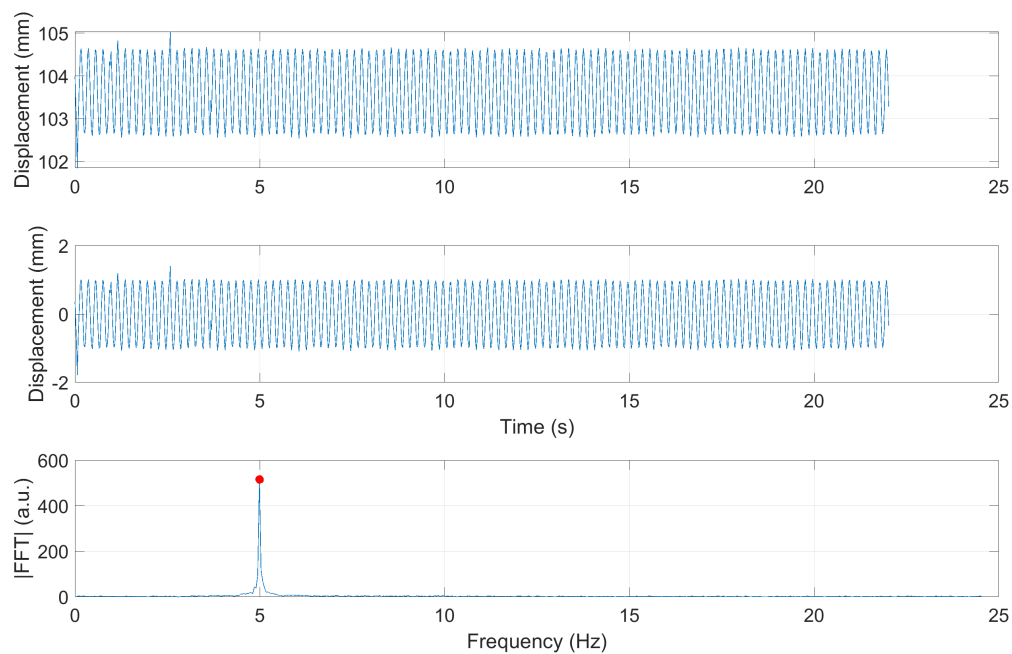


Figure P.5: Measured displacement, centered signal, and Fourier transform at 20 ms sampling interval.

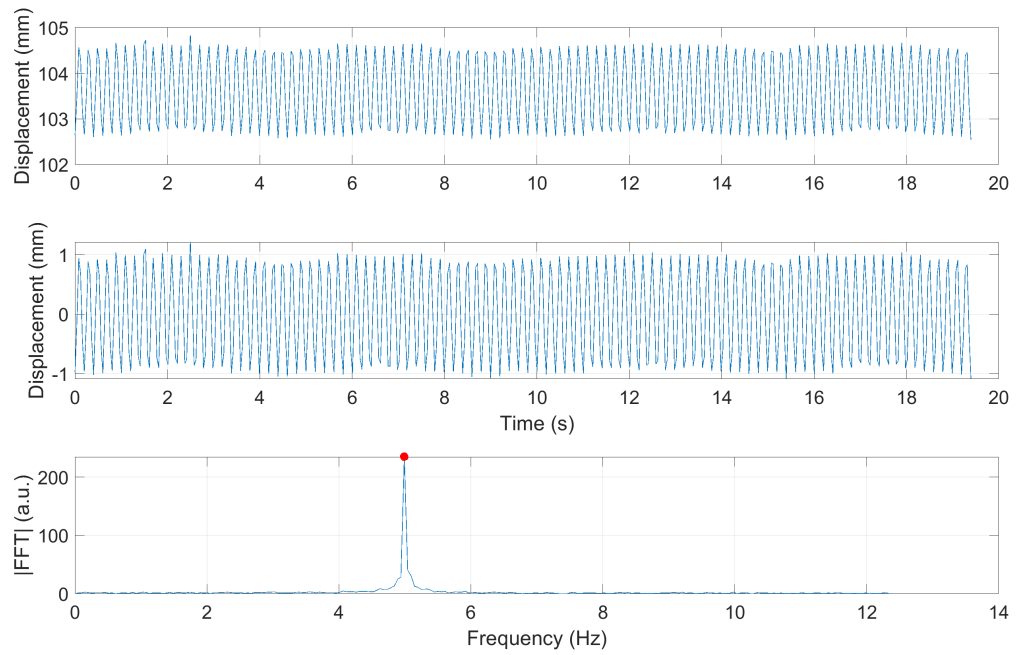
Sample interval 40 ms

Figure P.6: Measured displacement, centered signal, and Fourier transform at 40 ms sampling interval.

Q

Measured voltage at different sample intervals

Sample interval 1 ms

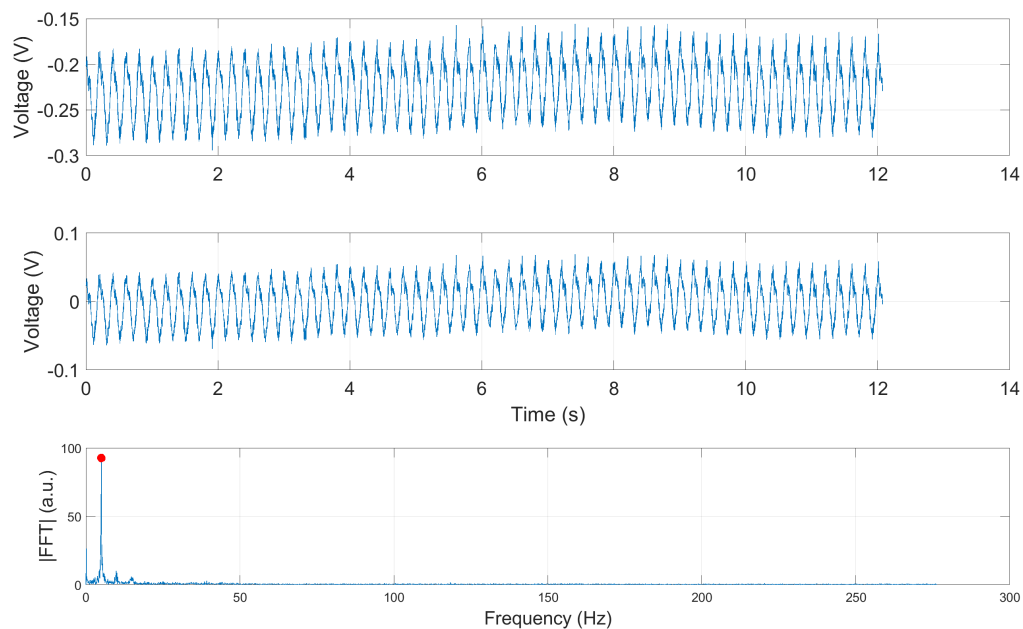


Figure Q.1: Measured voltage, centered signal, and Fourier transform at 1 ms sampling interval.

Sample interval 2 ms

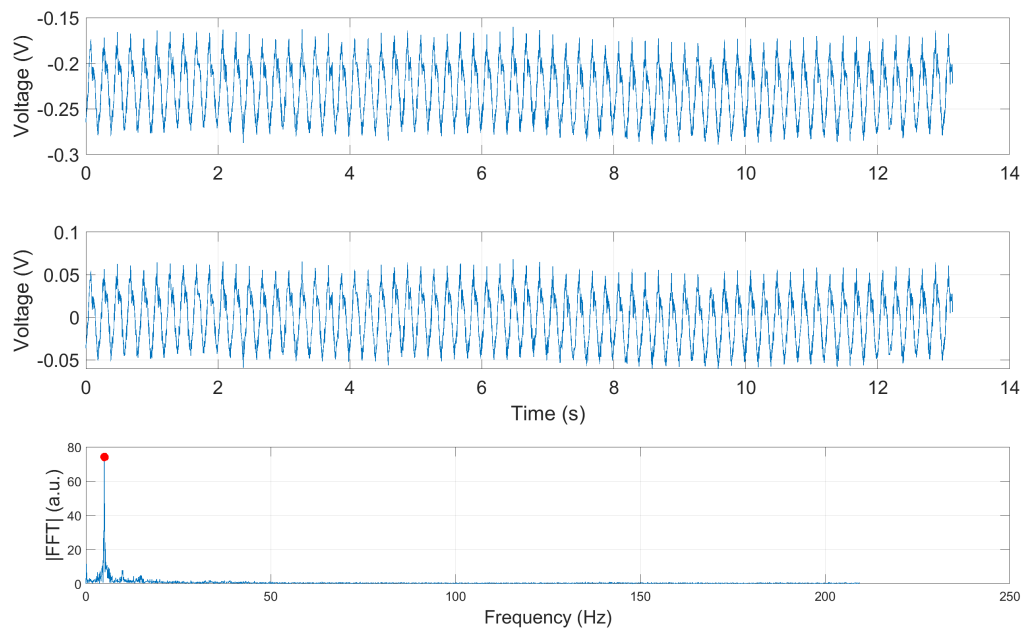


Figure Q.2: Measured voltage, centered signal, and Fourier transform at 2 ms sampling interval.

Sample interval 5 ms

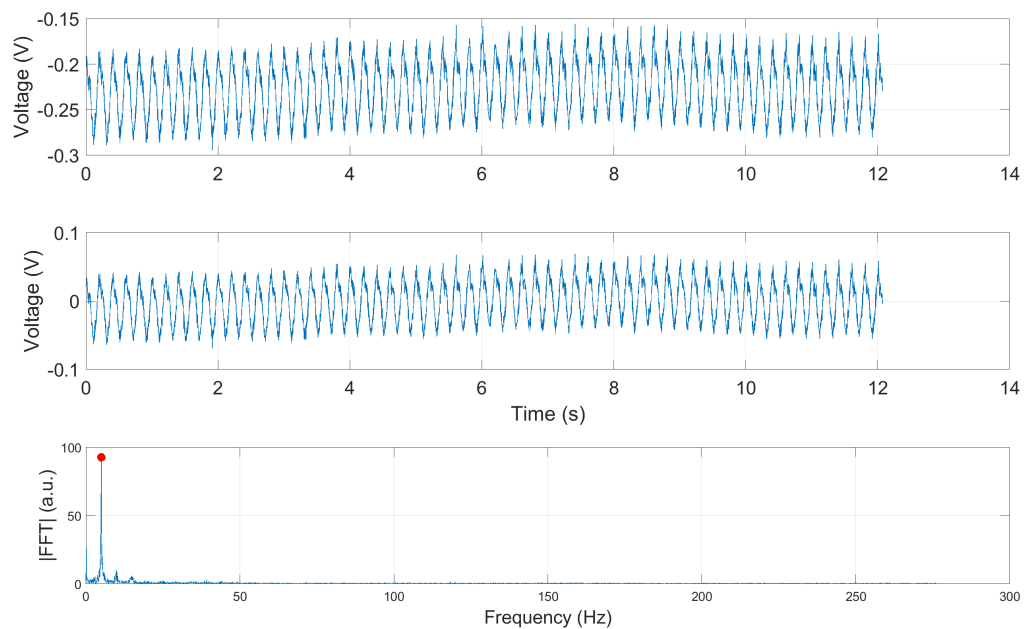


Figure Q.3: Measured voltage, centered signal, and Fourier transform at 5 ms sampling interval.

Sample interval 10 ms

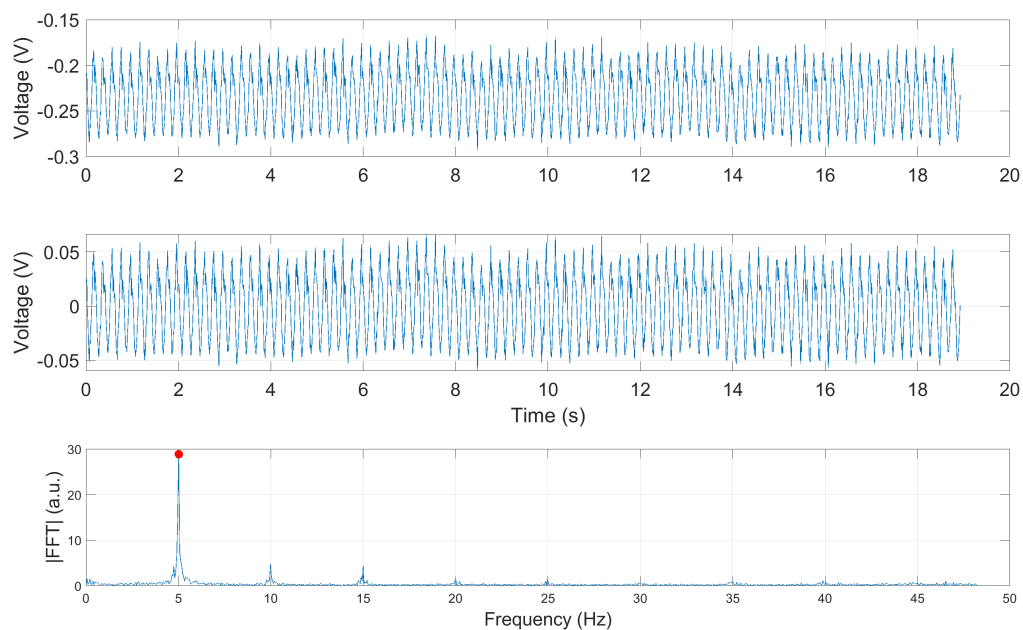


Figure Q.4: Measured voltage, centered signal, and Fourier transform at 10 ms sampling interval.

Sample interval 20 ms

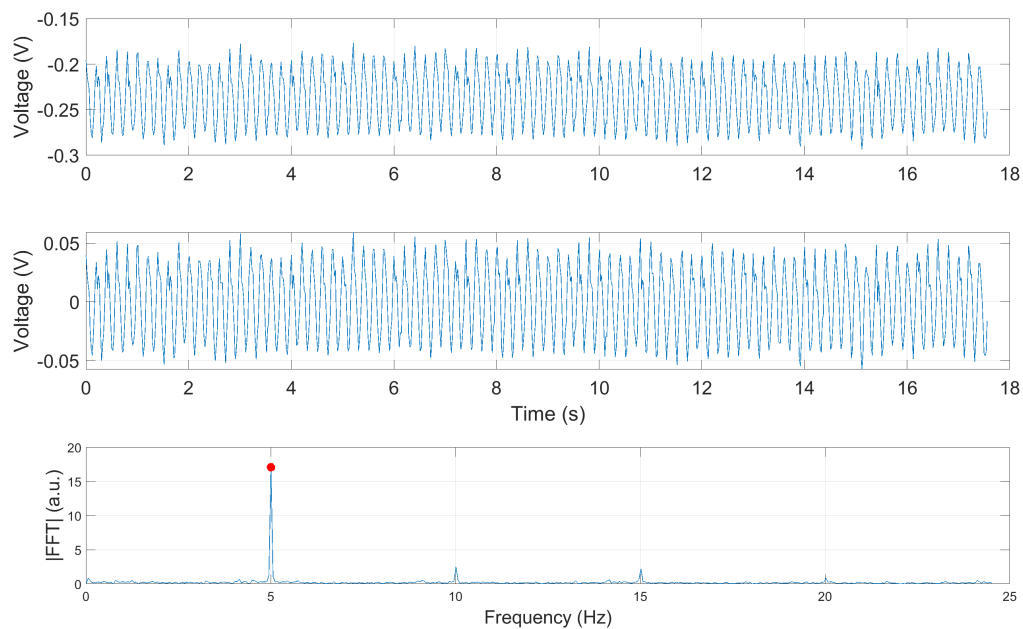


Figure Q.5: Measured voltage, centered signal, and Fourier transform at 20 ms sampling interval.

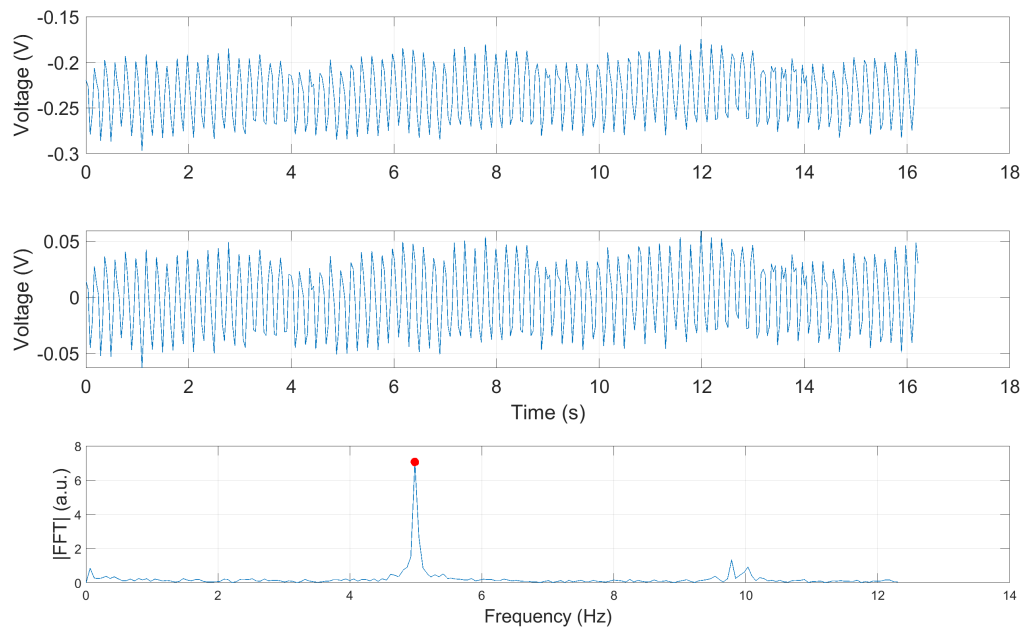
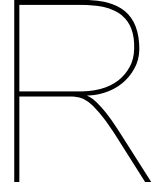
Sample interval 40 ms

Figure Q.6: Measured voltage, centered signal, and Fourier transform at 40 ms sampling interval.



Wavelength uncertainty data

This appendix presents the dataset used to evaluate propagated uncertainty in dominant wavelength estimation from a DIC-derived in-plane displacement vector field. Table R.1 reports:

- Theoretical wavelength λ_{mm} in millimeters (Column 1) and theoretical wavelength λ_{px} in pixels (Column 2).
- Uncertainties in spatial frequency resolution on wavelength $\delta\lambda_{\text{FFT}}$ (Column 3), uncertainty in radial spatial binning on wavelength $\delta\lambda_{\text{rad}}$ (Column 4), and uncertainty due to DIC noise $\delta\lambda_{\text{DIC}}$ (Column 5), all in pixels.
- Combined uncertainty on wavelength $\delta\lambda_{\text{px}}$ in pixels (Column 6) and combined uncertainty on wavelength $\delta\lambda_{\text{mm}}$ in millimeters (Column 7).
- Relative uncertainty as a percentage of λ (Column 8).

The following parameters were used in the uncertainty calculation:

- Calibrated pixel size: $p = 0.0600 \pm 0.0014$ mm/px
- Subset spacing (grid spacing): $s = 4$ px
- Grid size: $N = 295$
- Spatial frequency resolution: $\delta f_{\text{FFT}} = \frac{1}{N \cdot s}$
- Number of radial bins: 1200
- DIC noise standard deviation: $\sigma_{\text{DIC}} = 0.02$ px

Table R.1: Overview of expected Faraday wave wavelengths with associated uncertainty contributions. The table lists the wavelength in millimeters (λ_{mm}) and pixels (λ_{px}), together with the uncertainty contributions from the Fourier transform ($\delta\lambda_{\text{FFT}}$), radial averaging ($\delta\lambda_{\text{radial}}$), and Digital Image Correlation (DIC, $\delta\lambda_{\text{DIC}}$) in pixels. The total uncertainty in pixels ($\delta\lambda_{\text{total, px}}$) and millimeters ($\delta\lambda_{\text{mm}}$), as well as the relative error (%), are also provided.

λ_{mm} (mm)	λ_{px} (px)	$\delta\lambda_{\text{FFT}}$ (px)	$\delta\lambda_{\text{radial}}$ (px)	$\delta\lambda_{\text{DIC}}$ (px)	$\delta\lambda_{\text{total, px}}$ (px)	$\delta\lambda_{\text{mm}}$ (mm)	Error (%)
4.000	66.667	3.7665	0.1875	0.0753	3.7719	0.2448	6.12
4.429	73.810	4.6168	0.2298	0.0923	4.6235	0.2960	6.68
4.857	80.952	5.5536	0.2764	0.1111	5.5616	0.3524	7.26
5.286	88.095	6.5769	0.3274	0.1315	6.5864	0.4140	7.83
5.714	95.238	7.6867	0.3826	0.1537	7.6977	0.4807	8.41
6.143	102.381	8.8829	0.4421	0.1777	8.8957	0.5527	9.00
6.571	109.524	10.1656	0.5060	0.2033	10.1803	0.6298	9.58
7.000	116.667	11.5348	0.5741	0.2307	11.5514	0.7121	10.17
7.429	123.810	12.9905	0.6466	0.2598	13.0092	0.7996	10.76
7.857	130.952	14.5326	0.7233	0.2907	14.5535	0.8923	11.36
8.286	138.095	16.1613	0.8044	0.3232	16.1845	0.9901	11.95
8.714	145.238	17.8764	0.8898	0.3575	17.9021	1.0932	12.54
9.143	152.381	19.6779	0.9794	0.3936	19.7062	1.2015	13.14
9.571	159.524	21.5660	1.0734	0.4313	21.5970	1.3149	13.74
10.000	166.667	23.5405	1.1717	0.4708	23.5743	1.4336	14.34
10.429	173.810	25.6015	1.2743	0.5120	25.6383	1.5574	14.93
10.857	180.952	27.7490	1.3811	0.5550	27.7888	1.6865	15.53
11.286	188.095	29.9829	1.4923	0.5997	30.0260	1.8207	16.13
11.714	195.238	32.3033	1.6078	0.6461	32.3498	1.9601	16.73
12.143	202.381	34.7102	1.7276	0.6942	34.7601	2.1048	17.33
12.571	209.524	37.2036	1.8517	0.7441	37.2571	2.2546	17.93
13.000	216.667	39.7834	1.9801	0.7957	39.8406	2.4096	18.54
13.429	223.810	42.4497	2.1128	0.8490	42.5108	2.5698	19.14
13.857	230.952	45.2025	2.2499	0.9041	45.2675	2.7352	19.74
14.286	238.095	48.0418	2.3912	0.9608	48.1109	2.9058	20.34
14.714	245.238	50.9676	2.5368	1.0194	51.0408	3.0816	20.94
15.143	252.381	53.9798	2.6867	1.0796	54.0574	3.2626	21.55
15.571	259.524	57.0785	2.8409	1.1416	57.1605	3.4488	22.15
16.000	266.667	60.2637	2.9995	1.2053	60.3503	3.6402	22.75
16.429	273.810	63.5353	3.1623	1.2707	63.6266	3.8368	23.35
16.857	280.952	66.8934	3.3295	1.3379	66.9896	4.0386	23.96
17.286	288.095	70.3380	3.5009	1.4068	70.4391	4.2456	24.56
17.714	295.238	73.8691	3.6767	1.4774	73.9753	4.4577	25.16
18.143	302.381	77.4866	3.8567	1.5497	77.5980	4.6751	25.77
18.571	309.524	81.1907	4.0411	1.6238	81.3074	4.8977	26.37
19.000	316.667	84.9812	4.2297	1.6996	85.1033	5.1254	26.98
19.429	323.810	88.8581	4.4227	1.7772	88.9859	5.3584	27.58
19.857	330.952	92.8216	4.6200	1.8564	92.9550	5.5965	28.18
20.286	338.095	96.8715	4.8216	1.9374	97.0108	5.8399	28.79
20.714	345.238	101.0079	5.0274	2.0202	101.1531	6.0884	29.39
21.143	352.381	105.2308	5.2376	2.1046	105.3821	6.3421	30.00
21.571	359.524	109.5401	5.4521	2.1908	109.6976	6.6011	30.60
22.000	366.667	113.9360	5.6709	2.2787	114.0998	6.8652	31.21
22.429	373.810	118.4183	5.8940	2.3684	118.5885	7.1345	31.81
22.857	380.952	122.9870	6.1214	2.4597	123.1639	7.4091	32.41
23.286	388.095	127.6423	6.3531	2.5528	127.8258	7.6888	33.02
23.714	395.238	132.3840	6.5891	2.6477	132.5743	7.9737	33.62
24.143	402.381	137.2122	6.8294	2.7442	137.4095	8.2638	34.23
24.571	409.524	142.1269	7.0740	2.8425	142.3312	8.5591	34.83
25.000	416.667	147.1281	7.3230	2.9426	147.3396	8.8596	35.44